COVID-19's devastating march through the body p. 356

Watching skyrmions on the fly p. 386

Visualizing the radical transfer path in a protein complex p. 424

Science

$15
24 APRIL 2020

AAAS

INSECT DECLINE

Scattered gains, widespread losses pp. 368 & 417

CALL FOR PAPERS

SPJ
SCIENCE PARTNER JOURNALS

BIACD

Advanced Devices & Instrumentation

OPEN ACCESS

Advanced Devices & Instrumentation is an online-only open access journal published in affiliation with **Beijing Institute of Aerospace Control Devices (BIACD)** and distributed by the **American Association for the Advancement of Science (AAAS)**. *Advanced Devices & Instrumentation* aims to publish the latest investigations on novel ideas, methods, and techniques for the development and manufacture of advanced devices and instrumentation, as well as novel and practical solutions for existing applications.

Submit your research to *Advanced Devices & Instrumentation* today!

Learn more at **spj.sciencemag.org/adi**

The Science Partner Journals (SPJ) program was established by the American Association for the Advancement of Science (AAAS), the non-profit publisher of the *Science* family of journals. The SPJ program features high quality, online-only, editorially independent open-access publications produced in collaboration with international research institutions, foundations, funders and societies. Through these collaborations, AAAS expands its efforts to communicate science broadly and for the benefit of all people by providing a top-tier international research organization with the technology, visibility, and publishing expertise that AAAS is uniquely positioned to offer as the world's largest. Visit us at **spj.sciencemag.org**

@SPJournals **@SPJournals**

ARTICLE PROCESSING CHARGES WAIVED UNTIL 2023

Pushing the Boundaries of Knowledge

As AAAS's first multidisciplinary, open access journal, *Science Advances* publishes research that reflects the selectivity of high impact, innovative research you expect from the *Science* family of journals, published in an open access format to serve a vast and growing global audience. Check out the latest findings or learn how to submit your research: **ScienceAdvances.org**

Science Advances
AAAS

GOLD OPEN ACCESS, DIGITAL, AND FREE TO ALL READERS

LSAMP-NICE offers Bridge-to-Ph.D. programs as well as travel opportunities—such as to Bordeaux, France.

LSAMP-NICE BOOSTS INTERNATIONAL RESEARCH OPPORTUNITIES FOR UNDERREPRESENTED STEM STUDENTS

Graduate student Deisy Carvalho Fernandes had a puddle problem. The nanomaterials she studied at the University of Illinois at Chicago (UIC) could potentially form the raw material for 3D printing new electronic devices because of their ability to conduct electricity. But when used as the ink in a 3D printer, they were far too runny—forming useless small pools rather than holding a shape.

To find a solution, Carvalho Fernandes traveled 4,150 miles on an 8-hour flight across the Atlantic Ocean—twice—to conduct research in a materials science lab in Bordeaux, France. This unique 6-month collaboration not only resulted in a fix, it broadened her worldview of scientific research.

For almost 30 years, the Louis Stokes Alliances for Minority Participation (LSAMP) program, funded by the U.S. National Science Foundation (NSF), has supported undergraduate and graduate students from historically underrepresented minority groups across the United States in science, technology, engineering, and mathematics (STEM) fields through evidence-based strategies, such as Research Experiences for Undergraduates and Bridge-to-Ph.D. programs. Now, the new Louis Stokes Regional NSF International Center of Excellence (LSAMP-NICE) merges the knowledge and best practices of LSAMP alliance institutions with the power of NSF programs and collaborating global partners to broaden the participation of minority scientists in international research experiences.

"Science and innovation are global," says Zakiya Wilson-Kennedy, assistant dean for diversity and inclusion at Louisiana State University in Baton Rouge and an LSAMP-NICE co-principal investigator (PI). "Giving students a chance to engage in international research experiences puts them on the best path to be part of a global enterprise."

Numerous research and networking opportunities

Although LSAMP-NICE does not directly fund student programming or travel, it provides students and faculty members a network of expertise and resources for exploring international collaborative research opportunities. International partners include the National Research Foundation in Pretoria, South Africa; King Abdullah

PHOTO: SHUTTERSTOCK/WILLIAM POTTER

Deisy Carvalho Fernandes worked abroad for her project on 3D printing "inks."

University of Science and Technology in Thuwal, Saudi Arabia; the University of Bordeaux and the University of Toulouse in France; Feng Chia University in Taichung, Taiwan; and the countries of Brazil, Costa Rica, and Panama.

At these partner sites, undergraduate students work on short-term research experiences, and graduate students and their domestic and international faculty co-mentors are involved in collaborative research projects. The center ensures scientific research participation—not merely simple observation—through digital archiving and dissemination of students' scientific contributions.

"When working in research, success requires new ideas, and those come from people from diverse regions and with diverse backgrounds," says Vikas Berry, head of UIC's chemical engineering department and a nanotechnologist there, who is also Carvalho Fernandes's Ph.D. supervisor. "This program [LSAMP-NICE] exposes students to new ways of living or doing work and shows that those can still be successful."

Gelling with another approach

For her doctorate in chemical engineering, Carvalho Fernandes was investigating the properties of 2D nanomaterials with the overall goal of 3D printing unique electronic devices on demand. Currently, most 3D printing makes static structures, Berry explains. His group would like to eventually enable consumers to print working lightbulbs, solar panels, or carbon monoxide sensors at home.

Carvalho Fernandes studied nanomaterials based on graphene, a single-atom-thick sheet of carbon atoms that is extremely thin and very conductive of electricity, but not especially suited for use as the matrix ink of a 3D printer.

"When we concentrate graphene dispersion from a liquid into a gel, it can be extruded more like toothpaste, and can form 3D structures," explains Berry. "Inclusion of other polymers or nanomaterials into the gel can add functionality to the superior electrical properties of graphene."

LSAMP-NICE connected the Berry Lab with Research Director Philippe Poulin's laboratory at the Centre de Recherche Paul Pascal, University of Bordeaux, France, which studies gel inks for 3D printing. After spending a couple of 3-month stints working with Poulin's group, Carvalho Fernandes created several gel versions of her graphene- (and other nanomaterials)-based inks. Now, she's testing them back in Chicago for gelation, printability, conductivity, and temperature. These gel inks have been used to 3D print simple electronic devices that can produce light.

Travel benefits

The international research benefited Carvalho Fernandes' thesis work and professional development in several ways. She was exposed to a different research environment that took alternative approaches, and she also learned how to perform rheology experiments to strain-test materials, along with other techniques not available at UIC. She also says that the experience proves she can be a successful collaborator in the future.

Carvalho Fernandes, an LSAMP Bridge to the Doctorate fellow, is now finishing up her Ph.D. thesis and drafting a research paper in collaboration with the French group. "We were really excited to join forces with Poulin's group, and we produced such remarkable structures in this collaboration that wouldn't have happened without LSAMP-NICE," says Berry.

LSAMP-NICE gave its first Faculty Advisor Award to Berry, which allowed him to travel to the Bordeaux lab for a week while Carvalho Fernandes was there. He met his collaborators, saw their experimental equipment and techniques in person, and helped plan future experiments. "Having a physical presence in the lab really strengthened the collaboration," says Berry.

Carvalho Fernandes (middle) with her two mentors Vikas Berry (left) and Philippe Poulin (right). With help from LSAMP-NICE, she finished her project and a new collaboration among the three was born.

PHOTOS: COURTESY OF LSAMP

Louis Stokes Alliances for Minority Participation (LSAMP)

The Louis Stokes Alliances for Minority Participation (LSAMP), represented by 57 member alliances across the United States, has provided professional development and academic and financial support programming for undergraduate students from historically underrepresented minority groups in science, technology, engineering, and mathematics (STEM) disciplines. In 2003, graduate student programming was added via the LSAMP Bridge to the Doctorate program. The Louis Stokes Regional NSF International Center of Excellence (LSAMP-NICE) is one of six regional centers awarded in 2018. Specifically charged with the dissemination of information and best practices to broaden participation in international collaborative research, LSAMP-NICE is a collaboration of four institutions: Salish Kootenai College (SKC), a tribal college in Pablo, Montana; Jackson State University (JSU), a historically black college/university in Jackson, Mississippi; Louisiana State University (LSU), an R1 (doctoral university, very high research) institution in Baton Rouge, Louisiana; and the University of Illinois at Chicago (UIC), an R1 and Hispanic-serving institution. All LSAMP projects are funded through the NSF Broadening Participation initiative, spearheaded by A. James Hicks, program director of the NSF Directorate for Education and Human Resources. Hicks has been a champion for the development of underrepresented minority students in science for decades, and through his ongoing commitment to excellence in science, has positively affected the lives of literally hundreds of thousands of students across the country.

Widening the network

LSAMP-NICE was awarded funding to carry out a 5-year project that will support building bridges between existing LSAMP and NSF international projects and programs. "The center will provide foundations for new initiatives as well as build on partnerships already established," says Wilson-Kennedy.

A large component of this project will be to build a community of practice, bringing together individuals from the different LSAMP campuses to share best practices for serving underrepresented minority STEM students. Discussions will focus on how to develop and implement programs encouraging undergraduate student exposure to international collaboration and research; how best to incorporate international collaboration into the doctoral education experience; and how best to facilitate the cultural preparation and immersion process.

The work being done with indigenous populations by environmental scientist Jessica Black of Heritage University in Toppenish, Washington (an All Nations LSAMP member institution), is a best practice exemplar. Black organizes trips for Hispanic/Latinx and Native American students to travel to Panama and Costa Rica to partner with indigenous tribes in the field of natural resource management.

"What started out a small pilot in 2015 has developed into an annual collaborative event that the All Nations LSAMP students and faculty vie for a spot on each December," says Steve Dupuis, LSAMP-NICE PI and co-PI for All Nations LSAMP at Salish Kootenai College in Pablo, Montana.

Future directions

According to Denise Yates, co-PI and director for the LSAMP Bridge to the Doctorate at UIC, the partnership between Berry, Poulin, and Carvalho Fernandes was a perfect fit and an excellent model for the pilot demonstration of the feasibility and efficacy of international research collaboration for graduate students.

Berry says that the collaboration LSAMP-NICE facilitated has broadened both his own network and his students'. "This was a really powerful way to expand the capabilities and the reach of our research in the lab," he says. "When you start talking to and working with international collaborators, the math changes, where one plus one does not equal just two. It is at least four."

Sponsored by

LSAMP-NICE
NSF International Center of Excellence

CONTENTS

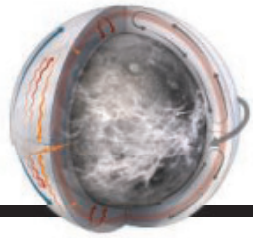

363 & 405
Winds on Venus

24 APRIL 2020 • VOLUME 368 • ISSUE 6489

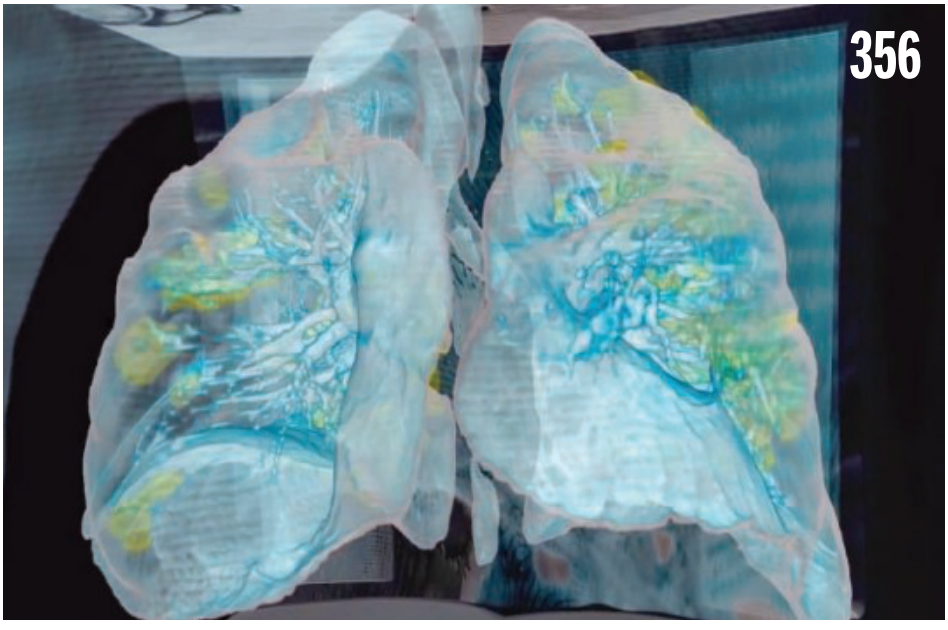

NEWS

IN BRIEF

348 News at a glance

IN DEPTH

350 First antibody surveys draw fire for quality, bias
Some study authors use serology data to call for easing lockdowns, but critics push back
By G. Vogel

351 NIH organizes hunt for drugs
Firms to help prioritize treatment and vaccine trials *By J. Kaiser*

352 Indigenous communities in Brazil fear pandemic's impact
Other infections and scant medical care may worsen toll
By I. Amigo

353 Mass screening weighed for type 1 diabetes risk
Studies find benefit to testing thousands of children for antibodies that precede symptoms
By J. Couzin-Frankel

354 Diamond microscope unlocks ancient rocks' magnetic secrets
Quantum sensor reveals clues about plate tectonics, planet formation, and climate change with exquisite resolution *By P. Voosen*
SCIENCE ADVANCES RESEARCH ARTICLE BY A. R. BRENNER *ET AL*. 10.1126/SCIADV.AAZ8670; PODCAST

355 Heat-protected plants offer cool surprise—greater yields
Engineered rice grows better at normal temperatures *By E. Stokstad*

FEATURES

356 A ramapage through the body
The lungs are ground zero, but COVID-19 also tears through organ systems from brain to blood vessles *By M. Wadman* et al.

359 Survivors' burden
By K. Servick
PODCAST

INSIGHTS

QQ群: 970508760

PERSPECTIVES

362 Mucosal immunity and the eradication of polio
Completing global polio eradication will require a new oral vaccine
By A. N. Donlan and W. A. Petri Jr.
RESEARCH ARTICLE p. 401

363 Super-rotating the venusian atmosphere
Analysis of spacecraft observations deciphers the source of fast atmospheric rotation *By S. Lebonnois*
REPORT p. 405

365 Cultivating fungal research
Growing interest in host-fungal interactions has implications for human health and disease
By H. H. Kong and J. A. Segre

367 Next-generation epigenetic inhibitors
Selective bromodomain inhibitors provide new opportunities to modulate transcription *By P. Filippakopoulos and S. Knapp*
RESEARCH ARTICLE p. 387

368 Nuanced changes in insect abundance
Trends in insect abundance vary across time, ecosystems, and continents
By M. Dornelas and G. N. Daskalova
REPORT p. 417

369 Calcium as a biased cofactor
Crystal structure of an anti-obesity drug target reveals an important calcium-binding site *By M. Chaturvedi and A. K. Shukla*
REPORT p. 428

371 Mary Lowe Good (1931–2019)
Renowned chemist, respected leader, and inspiring mentor *By M. A. Cavanaugh*

POLICY FORUM

372 Dissolved oxygen and pH criteria leave fisheries at risk
Regulations have not kept pace with scientific understanding of coastal hypoxia and acidification
By S. J. Tomasetti and C. J. Gobler

CREDITS (FROM TOP): C. BICKEL/*SCIENCE*; GEORGE WASHINGTON HOSPITAL AND SURGICAL THEATER; AFRICA STUDIO/SHUTTERSTOCK.COM

QQ群: 970508760

BOOKS *ET AL.*

374 The trouble with turning to nature
Our obsession with "natural" products and practices is a proxy for other values
By S. Camporesi

375 A history of the metaphorical brain
Analogies abound and inform our quest to understand the nervous system
By A. Gomez-Marin

LETTERS

376 Retraction
By C. Sow et al.

376 Canada's mines pose transboundary risks
By E. K. Sexton et al.

377 Investments' role in ecosystem degradation
By M. G. Ceddia

377 Response
By S. Díaz et al.

RESEARCH

IN BRIEF

381 From *Science* and other journals

REVIEW

384 Proteostasis
The integrated stress response: From mechanism to disease
M. Costa-Mattioli and P. Walter
REVIEW SUMMARY; FOR FULL TEXT: DX.DOI.ORG/10.1126/SCIENCE.AAT5314

RESEARCH ARTICLES

385 Structural biology
Structural basis of ER-associated protein degradation mediated by the Hrd1 ubiquitin ligase complex
X. Wu et al.
RESEARCH ARTICLE SUMMARY; FOR FULL TEXT: DX.DOI.ORG/10.1126/SCIENCE.AAZ2449

386 Ultrafast microscopy
Ultrafast vector imaging of plasmonic skyrmion dynamics with deep subwavelength resolution
T. J. Davis et al.
RESEARCH ARTICLE SUMMARY; FOR FULL TEXT: DX.DOI.ORG/10.1126/SCIENCE.ABA6415

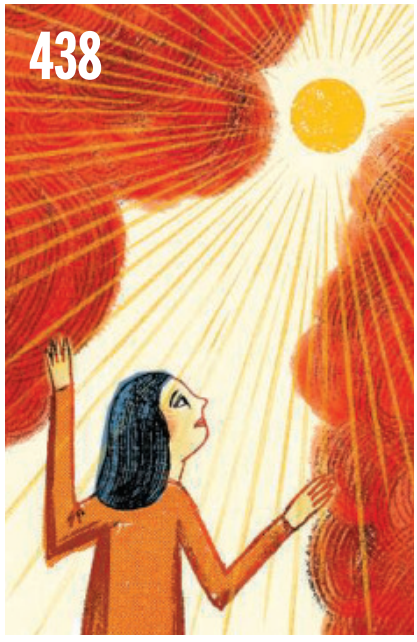

387 Drug discovery
Selective targeting of BD1 and BD2 of the BET proteins in cancer and immunoinflammation *O. Gilan* et al.
PERSPECTIVE p. 367

395 Coronavirus
The effect of travel restrictions on the spread of the 2019 novel coronavirus (COVID-19) outbreak *M. Chinazzi* et al.

401 Poliovirus
Evolving epidemiology of poliovirus serotype 2 following withdrawal of the serotype 2 oral poliovirus vaccine
G. R. Macklin et al.
PERSPECTIVE p. 362

REPORTS

405 Atmospheric physics
How waves and turbulence maintain the super-rotation of Venus' atmosphere
T. Horinouchi et al.
PERSPECTIVE p. 363

409 Coronavirus
Crystal structure of SARS-CoV-2 main protease provides a basis for design of improved α-ketoamide inhibitors
L. Zhang et al.

413 RNA structure
Structural basis for transcriptional start site control of HIV-1 RNA fate
J. D. Brown et al.

417 Insect populations
Meta-analysis reveals declines in terrestrial but increases in freshwater insect abundances
R. van Klink et al.
PERSPECTIVE p. 368

420 Paleontology
The spatial structure of Phanerozoic marine animal diversity
R. A. Close et al.

424 Protein radicals
Structure of a trapped radical transfer pathway within a ribonucleotide reductase holocomplex
G. Kang et al.

428 Structural biology
Determination of the melanocortin-4 receptor structure identifies Ca^{2+} as a cofactor for ligand binding
J. Yu et al.
PERSPECTIVE p. 369

DEPARTMENTS

341 Editorial
Why WHO?
By H. Holden Thorp

343 Editorial
Lost in transition
By Kathleen Newland

438 Working Life
Advice for the worried
By Jennifer Kong and Steven Chan

ON THE COVER

A collection of insects from different orders, representing some of the diversity of species found in North America. A new synthesis of existing data indicates overall declines among terrestrial insect assemblages but increases among freshwater assemblages. To accommodate as many orders as possible, insect sizes are not shown to scale. See pages 368 and 417.
Photo: David Liittschwager

Science Staff 342
AAAS News & Notes 379
Science Careers 434

SCIENCE (ISSN 0036-8075) is published weekly on Friday, except last week in December, by the American Association for the Advancement of Science, 1200 New York Avenue, NW, Washington, DC 20005. Periodicals mail postage (publication No. 484460) paid at Washington, DC, and additional mailing offices. Copyright © 2020 by the American Association for the Advancement of Science. The title SCIENCE is a registered trademark of the AAAS. Domestic individual membership, including subscription (12 months): $165 ($74 allocated to subscription). Domestic institutional subscription (51 issues): $2148; Foreign postage extra: Air assist delivery: $98. First class, airmail, student, and emeritus rates on request. Canadian rates with GST available upon request, GST #125488122. Publications Mail Agreement Number 1069624. **Printed in the U.S.A.**
Change of address: Allow 4 weeks, giving old and new addresses and 8-digit account number. **Postmaster:** Send change of address to AAAS, P.O. Box 96178, Washington, DC 20090–6178. **Single-copy sales:** $15 each plus shipping and handling available from backissues.sciencemag.org; bulk rate on request. **Authorization to reproduce** material for internal or personal use under circumstances not falling within the fair use provisions of the Copyright Act can be obtained through the Copyright Clearance Center (CCC), www.copyright.com. The identification code for *Science* is 0036-8075. *Science* is indexed in the *Reader's Guide to Periodical Literature* and in several specialized indexes.

ILLUSTRATION: ROBERT NEUBECKER

EDITORIAL

Why WHO?

Pandemics are international. A virus doesn't respect borders between countries—or between states, as we are seeing with severe acute respiratory syndrome–coronavirus 2 (SARS-CoV-2) in the United States. Unfortunately, too many world leaders want to treat the situation as a problem for their nation alone and not the world.

Science will rise to the challenge of coronavirus disease 2019 (COVID-19) and is doing so. The structures of the most important SARS-CoV-2 proteins are now known. Although we are still in the early stages of understanding human immunity to the virus, neutralizing antibodies are being identified. Clinical trials have begun on vaccines and drugs. There's no shortcut, but there's reason to think we can conquer this if we can get enough time and collaboration. Most world leaders don't seem focused on giving the scientific and biomedical communities these two things.

China didn't do well in all this. In February, I thought my editorial on how China's secrecy about the new coronavirus led to the loss of life was an "edgy" commentary. Now that piece doesn't seem so daring at all because it's clear that China's delays and secrecy cost lives. Sadly, other governments' delays in action and delivery of misinformation have been costly as well.

The United States needs to uphold two apparently conflicting ideas: China covered up the initial spread of the virus, and we can't solve this crisis without collaborating with China. The World Health Organization (WHO) has walked a very fine line of trying to manage the pandemic without offending China. Last week's decision by the United States to suspend support for the WHO is not only dangerous but could delay a resolution to the pandemic. As *Science*'s news reporter Kai Kupferschmidt tweeted, "This is like suspending firefighters while they are trying to save your house from the flames, pending a review of whether the trucks arrived later than they should."

The amount of money at stake in funding the WHO is a tiny fraction of the total of the other costs of the pandemic. The total annual budget of the WHO is less than $2.5 billion, which has been compared to the annual budget of one relatively large academic medical center in a major U.S. city. That's a small price to help the whole world manage this health crisis.

Furthermore, the time for assigning blame should be reserved for after—not during—the crisis. Plenty of politicians have had their differences with the WHO and the United Nations over the years. Is now a good time to air all of that? The U.S. administration passed on using the WHO's viral diagnostic test, but then the U.S. Centers for Disease Control and Prevention (CDC) bungled their own version, costing Americans at least a month in controlling viral spread. That doesn't exactly give the administration a strong case for bailing on the WHO.

Yes, China did a lot to create this problem. But the world can't solve this without cooperating with Chinese scientists. Most of the important papers that *Science* has published over the past 6 weeks have been from Chinese scientists or have included Chinese collaborators. And the United States has been happily selling its debt to China, educating their students, and letting them make most of our stuff for 40 years. If the United States has decided to change these policies, then doing so—and abruptly—would probably be impossible, especially in the midst of a global pandemic.

> "The WHO is not perfect, but it has helped put out many fires around the world for a long time."

Nobody wants to continue social distancing forever (or thinks they can). Even the most pessimistic modelers of COVID-19 spread agree that this degree of behavioral change can't be sustained for many months. But the tools needed to get to the next phase in the United States are still not showing up: increased testing, staffing and gear for the hospitals with the greatest needs, and masks for everyone.

Courageous and confident world leaders believe that nations work best together through international institutions; this process has benefited the world for decades. Weak leaders believe in this but only if it benefits their country alone or even themselves. The WHO is not perfect, but it has helped put out many fires around the world for a long time.

–H. Holden Thorp

PHOTO: CAMERON DAVIDSON

H. Holden Thorp
Editor-in-Chief,
Science journals.
hthorp@aaas.org;
@hholdenthorp

Published online 20 April 2020; 10.1126/science.abc3400

Science AAAS

Editor-in-Chief Holden Thorp, hthorp@aaas.org

Executive Editor Monica M. Bradford

Editors, Research Valda Vinson, Jake S. Yeston **Editor, Insights** Lisa D. Chong

DEPUTY EDITORS Julia Fahrenkamp-Uppenbrink (UK), Stella M. Hurtley (UK), Phillip D. Szuromi, Sacha Vignieri **SR. EDITORIAL FELLOW** Andrew M. Sugden (UK) **SR. EDITORS** Gemma Alderton (UK), Caroline Ash (UK), Brent Grocholski, Pamela J. Hines, Paula A. Kiberstis, Marc S. Lavine (Canada), Steve Mao, Ian S. Osborne (UK), Beverly A. Purnell, L. Bryan Ray, H. Jesse Smith, Keith T. Smith (UK), Jelena Stajic, Peter Stern (UK), Valerie B. Thompson, Brad Wible, Laura M. Zahn **ASSOCIATE EDITORS** Michael A. Funk, Priscilla N. Kelly, Tage S. Rai, Seth Thomas Scanlon (UK), Yury V. Suleymanov **LETTERS EDITOR** Jennifer Sills **LEAD CONTENT PRODUCTION EDITORS** Harry Jach, Lauren Kmec **CONTENT PRODUCTION EDITORS** Amelia Beyna, Jeffrey E. Cook, Chris Filiatreau, Julia Katris, Nida Masiulis, Suzanne M. White **SR. EDITORIAL COORDINATORS** Carolyn Kyle, Beverly Shields **EDITORIAL COORDINATORS** Aneera Dobbins, Joi S. Granger, Jeffrey Hearn, Lisa Johnson, Maryrose Madrid, Ope Martins, Shannon McMahon, Jerry Richardson, Hilary Stewart (UK), Alana Warnke, Alice Whaley (UK), Anita Wynn **PUBLICATIONS ASSISTANTS** Jeremy Dow, Alexander Kief, Ronmel Navas, Brian White **EXECUTIVE ASSISTANT** Jessica Slater **ASI DIRECTOR, OPERATIONS** Janet Clements (UK) **ASI SR. OFFICE ADMINISTRATOR** Jessica Waldock (UK)

News Editor Tim Appenzeller

NEWS MANAGING EDITOR John Travis **INTERNATIONAL EDITOR** Martin Enserink **DEPUTY NEWS EDITORS** Elizabeth Culotta, Lila Guterman, David Grimm, Eric Hand (Europe), David Malakoff **SR. CORRESPONDENTS** Daniel Clery (UK), Jon Cohen, Jeffrey Mervis, Elizabeth Pennisi **ASSOCIATE EDITORS** Jeffrey Brainard, Catherine Matacic **NEWS REPORTERS** Adrian Cho, Jennifer Couzin-Frankel, Jocelyn Kaiser, Kelly Servick, Robert F. Service, Erik Stokstad, Paul Voosen, Meredith Wadman **INTERNS** Eva Frederick, Rodrigo Perez Ortega **CONTRIBUTING CORRESPONDENTS** Warren Cornwall, Ann Gibbons, Mara Hvistendahl, Sam Kean, Eli Kintisch, Kai Kupferschmidt (Berlin), Andrew Lawler, Mitch Leslie, Eliot Marshall, Virginia Morell, Dennis Normile (Shanghai), Elisabeth Pain (Careers), Charles Piller, Michael Price, Tania Rabesandratana (Barcelona), Emily Underwood, Gretchen Vogel (Berlin), Lizzie Wade (Mexico City) **CAREERS** Donisha Adams, Rachel Bernstein (Editor), Katie Langin (Acting Editor) **COPY EDITORS** Julia Cole (Senior Copy Editor), Cyra Master (Copy Chief) **ADMINISTRATIVE SUPPORT** Meagan Weiland

Creative Director Beth Rakouskas

DESIGN MANAGING EDITOR Marcy Atarod **GRAPHICS MANAGING EDITOR** Alberto Cuadra **PHOTOGRAPHY MANAGING EDITOR** William Douthitt **WEB CONTENT STRATEGY MANAGER** Kara Estelle-Powers **SENIOR DESIGNER** Chrystal Smith **DESIGNER** Christina Aycock **GRAPHICS EDITOR** Nirja Desai **INTERACTIVE GRAPHICS EDITOR** Xing Liu **SENIOR SCIENTIFIC ILLUSTRATORS** Valerie Altounian, Chris Bickel **SCIENTIFIC ILLUSTRATOR** Alice Kitterman **SENIOR GRAPHICS SPECIALISTS** Holly Bishop, Nathalie Cary **SENIOR PHOTO EDITOR** Emily Petersen **PHOTO EDITOR** Kaitlyn Dolan

Chief Executive Officer and Executive Publisher Sudip Parikh

Publisher, Science Family of Journals Bill Moran

DIRECTOR, BUSINESS SYSTEMS AND FINANCIAL ANALYSIS Randy Yi **DIRECTOR, BUSINESS OPERATIONS & ANALYSIS** Eric Knott **DIRECTOR OF ANALYTICS** Enrique Gonzales **MANAGER, BUSINESS OPERATIONS** Jessica Tierney **SENIOR BUSINESS ANALYST** Cory Lipman, Meron Kebede **FINANCIAL ANALYST** Alexander Lee **ADVERTISING SYSTEM ADMINISTRATOR** Tina Burks **SENIOR SALES COORDINATOR** Shirley Young **DIGITAL/PRINT STRATEGY MANAGER** Jason Hillman **QUALITY TECHNICAL MANAGER** Marcus Spiegler **ASSISTANT MANAGER DIGITAL/PRINT** Rebecca Doshi **SENIOR CONTENT SPECIALISTS** Steve Forrester, Jacob Hedrick, Antoinette Hodal, Lori Murphy **DIGITAL PRODUCTION MANAGER** Lisa Stanford **CONTENT SPECIALIST** Kimberley Oster **ADVERTISING PRODUCTION OPERATIONS MANAGER** Deborah Tompkins **DESIGNER, CUSTOM PUBLISHING** Jeremy Huntsinger **SR. TRAFFIC ASSOCIATE** Christine Hall **SPECIAL PROJECTS ASSOCIATE** Sarah Dhere

ASSOCIATE DIRECTOR, BUSINESS DEVELOPMENT Justin Sawyers **GLOBAL MARKETING MANAGER** Allison Pritchard **DIGITAL MARKETING MANAGER** Aimee Aponte **JOURNALS MARKETING MANAGER** Shawana Arnold **MARKETING ASSOCIATES** Tori Velasquez, Mike Romano, Ashley Hylton **DIGITAL MARKETING SPECIALIST** Asleigh Rojanavongse **SENIOR DESIGNER** Kim Huynh

DIRECTOR AND SENIOR EDITOR, CUSTOM PUBLISHING Sean Sanders **ASSISTANT EDITOR, CUSTOM PUBLISHING** Jackie Oberst

DIRECTOR, PRODUCT & PUBLISHING DEVELOPMENT Chris Reid **DIRECTOR, BUSINESS STRATEGY AND PORTFOLIO MANAGEMENT** Sarah Whalen **ASSOCIATE DIRECTOR, PRODUCT MANAGMENT** Kris Bishop **SR. PRODUCT ASSOCIATE** Robert Koepke **DIGITAL PRODUCT STRATEGIST** Michael Hardesty **SPJ ASSOCIATE** Samantha Bruno Fuller

DIRECTOR, INSTITUTIONAL LICENSING Iquo Edim **ASSOCIATE DIRECTOR, RESEARCH & DEVELOPMENT** Elisabeth Leonard **MARKETING MANAGER** Kess Knight **SENIOR INSTITUTIONAL LICENSING MANAGER** Ryan Rexroth **INSTITUTIONAL LICENSING MANAGER** Marco Castellan **MANAGER, AGENT RELATIONS & CUSTOMER SUCCESS** Judy Lillibridge **SENIOR OPERATIONS ANALYST** Lana Guz **FULFILLMENT COORDINATOR** Melody Stringer **SALES COORDINATOR** Josh Haverlock

DIRECTOR, GLOBAL SALES Tracy Holmes **US EAST COAST AND MID WEST SALES** Stephanie O'Connor **US WEST COAST SALES** Lynne Stickrod **US SALES MANAGER, SCIENCE CAREERS** Claudia Paulsen-Young **US SALES REP, SCIENCE CAREERS** Tracy Anderson **ASSOCIATE DIRECTOR, ROW** Roger Goncalves **SALES REP, ROW** Sarah Lelarge **SALES ADMIN ASSISTANT, ROW** Bryony Cousins **DIRECTOR OF GLOBAL COLLABORATION AND ACADEMIC PUBLISHING RELATIONS, ASIA** Xiaoying Chu **ASSOCIATE DIRECTOR, INTERNATIONAL COLLABORATION** Grace Yao **SALES MANAGER** Danny Zhao **MARKETING MANAGER** Kilo Lan **ASCA CORPORATION, JAPAN** Kaoru Sasaki (Tokyo), Miyuki Tani (Osaka) **COLLABORATION/CUSTOM PUBLICATIONS/JAPAN** Adarsh Sandhu

DIRECTOR, COPYRIGHT, LICENSING AND SPECIAL PROJECTS Emilie David **RIGHTS AND LICENSING COORDINATOR** Jessica Adams **RIGHTS AND PERMISSIONS ASSOCIATE** Elizabeth Sandler **CONTRACTS AND LICENSING ASSOCIATE** Lili Catlett

MAIN HEADQUARTERS
Science/AAAS
1200 New York Ave. NW
Washington, DC 20005

SCIENCE INTERNATIONAL
Clarendon House
Clarendon Road
Cambridge, CB2 8FH, UK

SCIENCE CHINA
Room 1004, Culture Square
No. 59 Zhongguancun St.
Haidian District, Beijing, 100872

SCIENCE JAPAN
ASCA Corporation
Sibaura TY Bldg. 4F, 1-14-5
Shibaura Minato-ku
Tokyo, 108-0073 Japan

EDITORIAL
science_editors@aaas.org

NEWS
science_news@aaas.org

INFORMATION FOR AUTHORS
sciencemag.org/authors/science-information-authors

REPRINTS AND PERMISSIONS
sciencemag.org/help/reprints-and-permissions

MEDIA CONTACTS
scipak@aaas.org

MULTIMEDIA CONTACTS
SciencePodcast@aaas.org
ScienceVideo@aaas.org

INSTITUTIONAL SALES AND SITE LICENSES
sciencemag.org/librarian

PRODUCT ADVERTISING & CUSTOM PUBLISHING
advertising.sciencemag.org/products-services
science_advertising@aaas.org

CLASSIFIED ADVERTISING
advertising.sciencemag.org/science-careers
advertise@sciencecareers.org

JOB POSTING CUSTOMER SERVICE
employers.sciencecareers.org
support@sciencecareers.org

MEMBERSHIP AND INDIVIDUAL SUBSCRIPTIONS
sciencemag.org/subscriptions

MEMBER BENEFITS
aaas.org/membercentral

AAAS BOARD OF DIRECTORS
CHAIR Steven Chu
PRESIDENT Claire M. Fraser
PRESIDENT-ELECT Susan G. Amara
TREASURER Carolyn N. Ainslie
CHIEF EXECUTIVE OFFICER
Sudip Parikh
BOARD Cynthia M. Beall
Rosina M. Bierbaum
Ann Bostrom
Stephen P.A. Fodor
S. James Gates, Jr.
Laura H. Greene
Kaye Husbands Fealing
Maria M. Klawe
Robert B. Millard
Alondra Nelson
William D. Provine

Science serves as a forum for discussion of important issues related to the advancement of science by publishing material on which a consensus has been reached as well as including the presentation of minority or conflicting points of view. Accordingly, all articles published in *Science*—including editorials, news and comment, and book reviews—are signed and reflect the individual views of the authors and not official points of view adopted by AAAS or the institutions with which the authors are affiliated.

BOARD OF REVIEWING EDITORS (Statistics board members indicated with **(S)**)

Adriano Aguzzi, *U. Hospital Zürich*
Takuzo Aida, *U. of Tokyo*
Leslie Aiello, *Wenner-Gren Foundation*
Judith Allen, *U. of Manchester*
Sebastian Amigorena, *Institut Curie*
James Analytis, *U. of California, Berkeley*
Paola Arlotta, *Harvard U.*
Johan Auwerx, *EPFL*
David Awschalom, *U. of Chicago*
Clare Baker, *U. of Cambridge*
Nenad Ban, *ETH Zürich*
Franz Bauer, *Pontificia Universidad Católica de Chile*
Ray H. Baughman, *U. of Texas at Dallas*
Peter Bearman, *Columbia U.*
Carlo Beenakker, *Leiden U.*
Yasmine Belkaid, *NIAID, NIH*
Philip Benfey, *Duke U.*
Gabriele Bergers, *VIB*
Bradley Bernstein, *Mass. General Hospital*
Alessandra Biffi, *Harvard Med. School*
Peer Bork, *EMBL*
Chris Bowler, *École Normale Supérieure*
Ian Boyd, *U. of St. Andrews*
Emily Brodsky, *U. of California, Santa Cruz*
Ron Brookmeyer, *U. of California, Los Angeles* **(S)**
Christian Büchel, *UKE Hamburg*
Dennis Burton, *Scripps Research*
Carter Tribley Butts, *U. of California, Irvine*
György Buzsáki, *New York U. School of Med.*
Blanche Capel, *Duke U.*
Annmarie Carlton, *U. of California, Irvine*
Nick Chater, *U. of Warwick*
Zhijian Chen, *UT Southwestern Med. Ctr.*
Ib Chorkendorff, *Denmark TU*
James J. Collins, *MIT*
Robert Cook-Deegan, *Arizona State U.*
Alan Cowman, *Walter & Eliza Hall Inst.*
Carolyn Coyne, *U. of Pittsburgh*
Roberta Croce, *VU Amsterdam*
Jeff L. Dangl, *U. of North Carolina*
Tom Daniel, *U. of Washington*
Chiara Daraio, *Caltech*
Nicolas Dauphas, *U. of Chicago*
Frans de Waal, *Emory U.*
Claude Desplan, *New York U.*
Sandra Díaz, *Universidad Nacional de Córdoba*
Ulrike Diebold, *TU Wien*
Hong Ding, *Inst. of Physics, CAS*
Jennifer Dionne, *Stanford U.*
Dennis Discher, *U. of Penn.*
Gerald Dorn, *Washington U. in St. Louis*
Jennifer A. Doudna, *U. of California, Berkeley*
Bruce Dunn, *U. of California, Los Angeles*
William Dunphy, *Caltech*
Christopher Dye, *U. of Oxford*
Todd Ehlers, *U. of Tübingen*
Jennifer Elisseeff, *Johns Hopkins U.*
Tim Elston, *U. of North Carolina*
Andrea Encalada, *U. San Francisco de Quito*
Nader Engheta, *U. of Penn.*
Karen Ersche, *U. of Cambridge*
Barry Everitt, *U. of Cambridge*
Vanessa Ezenwa, *U. of Georgia*
Michael Feuer, *The George Washington U.*
Toren Finkel, *U. of Pittsburgh Med. Ctr.*
Gwenn Flowers, *Simon Fraser U.*
Peter Fratzl, *Max Planck Inst. Potsdam*
Elaine Fuchs, *Rockefeller U.*
Eileen Furlong, *EMBL*
Jay Gallagher, *U. of Wisconsin*
Daniel Geschwind, *U. of California, Los Angeles*
Karl-Heinz Glassmeier, *TU Braunschweig*
Ramon Gonzalez, *U. of South Florida*
Elizabeth Grove, *U. of Chicago*
Nicolas Gruber, *ETH Zürich*
Hua Guo, *U. of New Mexico*
Kip Guy, *U. of Kentucky College of Pharmacy*
Taekjip Ha, *Johns Hopkins U.*
Christian Haass, *Ludwig Maximilians U.*
Sharon Hammes-Schiffer, *Yale U.*
Wolf-Dietrich Hardt, *ETH Zürich*
Louise Harra, *U. College London*
Jian He, *Clemson U.*
Carl-Philipp Heisenberg, *IST Austria*
Ykä Helariutta, *U. of Cambridge*
Janet G. Hering, *Eawag*
Hans Hilgenkamp, *U. of Twente*
Kai-Uwe Hinrichs, *U. of Bremen*
Lora Hooper, *UT Southwestern Med. Ctr.*
Fred Hughson, *Princeton U.*
Randall Hulet, *Rice U.*
Auke Ijspeert, *EPFL*
Akiko Iwasaki, *Yale U.*
Stephen Jackson, *USGS and U. of Arizona*
Kai Johnsson, *EPFL*
Peter Jonas, *IST Austria*
Matt Kaeberlein, *U. of Washington*
William Kaelin Jr., *Dana-Farber Cancer Inst.*
Daniel Kammen, *U. of California, Berkeley*
V. Narry Kim, *Seoul Nat. U.*
Robert Kingston, *Harvard Med. School*
Nancy Knowlton, *Smithsonian Institution*
Etienne Koechlin, *École Normale Supérieure*
Alexander L. Kolodkin, *Johns Hopkins U.*
Julija Krupic, *U. of Cambridge*
Thomas Langer, *Max Planck Inst. Cologne*
Mitchell A. Lazar, *U. of Penn.*
Ottoline Leyser, *U. of Cambridge*
Wendell Lim, *U. of California, San Francisco*
Jianguo Liu, *Michigan State U.*
Luis Liz-Marzán, *CIC biomaGUNE*
Jonathan Losos, *Washington U. in St. Louis*
Ke Lu, *Chinese Acad. of Sciences*
Christian Lüscher, *U. of Geneva*
Jean Lynch-Stieglitz, *Georgia Inst. of Tech.*
Fabienne Mackay, *U. of Melbourne*
Anne Magurran, *U. of St. Andrews*
Oscar Marín, *King's College London*
Charles Marshall, *U. of California, Berkeley*
Christopher Marx, *U. of Idaho*
Geraldine Masson, *CNRS*
C. Robertson McClung, *Dartmouth College*
Rodrigo Medellín, *U. Nacional Autónoma de México*
Graham Medley, *London School of Hygiene & Tropical Med.*
Jane Memmott, *U. of Bristol*
Baoxia Mi, *U. of California, Berkeley*
Edward Miguel, *U. of California, Berkeley*
Tom Misteli, *NCI, NIH*
Yasushi Miyashita, *U. of Tokyo*
Alison Motsinger-Reif, *NIEHS, NIH* **(S)**
Daniel Nettle, *Newcastle U.*
Daniel Neumark, *U. of California, Berkeley*
Beatriz Noheda, *U. of Groningen*
Helga Nowotny, *Vienna Science, Research & Tech. Fund*
Rachel O'Reilly, *U. of Birmingham*
Harry Orr, *U. of Minnesota*
Pilar Ossorio, *U. of Wisconsin*
Andrew Oswald, *U. of Warwick*
Isabella Pagano, *Istituto Nazionale di Astrofisica*
Margaret Palmer, *U. of Maryland*
Elizabeth Levy Paluck, *Princeton U.*
Jane Parker, *Max Planck Inst. Cologne*
Giovanni Parmigiani, *Dana-Farber Cancer Inst.* **(S)**
Samuel Pfaff, *Salk Inst. for Biological Studies*
Julie Pfeiffer, *UT Southwestern Med. Ctr.*
Matthieu Piel, *Institut Curie*
Kathrin Plath, *U. of California, Los Angeles*
Martin Plenio, *Ulm U.*
Katherine Pollard, *U. of California, San Francisco*
Elvira Poloczanska, *Alfred-Wegener-Inst.*
Julia Pongratz, *Ludwig Maximilians U.*
Philippe Poulin, *CNRS*
Jonathan Pritchard, *Stanford U.*
Félix A. Rey, *Institut Pasteur*
Trevor Robbins, *U. of Cambridge*
Joeri Rogelj, *Imperial College London*
Amy Rosenzweig, *Northwestern U.*
Mike Ryan, *U. of Texas at Austin*
Mitinori Saitou, *Kyoto U.*
Shimon Sakaguchi, *Osaka U.*
Miquel Salmeron, *Lawrence Berkeley Nat. Lab*
Nitin Samarth, *Penn. State U.*
Jürgen Sandkühler, *Med. U. of Vienna*
Alexander Schier, *Harvard U.*
Wolfram Schlenker, *Columbia U.*
Susannah Scott, *U. of California, Santa Barbara*
Rebecca Sear, *London School of Hygiene & Tropical Med.*
Vladimir Shalaev, *Purdue U.*
Jie Shan, *Cornell U.*
Beth Shapiro, *U. of California, Santa Cruz*
Jay Shendure, *U. of Washington*
Steve Sherwood, *U. of New South Wales*
Brian Shoichet, *U. of California, San Francisco*
Robert Siliciano, *Johns Hopkins U. School of Med.*
Lucia Sivilotti, *U. College London*
Alison Smith, *John Innes Centre*
Richard Smith, *U. of North Carolina* **(S)**
Mark Smyth, *QIMR Berghofer*
Pam Soltis, *U. of Florida*
John Speakman, *U. of Aberdeen*
Tara Spires-Jones, *U. of Edinburgh*
Allan C. Spradling, *Carnegie Institution for Science*
V. S. Subrahmanian, *Dartmouth College*
Ira Tabas, *Columbia U.*
Sarah Teichmann, *Wellcome Sanger Inst.*
Rocio Titiunik, *Princeton U.*
Shubha Tole, *Tata Inst. of Fundamental Research*
Wim van der Putten, *Netherlands Inst. of Ecology*
Reinhilde Veugelers, *KU Leuven*
Bert Vogelstein, *Johns Hopkins U.*
Kathleen Vohs, *U. of Minnesota*
David Wallach, *Weizmann Inst. of Science*
Jane-Ling Wang, *U. of California, Davis* **(S)**
David Waxman, *Fudan U.*
Jonathan Weissman, *U. of California, San Francisco*
Chris Wikle, *U. of Missouri* **(S)**
Terrie Williams, *U. of California, Santa Cruz*
Ian A. Wilson, *Scripps Research* **(S)**
Yu Xie, *Princeton U.*
Jan Zaanen, *Leiden U.*
Kenneth Zaret, *U. of Penn. School of Med.*
Jonathan Zehr, *U. of California, Santa Cruz*
Xiaowei Zhuang, *Harvard U.*
Maria Zuber, *MIT*

EDITORIAL

Lost in transition

Coronavirus disease 2019 (COVID-19) has been the greatest disruption to the movement of people since World War II. Many who had plans—and permission—to move permanently from one country to another have seen their transition put on hold. Worldwide, the flows of tourists, business and professional travelers, and students are all affected. But those most vulnerable to the virus and virus-related policies are low-paid migrant workers who have lost their jobs, and refugees or displaced people. Their lives were precarious even before the pandemic spread.

Migrant workers suffer as they struggle to return home with little or no money, often in the face of travel restrictions and suspension of transport links. In India, after Prime Minister Modi imposed a country-wide lockdown on 24 March, hundreds of thousands of internal migrants crowded the roads on foot, creating the very conditions that the lockdown was meant to prevent. Many foreigners are being summarily expelled, such as in India and Saudi Arabia. Others are stranded in foreign countries. Losing jobs creates a cascade of other losses for migrant workers—of legal status and access to health care and other public services. Only a few places, including Portugal and New York state, have opened their health care systems to migrants regardless of legal status (as Thailand has done since 2013 in response to the AIDS epidemic and other infectious diseases brought to the country by migrant workers). These migrants' families back home will suffer too, from the loss of remittances that fund health care, housing, education, and better nutrition. The departure of temporary migrant workers also creates risks for the native population. Agricultural producers in Europe, for example, are predicting crippling labor shortages this spring and summer.

> "...those most vulnerable... are low-paid migrant workers who have lost their jobs, and refugees or displaced people."

Refugee camps are densely packed—the largest one in the world, in the Cox's Bazar District of Bangladesh, has three times the population density of New York City, without a single high-rise building. Social distancing is impossible in such a setting. Clean water for handwashing is scarce. Medical resources are thin, although humanitarian agencies are ramping up hand-washing stations, protective gear, isolation units, and ambulance services. Conditions in European "reception centers" for refugees and asylum seekers, like that near Moria village on the Greek island of Lesvos, are worse than in many refugee camps in poor countries. Moria holds about 22,000 people in a site built for 3000. There are 1300 residents per water tap. So far, the only refugee camps known to have confirmed cases of COVID-19 (Ritsona and Malakasa) are in Greece.

Perhaps the most critical resource is information. The 120,000 people in Jordan's two main refugee camps are taking preventive measures (avoiding crowds) after a blizzard of electronic messages from the United Nations Refugee Agency (UNHCR). For most refugees and poor migrants who live in urban areas rather than camps, access to authoritative information is a lifeline. But many, especially in remote rural areas, do not have internet access. In the Cox's Bazar camps, the government forbids mobile phones. In every country, rich or poor, the provision of accurate and timely information is among the most urgent responsibilities of governments.

Unlike most natural disasters, COVID-19 has so far affected rich and upper-middle-income countries (including China, Iran, Turkey, Brazil, and South Africa) more than poorer ones. But that will quickly change in countries whose health care systems are ill-equipped to cope. Displaced people and poor migrants are often the last in line for health services. The virus cannot be suppressed if vulnerable migrants and refugees are not integrated into COVID-19 responses.

UN organizations, particularly the UNHCR and the International Organization for Migration, and a host of national and global humanitarian nongovernmental organizations (NGOs), are working frantically with national governments to stop COVID-19 from taking hold in refugee settings and to educate migrant populations and host communities on prevention. The special appeals have gone out: The UN Global Humanitarian Response Plan for COVID-19 is asking for $2.01 billion dollars to cover the actions of all its agencies and NGO partners. These organizations have experience in suppressing epidemics in deprived settings: ebola, cholera, dengue fever, and more. It is vital to everyone's safety that governments give them the funds they need in this global crisis.

– Kathleen Newland

Kathleen Newland is a senior fellow and cofounder of the Migration Policy Institute, Washington, DC, USA. knewland@migrationpolicy.org

PHOTO: JASPER GILARDI

10.1126/science.abc3197

CALL FOR PAPERS

SPJ
SCIENCE PARTNER JOURNALS

spj.sciencemag.org/bmef

BME Frontiers

OPEN ACCESS

Biomedical Engineering (BME) Frontiers is a **Science Partner Journal** distributed by the **American Association for the Advancement of Science** (AAAS) in collaboration with the **Suzhou Institute of Biomedical Engineering and Technology, Chinese Academy of Sciences** (SIBET CAS). *BME Frontiers* aims to serve as an effective platform for the multidisciplinary community of biomedical engineering. The journal will publish breakthrough research in the fields of pathogenic mechanisms as well as disease prevention, diagnosis, treatment, and assessment.

The Science Partner Journals (SPJ) program was established by the American Association for the Advancement of Science (AAAS), the nonprofit publisher of the *Science* family of journals. The SPJ program features high-quality, online-only, open access publications produced in collaboration with international research institutions, foundations, funders and societies. Through these collaborations, AAAS expands its efforts to communicate science broadly and for the benefit of all people by providing top-tier international research organizations with the technology, visibility and publishing expertise that AAAS is uniquely positioned to **offer as the world's largest general science membership society**.

Submit your research to *Biomedical Engineering Frontiers* today!
Learn more at: **spj.sciencemag.org/bmef**

ARTICLE PROCESSING CHARGES WAIVED UNTIL 2021

CALL FOR PAPERS

SPJ
SCIENCE PARTNER JOURNALS

BioDesign Research

OPEN ACCESS

BioDesign Research is a Science Partner Journal published in affiliation with **Nanjing Agricultural University (NAU)** and distributed by the **American Association for the Advancement of Science (AAAS).** *BioDesign Research* publishes high quality breakthrough research, reviews, editorials, and perspectives focusing on in silico biosystems design, genetic or epigenetic modifications, and genome writing or rewriting in any organism.

Submit your research to *BioDesign Research* today!

Learn more at **spj.sciencemag.org/bdr**

The Science Partner Journals (SPJ) program was established by the American Association for the Advancement of Science (AAAS), the non-profit publisher of the *Science* family of journals. The SPJ program features high quality, online-only, editorially independent open-access publications produced in collaboration with international research institutions, foundations, funders and societies. Through these collaborations, AAAS expands its efforts to communicate science broadly and for the benefit of all people by providing a top-tier international research organization with the technology, visibility, and publishing expertise that AAAS is uniquely positioned to offer as the world's largest general science membership society.

Learn more at **spj.sciencemag.org**

@SPJournals **@SPJournals**

ARTICLE PROCESSING CHARGES WAIVED UNTIL 2022

ScienceImmunology.org

READY TO PUT THE SPOTLIGHT ON YOUR RESEARCH?

Submit your research:
cts.ScienceMag.org

Science Immunology
AAAS

Twitter: @SciImmunologyl
Facebook: @ScienceImmunology

ScienceSignaling.org

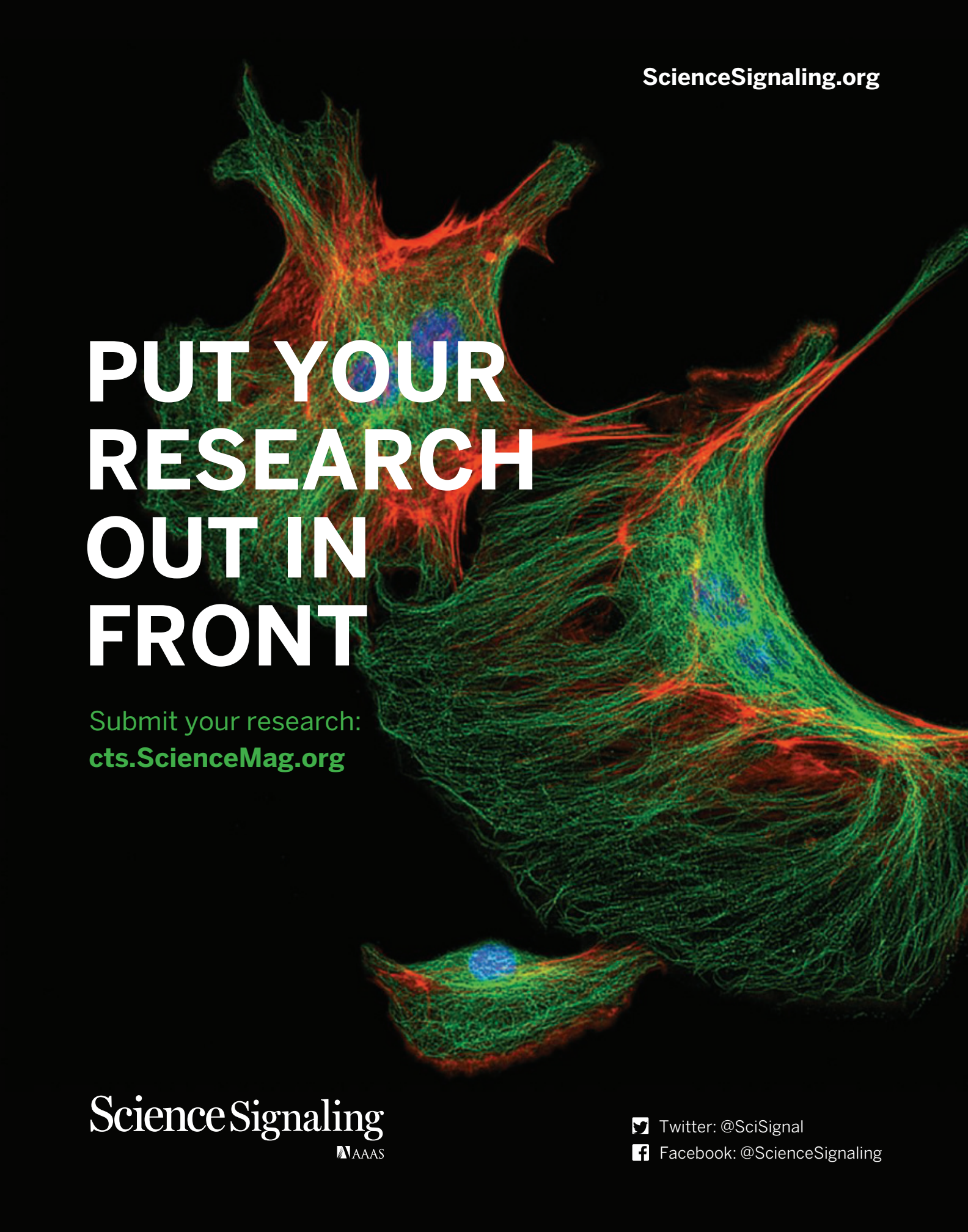

PUT YOUR RESEARCH OUT IN FRONT

Submit your research:
cts.ScienceMag.org

Science Signaling
AAAS

Twitter: @SciSignal
Facebook: @ScienceSignaling

NEWS

On Easter Sunday, lighting transformed the Christ the Redeemer statue in Rio de Janeiro into a physician, honoring those treating COVID-19 patients.

IN BRIEF

Edited by **Jeffrey Brainard**

DISPATCHES FROM THE PANDEMIC

Trump's WHO freeze knocked

GLOBAL HEALTH | Public health experts assailed President Donald Trump's 14 April decision to pause U.S. funding for the World Health Organization while U.S. officials review WHO's pandemic response. Trump asserted WHO failed to promptly confront the pandemic and was too trusting of China's initial accounts of the severity of the outbreak. However, Jeremy Konyndyk of the Center for Global Development says the move is "a transparent attempt to shift the blame for the U.S. administration's own failings." The United States is WHO's largest donor, providing more than $400 million annually in dues and voluntary contributions, including $58 million already sent this year. Withholding already appropriated funds could be illegal, say Democrats in Congress, who are examining legal challenges.

Ask the disease forecaster

EPIDEMIOLOGY | Statistical models of infectious disease are vital for understanding where the COVID-19 pandemic is headed. But their predictive power can be limited by sparse data and rapidly changing circumstances. A useful complement to numerical models is forecasts made by experts using their informed judgment, says Tom McAndrew, a biostatistics postdoctoral researcher at the University of Massachusetts, Amherst. Since February, each week he has been surveying about 20 experts in public health and infectious disease, asking them for their best estimates of future COVID-19 cases, hospitalizations, and deaths. The experts' understanding of the dynamics of disease outbreaks informs their estimates, McAndrew says, much as weather forecasters craft predictions based on data and experience. The latest survey results, from last week, support a consensus that total U.S. deaths from COVID-19 will rise substantially in coming weeks; on average, the experts estimate that in the most likely scenario, the number of deaths will reach 45,157 on 1 May and 74,631 on 1 June. On a hopeful note, the group estimates the United States will reach its peak number of monthly deaths no later than April.

Judgment calls

In a survey last week, 19 disease modelers offered a range of estimates for future COVID-19 death totals in the United States.

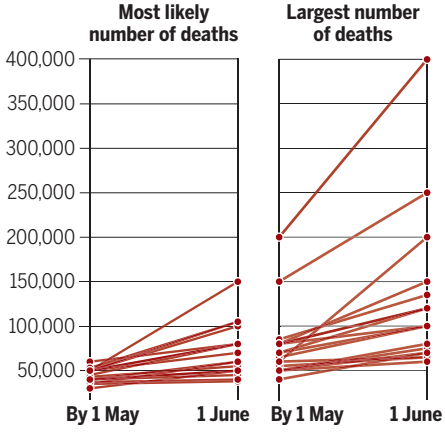

A call for bold vaccine approach

POLICY | Members of Congress this week called for U.S. regulators to embrace the controversial strategy of intentionally infecting volunteers with the virus that causes COVID-19 in order to test experimental vaccines. Such human challenge trials could greatly accelerate the development of an effective vaccine, 35 members of the House of Representatives argue in a letter sent to the heads of the U.S. Food and Drug Administration and its parent, the Department of Health and Human Services. The bipartisan group of lawmakers also backs the idea of parallel, simultaneous testing of different doses of a vaccine. In theory, challenge trials could enroll volunteers who are at low risk of harm from COVID-19, such as young adults who rarely develop serious symptoms after becoming infected naturally. According to the latest tally by the World Health Organization, 76 vaccine candidates are under development around the world.

CREDITS: (PHOTO) BUDA MENDES/GETTY IMAGES; (GRAPHIC) N. DESAI/*SCIENCE*; (DATA) THOMAS MCANDREW/UNIVERSITY OF MASSACHUSETTS, AMHERST

Scientists receive death threats

SAFETY | Researchers in Brazil studying chloroquine therapy for COVID-19 received death threats after identifying possible side effects of a drug that President Jair Bolsonaro and conservative political activists have promoted despite a dearth of evidence of its efficacy. Scientists from several institutions, working at a public hospital in Manaus, were comparing low- and high-dose regimens but ended the high-dose arm on 6 April after 11 of the 81 enrolled patients died, including seven in the high-dosage group. Conservative media outlets and political activists accused the researchers of intentionally administering extreme doses to disqualify the drug, and aggressive attacks against them followed on social media, starting on 16 April. "I've never felt so exposed," Marcus Lacerda, the physician in charge of the study, told *Science*. The study has continued with about 200 patients in the low-dosage arm.

Sewage reveals virus outbreaks

DISEASE MONITORING | Sampling sewage across a metropolitan area can reveal a spike in coronavirus concentrations before an explosion in confirmed COVID-19 cases shows up in the clinic, a study indicates. Wastewater sampling across greater Paris for more than 1 month points to its potential as a cheap, noninvasive way to get an early warning of outbreaks, researchers at Eau de Paris, the city's public water utility, and Sorbonne University wrote in a preprint posted on medRxiv last week. Fragments of the viral RNA survive in wastewater, where polymerase chain reaction screening can detect them. The approach is valuable because of shortages of COVID-19 testing kits and because it can detect asymptomatic carriers, the researchers say.

MORE FROM ONLINE

Read additional *Science* coverage of the pandemic at sciencemag.org/tags/coronavirus.

Antibiotic treatment for COVID-19 complications could fuel resistant bacteria. Major study will examine antibiotic use and secondary infections.

Crushing coronavirus means 'breaking the habits of a lifetime.' Behavior scientists have some tips. Subtle cues can change people's behavior.

'Open the doors for us.' Indonesian scientists say government snubs offers to help fight coronavirus. Researchers describe a chaotic response and shortage of COVID-19 tests.

PHOTO: WIPAWAN PAWITAYALARP

SCIENCE ADVICE

Court says EPA grantees can advise agency

The U.S. Environmental Protection Agency (EPA) may not bar recipients of agency grants from serving on its scientific advisory boards, a federal district court judge ruled on 15 April. The controversial ban was imposed in 2017 by former EPA Administrator Scott Pruitt, who said it was intended to prevent potential conflicts of interest. But the policy has drawn multiple legal challenges from scientific and environmental groups, who say it blocks well-qualified academic scientists from advisory panels while still allowing industry researchers to serve. The new ruling, on a challenge brought by the Natural Resources Defense Council, isn't likely to settle the fight. Several other courts, including two federal appellate courts, are also considering the policy's legality.

Which AI will top the pops?

COMPUTER SCIENCE | A contest inspired by the popular annual Eurovision music competition has drawn entries composed with the help of unusual songwriters—artificial intelligence (AI) programs. For the first time, 13 teams from Europe and Australia, each made up of scientists, programmers, and musicians, submitted tunes this month to the AI Song Contest, sponsored by Dutch public broadcaster VPRO. They wrote AI programs or adapted existing ones to craft lyrics, melodies, and harmonies for songs lasting no more than 3 minutes each. One of them, Australian team Uncanny Valley, created "Beautiful The World" by training a neural network with audio from koalas, kookaburras, and Tasmanian devils to honor those animals lost to the country's wildfires in 2019. A three-person panel—two AI scientists and a composer—and the public will rate the songs, with results to be announced on 12 May. The winning song will be broadcast.

Thailand fights horse virus

INFECTIOUS DISEASE | Already battling the spread of COVID-19, Thailand is contending with another deadly viral outbreak—in horses. Hundreds of horses there have died from African horse sickness during the past month in an outbreak that some scientists suspect was caused by zebras imported from Africa. It is the first major occurrence of the disease outside Africa in 30 years, and scientists are worried that it could spread to neighboring countries in Southeast Asia and burden poor workers who depend on horses for income.

Netting isolates horses in Thailand from midges that spread African horse sickness.

Biting midges spread the virus, which causes severe heart and lung damage in infected horses, killing at least 70%. Zebras and most donkeys are spared, and act as reservoirs for the virus. Owners of horses in Thailand are rushing to seal them indoors with netting, and veterinary authorities are ramping up testing and vaccinations.

Trump shelves mercury ruling

AIR POLLUTION | The U.S. Environmental Protection Agency last week reversed a policy it had used in 2012 to regulate mercury and other pollutants emitted by power plants—a move that could help the coal industry's fight to abolish the emissions regulations themselves. President Donald Trump's administration had criticized the legal justification for the compliance costs. Environmental groups and even some power companies criticized the reversal, saying costs had been lower than predicted.

IN DEPTH

Stanford University medical students conduct blood tests in California's Santa Clara county to assess the prevalence of antibodies to the pandemic coronavirus.

COVID-19

First antibody surveys draw fire for quality, bias

Some study authors use serology data to call for easing lockdowns, but critics push back

QQ group: 970508760

By **Gretchen Vogel**

Surveying large swaths of the public for antibodies to the new coronavirus promises to show how widespread undiagnosed infections are, how deadly the virus really is, and whether enough of the population has become immune for social distancing measures to be eased. But the first batch of results has generated more controversy than clarity.

The survey results, from Germany, the Netherlands, and several locations in the United States, find that anywhere from 2% to 30% of certain populations have already been infected with the virus. The numbers imply that confirmed COVID-19 cases are an even smaller fraction of the true number of people infected than many had estimated and that the vast majority of infections are mild. But many scientists question the accuracy of the antibody tests and complain that several of the research groups announced their findings in the press rather than in preprints or published papers, where their data could be scrutinized. Critics are also wary because some of the researchers are on record advocating for an early end to lockdowns and other control measures, and claim the new prevalence figures support that call.

Some observers warn the coronavirus' march through the population has only just begun, and that even if the antibody results can be believed, they don't justify easing controls. "You would have hoped for 45% or even 60% positive," says Mark Perkins, a diagnostics expert at the World Health Organization. "That would mean that there is lots of silent transmission, and a lot of immunity in the population. It now looks like, sadly, that's not true. Even the high numbers are relatively small."

The many different academic and commercial tests for coronavirus antibodies are still being refined and validated. They can show whether someone's immune system has encountered the virus. But because no one knows what level of antibodies, if any, confers protection against the new virus, the tests can't tell whether a person is immune to a future infection. And no one knows how long such immunity might last.

A German antibody survey was the first out of the gate several weeks ago. At a press conference on 9 April, virologist Hendrik Streeck from the University of Bonn announced preliminary results from a town of about 12,500 in Heinsberg, a region in Germany that had been hit hard by COVID-19. He told reporters his team had found antibodies to the virus in 14% of the 500 people tested. By comparing that number with the recorded deaths in the town, the study suggested the virus kills only 0.37% of the people infected. (The rate for seasonal influenza is about 0.1%.) The team concluded in a two-page summary that "15% of the population can no longer be infected with SARS-CoV-2, and the process of reaching herd immunity is already underway." They recommended that politicians start to lift some of the regions' restrictions.

Streeck had argued even before the study that the virus is less serious than feared and that the effects of long shutdowns may be just as bad if not worse than the damage the virus could do. However, Christian Drosten, a virologist at Charité University Hospital in Berlin, told reporters later that day that no meaningful conclusions could be drawn from the antibody study based on the limited information Streeck presented. Drosten cited uncertainty about what level of antibodies provides protection and noted that the study sampled entire households. That can lead to overestimating infections, because people living together often infect each other.

Streeck and his colleagues claimed the commercial antibody test they used has "more than 99% specificity," but a Danish group found the test produced three false positives in a sample of 82 controls, for a specificity of only 96%. That means that in the Heinsberg sample of 500, the test could have produced more than a dozen false positives out of roughly 70 the team found.

PHOTO: RAY CHAVEZ/MEDIANEWS GROUP/*THE MERCURY NEWS* VIA GETTY IMAGES

A California serology study of 3300 people released last week in a preprint also drew strong criticisms. The lead authors of the study, Jay Bhattacharya and Eran Bendavid, who study health policy at Stanford University, worked with colleagues to recruit the residents of Santa Clara county through ads on Facebook. Fifty antibody tests were positive—about 1.5%. But after adjusting the statistics to better reflect the county's demographics, the researchers concluded that between 2.49% and 4.16% of the county's residents had likely been infected. That suggests, they say, that the real number of infections was as many as 80,000. That's more than 50 times as many as viral gene tests had confirmed and implies a low fatality rate—a reason to consider whether strict lockdowns are worthwhile, argue Bendavid and co-author John Ioannidis, who studies public health at Stanford.

On the day the preprint posted, co-author Andrew Bogan—a venture capitalist with a molecular biology Ph.D.—published an op-ed in *The Wall Street Journal* asking, "If policy makers were aware from the outset that the Covid-19 death toll would be closer to that of seasonal flu … would they have risked tens of millions of jobs and livelihoods?" He did not disclose his role in the study.

Science's COVID-19 coverage is supported by the Pulitzer Center.

Yet Twitter threads and blog posts outlined a litany of apparent problems with the Santa Clara study. Recruiting through Facebook likely attracted people with COVID-19–like symptoms who wanted to be tested, boosting the apparent positive rate. Because the absolute numbers of positive tests were so small, false positives may have been nearly as common as real infections. The study also had relatively few participants from low-income and minority populations, meaning the statistical adjustments the researchers made could be way off. "I think the authors of the paper owe us all an apology," wrote Columbia University statistician and political scientist Andrew Gelman in an online commentary. The numbers "were essentially the product of a statistical error." Bhattacharya says he is preparing an appendix that addresses the criticisms. But, he says, "The argument that the test is not specific enough to detect real positives is deeply flawed."

Bhattacharya and Bendavid have also collaborated with Neeraj Sood, a health policy expert at the University of Southern California, to do a similar study in Los Angeles county. They used the same antibody test on 846 people selected by a marketing firm to represent the county's demographics. In a press release issued this week, they estimated that roughly 4% of the county's adult population has antibodies to the virus—as many as 300,000 people. (Sood told *Science* that 35 subjects tested positive.)

Another serology study, in the Netherlands, produced a similar figure for antibody prevalence that was revealed in the country's House of Representatives on 16 April. Hans Zaaijer, a virologist at Sanquin, the Dutch national blood bank, who helped lead the study, says the team used a commercial test, which "consistently shows superior results" in validation studies, but didn't provide more details. The results made it clear that the country was not yet near the "herd immunity" that some had hoped for. Nevertheless, the government said on 21 April that it would start to lift some restrictions in the coming weeks, opening elementary schools and allowing children's sports teams to practice.

A small study in the Boston suburb of Chelsea has found the highest prevalence of antibodies so far. Prompted by the striking number of COVID-19 patients from Chelsea colleagues had seen, Massachusetts General Hospital pathologists John Iafrate and Vivek Naranbhai quickly organized a local serology survey. Within 2 days, they collected blood samples from 200 passersby on a street corner. That evening, they processed the samples—and shared the results with a reporter from *The Boston Globe*. Sixty-three were positive—31.5%. The result carries several large caveats. The team used a test whose maker, BioMedomics, says it has a specificity of only about 90%, though Iafrate says MGH's own validation tests found a specificity of higher than 99.5%. And pedestrians on a single corner "aren't a representative sample" of the town, Naranbhai acknowledges.

The pair says a paper describing the team's results has been submitted to a journal but they shared the data with *The Boston Globe* first because "we felt there was an urgent infection control issue in Chelsea that warranted getting the information out." The Boston researchers do not think quarantines should be eased, however. Better containment is urgently needed in Chelsea, they say, to help prevent further spread both within the community and in the larger Boston area.

Even if the antibody surveys show a COVID-19 death rate well below 1%, says Michael Osterholm, an infectious disease expert at the University of Minnesota, Twin Cities, control measures will be needed for a long time to avoid overwhelmed hospitals. "The seroprevalence data only confirm the challenge we face. The data [these studies] are generating … is just showing how hard this is." ■

COVID-19

NIH organizes hunt for drugs

Firms to help prioritize treatment and vaccine trials

By **Jocelyn Kaiser**

In a remarkable display of urgency, researchers are already developing more than 100 treatments and vaccines to stem the COVID-19 pandemic. But some onlookers worry the sprawling effort could waste time and resources on duplicated studies and weak candidates. So, last week, the National Institutes of Health (NIH) and 16 drug companies announced an effort to impose some order.

In one key activity, the Accelerating COVID-19 Therapeutic Interventions and Vaccines (ACTIV) initiative will inventory drug and vaccine candidates and decide which should get priority for U.S. funding and testing in humans. The top-rated compounds will get preferred access to NIH's $1.8 billion pot of COVID-19 research money, as well as to a dozen or more NIH clinical trial networks originally set up for other diseases. ACTIV also aims to streamline trials by establishing "master protocols" for assessing a drug's efficacy. The public-private partnership will "bring all the full resources and ideas together in a variety of ways that neither sector could do alone," NIH Director Francis Collins said.

NIH says ACTIV is primarily focused on the United States, but it will work with the European Medicines Agency and other COVID-19 research coordination efforts around the world to avoid duplication.

One major player is noticeably absent from the list of ACTIV's partners: the World Health Organization (WHO), which is coordinating a large global trial of several drugs called SOLIDARITY (*Science*, 27 March, p. 1412). WHO Chief Scientist Soumya Swaminathan says her agency welcomes ACTIV, especially to develop treatments. For vaccines, she says WHO is well-positioned to coordinate global trials. "The best and most efficient way would be to consider one large global study which would look at different vaccine candidates," she says. NIH says ACTIV will take WHO's programs into account as it seeks to accelerate studies. ■

With reporting by Jon Cohen and David Malakoff.

Members of the Waiapi Indigenous reserve in Brazil's Amapá state seek medical care at a small clinic.

PHOTO: GERD LUDWIG/NATGEO CREATIVE

COVID-19

Indigenous communities in Brazil fear pandemic's impact

Other infections and scant medical care may worsen toll

By **Ignacio Amigo**

To the older generation of the Paiter Surui, the COVID-19 pandemic looks disturbingly familiar. The Indigenous people, who inhabit the border of the Brazilian states of Rondônia and Mato Grosso, suffered hundreds of deaths from measles and other infectious diseases in the decades after they first made contact with non-Indigenous people in 1969. The survivors "already experienced what is happening in the world today with the coronavirus," says Rubens Naraikoe Surui, a young Indigenous leader.

Now, as the number of coronavirus cases soars in Brazil, the Pater Surui and other Indigenous people worry they could be hard hit. So far, 27 members of such groups are known to have had COVID-19 infections, and three have died: a 15-year-old Yanomami boy, a 78-year-old Tikuna man, and a 44-year-old Kokama woman.

The region seems ripe for further spread. The state of Amazonas, where most Indigenous groups live, now has the most cases per capita in Brazil. As *Science* went to press, the state capital Manaus had 1772 confirmed cases and 156 deaths, and local authorities said its health care system was on the brink of collapse. The city opened two emergency hospitals in the past week.

Although Indigenous populations were devastated by infectious diseases in the past, the idea that they are somehow biologically more vulnerable to new diseases is a myth, says Carlos Coimbra, an epidemiologist at the Oswaldo Cruz Foundation who specializes in Indigenous health. "There's no scientific basis to support that," Coimbra says. Anytime a new virus enters a population that is "immunologically naïve," as happened with measles and the Paiter Surui, it will spread rapidly. Today, vaccines and regular contact with non-Indigenous people have boosted Indigenous groups' immunity to measles, influenza, and other diseases, Coimbra says. COVID-19, on the other hand, is new to the entire world.

What could make these populations unusually vulnerable to the disease are other medical, social, and environmental factors, such as a high prevalence of tuberculosis and malaria, a lack of safe drinking water, and malnutrition, Coimbra says. And the Amazon region, where most Indigenous communities live, has few hospitals with intensive care units and a limited number of ventilators, required for the most severe COVID-19 cases.

Isolation may help protect communities. São Gabriel da Cachoeira, a municipality in northwest Amazonas that has the highest numbers of Indigenous people in the country, is under a self-imposed shutdown. Local authorities have suspended passenger transport into the city of just over 40,000 people, which can only be reached by plane or boat, and so far, no COVID-19 cases have been reported. "We are focusing specifically on prevention. Our goal is to buy time," says Marivelton Barroso, president of the Federation of Indigenous Organizations of Rio Negro. Along with other organizations and government bodies, the federation is distributing food and other basic items to rural communities.

Other Indigenous territories across Brazil are also isolating themselves. In the Uru-Eu-Wau-Wau Indigenous land in Rondônia, only a limited number of representatives of the Indigenous health services can enter, and residents are urged to stay in their villages. History may encourage them to take the advice seriously: In the 1980s, the Uru-Eu-Wau-Wau population was reduced to less than half by respiratory diseases. COVID-19 "could be fatal for us," says Bitate Uru Eu Wau Wau, coordinator of the Jupaú association of the Uru Eu Wau Wau people.

Brazil's wider response to the coronavirus outbreak has been confusing at best. Most state governors and mayors have decided to enforce social distancing, but President Jair Bolsonaro has repeatedly downplayed the risks of the pandemic and argued in favor of ending the lockdowns. On 16 April, he fired his health minister, Luiz Henrique Mandetta, who supported distancing measures similar to those implemented in most countries. (His replacement, oncologist and entrepreneur Nelson Teich, said in his first speech that there would be no abrupt changes in Brazil's COVID-19 policy.)

The Brazilian Congress recently approved an emergency aid package of 600 reais ($115) per month per person for the most vulnerable populations. The money should help cut-off communities, but it can only be collected in cities, forcing Indigenous people to leave their villages and risk becoming infected. To prevent this, the National Indian Foundation will recommend that people stay in their communities for as long as they can, because the money will be available for 90 days.

Despite the worries, Elisângela da Silva, an Indigenous leader from the Baré ethnicity, sees a silver lining: As more people worry about staying safe, some traditional plants and remedies are becoming popular again. Whether they work remains to be seen, of course, but at least "the pandemic is helping us rescue our traditions," da Silva says. ■

Ignacio Amigo is a science journalist in Manaus, Brazil.

BIOMEDICINE

Mass screening weighed for type 1 diabetes risk

Studies find benefit to testing thousands of children for antibodies that precede symptoms

By **Jennifer Couzin-Frankel**

Long before type 1 diabetes is diagnosed in patients, who sometimes show up at the hospital so sick they need to be admitted to intensive care, it has taken a silent toll: The immune system has mounted stealth attacks on insulinmaking cells in the pancreas. Scientists are now weighing whether to routinely screen children for those hidden attacks, which could spot youngsters at risk years before symptoms surge.

At the moment, there is no way to prevent the disease. But screening trials suggest finding high-risk children can avert severe illness at diagnosis. Identifying those likely to develop diabetes could also accelerate the testing of preventive therapies.

Still, screening across populations carries caveats. "Is this plausible" on a grand scale, asks Anette-Gabriele Ziegler, director of the Institute of Diabetes Research at Helmholtz Zentrum Munich. Cost effectiveness is also critical, and "different in every country," she says.

At least one in 300 children in many countries develops type 1 diabetes by age 18. The disease calls for constant blood sugar monitoring and can cause complications including heart disease. Past studies have tested family members of affected people for several different autoantibodies in the blood that provide an early warning of the immune assault. The screening works: Studies show that each year, about 10% of children with two or more autoantibodies will develop diabetes, and after 15 years, about 85% have the disease.

But just 10% of people diagnosed have affected relatives. With growing hope that treatments to stave off disease are possible, screening efforts are now stretching to thousands of children with no family history. In January, Ziegler's team reported results in *JAMA* from the first mass screening effort, after enlisting hundreds of pediatricians to collect blood from finger pricks of 90,000 2- to 5-year-olds in Bavaria. Similar efforts are underway in northwestern Germany and Colorado.

In medicine, it is unusual to screen for disease risk without a prevention strategy. The paradox, some say, is that without mass screening to find at-risk people, preventives are harder to test. "We need the screening to develop these therapies. We cannot do the one without the other," Ziegler says.

A case in point was the first successful trial to delay diabetes, published last year. Screening to identify participants was limited to people with a family history, and it took more than 6 years to find the 76 enrollees. The trial reported that the experimental drug teplizumab, a monoclonal antibody that blunts immune activity, pushed back disease by about 2 years (*Science*, 14 June 2019, p. 1021). That finding "changes the thinking" around prevention, says Olga Kordonouri, who specializes in pediatric diabetes at Children's Hospital in Hanover, Germany, and is leading a screening study in Lower Saxony.

Children with type 1 diabetes must aggressively monitor their blood sugar.

Ziegler's study suggested mass screening could also avert a complication of the disease: a dangerous condition called diabetic ketoacidosis (DKA). DKA occurs when lack of insulin prompts the body to break down fat for fuel, resulting in high blood levels of compounds called ketones. Marked by vomiting, shortness of breath, and confusion, DKA can be life threatening and is associated with longer term difficulties in controlling blood sugar. In Europe, about 20% of children have DKA upon diagnosis of type 1 diabetes, and in the United States, about 40%.

Because the 280 children identified as high risk in Ziegler's study were referred to specialists and their families were educated about diabetes, just two children developed DKA—out of 43 who progressed to diabetes over 2.5 years.

Marian Rewers, executive director of the Barbara Davis Center for Diabetes at the University of Colorado School of Medicine, is leading the screening trial in Colorado. So far, his study has tested nearly 25,000 children, with results similar to Ziegler's: two DKA cases among the 22 children who have developed diabetes.

Although those numbers are hopeful, some say screening for all would be premature. One concern is that finding a child has autoantibodies "doesn't absolutely guarantee you're going to have diabetes," says David Nathan, director of the diabetes center at Massachusetts General Hospital. He's curious whether screening studies that continue to follow participants can find ways to better refine who is at highest risk.

And even though Rewers and Ziegler have found physicians and families eager to participate, "There is a high bar to adding anything to the routine screening in any country," Rewers says. Some screening proponents are trying to think practically. In the United States, many toddlers get a blood test for lead levels, so diabetes screening could be bundled in, says Jessica Dunne, director of the prevention program at JDRF, which helps fund and advise some screening projects. Rewers's study combines diabetes screening with a test for an autoantibody that appears in celiac disease, in which the body can't tolerate gluten. The study led by Kordonouri includes a cholesterol test, which in young children can indicate the genetic condition familial hypercholesteremia.

Ziegler is now studying the cost effectiveness of mass screening in Germany and trying to define the best age to screen. Australia and Israel are weighing mass screening. Different health systems and the results of the studies now running will play into the decisions, but Rewers is optimistic. "Support," he says, "is snowballing." ■

PHOTO: AFRICA STUDIO/SHUTTERSTOCK.COM

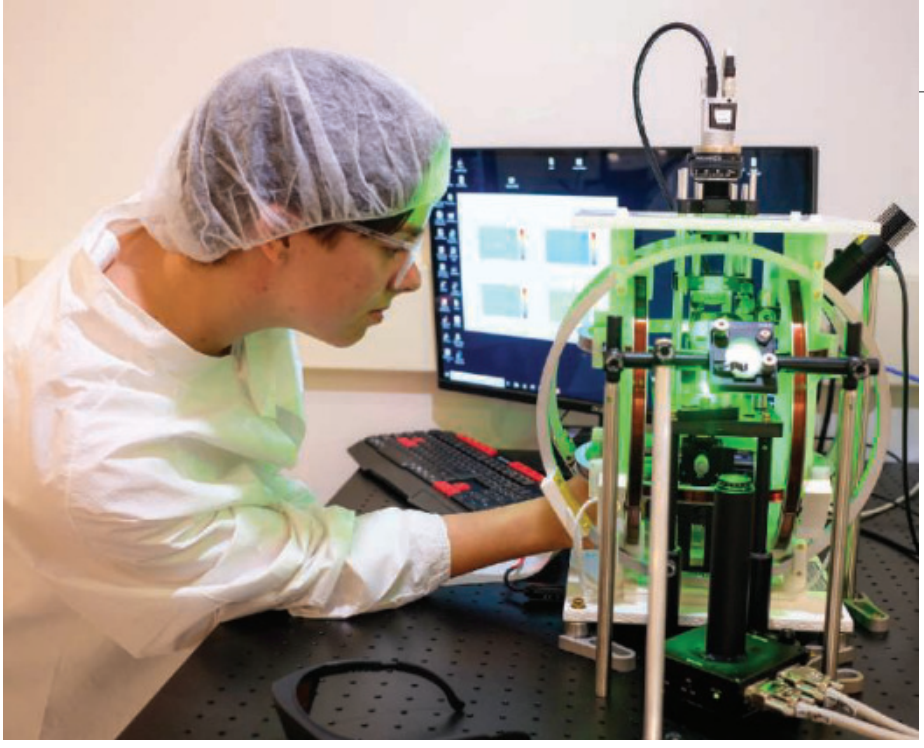

A quantum diamond microscope contains a doped diamond slide that is excited by tiny magnetic fields.

PHOTO: HARVARD PALEOMAGNETICS LAB

EARTH SCIENCE

Diamond microscope unlocks ancient rocks' magnetic secrets

Quantum sensor reveals clues about plate tectonics, planet formation, and climate change with exquisite resolution

By **Paul Voosen**

On a table inside the magnetically shielded lab of Roger Fu, a planetary scientist at Harvard University, sits a modest contraption that is telling profound stories about the geologic past. The quantum diamond microscope (QDM) consists of a few electromagnetic coils wrapped around a camera, a small laser, and what looks like a rose-tinted sample slide. The slide is not glass, however; it is a diamond, doped with defects sensitive to tiny magnetic fields. Using this diamond sensor, the microscope can map the fields imprinted in rock grains at scales smaller than the width of a human hair, allowing geologists to tease out history that coarser techniques overlook.

Fu's lab is using the microscope to probe meteorites for clues about the Solar System's earliest days; chronicle rainfall thousands of years ago from stalactites; and, as detailed this week in *Science Advances*, detect some of the earliest motions of Earth's tectonic plates in ancient lavas. "It's a completely new principle in earth science," Fu says.

And it's catching on. The National Science Foundation has paid for Fu's team to build microscopes at the University of California, Berkeley, and the University of Minnesota, while NASA funded a third at the Massachusetts Institute of Technology (MIT). He's building another for a Dutch lab. "Roger has been the great Johnny Appleseed of QDMs," says Ronald Walsworth, a physicist at the University of Maryland, College Park, who pioneered the diamond technology some 15 years ago.

The microscope relies on minuscule defects in diamond created when a nitrogen atom knocks two carbons out of the crystal lattice; the impurities exist in nature, but can also be manufactured. The result is a void next to the nitrogen that traps electrons whose quantum states are sensitive: Laser light, microwaves, and magnetic fields can all manipulate their energy levels and spin states. The diamond defects are a promising technology for hosting qubits, the logical elements in quantum computers. But for experiments in basic physics, their hair-trigger magnetic sensitivity could be annoying, Walsworth says. "Then we started thinking, 'If it's so sensitive, maybe that's a feature, not a bug?'" Walsworth eventually connected with Fu, who was eager to exploit the feature.

An analysis of zircon crystals more than 4 billion years old from the Jack Hills in Western Australia provided an early test. Traditional paleomagnetic measurements using superconducting sensors had found faint fields preserved in the zircons, a clue that Earth had a magnetic field half a billion years earlier than expected. But the superconducting sensors could measure only the average field across the zircons, which are as small as motes of dust. To scrutinize the Jack Hill specimens at a finer scale, Fu placed them on the diamond slide and illuminated the slide with a green laser. The nitrogen vacancy centers, primed by the electromagnetic coils, responded by emitting red light at a brightness that depended on the sample's magnetism.

The finer spatial resolution of the QDM showed the fields came not from the crystals' interiors, but from rims of iron that had, presumably, formed much later in their history. The fields "are not born with the zircons," Fu says, fueling debate about the claims of a 4-billion-year-old field.

Now, Fu and his colleagues have applied the technique to other rocks from Western Australia—its 3.2-billion-year-old Honeyeater Basalt. Using traditional superconducting sensors, which still beat the QDM for overall sensitivity, they measured the magnetic field strengths and directions captured in 235 samples of the rocks. But they couldn't be sure those fields were primordial: Over its lifetime, the Honeyeater Basalt had been deeply altered and buried under the sea floor, where water and immense strains could have allowed later sources of magnetism to contaminate it. It was up to the QDM to deduce whether its magnetic field was a native or immigrant.

The fine-scale magnetic map the instrument produced showed the fields came not from mineral grains, but from halos around them, which had formed underwater, almost immediately after the lava likely oozed out of fissures in the sea floor, says Alec Brenner, lead author of the *Science Advances* study and Fu's graduate student. "Technically that means they did not form with the rock," he says. But for practical purposes, the halos were just as old; the team could say with confidence that the fields were 3.2 billion years old.

Earth's magnetic field lines plunge into the ground at angles that increase from the equator to the poles. So the field directions preserved in the Honeyeater samples reveal the latitude at which the basalt formed. Last decade, another team of geologists analyzed ancient magnetism in nearby 3.35-billion-

year-old rocks to show they formed at a different "paleolatitude." From the difference in latitudes, Fu's group calculated that Earth's crust moved, at a minimum, some 2 centimeters per year during this span of 150 million years. "That's roughly comparable to modern plate motion," Brenner says.

The result "is by itself quite an achievement," says Jun Korenaga, a geophysicist at Yale University, and suggests studies of even older rocks could pin down when plate tectonics began. Credible arguments based on how fast the infant Earth cooled put the start anywhere from 4.5 billion years ago, soon after Earth's formation, to 3 billion years ago. "If they can pursue this direction and go deeper in time, that would be interesting," Korenaga says.

Meteorites, time capsules from the early Solar System, are another natural subject for the QDM, Fu says. In a new study accepted at the *Journal of Geophysical Research: Planets*, Fu used the microscope to zoom in on the sulfide rims of a crystalized droplet of primordial melt within a meteorite that likely formed beyond Jupiter. Just 100 micrometers wide, the rims are too small for older techniques to isolate and measure, but the QDM revealed a weak relic magnetism. Combined with past measures of a stronger field in a meteorite formed closer to the Sun, the finding indicates that 4.6 billion year ago, the disk of material that gave rise to the planets might have had a patchy magnetic field. Fu says that indicates magnetism, not just gravitational dynamics, may have played a role in the planets' coalescence out of the disk.

Closer to home, scientists have long used cave formations to gauge rainfall, based on ratios of oxygen isotopes left in stalactites and stalagmites by seeping water. But the isotope ratios can be an unreliable indicator. The water is also known to deposit microscopic magnetic grains picked up from soil and rock, in amounts that vary with rainfall. In samples collected from the Brazilian rainforest, Fu's team found that the QDM appears capable of measuring those grain abundances over time as a proxy for rainfall, he says. This would "unlock a whole new source of data about past environmental change," says Joshua Feinberg, a geologist at the University of Minnesota, Twin Cities.

Although it has only migrated to a few labs so far, the QDM could become the go-to tool for resolving controversial claims of paleomagnetism, says Claire Nichols, a geologist at MIT. Nichols has reported finding magnetic fields in 3.7-billion-year-old rocks from Greenland—another sign of an early magnetic dynamo on Earth. A QDM map would bolster that claim. "It's now going to become the gold standard," she says. ■

PHOTO: RK1979/SHUTTERSTOCK.COM

PLANT BIOLOGY

Heat-protected plants offer cool surprise—greater yields

Engineered rice grows better at normal temperatures

By **Erik Stokstad**

As plants convert sunlight into sugar, their cells are playing with fire. Photosynthesis generates chemical byproducts that can damage the light-converting machinery itself—and the hotter the weather, the more likely the process is to run amok as some chemical reactions accelerate and others slow. Now, a team of geneticists has engineered plants so they can better repair heat damage, an advance that could help preserve crop yields as global warming makes heat waves more common. And in a surprise, the change made plants more productive at normal temperatures.

"This is exciting news," says Maria Ermakova of Australian National University, who works on improving photosynthesis. The genetic modification worked in three kinds of plants, a mustard that is the most common plant model, tobacco, and rice, suggesting any crop plant could be helped. The work bucked conventional wisdom among photosynthesis scientists, and some plant biologists wonder exactly how the added gene produces the benefits. Still, Peter Nixon, a plant biochemist at Imperial College London, predicts the study will "attract considerable attention."

Extreme heat impairs photosynthesis, depressing yields of crops like rice.

When plants are exposed to light, a complex of proteins called photosystem II (PSII) energizes electrons that then help power photosynthesis. But heat or intense light can lead to damage in a key subunit, known as D1, halting PSII's work until the plant makes and inserts a new one into the complex. Plants that make extra D1 should help speed those repairs. Chloroplasts, the organelles that host photosynthesis, have their own DNA, including a gene for D1, and most biologists assumed the protein had to be made there. But the chloroplast genome is much harder to tweak than genes in a plant cell's nucleus.

A team led by plant molecular biologist Fang-Qing Guo of the Chinese Academy of Sciences bet that D1 made by a nuclear gene could work just as well—and be made more efficiently, as its synthesis in the cytoplasm instead of the chloroplast would be protected from the corrosive byproducts of photosynthetic reactions. Guo and colleagues tested the idea in the mustard *Arabidopsis thaliana*. They took its chloroplast gene for D1, coupled it to a stretch of DNA that turns on during heat stress, and moved it to the nucleus.

The team found that modified *Arabidopsis* seedlings could survive extreme heat in the lab—8.5 hours at 41°C—that killed most of the control plants. The same *Arabidopsis* gene also protected tobacco and rice. In all three species, photosynthesis and growth decreased less than in the surviving control plants. And in 2017, when Shanghai exceeded 36°C for 18 days, transgenic rice planted in test plots yielded 8% to 10% more grain than control plants, the team reports this week in *Nature Plants*.

The shock was what happened at normal temperatures. Engineered plants of all three species had more photosynthesis—tobacco's rate increased by 48%—and grew more than control plants. In the field, the transgenic rice yielded up to 20% more grain. "It truly surprised us," Guo says. "I felt that we have caught a big fish."

Veteran photosynthesis researcher Donald Ort of the University of Illinois, Urbana-Champaign, says the group presents credible evidence of plant benefits, but he's not yet convinced that the D1 made by nuclear genes repaired PSII. "Anything this potentially important is going to be met with some skepticism. There are lots of experiments to do, to figure out why this works," he says.

Guo plans further tests of the mechanism. He also has a practical goal: heftier yield increases in rice. The productivity boost his team saw in modified *Arabidopsis* was much larger—80% more biomass than controls—perhaps because the researchers simply moved *Arabidopsis*'s own D1 gene. He thinks rice yield might also burgeon if it could be modified with its own chloroplast gene rather than mustard's—further heating up these already hot results. ■

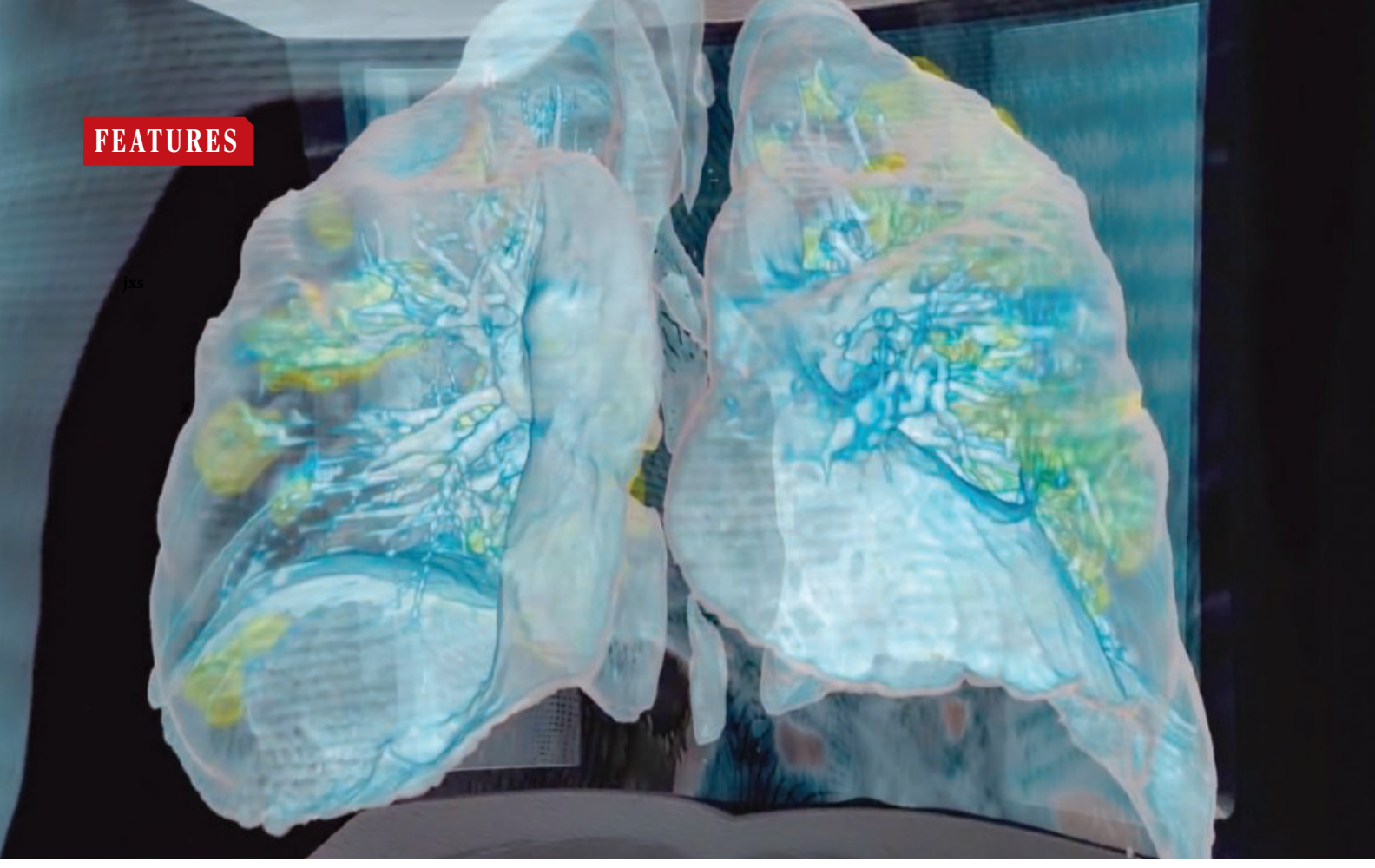

IMAGE: GEORGE WASHINGTON HOSPITAL AND SURGICAL THEATER

A RAMPAGE THROUGH THE BODY

The lungs are ground zero, but COVID-19 also tears through organ systems from brain to blood vessels

QQ group: 970508760

By **Meredith Wadman**, **Jennifer Couzin-Frankel**, **Jocelyn Kaiser**, *and* **Catherine Matacic**

On rounds in a 20-bed intensive care unit one recent day, physician Joshua Denson assessed two patients with seizures, many with respiratory failure, and others whose kidneys were on a dangerous downhill slide. Days earlier, his rounds had been interrupted as his team tried, and failed, to resuscitate a young woman whose heart had stopped. All of the patients shared one thing, says Denson, a pulmonary and critical care physician at the Tulane University School of Medicine. "They are all COVID positive."

As the number of confirmed cases of COVID-19 approaches 2.5 million globally and deaths surpass 166,000, clinicians and pathologists are struggling to understand the damage wrought by the coronavirus as it tears through the body. They are realizing that although the lungs are ground zero, the virus' reach can extend to many organs including the heart and blood vessels, kidneys, gut, and brain.

"[The disease] can attack almost anything in the body with devastating consequences," says cardiologist Harlan Krumholz of Yale University and Yale-New Haven Hospital, who is leading multiple efforts to gather clinical data on COVID-19. "Its ferocity is breathtaking and humbling."

Understanding the rampage could help doctors on the front lines treat the roughly

The coronavirus wreaked extensive damage (yellow) on the lungs of a 59-year-old man who died at George Washington University Hospital, as seen in a 3D model based on computed tomography scans.

5% of infected people who become desperately and sometimes mysteriously ill. Does a dangerous, newly observed tendency to blood clotting transform some mild cases into life-threatening emergencies? Is an overzealous immune response behind the worst cases, suggesting treatment with immune-suppressing drugs could help? And what explains the startlingly low blood oxygen that some physicians are reporting in patients who nonetheless are not gasping for breath? "Taking a systems approach may be beneficial as we start thinking about therapies," says Nilam Mangalmurti, a pulmonary intensivist at the Hospital of the University of Pennsylvania (HUP).

What follows is a snapshot of the fast-evolving understanding of how the virus attacks cells around the body. Despite the more than 1500 papers now spilling into journals and onto preprint servers every week, a clear picture is elusive, as the virus acts like no pathogen humanity has ever seen. Without larger, controlled studies that are only now being launched, scientists must pull information from small studies and case reports, often published at warp speed and not yet peer reviewed. "We need to keep a very open mind as this phenomenon goes forward," says Nancy Reau, a liver transplant physician who has been treating COVID-19 patients at Rush University Medical Center. "We are still learning."

Science's COVID-19 coverage is supported by the Pulitzer Center.

WHEN AN INFECTED PERSON expels virus-laden droplets and someone else inhales them, the novel coronavirus, called SARS-CoV-2, enters the nose and throat. It finds a welcome home in the lining of the nose, according to a recent arXiv preprint, because cells there are rich in a cell-surface receptor called angiotensin-converting enzyme 2 (ACE2). Throughout the body, the presence of ACE2, which normally helps regulate blood pressure, marks tissues potentially vulnerable to infection, because the virus requires that receptor to enter a cell. Once inside, the virus hijacks the cell's machinery, making myriad copies of itself and invading new cells.

As the virus multiplies, an infected person may shed copious amounts of it, especially during the first week or so. Symptoms may be absent at this point. Or the virus' new victim may develop a fever, dry cough, sore throat, loss of smell and taste, or head and body aches.

If the immune system doesn't beat back SARS-CoV-2 during this initial phase, the virus then marches down the windpipe to attack the lungs, where it can turn deadly. The thinner, distant branches of the lung's respiratory tree end in tiny air sacs called alveoli, each lined by a single layer of cells that are also rich in ACE2 receptors.

Normally, oxygen crosses the alveoli into the capillaries, tiny blood vessels that lie beside the air sacs; the oxygen is then carried to the rest of the body. But as the immune system wars with the invader, the battle itself disrupts healthy oxygen transfer. Frontline white blood cells release inflammatory molecules called chemokines, which in turn summon more immune cells that target and kill virus-infected cells, leaving a stew of fluid and dead cells—pus—behind (see graphic, p. 358). This is the underlying pathology of pneumonia, with its corresponding symptoms: coughing; fever; and rapid, shallow respiration. Some COVID-19 patients recover, sometimes with no more support than oxygen breathed in through nasal prongs.

But others deteriorate, often suddenly, developing a condition called acute respiratory distress syndrome. Oxygen levels in their blood plummet, and they struggle ever harder to breathe. On x-rays and computed tomography scans, their lungs are riddled with white opacities where black space—air—should be. Commonly, these patients end up on ventilators. Many die, and survivors may face long-term complications (see sidebar, p. 359). Autopsies show their alveoli became stuffed with fluid, white blood cells, mucus, and the detritus of destroyed lung cells.

Some clinicians suspect the driving force in many gravely ill patients' downhill trajectories is a disastrous overreaction of the immune system known as a "cytokine storm," which other viral infections are known to trigger. Cytokines are chemical signaling molecules that guide a healthy immune response; but in a cytokine storm, levels of certain cytokines soar far beyond what's needed, and immune cells start to attack healthy tissues. Blood vessels leak, blood pressure drops, clots form, and catastrophic organ failure can ensue.

Some studies have shown elevated levels of these inflammation-inducing cytokines in the blood of hospitalized COVID-19 patients. "The real morbidity and mortality of this disease is probably driven by this out of proportion inflammatory response to the virus," says Jamie Garfield, a pulmonologist who cares for COVID-19 patients at Temple University Hospital.

But others aren't convinced. "There seems to have been a quick move to associate COVID-19 with these hyperinflammatory states. I haven't really seen convincing data that that is the case," says Joseph Levitt, a pulmonary critical care physician at the Stanford University School of Medicine.

He's also worried that efforts to dampen a cytokine response could backfire. Several drugs targeting specific cytokines are in clinical trials in COVID-19 patients. But Levitt fears those drugs may suppress the immune response that the body needs to fight off the virus. "There's a real risk that we allow more viral replication," Levitt says.

Meanwhile, other scientists are zeroing in on an entirely different organ system that they say is driving some patients' rapid deterioration: the heart and blood vessels.

IN BRESCIA, ITALY, a 53-year-old woman walked into the emergency room of her local hospital with all the classic symptoms of a heart attack, including telltale signs in her electrocardiogram and high levels of a blood marker suggesting damaged cardiac muscles. Further tests showed cardiac swelling and scarring, and a left ventricle—normally the powerhouse chamber of the heart—so weak that it could only pump one-third its normal amount of blood. But when doctors injected dye in her coronary arteries, looking for the blockage that signifies a heart attack, they found none. Another test revealed the real cause: COVID-19.

How the virus attacks the heart and blood vessels is a mystery, but dozens of preprints and papers attest that such damage is common. A 25 March paper in *JAMA Cardiology* found heart damage in nearly 20% of patients out of 416 hospitalized for COVID-19 in Wuhan, China. In another Wuhan study, 44% of 36 patients admitted to the intensive care unit (ICU) had arrhythmias.

The disruption seems to extend to the blood itself. Among 184 COVID-19 patients in a Dutch ICU, 38% had blood that clotted abnormally, and almost one-third already had clots, according to a 10 April paper in *Thrombosis Research*. Blood clots can break apart and land in the lungs, blocking vital arteries—a condition known as pulmonary embolism, which has reportedly killed COVID-19 patients. Clots from arteries can also lodge in the brain, causing stroke. Many patients have "dramatically" high levels of D-dimer, a byproduct of blood clots, says Behnood Bikdeli, a cardiovascular medicine fellow at Columbia University Medical Center.

"The more we look, the more likely it becomes that blood clots are a major player in the disease severity and mortality from COVID-19," Bikdeli says.

Infection may also lead to blood vessel constriction. Reports are emerging of isch-

An invader's impact

In serious cases, SARS-CoV-2 lands in the lungs and can do deep damage there. But the virus, or the body's response to it, can injure many other organs. Scientists are just beginning to probe the scope and nature of that harm.

1 Lungs
A cross section shows immune cells crowding an inflamed alveolus, or air sac, whose walls break down during attack by the virus, diminishing oxygen uptake. Patients cough, fevers rise, and breathing becomes labored.

2 Heart and blood vessels
The virus (teal) enters cells, likely including those lining blood vessels, by binding to angiotensin-converting enzyme 2 (ACE2) receptors on the cell surface. Infection can also promote blood clots, heart attacks, and cardiac inflammation.

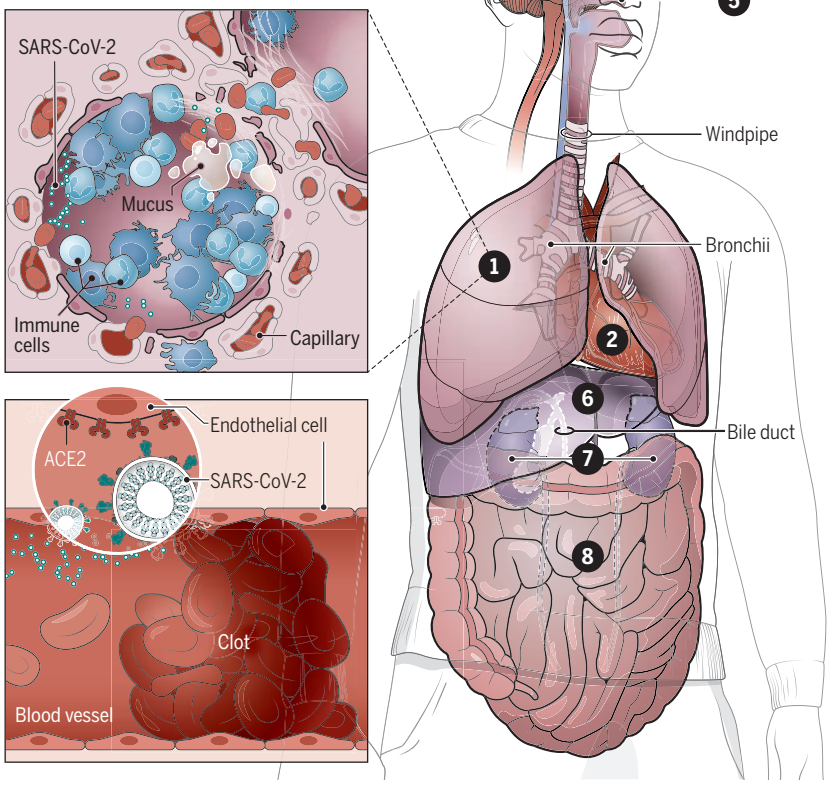

3 Brain
Some COVID-19 patients have strokes, seizures, confusion, and brain inflammation. Doctors are trying to understand which are directly caused by the virus.

4 Eyes
Conjunctivitis, inflammation of the membrane that lines the front of the eye and inner eyelid, is more common in the sickest patients.

5 Nose
Some patients lose their sense of smell. Scientists speculate that the virus may move up the nose's nerve endings and damage cells.

6 Liver
Up to half of hospitalized patients have enzyme levels that signal a struggling liver. An immune system in overdrive and drugs given to fight the virus may be causing the damage.

7 Kidneys
Kidney damage is common in severe cases and makes death more likely. The virus may attack the kidneys directly, or kidney failure may be part of whole-body events like plummeting blood pressure.

8 Intestines
Patient reports and biopsy data suggest the virus can infect the lower gastrointestinal tract, which is rich in ACE2 receptors. Some 20% or more of patients have diarrhea.

GRAPHIC: V. ALTOUNIAN/*SCIENCE*

emia in the fingers and toes—a reduction in blood flow that can lead to swollen, painful digits and tissue death.

In the lungs, blood vessel constriction might help explain anecdotal reports of a perplexing phenomenon seen in pneumonia caused by COVID-19: Some patients have extremely low blood-oxygen levels and yet are not gasping for breath. In this scenario, oxygen uptake is impeded by constricted blood vessels rather than by clogged alveoli. "One theory is that the virus affects the vascular biology and that's why we see these really low oxygen levels," Levitt says.

If COVID-19 targets blood vessels, that could also help explain why patients with pre-existing damage to those vessels, for example from diabetes and high blood pressure, face higher risk of serious disease. Recent Centers for Disease Control and Prevention (CDC) data on hospitalized patients in 14 U.S. states found that about one-third had chronic lung disease—but nearly as many had diabetes, and fully half had pre-existing high blood pressure.

Mangalmurti says she has been "shocked by the fact that we don't have a huge number of asthmatics" or patients with other respiratory diseases in her hospital's ICU. "It's very striking to us that risk factors seem to be vascular: diabetes, obesity, age, hypertension."

Scientists are struggling to understand exactly what causes the cardiovascular damage. The virus may directly attack the lining of the heart and blood vessels, which, like the nose and alveoli, are rich in ACE2 receptors. By altering the delicate balance of hormones that help regulate blood pressure, the virus might constrict blood vessels going to the lungs. Another possibility is that lack of oxygen, due to the chaos in the lungs, damages blood vessels. Or a cytokine storm could ravage the heart as it does other organs.

"We're still at the beginning," Krumholz says. "We really don't understand who is vulnerable, why some people are affected so severely, why it comes on so rapidly … and why it is so hard [for some] to recover."

THE WORLDWIDE FEARS of ventilator shortages for failing lungs have received plenty of attention. Not so a scramble for another type of equipment: kidney dialysis machines. "If these folks are not dying of lung failure, they're dying of renal failure," says neurologist Jennifer Frontera of New York University's Langone Medical Center, which has treated thousands of COVID-19 patients. Her hospital is developing a dialysis protocol with a different kind of machine to support more patients. What she and her colleagues are seeing suggests the virus may target the kidneys, which are abundantly endowed with ACE2 receptors.

According to one preprint, 27% of 85 hospitalized patients in Wuhan had kidney failure. Another preprint reported that 59% of nearly 200 hospitalized COVID-19 patients in China's Hubei and Sichuan provinces had protein in their urine, and 44% had blood; both suggest kidney damage. Those with acute kidney injury were more than five times as likely to die as COVID-19 patients without it, that preprint reported.

"The lung is the primary battle zone. But a fraction of the virus possibly attacks the kidney. And as on the real battlefield, if two places are being attacked at the same time, each place gets worse," says co-author Hongbo Jia, a neuroscientist at the Chinese Academy of Sciences's Suzhou Institute of Biomedical Engineering and Technology.

Survivors' burden

By **Kelly Servick**

Among those hospitalized with severe COVID-19, these are the lucky ones: people who recover, come off mechanical ventilators that have kept them breathing, and leave the hospital. As more and more of these patients return home, clinicians are turning their attention to potential lingering effects of both the virus and the emergency treatments that allow people to survive it.

"The issue we're all going to be faced with the most in the coming months is how we're going to help these people recover," says Lauren Ferrante, a pulmonary and critical care physician at the Yale School of Medicine.

COVID-19 damages not just the lungs, but the kidneys, blood vessels, heart, brain, and other organs (see main story, p. 356). Doctors don't yet know what lasting disabilities the virus will cause, but clues come from studies of severe pneumonia—an infection that inflames the air sacs in the lungs, as COVID-19 does. Such infections can progress to acute respiratory distress syndrome (ARDS), in which those sacs fill with fluid. Most patients eventually recover their lung function, but ARDS sometimes leads to scarring that can cause long-term breathing problems, Ferrante says.

After any severe case of pneumonia, a combination of underlying chronic diseases and prolonged inflammation seems to increase the risk of other illnesses, including heart attack, stroke, and kidney disease, says Sachin Yende, an epidemiologist and critical care physician at the University of Pittsburgh Medical Center. COVID-19 might prompt "a big increase in these sorts of events," he says.

Patients who spend time in an intensive care unit (ICU), regardless of the illness that put them there, are also prone to a set of physical, cognitive, and mental health problems after leaving. The coronavirus might put ICU survivors at particular risk for some of these problems, in part because its severe lung injury leads many patients to spend prolonged periods on a ventilator under deep sedation, says Dale Needham, a critical care physician at Johns Hopkins University's School of Medicine.

Those few patients who survive long periods of ventilation are prone to muscle atrophy and weakness. Keeping a critically ill patient moving—helping them raise their arms and legs, and eventually sit, stand, and walk—can reduce that weakness and get them off the ventilator faster. But in some hospitals, a shortage of protective equipment has kept physical therapists away from COVID-19 patients.

Another risk is delirium—a state of confused thinking that can lead to long-term cognitive impairments such as memory deficits. "What we're finding in COVID is that there's a ton of delirium," says E. Wesley Ely, a pulmonologist and critical care physician at Vanderbilt University. One cause is the virus itself, which may infect the brain. But the sedatives prescribed to suppress violent coughing and help patients tolerate the discomfort of a breathing tube can also increase delirium risk. And as hospitals run short of the most commonly used sedatives, they're turning to other drugs that can cause "intense and prolonged delirium," Ely says.

ICU patient care guidelines that Ely and colleagues have developed over many years recommend a daily interruption of narcotics and sedatives to test whether patients can wake up, breathe, and tolerate the ventilator without drugs. But the practice requires close monitoring that is difficult in overstretched ICUs, Ely says. "Everybody out there is trying to do their best. … But let's not throw out all the things we've learned in the last 20 years."

The threat of infection has also limited the bedside interactions that can calm patients and reduce the need for delirium-inducing drugs. "If you could design a system to be bad for how you care for older adults … the family would not be allowed to visit, and [health care workers would] go in with face masks and all gowned up, so they're completely frightening," says Sharon Inouye, a geriatrician at Harvard Medical School's Hebrew SeniorLife health care system.

Some critical care doctors are starting to question recommendations for ventilator use early in the course of disease. "If we're putting more people on ventilators than maybe we need to, that certainly is going to affect the population health after recovery," says C. Terri Hough, a pulmonary critical care physician at the University of Washington, Seattle.

As some hospitals move past the initial surge in cases, researchers are also trying to look ahead. Ely's team is testing a tablet-based rehabilitation program for people who have cognitive impairment after being hospitalized for a critical illness. Yende's team is piloting a care approach for discharged pneumonia and sepsis patients that includes remote monitoring and treatment and inhome visits to prevent readmission to the hospital.

Others are preparing for a surge in mental health problems among survivors, among them anxiety, depression, and post-traumatic stress disorder. Hough and her collaborators are testing a mobile app that promotes mindfulness and coping skills for people leaving the hospital. For survivors of all critical illnesses, she says, "this we're-all-in-this-together attitude around coronavirus may actually provide hope that wasn't there before." ■

Survivors of COVID-19 who spent time on a ventilator may be at risk of long-term disability and illness.

PHOTO: FARHAD BABAEI/MAGNUS NEW/SIPA/NEWSCOM

One study identified viral particles in electron micrographs of kidneys from autopsies, suggesting a direct viral attack. But kidney injury may also be collateral damage. Ventilators boost the risk of kidney damage, as do antiviral compounds including remdesivir, which is being deployed experimentally in COVID-19 patients. Cytokine storms can also dramatically reduce blood flow to the kidney, causing often-fatal damage. And pre-existing diseases like diabetes can increase the chances of kidney injury. "There is a whole bucket of people who already have some chronic kidney disease who are at higher risk for acute kidney injury," says Suzanne Watnick, chief medical officer at Northwest Kidney Centers.

ANOTHER STRIKING SET of symptoms in COVID-19 patients centers on the brain and nervous system. Frontera says 5% to 10% of coronavirus patients at her hospital have neurological symptoms. But she says that "is probably a gross underestimate" of the number whose brains are struggling, especially because many are sedated and on ventilators.

Frontera has seen patients with the brain inflammation encephalitis, seizures, and a "sympathetic storm," a hyperreaction of the sympathetic nervous system that causes seizurelike symptoms and is most common after a traumatic brain injury. Some people with COVID-19 briefly lose consciousness. Others have strokes. Many report losing their sense of smell and taste. And Frontera and others wonder whether, in some cases, infection depresses the brain stem reflex that senses oxygen starvation—another explanation for anecdotal observations that some patients aren't gasping for air, despite dangerously low blood oxygen levels.

ACE2 receptors are present in the neural cortex and brain stem, says Robert Stevens, an intensive care physician at Johns Hopkins Medicine. And the coronavirus behind the 2003 severe acute respiratory syndrome (SARS) epidemic—a close cousin of today's culprit—was able to infiltrate neurons and sometimes caused encephalitis. On 3 April, a case study in the *International Journal of Infectious Diseases*, from a team in Japan, reported traces of new coronavirus in the cerebrospinal fluid of a COVID-19 patient who developed meningitis and encephalitis, suggesting it, too, can penetrate the central nervous system.

But other factors could be damaging the brain. For example, a cytokine storm could cause brain swelling. The blood's exaggerated tendency to clot could trigger strokes. The challenge now is to shift from conjecture to confidence, at a time when staff are focused on saving lives, and even neurologic assessments like inducing the gag reflex or transporting patients for brain scans risk spreading the virus.

Last month, Sherry Chou, a neurologist at the University of Pittsburgh Medical Center, began to organize a worldwide consortium that now includes 50 centers to draw neurological data from care patients already receive. Early goals are simple: Identify the prevalence of neurologic complications in hospitalized patients and document how they fare. Longer term, Chou and her colleagues hope to gather scans and data from lab tests to better understand the virus' impact on the nervous system, including the brain.

No one knows when or how the virus might penetrate the brain. But Chou speculates about a possible invasion route: through the nose, then upward and through the olfactory bulb—explaining reports of a loss of smell—which connects to the brain. "It's a nice sounding theory," she says. "We really have to go and prove that."

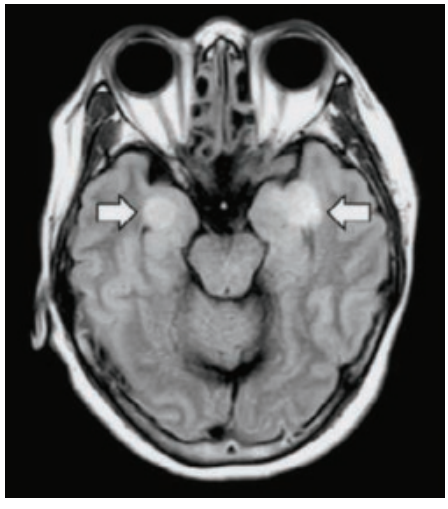

A 58-year-old woman with COVID-19 developed encephalitis, with tissue damage in the brain (arrows).

Most neurological symptoms "are reported from colleague to colleague by word of mouth," Chou adds. "I don't think anybody, and certainly not me, can say we're experts."

IN EARLY MARCH, a 71-year-old Michigan woman returned from a Nile River cruise with bloody diarrhea, vomiting, and abdominal pain. Initially doctors suspected she had a common stomach bug, such as *Salmonella*. But after she developed a cough, doctors took a nasal swab and found her positive for the novel coronavirus. A stool sample positive for viral RNA, as well as signs of colon injury seen in an endoscopy, pointed to a gastrointestinal (GI) infection with the coronavirus, according to a paper posted online in *The American Journal of Gastroenterology* (*AJG*).

Her case adds to a growing body of evidence suggesting the new coronavirus, like its cousin SARS, can infect the lining of the lower digestive tract, where ACE2 receptors are abundant. Viral RNA has been found in as many as 53% of sampled patients' stool samples. And in a paper in press at *Gastroenterology*, a Chinese team reported finding the virus' protein shell in gastric, duodenal, and rectal cells in biopsies from a COVID-19 patient. "I think it probably does replicate in the gastrointestinal tract," says Mary Estes, a virologist at Baylor College of Medicine.

Recent reports suggest up to half of patients, averaging about 20% across studies, experience diarrhea, says Brennan Spiegel of Cedars-Sinai Medical Center in Los Angeles, co–editor-in-chief of *AJG*. GI symptoms aren't on CDC's list of COVID-19 symptoms, which could cause some COVID-19 cases to go undetected, Spiegel and others say. "If you mainly have fever and diarrhea, you won't be tested for COVID," says Douglas Corley of Kaiser Permanente, Northern California, co-editor of *Gastroenterology*.

The presence of virus in the GI tract raises the unsettling possibility that it could be passed on through feces. But it's not yet clear whether stool contains intact, infectious virus, or only RNA and proteins. To date, "We have no evidence" that fecal transmission is important, says coronavirus expert Stanley Perlman of the University of Iowa. CDC says that, based on experiences with SARS and with the coronavirus that causes Middle East respiratory syndrome, the risk from fecal transmission is probably low.

The intestines are not the end of the disease's march through the body. For example, up to one-third of hospitalized patients develop conjunctivitis—pink, watery eyes—although it's not clear that the virus directly invades the eye.

Other reports suggest liver damage: More than half of COVID-19 patients hospitalized in two Chinese centers had elevated levels of enzymes indicating injury to the liver or bile ducts. But several experts told *Science* that direct viral invasion isn't likely the culprit. They say other events in a failing body, like drugs or an immune system in overdrive, are more likely causes of the liver damage.

This map of the devastation that COVID-19 can inflict on the body is still just a sketch. It will take years of painstaking research to sharpen the picture of its reach, and the cascade of effects in the body's complex and interconnected systems that it might set in motion. As science races ahead, from probing tissues under microscopes to testing drugs on patients, the hope is for treatments more wily than the virus that has stopped the world in its tracks. ■

IMAGE: N. POYIADJI *ET AL.*, *RADIOLOGY*. (2020) DOI.ORG/10.1148/RADIOL.2020201187

eppendorf & Science

PRIZE FOR NEURO BIOLOGY

2019 Winner
Lauren Orefice, Ph.D.

For research on the causes and potential therapies for autism spectrum disorders

Application Deadline
June 15, 2020

Now It's Your Turn!

Eppendorf & Science Prize for Neurobiology
The annual Eppendorf & Science Prize for Neurobiology is an annual international prize which honors young scientists for their outstanding contributions to neurobiological research based on methods of molecular and cell biology. The winner and finalists are selected by a committee of independent scientists, chaired by *Science's* Senior Editor, Dr. Peter Stern. If you are 35 years of age or younger and doing great research, now is the time to apply for this prize.

As the Grand Prize Winner, you could be next to receive
> Prize money of US$25,000
> Publication of your work in *Science*
> Full support to attend the Prize Ceremony held in conjunction with the Annual Meeting of the Society for Neuroscience in the USA
> 10-year AAAS membership and online subscription to *Science*
> Complimentary products worth US$1,000 from Eppendorf
> An invitation to visit Eppendorf in Hamburg, Germany

It's easy to apply! Write a 1,000-word essay and tell the world about your work. Learn more at:

www.eppendorf.com/prize

eppendorf Science AAAS

AAAS® and Science® are registered trademarks of the American Association for the Advancement of Science, USA. Eppendorf® and the Eppendorf Brand Design are registered trademarks of Eppendorf AG, Germany. All rights reserved, including graphics and images. Copyright © 2020 by Eppendorf AG. Kurstin Roe Photography.

EPIDEMIOLOGY

Mucosal immunity and the eradication of polio

Completing global polio eradication will require a new oral vaccine

By **Alexandra N. Donlan**[1,2] *and* **William A. Petri Jr.**[1,2,3]

Epidemics of paralytic disease due to poliovirus were an annual occurrence in the early 20th century. In 1916, there were 2000 deaths in New York City alone from the nationwide epidemic. Closures of swimming pools and movie theaters, and not shaking hands or handling money during summertime polio epidemics, predated the social distancing we practice today due to the coronavirus disease 2019 (COVID-19) pandemic. Because of successful vaccination programs, the Americas, Europe, Southeast Asia, and the Western Pacific are considered polio-free. However, poliovirus is still a threat in many countries, and vaccination initiatives have been active in those regions. On page 401 of this issue, Macklin *et al.* (*1*) report on an emerging problem of a polio outbreak in Africa and Asia that is derived from a strain used in the vaccination campaigns. This highlights a need for new approaches to vaccine development to avoid vaccine-derived polio.

Prevention of polio epidemics by vaccination was a signature success of science in the 20th century. Cultivation of poliovirus in the laboratory was reported in 1949 (*2*), and 6 years later, Jonas Salk made an injectable polio vaccine (IPV) by inactivating the lab-cultured poliovirus with formalin. Its effectiveness was tested in a herculean vaccine trial involving nearly 2 million children (*3*), and its success led to a nationwide celebration and Salk's invitation to the White House. Today, the faith in, and support of, scientific research by the American public is, arguably, founded on the polio vaccine.

By the beginning of the 1960s, there were two polio vaccines, the IPV and the oral polio vaccine (OPV). Together, these have been the tools for polio eradication worldwide. The OPV was developed by Albert Sabin as live attenuated poliovirus. This was achieved in the laboratory by "passaging" poliovirus in cell culture multiple times until it was no longer capable of causing paralysis in animal models. The OPV and IPV each stimulate systemic immunity that protects against paralytic polio. Vaccination with the OPV additionally provides mucosal immunity that prevents infection in the gut.

The IPV and OPV have distinct effects on the systemic and mucosal immune systems. Systemic immunity encompasses the entire body and utilizes, in part, immunoglobulin G (IgG) antibody, which circulates in the blood-

[1]Department of Medicine, University of Virginia, VA, USA. [2]Department of Microbiology, Immunology and Cancer Biology, University of Virginia, VA, USA. [3]Department of Pathology, University of Virginia, VA, USA. Email: wap3g@virginia.edu

PHOTO: SUNDAY ALAMBA/AP PHOTO

A health official administers a polio vaccine to a child in Kawo Kano, Nigeria, in 2014.

stream. By contrast, mucosal immunity utilizes locally produced IgA antibody to protect the respiratory, gastrointestinal, and urogenital tracts. Thus, mucosal immune responses provide a first layer of defense to limit the replication and invasion of pathogenic microbes to the systemic circulation (*4*).

Following oral administration, the OPV induces production of IgA antibodies against poliovirus in the gut (*5, 6*) by harnessing gut-associated $CD4^+$ T helper cells and locally produced cytokines and vitamin A, to collectively drive the development of B cells that produce poliovirus-targeting IgA (*4*, *7*, *8*). These B cells in the mucosa express the J (or joining) chain that links two IgA molecules together. As the dimer, IgA is transported across the intestinal epithelium and into the gut lumen (*8*). This secretory IgA is positively correlated with intestinal immunity to poliovirus (*9*) and is predicted to be the main mechanism through which the OPV prevents viral colonization and shedding (*9*, *10*), although T cell–mediated protection is likely a player as well.

By contrast, the IPV, which is administered by injection, only stimulates a systemic response of IgG and monomeric IgA (*5, 10*). Likely because of its inability to trigger a mucosal immune response, viral colonization and shedding can still occur after infection (*9*). The OPV therefore is essential because of its ability to stimulate colonization-blocking secretory IgA and promote nonspecific innate immunity to other infections (*10*).

Unfortunately, the OPV is also the Achilles heel of global eradication. Macklin *et al.* analyzed outbreaks of serotype 2 vaccine-derived poliovirus (VDPV2) in Africa and Asia. Because the OPV is composed of attenuated poliovirus, it is excreted as live virus in the stool after vaccination. Thus, contact with family members and the community can lead to viral spread in a bystander fashion (*11*). Person-to-person spread of VDPV2 is a potential problem, as poliovirus can revert (although rarely) from its attenuated state to a more virulent state. This can then circulate in populations and even cause paralysis. Multiple outbreaks of VDPV2 began in 2016 in Nigeria and the Democratic Republic of the Congo and are now widely spread across Africa and parts of Asia.

Paradoxically, this situation arose from the success of the Global Polio Eradication Initiative that eliminated transmission of serotype 2 wild poliovirus in 2015 (and serotype 3 wild poliovirus in 2019). In April 2016, the OPV to type 2 wild poliovirus (OPV2) was withdrawn from the trivalent OPV (targeting serotypes 1, 2, and 3) to prevent outbreaks of VDPV2. It had been expected that some VDPV2 would be left over from the OPV2 component in trivalent OPV, and that these outbreaks could be controlled by campaigns of mass vaccination with a monovalent OPV2 (mOPV2, a vaccine composed of only live attenuated type 2 wild poliovirus). However, Macklin *et al.* used the rate of mutation in poliovirus protein 1 to determine the timing of when the VDPV2 arose. The important finding is that most of these outbreaks occurred after the switch to the bivalent vaccine, and that the majority of cases could be linked to the additional mOPV2 campaign within the same country where a VDPV2 outbreak emerged.

The dilemma to polio eradication therefore is that eradication of VDPV2 requires the use of the mOPV2—fighting fire with fire, as it were. In response to this problem, the development of a "new" OPV2 is currently fast tracked in clinical trials. The new OPV2 candidates are engineered to prevent loss of the major attenuating mutations in the viral 5′–untranslated region of the poliovirus RNA genome that controls viral protein production (*12*, *13*). It is not unreasonable to hope that replacing the old mOPV2 with new OPV2 will be the answer to the current relapse in the global eradication campaign. In the meantime, eradication efforts will continue with the current vaccines—that is, the bivalent OPV and the trivalent IPV, with mOPV2 used to control outbreaks of serotype VDPV2.

As the world faces COVID-19, it is heartening to see the same application of science to public health for the severe acute respiratory syndrome–coronavirus 2 (SARS-CoV-2) as the one used for the last 70 years of poliovirus research. ■

REFERENCES AND NOTES

1. G. R. Macklin *et al.*, *Science* **368**, 401 (2020).
2. J. F. Enders, T. H. Weller, F. C. Robbins, *Science* **109**, 85 (1949).
3. Poliomyelitis Vaccine Evaluation Center, *Am. J. Public Health Nations Health* **45**, 49 (1955).
4. P. N. Boyaka, *J. Immunol.* **199**, 9 (2017).
5. R. W. Sutter, O. M. Kew, S. L. Cochi, R. B. Aylward, in Vaccines, S. A. Plotkin, W. A. Orenstein P. A. Offit, Eds. (Saunders Elsevier, ed. 6, 2012), chap. 26, p. 598.
6. P. L. Ogra, M. Fishaut, M. R. Gallagher, *Rev. Infect. Dis.* **2**, 352 (1980).
7. K. Chen, G. Magri, E. K. Grasset, A. Cerutti, *Nat. Rev. Immunol*. 10.1038/s41577-019-0261-1 (2020).
8. C. D. Castro, M. F. Flajnik, *J. Immunol.* **193**, 3248 (2014).
9. P. F. Wright *et al.*, *J. Infect. Dis.* **209**, 1628 (2014).
10. A. Upfill-Brown *et al.*, *Clin. Infect. Dis.* **65**, 414 (2017).
11. M. Taniuchi *et al.*, *Lancet Infect. Dis.* **17**, 1069 (2017).
12. A. L. Gutiérrez, M. Denova-Ocampo, V. R. Racaniello, R. M. del Angel, *J. Virol.* **71**, 3826 (1997).
13. P. Van Damme *et al.*, *Lancet* **394**, 148 (2019).

ACKNOWLEDGMENTS

Work from the authors' lab is supported by NIH grant AI043596, the Henske family, and the Bill & Melinda Gates Foundation. A.D. was supported by NIH grant T32 5T32AI007496.

10.1126/science.abb8588

PLANETARY SCIENCE

Super-rotating the venusian atmosphere

Analysis of spacecraft observations deciphers the source of fast atmospheric rotation

By **Sebastien Lebonnois**

Among the intriguing mysteries that remain for planetary atmospheres, the phenomenon of super-rotation is still a teasing problem. An atmosphere in super-rotation rotates globally faster than the solid body of the planet. In our solar system, super-rotation is observed on Venus and the largest moon of Saturn, Titan (*1*). The challenge is to explain how angular momentum can accumulate in the atmosphere and what controls the atmospheric angular momentum budget. On page 405 of this issue, Horinouchi *et al.* (*2*) address this by analyzing observation data from the onboard cameras of the Venus-orbiting Akatsuki spacecraft.

The Akatsuki spacecraft has been in equatorial orbit around Venus since December 2015. Understanding the angular momentum transport in the equatorial regions is key to solving the puzzle of super-rotation. The authors retrieved several components of the angular momentum balance in

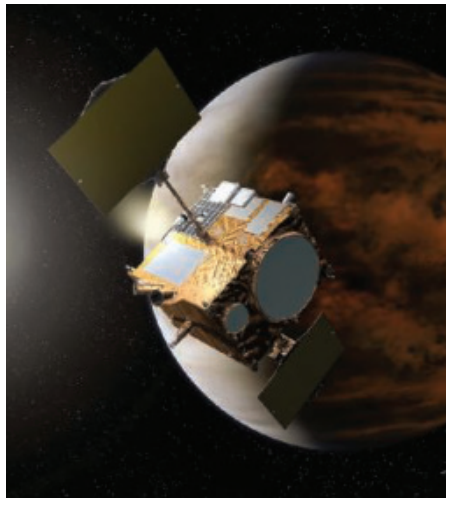

The Akatsuki spacecraft has been orbiting Venus since December 2015.

ILLUSTRATION: © JAPAN AEROSPACE EXPLORATION AGENCY (JAXA)

Supercharging wind speed

The atmosphere of Venus can circle the planet up to 60 times as fast as the rotation of the planet itself, which requires 243 Earth days. This phenomenon is called super-rotation. The angular momentum budget that causes this is a complicated combination of transport by mean meridional circulation (dark blue), thermal tides (orange), planetary-scale waves (red), and turbulent eddies (pink).

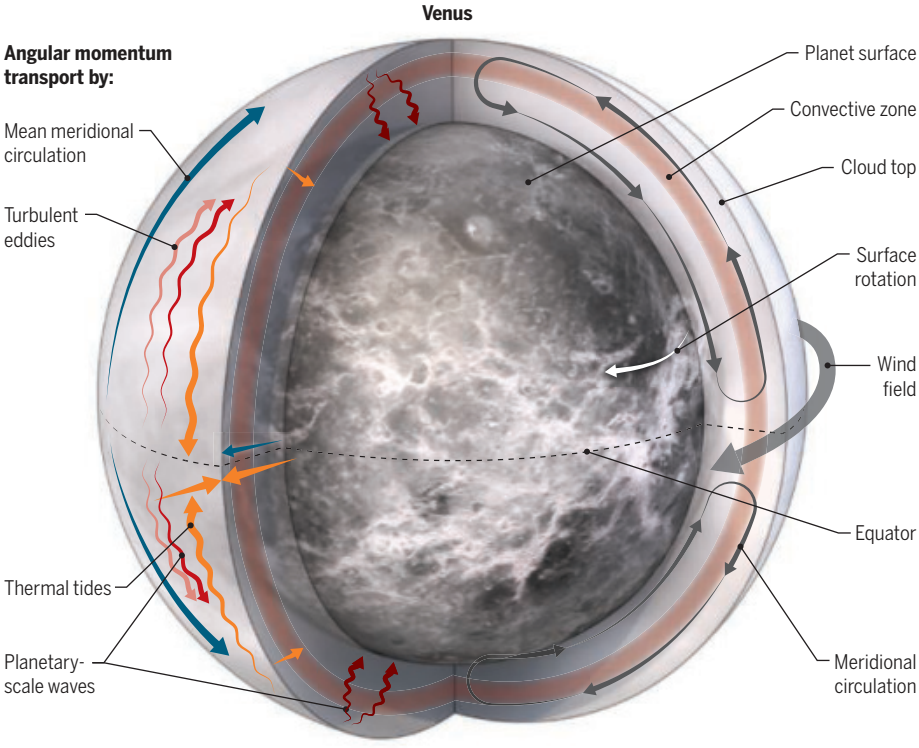

the cloud-top region, located around 70 km of altitude. This region is where the zonal wind speed of the venusian atmosphere is at a maximum, with values around 110 m/s between 45°N and 45°S. From a theoretical point of view, the super-rotation is based on a balance between the transport of angular momentum by the mean meridional circulation and by transient wave activity (*3*, *4*). The mean meridional circulation on Venus is characterized by an equator-to-pole thermally direct circulation, transporting angular momentum upward and poleward (see the figure). The whole question is then the nature of the transients that may be the dominant players to counteract this transport. Several scenarios have been proposed, including vertical transport by eddies (such as thermal tides) and horizontal equatorward transport by planetary-scale waves. Without additional elements, answering the super-rotation question is not possible through theory alone.

General circulation models (GCMs) developed for Earth's atmosphere play a vital role in understanding atmospheric evolution. They also can be used to provide insight into other planetary atmospheres, including features not observed in Earth's atmosphere. These models are complex but extremely useful tools to explore the mechanisms taking place in the atmospheric circulation of a given planet. In the case of Venus and super-rotation, the simulations can help to decipher the relative role of each of the potential contributors to angular momentum transport (*5*). However, the development of realistic simulations of the atmosphere of Venus by GCMs is not an easy task. Several GCMs have finally obtained circulation and temperature structures that can fit observed fields with a reasonable agreement (*6*–*8*).

Balancing of angular momentum in the system confirms the role of transport by the mean meridional circulation and its theoretical characteristics. The models also confirm that different transient wave activities play a role in balancing this transport. In particular, thermal tides have an emphasized role in the vertical transport of angular momentum in the equatorial region. However, the wave activities that develop in these models are not always robustly established and seem to be very sensitive to model characteristics such as resolution, thermal forcing, or dynamical core structure (*9*). Therefore, as with the theory alone, this sensitivity precludes these numerical models from being fully conclusive with respect to the super-rotation mechanisms.

This is where Horinouchi *et al.*'s analysis of the Akatsuki observational datasets becomes a key element in resolving the super-rotation mystery. The authors tracked the contrast features in the ultraviolet images of the clouds that cover the planet and analyzed heat transport using maps of brightness temperature obtained in the thermal infrared. This allowed the authors to measure or estimate horizontal and vertical transport of angular momentum by thermal tides. Other terms were also obtained: transport by horizontal Rossby waves and other transient disturbances. This strategy gives a consistent picture of the angular momentum balance at the cloud-top level, revealing a strong equatorward horizontal transport of angular momentum by thermal tides in the low-latitude region, mitigated by an unexpected poleward transport by horizontal turbulence.

Horinouchi *et al.* provide an important piece of the super-rotation puzzle that can offer a strong constraint on numerical simulations of the venusian atmosphere. However, the question of whether their analysis presents a complete picture of the angular momentum balance may still be open. The observation and analysis focus on only one level of the thick atmosphere of Venus. The possibility remains that the multiple wave activities and their impact on this very sensitive balance may be different at other levels within the 20-km-thick cloud layer. Unfortunately, investigating other levels will be very complex because of the observational challenges of such a thick atmosphere. Many viewpoints are needed to solve this type of puzzle, and the best answer to the super-rotation question will likely depend on a combination of observations, theory, and GCM simulations. ■

Laboratoire de Météorologie Dynamique (LMD/IPSL), Sorbonne Université, ENS, PSL Research University, Ecole Polytechnique, Institut Polytechnique de Paris, CNRS, Paris, France. Email: sebastien.lebonnois@lmd.jussieu.fr

REFERENCES AND NOTES

1. P. L. Read, S. Lebonnois, *Annu. Rev. Earth Planet. Sci.* **46**, 175 (2018).
2. T. Horinouchi *et al.*, *Science* **368**, 405 (2020).
3. P. Gierasch, *J. Atmos. Sci.* **32**, 1038 (1975).
4. W. B. Rossow, G. P. Williams, *J. Atmos. Sci.* **36**, 377 (1979).
5. A. Sánchez-Lavega, S. Lebonnois, T. Imamura, P. Read, D. Luz, *Space Sci. Rev.* **212**, 1541 (2017).
6. S. Lebonnois, N. Sugimoto, G. Gilli, *Icarus* **278**, 38 (2016).
7. N. Sugimoto, M. Takagi, Y. Matsuda, *J. Geophys. Res. Planets* **119**, 1950 (2014).
8. J. Mendonça, P. L. Read, *Planet. Space Sci.* **134**, 1 (2016).
9. S. Lebonnois *et al.*, *ISSI Sci. Rep. Ser.* **11**, 129 (2013).

ACKNOWLEDGMENTS

I thank the Centre National d'Etudes Spatiales (CNES) for support.

10.1126/science.abb2424

GRAPHIC: C. BICKEL/*SCIENCE*

MICROBIOLOGY

Cultivating fungal research

Growing interest in host-fungal interactions has implications for human health and disease

By **Heidi H. Kong**[1] and **Julia A. Segre**[2]

Fungi cover epithelial surfaces of the human body, engaging in many mutualistic interactions with the host and other microbiota such as the more prevalent bacteria. These interactions are shaped by multiple factors, including host physiology and immunity, as well as nutrient competition. The beneficial effects of fungal colonization for hosts include resistance to pathogens and tuning of the immune system. Although health benefits continue to be explored, recent studies have revealed expanded roles of fungi in human disease, including inflammatory disorders and specific cancers. The global burden of fungal infections is also expanding, with increased numbers of at-risk patients and increased resistance to limited antifungal drugs. More fungal research is needed to overcome these unmet needs.

Fungi exist as single-celled yeast, multicellular molds, or dimorphic species occurring as both yeast and filamentous cells. *Saccharomyces cerevisiae*, *Cryptococcus neoformans*, and *Candida* and *Malassezia* spp. are frequently studied yeast, whereas *Penicillium*, *Mucor*, and *Aspergillus* are well-known molds. As with many microbiota, fungi are classically recognized for their roles as human-associated pathogens. Candidal bloodstream infections are the most common form of fungal invasive disease, affecting about 1 in 10,000 people in the United States. Globally, cryptococcal meningitis contributes to a substantial burden of disease, particularly in HIV-positive individuals. The paucity of available antifungal treatments contributes to the morbidity and mortality of fungal infections. Classes of antifungals include azoles (e.g., fluconazole), echinocandins, and amphotericin B. However, fluconazole is the only antifungal drug available in many parts of the world. Additionally, some fungal diseases can be difficult to diagnose because of nonspecific patient symptoms, invasive tissue sampling, specific culture conditions, and identification requiring sophisticated techniques.

Recent studies have begun to explore how fungi are multifaceted in their potential to lead to beneficial as well as pathogenic outcomes for the host. Commensalism in the context of human fungi is exemplified by colonization resistance against pathogens. An example of a beneficial effect is the dominant human skin–associated *Malassezia*, which have adapted to their niche by making use of skin lipids as a nutrient, and then secreting antimicrobial products that deter bacterial pathogens (*1*). Another example of the importance of colonization resistance is *Candida albicans* commensalism in the gastrointestinal tract. In an evolutionary experiment, *C. albicans* strains acquired genetic mutations that enabled them to more stably colonize the mouse gastrointestinal tract. These evolved *C. albicans* strains provided protection against subsequent experimental challenges with different virulent fungi (*C. albicans, Aspergillus fumigatus*) and bacteria (*Staphylococcus aureus, Pseudomonas aeruginosa*) (*2*). However, these *C. albicans* strains evolved only in antibiotic-treated mice and were unable to stably colonize mice with endogenous gut bacteria, highlighting the genetic tradeoffs of adaptation to the host and competition within mixed microbial communities. Complementary studies demonstrated that mutations in transcription factors that regulate morphology are key determinants of the gut commensal fitness of *C. albicans* (*3*).

In addition to these direct host-microbial interactions, mouse gut colonization with *C. albicans* tuned host immunity, resulting in a systemic increase in fungal-specific T helper 17 (T_H17) $CD4^+$ T cells and interleukin-17 (IL-17)–responsive circulating neutrophils, which protected against more invasive bacterial and fungal, but not viral, infections (*4*). Ex vivo experiments showed that *C. albicans* elicited robust IL-17A and IL-22 responses from peripheral *C. albicans*– and *A. fumigatus*–specific T_H17 $CD4^+$ T cells from healthy human donors, demonstrating that *C. albicans* can modulate human immunity as well (*5*).

Given the complexity of host-microbial interactions, any alteration in the host or microbiota can result in infections, ranging from chronic chromoblastomycosis of the skin, dermatophyte nail infections, and acute vaginal yeast infections to potentially fatal mucormycosis in diabetics, candidal sepsis, and disseminated aspergillosis. Deficiencies in human immunity provide insight into the host-microbiota interplay. For example, patients with advanced HIV infections suffer from specific opportunistic fungal infections such as cryptococcal meningitis, mucosal candidiasis, and *Pneumocystis jirovecii* pneumonia. In patients receiving a hematopoietic stem cell transplant, candidal bloodstream infections were preceded by blooms of intestinal *Candida* spp. with altered bacterial communities, which could be used as biomarkers to identify and alter medical management (*6*). Additionally, the specificity of host-fungal immune interactions is reflected in patients with genetically defined primary immunodeficiency syndromes such as chronic granulomatous disease, autoimmune polyendocrinopathy–candidiasis–ectodermal dystrophy (APECED), or caspase recruitment domain–containing protein 9 (CARD9) deficiency, each of which renders patients susceptible to a specific fungal infection.

Other examples of host-specific fungal susceptibilities include mice deficient in the chemokine (C-X-C motif) receptor 1 (*Cxcr1*) gene, which have defective neutrophil killing of *Candida*, decreased survival, and higher fungal burden. This phenotype is similar to that of disseminated candidiasis patients and healthy donors with the *CXCR1-T276* allele who also demonstrate impaired neutrophil killing of *Candida* (*7*). Recurrent vulvovaginal candidiasis, a localized fungal infection, is estimated to affect more than 100 million women worldwide annually and has been linked with a functional variant in the *SIGLEC15* (sialic acid–binding immunoglobulin-like lectin 15) gene (*8*). Expressed on immune cells, SIGLEC15 can bind *C. albicans* and induces IL-17A and interferon-γ (IFN-γ) production, suggesting a role in anti–*C. albicans* immune responses. Host susceptibility contributes to the development of more persistent or severe fungal infections—for example, from dermatophytes or penetrating wounds. Studies of other single-nucleotide polymorphism (SNP) variants in immune-related genes that correlate with increased susceptibility to mucosal or life-threatening fungal infections hold promise for the future development of precision medicine approaches for risk stratification and preventive treatment of patients at the highest risk for fungal disease.

Inflammatory and autoimmune diseases are increasingly linked to alterations in fungal communities, particularly in ge-

[1]Cutaneous Microbiome and Inflammation Section, Dermatology Branch, National Institute of Arthritis and Musculoskeletal and Skin Diseases, Bethesda, MD 20892, USA. [2]Microbial Genomics Section, Translational and Functional Genomics Branch, National Human Genome Research Institute, Bethesda, MD 20892, USA.
Email: konghe@mail.nih.gov; jsegre@nhgri.nih.gov

netically defined hosts. SNPs in *CARD9* and *CLEC7A* (C-type lectin domain–containing 7A), which encodes Dectin-1, have been associated with inflammatory bowel diseases in humans. Dectin-1 is a C-type lectin receptor (CLR) that recognizes β-glucan in fungal cell walls and, through CARD9, signals to induce inflammatory mediators and T_H1 and T_H17 cell differentiation. Mice deficient in Dectin-1 had more severe experimentally induced colitis with increased *C. tropicalis* burden, and a SNP in human *CLEC7A* is associated with more severe ulcerative colitis (*9*). Similarly, Crohn's disease patients have higher relative abundances of intestinal *Malassezia* compared with healthy controls, and oral gavage of *Malassezia* demonstrated worsening of experimental colitis in mice, again through activation of CARD9 signaling and downstream T_H1 and T_H17 cell polarization (*10*). Genetic ablation of $CX3CR1^+$ mononuclear phagocytes, which express antifungal CLRs, also exacerbated experimental colitis in mice. Furthermore, a missense mutation in *CX3CR1* in Crohn's disease patients has been associated with reduced immunoglobulin G (IgG) responses to fungi (*11*). These and other studies suggest that inflammatory diseases may result from host-fungal imbalances.

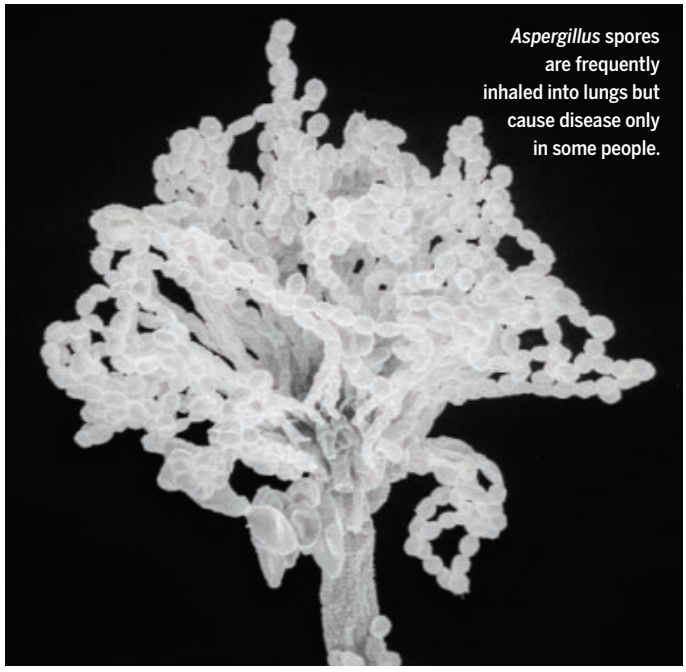

Aspergillus spores are frequently inhaled into lungs but cause disease only in some people.

Although bacteria and viruses have been implicated in cancer, fungi typically have not been. Histologic observations revealed higher amounts of intratumoral fungi, particularly of *Malassezia*, infiltrating human pancreatic ductal adenocarcinomas (PDAs). Further investigation of mouse models of PDA demonstrated fungal translocation from the intestinal tract into the pancreas, increased burden of *Malassezia* accelerated PDA progression, and antifungal treatment slowed pancreatic cancer growth (*12*). The complement cascade integrates immune recognition and fungal killing with tumor development by stimulating proinflammatory pathways. Human tissue expression of mannose-binding lectin (MBL), which activates the complement cascade, was associated with worse survival in PDA patients. Similarly, PDA progression in mice depended on *Malassezia* stimulation of MBL, linking fungi, inflammation, and tumorigenesis. This study has prompted researchers to reconsider the potential relationships between fungi and broader human diseases.

Candida auris epitomizes the gravest concerns about an emerging fungal pathogen because it has evolved resistance to all classes of antifungal drugs, particularly azoles. Numerous countries have reported active outbreaks, with increasing cases of *C. auris* bloodstream infections. The high prevalence of resistance renders these infections difficult to treat, with resultant high mortality. Over the past decade, four distinct strains of *C. auris* have emerged independently on different continents. The origin of *C. auris* as a human pathogen has remained a mystery since it was first identified in 2009. The propensity of *C. auris* to colonize human skin for a long time, which is an atypical feature for non-*auris Candida* species, is of substantial concern because shedding from patients into the environment facilitates transmissions within health care facilities (*13*). The emergence of a new human fungal pathogen points to urgent unmet medical needs for new antifungal drugs and environmental disinfectants, genomic datasets that include fungal sequences to map global fungal diversity, and a coordinated global health response.

Investigations into the role of fungi in human health and disease are challenging. Despite a myriad of bacteria, fungi, and viruses existing together in and on humans, researchers tend to focus on a few microbial species because they are more tractable to study. Diverse culture conditions or inclusion of metabolically distinct forms of dimorphic fungi (*3*) may reveal different functions and interactions. In vivo systems also have limitations. For example, conventional laboratory mice have a lower fungal burden and different immune profiles than those of wild-type mice (*14*). Additionally, adaptation to stress—induced by, for example, culture conditions, passaging through mammalian hosts, antifungal pressures, high temperatures, or acidic pH—can lead to alterations in morphology, fungal capsule, and cell wall components. This can result in evasion or triggering of host immunity and radically altered genomes in fungal cells. Genomic plasticity in fungi, including loss of heterozygosity, copy number variation, and aneuploidy, underscores the importance of incorporating metagenomic analyses into studies of fungal community adaptation to different niches (*15*).

Fungal research is an area of considerable potential. This includes understanding how fungi are beneficial to human health and mining the multiple compounds produced by fungi that may benefit clinical medicine (for example, penicillin is derived from the fungal species *Penicillium* spp.). The emergence of multidrug-resistant *C. auris* has been postulated to be due in part to rising temperatures and to the widespread use of azoles in agriculture and in the clinic. Because these pressures on host-microbial homeostasis are likely to persist and evolve, the development of new antifungal drugs is critical to counteract outbreaks from existing and future pathogens. Advances in technology, such as targeted CRISPR-Cas9–mediated gene deletion for fungal mutagenesis, can provide precise tools for testing genetic hypotheses and elucidating fungal pathophysiology. Further advances will continue to improve our understanding of how fungi affect human health and disease. ■

REFERENCES AND NOTES

1. G. Wu *et al.*, *PLOS Genet.* **11**, e1005614 (2015).
2. G. H. W. Tso *et al.*, *Science* **362**, 589 (2018).
3. J. N. Witchley *et al.*, *Cell Host Microbe* **25**, 432 (2019).
4. T. Y. Shao *et al.*, *Cell Host Microbe* **25**, 404 (2019).
5. P. Bacher *et al.*, *Cell* **176**, 1340 (2019).
6. B. Zhai *et al.*, *Nat. Med.* **26**, 59 (2020).
7. M. Swamydas *et al.*, *Sci. Transl. Med.* **8**, 322ra10 (2016).
8. M. Jaeger *et al.*, *Sci. Transl. Med.* **11**, eaar3558 (2019).
9. I. D. Iliev *et al.*, *Science* **336**, 1314 (2012).
10. J. J. Limon *et al.*, *Cell Host Microbe* **25**, 377 (2019).
11. I. Leonardi *et al.*, *Science* **359**, 232 (2018).
12. B. Aykut *et al.*, *Nature* **574**, 264 (2019).
13. B. R. Jackson *et al.*, *J. Fungi* **5**, 58 (2019).
14. S. P. Rosshart *et al.*, *Science* **365**, eaaw4361 (2019).
15. A. Forche *et al.*, *mBio* **2**, e00129 (2011).

ACKNOWLEDGMENTS

The authors are supported by the National Institute of Arthritis and Musculoskeletal and Skin Diseases (H.H.K.) and the National Human Genome Research Institute (J.A.S.).

10.1126/science.aaz8086

PHOTO: THE NATURAL HISTORY MUSEUM, LONDON/SCIENCE SOURCE

Next-generation epigenetic inhibitors

Selective bromodomain inhibitors provide new opportunities to modulate transcription

By **Panagis Filippakopoulos**[1] *and* **Stefan Knapp**[2]

Ten years ago, the discovery of potent inhibitors targeting the bromodomains of the BET (bromo- and extraterminal) family caused considerable excitement (*1*, *2*). The surprising efficacy of these pan-BET inhibitors in mouse models of various diseases, including cancer, led to rapid translation into the clinic. However, pleiotropic effects of pan-BET inhibitors have limited clinical applications to oncology. Moreover, their equipotent activity toward all BET bromodomains complicated mechanistic studies aiming to delineate the functions of the first (BD1) and second (BD2) bromodomains present in each of the four human BET proteins. On page 387 of this issue, Gilan *et al*. (*3*) developed BD1- and BD2-selective inhibitors with unprecedented selectivity. These will enable future research on the role of BD1 and BD2 in transcriptional control and the development of more specific BET-targeting therapies.

Histones contain a large number of posttranslational modifications that constitute the epigenetic code, a complex language that is interpreted by a large diversity of protein interaction domains that "read" these modifications. Acetylation of lysines is a frequent modification in histones that is recognized (read) by BET proteins. These comprise a family of bromodomains consisting of four members [bromodomain-containing 2 (BRD2), BRD3, BRD4, and bromodomain testis–specific protein (BRDT)]. Each BET protein harbors two highly homologous bromodomains (BD1 and BD2). The roles of BET proteins in transcription were initially thought to be limited to the recruitment of P-TEFb (positive transcription elongation factor-b), a factor required for transcriptional elongation, by BRD4 and BRDT. However, pan-BET inhibitors (*1*, *2*) revealed specific effects on gene expression that often affected lineage-specific genes. This unexpected finding was rationalized by the presence of BET proteins bound to acetylated chromatin at cell type–specific enhancers and superenhancers, which are transcriptional regulatory regions that increase gene expression (*4*). The specific down-regulation of expression of cell type–specific regulatory genes by pan-BET inhibitors led to numerous potential applications in seemingly unrelated diseases. In oncology, the strong down-regulation of expression of the *MYC* proto-oncogene provided a key biomarker for pan-BET inhibitors and made a compelling case for targeting BET proteins in MYC-driven cancers (*5*).

The excitement of this discovery resulted in countless preclinical studies and the initiation of 39 clinical trials. However, the general role of BET proteins in regulating tissue-specific gene expression resulted in pleiotropic effects in vivo and toxicity in some clinical studies, albeit with encouraging but often short-lived efficacy (*6*). Moreover, the rapid translation of these targets into the clinic, and their poorly understood mechanism of action, raised concerns that "clinical trials run ahead of science" (*7*), making a case for more basic research. An important tool for such studies would be inhibitors with improved selectivity for one of the four BET family members or for BD1 or BD2.

Owing to sequence conservation within the acetyl-lysine binding site of BD1 and BD2, the development of protein- or domain-specific inhibitors represents a considerable challenge (*8*). Early indications that domain selectivity might be achievable came from relatively weak BET inhibitors such as RVX-208 that exhibits ~8- to 20-fold selectivity for BD2 over BD1 (*9*). This inhibitor interacted with a histidine located at the rim of the acetyl-lysine–binding site, which is conserved in all BD2s, but not in BD1s (which harbor an aspartate at this position). This residue variation has been exploited in the development of the BD2-selective inhibitor ABBV-744 (*10*).

In contrast to pan-BET inhibitors, ABBV-744 showed a narrow antiproliferative activity restricted to hormone-dependent breast and prostate cancers and some types of leukemia. Similar to the effect of RVX-208, BD2 inhibition by ABBV-744 yielded limited transcriptional changes. In prostate cancer, ABBV-744 displaced BRD4 from androgen receptor–containing superenhancers, whereas P-TEFb recruitment to promoters was not affected, demonstrating a more restricted mode of action. ABBV-744 has now entered clinical testing in patients with relapsed and refractory acute myeloid leukemia (NCT03360006).

The study by Gilan *et al*. expands the chemical toolbox for examining BD1 and BD2 selectivity. The authors report the development of GSK046 (iBET-BD2), a potent BD2-selective inhibitor with >1000-fold selectivity over BD1. They also report the development of GSK620, an orally bioavailable BD2-selective inhibitor, and GSK778 (iBET-BD1), a BD1-selective inhibitor (see the figure). The authors found that in mouse models of various cancers, BD1 inhibition is reminiscent of pan-BET inhibition. This was explained by displacement of BET proteins from promoter and enhancer regions that control *MYC* expression, suggesting that BD1 anchors BET proteins to acety-

Diverse roles of bromodomains in transcription

BET (bromo- and extraterminal) proteins contain two bromodomains, BD1 and BD2, that bind acetylated (Ac) lysine on histone H4. Selective inhibitors of BD1 (iBET-BD1) and BD2 (iBET-BD2) delineate the role of BET proteins in modulating gene expression and identify bromodomain-specific areas for drug development.

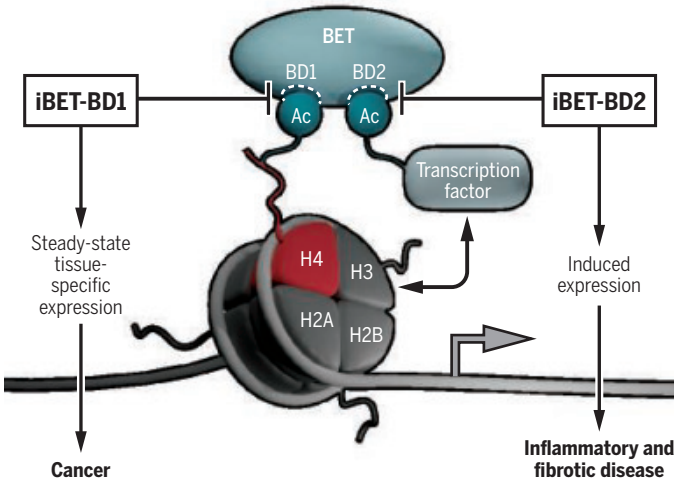

GRAPHIC: A. KITTERMAN/*SCIENCE*

[1]University of Oxford, Old Road Campus, Oxford, OX3 7DQ, UK. [2]Goethe-University Frankfurt, Institute of Pharmaceutical Chemistry, Frankfurt, Germany. Email: knapp@pharmchem.uni-frankfurt.de

lated lysine residues in histones through its affinity to diacetylated histone H4 (*11*).

By contrast, BD2 inhibition did not yield strong antiproliferative effects in cancer cell lines that are sensitive to BD1 inhibitors and did not displace BET proteins from chromatin. Thus, BD2 mediates interactions with nonhistone proteins, such as transcription factors. In support of this idea, BD2 inhibition altered gene expression signatures triggered by extracellular stimuli such as interferon-γ and phorbol-myristate, which activate specific transcription factors. The requirement of BD2 for induced gene expression was also evident in stimulated primary $CD4^+$ T cells, in which strong suppression of proinflammatory cytokine expression suggested applications of BD2-specific inhibitors in inflammatory disease. Indeed, selective BD2 inhibition showed efficacy in mouse models of arthritis and psoriasis, which are characterized by pathogenic inflammation. In addition, encouraging activity was also observed in mouse models of nonalcoholic fatty liver disease, in which GSK620 reduced deposition of fat in the liver (steatosis) and scarring of liver tissue (fibrosis).

Taken together, the development of BD1- and BD2-selective inhibitors will help to delineate the functions of these conserved proteins. The role of BD2 in induced transcription programs predestines BD2-selective inhibitors for treatment of inflammatory disease and fibrosis, potentially bypassing the rewiring of BET-protein interactions observed with pan-BET inhibitors (*12*). The effect of BD2 inhibition on hematopoiesis, a differentiation program that is also regulated by a myriad of transcription factors, remains to be investigated. In clinical studies, side effects of pan-BET inhibitors have been associated with defects in blood cell differentiation such as low platelet counts causing abnormal blood clotting. However, this new generation of domain-selective inhibitors will provide exciting research tools for studying transcriptional regulation by epigenetic readers. ■

REFERENCES AND NOTES

1. P. Filippakopoulos *et al.*, *Nature* **468**, 1067 (2010).
2. E. Nicodeme *et al.*, *Nature* **468**, 1119 (2010).
3. O. Gilan *et al.*, *Science* **368**, 387 (2020).
4. J. Lovén *et al.*, *Cell* **153**, 320 (2013).
5. J. Zuber *et al.*, *Nature* **478**, 524 (2011).
6. S. Postel-Vinay *et al.*, *Eur. J. Cancer* **109**, 103 (2019).
7. G. Andrieu A. C. Belkina, G. V. Denis, *Drug Discov. Today Technol.* **19**, 45 (2016).
8. Z. Liu *et al.*, *Eur. J. Med. Chem.* **151**, 450 (2018).
9. S. Picaud *et al.*, *Proc. Natl. Acad. Sci. U.S.A.* **110**, 19754 (2013).
10. E. J. Faivre *et al.*, *Nature* **578**, 306 (2020).
11. P. Filippakopoulos *et al.*, *Cell* **149**, 214 (2012).
12. J. P. Lambert *et al.*, *Mol. Cell* **73**, 621 (2019).

ACKNOWLEDGMENTS

The authors are supported by the Structure Genomics Consortium. S.K. acknowledges support by the German Cancer network DKTK and the Frankfurt Cancer Centre (FCI).

10.1126/science.abb5060

ECOLOGY

Nuanced changes in insect abundance

Trends in insect abundance vary across time, ecosystems, and continents

By **Maria Dornelas**[1] *and* **Gergana N. Daskalova**[2]

Drastic declines in insect biomass, abundance, and diversity reported in the literature have raised concerns among scientists and the public (*1*–*3*). If extrapolated across Earth, biomass losses of ~25% per decade (*1*) project a potential catastrophe developing unnoticed under our noses. The phrase "insect Armageddon" has captured the collective attention and shined a spotlight on one of the most numerous and diverse groups of organisms on the planet. Yet, insects are critically understudied. For example, the BioTIME database (*4*)—a compilation of biodiversity time series—contains records for 22% of known bird species but only 3% of arthropods (the phylum that includes insects and spiders). On page 417 of this issue, van Klink *et al.* conduct a thorough global assessment of insect abundance and biomass trends and paint a more nuanced picture than that predicted by extrapolations (*5*).

Given the critical environmental functions of insects, the consequences of their declines could propagate across ecosystems and affect the services they provide (for example, pollination of crops such as almonds, apples, and cherries). The prospect of widespread insect decline has prompted calls for rigorous scientific study and monitoring (*6*–*8*). The drivers of biodiversity changes are almost never simple, and their discovery requires context. Thus, simple extrapolation from a handful of locations is unlikely to reveal the layers of complexity that underpin real-world biodiversity change (*6*, *9*). To unpick insect-decline events, scientists must decipher whether site- and region-specific declines are representative of the state of insects around the world. This requires a systematic assessment of insect-abundance trends.

In what is the largest and most complete meta-analysis to date, van Klink *et al.* revealed substantial variation—surges and declines—in abundance and biomass trends. Similar to what is found across other taxa (*10*), the meta-analysis in the new study detected no net directional trend among 166 studies of 1676 geographical sites in 41 countries. Yet, van Klink *et al.* found that terrestrial insects declined in abundance by 9% per decade on average, whereas freshwater insects increased by 15%. The authors also noted variation across continents, with North America and some European regions emerging as hotspots of decline in insect abundance.

The findings of heterogeneity in insect abundance and biomass trends over time reinforce the need to consider spatial variation in biodiversity change (*11*). Other

[1]Centre for Biological Diversity, School of Biology, University of St Andrews, St Andrews KY16 9TH, Scotland, UK. [2]School of GeoSciences, University of Edinburgh, West Mains Road, Edinburgh EH9 3FF, Scotland, UK. Email: maadd@st-andrews.ac.uk; gndaskalova@gmail.com

PHOTOS: DAVID LIITTSCHWAGER

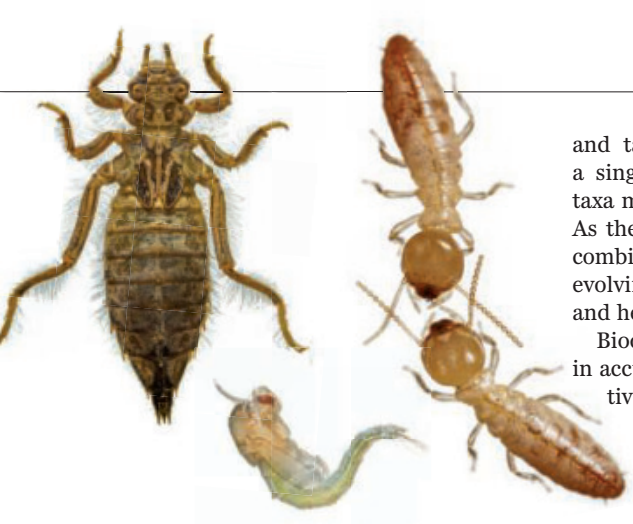

Insects are incredibly diverse, as are the trends of their abundance and biomass over time.

PHOTOS: DAVID LIITTSCHWAGER

studies with long-term monitoring have revealed additional layers of variation in patterns of invertebrate change. For example, occupancy (a metric of spatial abundance) of terrestrial insects in the United Kingdom has increased, whereas that of noninsect invertebrates has declined (*12*). Some trends vary across time, such as periods of increase in abundance of U.K. moths followed by periods of decline (*13*). The patterns that emerge across all insect-abundance studies to date are those of variation in trends across space, taxa, and time.

The drivers of change in insect biodiversity around the world remain to be fully ascertained. Because of their short life spans and quick population dynamics, insect abundances are naturally highly variable, which presents a challenge for quantifying long-term trends (*8*). Species exposure to global change, as well as their sensitivity and resilience, likely all interact to drive ongoing biodiversity changes.

Across the sites represented in the new study, declining trends seemed to be associated with land-use intensification, with no signals of climatic influences. Increasing trends, namely in the freshwater realm, coincided with the establishment of stricter water policies, demonstrating that appropriate legislation can bring positive biodiversity outcomes. Yet, the world is a complex mosaic of threats (*14*). As scientists tackle the challenge of disentangling drivers of various insect-biodiversity trends (*8*), they will be better poised to predict the consequences for ecosystem function and services, such as pollination, decomposition of organic matter, and pest control (*15*).

The variation in insect trends has several broader implications. Variation adds to the doubts that biodiversity change can be represented by a single trend. Thus, it is wise for scientists to heed this lesson as they debate biodiversity targets. To understand the complexities of biodiversity change, ecologists require data on realm-, region- and taxa-specific trends. Inferences from a single global scenario or one indicator taxa must be treated with extreme caution. As these smaller studies accumulate, their combined results should contribute to the evolving patchwork of biodiversity changes and help to elucidate the various drivers.

Biodiversity monitoring should increase in accuracy as it becomes more representative of the biosphere itself. Therefore, in addition to advancing our knowledge of insect biology and behavior, scientists must approximate stratified random sampling of biodiversity across space and taxa, as insects are not the only understudied group of organisms. Researchers should also widen their focus on drivers of individual global changes to incorporate the complex interactions among different types of environmental shifts (*14*), natural species' variability over time, and species' sensitivity and resilience in the Anthropocene (*8*). Advances in our knowledge about ongoing biodiversity changes and ability to predict future ones will require the incorporation of layers of nuance in patterns of change and drivers of that change.

The temptation to draw overly simple and sensational conclusions is understandable, because it captures the attention of the public and can potentially catalyze much needed action in policy development and research arenas. However, fear-based messages often backfire. This strategy has the grave risk of undermining trust in science and can lead to denialism, fatigue, and apathy. Embracing nuance allows us to balance accurate reporting of worrying losses with hopeful examples of wins. Hope is a more powerful engine of change than fear. ■

REFERENCES AND NOTES

1. C. A. Hallmann *et al.*, *PLOS ONE* **12**, e0185809 (2017).
2. B. C. Lister, A. Garcia, *Proc. Natl. Acad. Sci. U.S.A.* **115**, E10397 (2018).
3. S. Seibold *et al.*, *Nature* **574**, 671 (2019).
4. M. Dornelas *et al.*, *Glob. Ecol. Biogeogr.* **27**, 76 (2018).
5. R. van Klink *et al.*, *Science* **368**, 417 (2020).
6. C. D. Thomas *et al.*, *Glob. Change Biol.* **25**, 1891 (2019).
7. M. E. Saunders, *Nat. Ecol. Evol.* **3**, 1616 (2019).
8. R. K. Didham *et al.*, *Insect Conserv. Divers.* **13**, 103 (2020).
9. G. A. Montgomery *et al.*, *Biol. Conserv.* **241**, 108327 (2020).
10. M. Dornelas *et al.*, *Science* **344**, 296 (2014).
11. S. A. Blowes *et al.*, *Science* **366**, 339 (2019).
12. C. L. Outhwaite, R. D. Gregory, R. E. Chandler, B. Collen, N. J. B. Isaac, *Nat. Ecol. Evol.* **4**, 384 (2020).
13. C. J. Macgregor, J. H. Williams, J. R. Bell, C. D. Thomas, *Nat. Ecol. Evol.* **3**, 1645 (2019).
14. D. E. Bowler *et al.*, *People and Nature* **00**, 1 (2020).
15. O. Dangles, J. Casas, *Ecosyst. Serv.* **35**, 109 (2019).

ACKNOWLEDGMENTS

M.D. thanks M. Barbosa for support. Funding for M.D. is from the University of St Andrews and the Leverhulme Centre for Anthropocene Biodiversity. G.D. is funded by a Natural Environment Research Council doctoral training partnership grant (NE/L002558/1) at the University of Edinburgh and the Carnegie Trust for the Universities of Scotland.

10.1126/science.abb6861

SIGNALING

Calcium as a biased cofactor

Crystal structure of an anti-obesity drug target reveals an important calcium-binding site

By **Madhu Chaturvedi** *and* **Arun K. Shukla**

The α-melanocyte–stimulating hormone (α-MSH) is a neuropeptide that is secreted by the cells in the intermediate lobe of the pituitary gland in the brain. In humans, α-MSH plays a pivotal role in the regulation of feeding behavior, energy homeostasis, and sexual activity, in addition to its primary function of regulating melanogenesis, the process of hair and skin pigmentation (*1*). α-MSH activates four of the five melanocortin receptors [melanocortin-1 receptor (MC1R), MC3R, MC4R, and MC5R but not MC2R] (*1*). Of these, MC4R is of peculiar interest as a drug target because mutations in this receptor are associated with different forms of obesity in humans (*2*). On page 428 of this issue, Yu *et al.* (*3*) present a crystal structure of human MC4R in complex with a peptide antagonist, SHU9119. This reveals a calcium-binding site on MC4R, and Ca^{2+} is found to be an important modulator of MC4R activation, which could potentially facilitate therapeutic development.

High-resolution structural analysis of heterotrimeric GTP-binding protein (G protein)–coupled receptors (GPCRs)—such as MC4R, the largest class of cell-surface receptors in the human body—has seen unprecedented progress in the past decade owing to numerous methodological and technological advances (*4*). As a result, understanding of these receptors has reached a new level with structural insights into their activation, signaling, and regulation, providing previously lacking frameworks for drug discovery (*5*, *6*). MC4R is expressed on neurons in the hypothalamus and brainstem. It is a prototypical, rhodopsin-like class A GPCR and primarily couples to the Gαs subfamily of heterotrimeric G proteins upon agonist activation (*7*). Gain-of-function mutations in MC4R appear to impart a protective ef-

Department of Biological Sciences and Bioengineering, Indian Institute of Technology, Kanpur 208016, India. Email: arshukla@iitk.ac.in

fect from obesity (*8*), whereas mutations that result in reduced Gαs coupling are associated with early onset syndromic obesity (*9*). The agouti-related protein (AgRP), a potent appetite-stimulating neuropeptide produced by AgRP neurons in the hypothalamus, acts as an antagonist of MC4R (*10*). Although α-MSH binding to MC4R leads to a reduction in appetite, the binding of AgRP exerts the opposite effect, and therefore, a balanced action of these two hormones is crucial to regulate food intake and energy homeostasis (*11*) (see the figure). Setmelanotide, a cyclic peptide agonist of MC4R, has been reported to exert therapeutic effects in monogenic and syndromic obesity patients, although other small-molecule MC4R agonists have not been so promising in clinical trials (*2*). Therefore, a better understanding of ligand-MC4R interaction is important to facilitate future drug discovery efforts.

The crystal structure determined by Yu *et al.* uncovers the molecular details of SHU9119 binding, which makes extensive interactions with multiple residues from the amino terminus, the extracellular loop 2, and transmembrane helices of the receptor. The structure also reveals the binding of a Ca^{2+} ion to MC4R, coordinated by the amino acid residues from both the receptor and SHU9119. Comparison of the MC4R crystal structure with that of other class A GPCRs suggests a similarity with the lipid-activated receptors compared with the peptide-binding receptors, an observation that needs additional studies to establish physiological importance. Ca^{2+} also increases the binding affinity of α-MSH by more than 30-fold but has no effect on SUH9119 and AgRP binding. This effect of Ca^{2+} on α-MSH binding translates into potentiation of cyclic adenosine monophosphate (cAMP) response, which is a typical readout of Gαs coupling, and the closure of inward rectifier potassium channel (KIR7.1) upon α-MSH stimulation in cellular assays using a human cell line (*3*). This suggests that the effect of Ca^{2+} on α-MSH binding to MC4R enhances transducer coupling and downstream signaling.

Previous studies have identified Na^+-binding sites in multiple class A GPCRs, which has emerged as an important paradigm of allosteric modulation of these receptors, harboring inherent potential to influence the efficacy and selectivity of GPCR-targeting drugs (*12*, *13*). Moreover, a Zn^{2+}-binding site has been visualized in the crystal structure of the human platelet-activating factor receptor (PAF1R), also a class A GPCR (*14*). However, the Ca^{2+}-binding site in MC4R is distinct from the Na^+- and Zn^{2+}-binding sites and therefore hints at a much broader role and distinct modes of action of ionic cofactors in GPCR activation, signaling, and regulation than anticipated. It is also intriguing that Ca^{2+} selectively modulates α-MSH binding to MC4R but not the binding of AgRP. Thus, it is possible that the ionic cofactors may have an untapped potential in the context of GPCR-biased agonism, the ability of certain ligands to preferentially engage different downstream signaling pathways and a framework that holds tremendous potential for drug discovery (*6*, *15*).

Furthermore, the MC4R structure allows the mapping of the gain-of-function and loss-of-function mutations in the receptor that are linked to syndromic obesity on a structural template, which may lead to testable hypotheses in order to better understand the links between receptor activation and disease manifestation (*8*, *9*). For example, it allows visualization of how these mutations may potentially affect the intra- and interhelical interactions in the receptor, modulating receptor activation, transducer coupling, and downstream signaling response. This study also raises several interesting questions for future studies. For example, how generic is the role of Ca^{2+} on the ligand binding and activation of different subtypes of the melanocortin receptors, and by extension, to other GPCRs? Taken together with previous observations of Na^+- and Zn^{2+}-binding sites on other GPCRs, it is possible that different ions provide an additional level of regulation for different receptors depending on the tissue context and physiological settings. Answering these questions will require comprehensive structural, pharmacological, and in vivo analysis on multiple receptor systems. ■

Calcium binding influences hunger signaling

Melanocortin-4 receptor (MC4R) is expressed primarily in the hypothalamus and brainstem. It binds to two different neuropeptides, α-melanocyte–stimulating hormone [α-MSH, from proopiomelanocortin (POMC) neurons] and agouti-related protein (AgRP), which exert opposing effects on downstream responses. A crystal structure of MC4R in complex with the cyclic peptide antagonist, SHU9119, revealed a Ca^{2+}-binding site that influences downstream signaling.

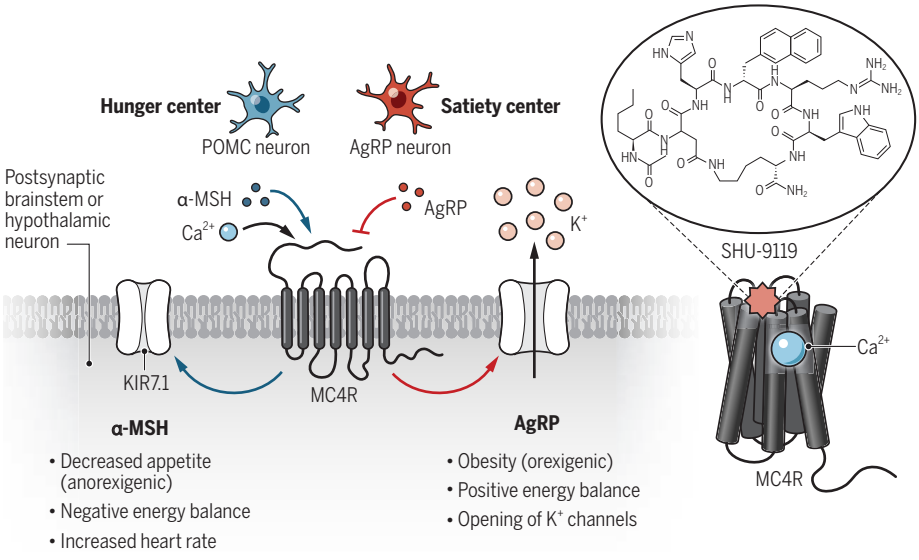

REFERENCES AND NOTES

1. E. J. Anderson *et al.*, *J. Mol. Endocrinol.* **56**, T157 (2016).
2. P. Kühnen, H. Krude, H. Biebermann, *Trends Mol. Med.* **25**, 136 (2019).
3. J. Yu *et al.*, *Science* **368**, 428 (2020).
4. E. Ghosh, P. Kumari, D. Jaiman, A. K. Shukla, *Nat. Rev. Mol. Cell Biol.* **16**, 69 (2015).
5. H. C. S. Chan, Y. Li, T. Dahoun, H. Vogel, S. Yuan, *Trends Biochem. Sci.* **44**, 312 (2019).
6. D. Wootten, A. Christopoulos, M. Marti-Solano, M. M. Babu, P. M. Sexton, *Nat. Rev. Mol. Cell Biol.* **19**, 638 (2018).
7. Y. X. Tao, *Endocr. Rev.* **31**, 506 (2010).
8. L. A. Lotta *et al.*, *Cell* **177**, 597 (2019).
9. C. Lubrano-Berthelier *et al.*, *J. Clin. Endocrinol. Metab.* **91**, 1811 (2006).
10. M. M. Ollmann *et al.*, *Science* **278**, 135 (1997).
11. L. E. Pritchard, A. White, *Peptides* **26**, 1759 (2005).
12. V. Katritch *et al.*, *Trends Biochem. Sci.* **39**, 233 (2014).
13. B. Zarzycka, S. A. Zaidi, B. L. Roth, V. Katritch, *Pharmacol. Rev.* **71**, 571 (2019).
14. C. Cao *et al.*, *Nat. Struct. Mol. Biol.* **25**, 488 (2018).
15. P. Kumari, E. Ghosh, A. K. Shukla, *Trends Mol. Med.* **21**, 687 (2015).

ACKNOWLEDGMENTS

The authors are supported by the Wellcome Trust/Department of Biotechnology (DBT) India Alliance (IA/I/14/1/501285); Department of Science and Technology, India Ministry of Science and Technology (DST/SJF/LSA-03/2017-18); Science and Engineering Research Board (SERB) (EMR/2017/003804); DBT (BT/PR29041/BRB/10/1697/2018), Council of Scientific and Industrial Research [37(1730)/19/EMR-II]; and Indian Institute of Technology Kanpur.

10.1126/science.abb4393

GRAPHIC: KELLIE HOLOSKI/*SCIENCE*

RETROSPECTIVE

Mary Lowe Good (1931–2019)

Renowned chemist, respected leader, and inspiring mentor

By **Margaret A. Cavanaugh**

Mary Lowe Good, one of the most renowned female scientists of her generation, died on 20 November 2019. She was 88. Mary won acclaim for her accomplishments in academe, industry, and government. As a physical inorganic chemist, she adapted Mössbauer spectroscopy to characterize ruthenium catalysts. She went on to lead an industrial materials research organization and later the Clean Car initiative as undersecretary for technology at the U.S. Department of Commerce.

Mary was proud of her roots. She was born in Grapevine, Texas, on 20 June 1931 and moved with her family to Arkansas in 1943. Her schoolteacher parents valued education, and she described her mother as the smartest person she ever knew. The oldest of four, Mary enjoyed accompanying her father on fishing and hunting outings. She began college at Arkansas State Teachers College (now the University of Central Arkansas) as a home economics major, but her freshman chemistry teacher encouraged her interest in science. She earned her bachelor's degree in chemistry in 1950, just before her 19th birthday, and 5 years later earned a doctorate in radiochemistry at the University of Arkansas.

In 1952, Mary married physicist Bill Good, who was her physical chemistry lab partner at Arkansas State. Their first son, John, was born as she was finishing her master's degree in 1953, and their second, James, was born in 1958. Students sometimes asked Mary for advice about when to have children without hindering their careers. She responded that during graduate school had worked well for her.

Mary began her first academic position as an instructor at Louisiana State University (LSU) in 1954, before completing her doctorate. After graduating and being awarded a grant from Research Corporation for Science Advancement, she was promoted to assistant professor. In 1958, Mary and her family moved to the new LSU campus in New Orleans, where she and Bill would spend the next 20 years building the university. By 1974, she was named a distinguished Boyd Professor of Chemistry, having developed a curriculum, equipped a research laboratory, and planned a science building. By 1980, she had received numerous grants and authored more than 100 research papers in solvent separations and characterization of metallic species, solid-state chemistry and electron exchange, and testing methods for tin antifouling coatings.

A new phase of Mary's career began in 1980 when she became vice president and director of research for Universal Oil Products, a Signal Companies subsidiary. She added materials science and biotechnology to the catalytic processes for which the company was known. After a series of mergers, she became senior vice president for technology for Allied-Signal, with laboratories in three states.

PHOTO: UA LITTLE ROCK

Mary is perhaps best known for her public service. Always active in the American Chemical Society (ACS), she became a board member in 1972, board chair in 1978, and president of the society in 1987. She was appointed to the National Science Board in 1980 and later became its chair. George H. W. Bush appointed her to the prestigious President's Council of Advisors on Science and Technology. Mary was elected president of the American Association for the Advancement of Science (AAAS, the publisher of *Science*) in 2001.

In 1993, Mary left Allied-Signal to become undersecretary for technology at the U.S. Department of Commerce during the Clinton administration. Briefly, she served as acting secretary of commerce after the tragic death of Secretary Ronald H. Brown in 1996. In 1997, Mary became the Donaghey University Professor at the University of Arkansas at Little Rock. A year later, she agreed to a 2-year term as the founding dean of the Donaghey College of Engineering and Information Technology at University of Arkansas at Little Rock. She retired from that position 13 years later, as dean emeritus and special adviser to the chancellor in the field of economic development. She occupied an office at the university until 2017. As usual, she had developed recognized programs in systems engineering and modeling and simulation.

Mary was the first woman to attain a particular position or honor countless times, starting with being the first woman from Arkansas to earn a Ph.D. in a physical science. She received dozens of important awards, including the National Science Foundation's highest honor, the Vannevar Bush Award; the ACS Priestley Medal; AAAS's prestigious Philip Hauge Abelson Prize; and the Heinz Award in Technology, the Economy and Employment, as well as 21 honorary degrees. She was also a member of the National Academy of Engineering.

In the eyes of the many female chemists for whom Mary served as a role model, the most cherished recognition she received may have been ACS's Francis P. Garvan–John M. Olin Medal. This national prize was a breakthrough for Mary and has been a stepping-stone to recognition for many other female chemists. Mary received the award in 1973, the same year that I joined her group as a postdoctoral researcher. Little did I know how life-changing the experience would be; she offered not only an environment in which to cultivate scientific skills but also a leadership opportunity and an introduction to public service. She took me to my first national ACS meeting, making sure I presented a paper and going out of her way to introduce me to well-known chemists and board members, thus paving the way for my own ACS governance service.

Mary was direct and down-to-earth, an irresistible dynamo who shared her success with her students and colleagues. Her thoughts on the direction of industry, research, and governance were sought out not just by colleagues but by journalists and policy-makers. She was always involved, highly energetic, and forward looking. Her curiosity and social involvement never abated as she worked on her many projects with organization, strategic intelligence, and good humor. When she wasn't reading science, she was reading English literature. She sought out ways to encourage young people, especially young women, to advance their science education. Her own heroine, Marie Curie, would have been astonished and proud. ■

Former Deputy Assistant Director for Biological Sciences, National Science Foundation, Alexandria, VA, USA.
Email: mcavana@outlook.com

10.1126/science.abb9780

POLICY FORUM

Fish kills and shellfish mortality events may become more common in coastal ecosystems without reconsideration of water quality criteria.

PHOTO: FELIX MARQUEZ/AP PHOTO

ENVIRONMENTAL REGULATION

Dissolved oxygen and pH criteria leave fisheries at risk

Regulations have not kept pace with scientific understanding of coastal hypoxia and acidification

By **Stephen J. Tomasetti** *and* **Christopher J. Gobler**

Changes in human population centers and agricultural fertilizer use have accelerated delivery rates of nitrogen and phosphorus to coastal waters, often stimulating rapid accumulations of primary production (*1*). Whereas resulting eutrophication processes are of less environmental relevance in well-mixed, ocean ecosystems, when they occur in warm, stratified, and/or poorly mixed waters, they can result in hypoxia [depletion of dissolved oxygen (DO)] and acidification (decrease in pH), both of which individually can have adverse effects on aquatic life, affecting a suite of physiological processes and increasing mortality rates (*2*, *3*). Only recently, however, have studies of aquatic hypoxia begun to consider coeffects of low pH (*4*). Many ecologically and/or economically important shellfish and finfish that experience decreased survival and/or growth when exposed to hypoxia are further impaired by concurrent acidification (*4*). Yet although scientific understanding of DO and pH variability and documentation of coastal hypoxic and acidification events have improved, regulatory reform has not kept pace. We suggest that more stringent DO and pH numeric criteria be considered to account for the negative effects of low pH on marine life and the combined impairment from low DO and low pH.

Global ocean DO levels have been decreasing because of both climate change and increased nutrient export from land to sea (*5*). Most commonly, coastal hypoxia is eutrophication-induced, whereas the persistence and severity of hypoxic events are often modulated by climatic factors. Rising sea surface temperatures, for example, lower oxygen solubility and contribute to water-column stratification, restricting the vertical mixing of atmospheric oxygen into deeper waters (*5*). Still, rates of DO decline in the nearshore environment outpace those of the open ocean (*5*), underscoring the direct influence of anthropogenic nutrient loading on coastal water bodies and the need for careful regulatory policies and effective management.

Similarly, pH levels are affected by a combination of local and global processes acting on differing spatial and temporal scales. Globally, ocean assimilation of rising atmospheric CO_2 has resulted in a 0.1 unit decrease in ocean pH since preindustrial times, with decreases of an additional 0.2 to 0.3 units predicted for the end of the century (*6*). Acting over shorter temporal and smaller spatial scales, increased freshwater input, upwelling, and eutrophication can elicit additional local depression of pH in coastal waters to levels that can exceed the changes anticipated for the open ocean at the end of the century (*7*).

Within many eutrophic coastal systems, the production of respired CO_2 constitutes a major source of acidity and, therefore, intensifies acidification (*8*, *9*). Eutrophication-induced increases in CO_2 can interact synergistically with ocean acidification to lower pH levels below those predicted by the sum of eutrophication and ocean acidification alone, owing to the reduced buffering capacity of hypoxic, metabolically acidified waters (*8*). Thus, hypoxic waters are necessarily acidified, and many organisms exposed to hypoxic stress must also cope with acidification (*4*).

DO AND pH CRITERIA

The global proliferation of coastal hypoxia and acidification underscores a universal need to adopt and implement DO and pH regulations reflective of evolving environmental conditions. In recent decades, the acceleration of climate change, advancements in in situ monitoring technology, and emerging experimental data have collectively established a new global paradigm in which policies developed in the 20th century are, in some cases, misaligned with conditions needed to protect marine life. In the United States, the Clean Water Act (CWA) establishes the basic structure for ameliorating and preventing surface water impairment. Because many countries have developed seawater quality standards partly modeled on U.S. standards, similar policy challenges can be found internationally—for example, in China (*10*) and Brazil (*11*).

Among its many provisions to restore and protect national waters, the CWA authorizes U.S. states, territories (henceforth referred to as states), and approved tribes to establish water-quality standards for waters of the United States, including territorial seas (*12*). Federally approved water-quality standards consist of at least three elements: (i) designated uses (protection and propagation of fish, shellfish, and wildlife; recreation), (ii) water-quality criteria to protect designated uses, and (iii) antidegradation requirements that safeguard unimpaired waters. When

School of Marine and Atmospheric Sciences, Stony Brook University, Southampton, NY, USA.
Email: christopher.gobler@stonybrook.edu

water-quality standards are not satisfied by existing restraints on pollution, such waters can be reported to the U.S. Environmental Protection Agency (EPA) through the 303(d) impaired waters list (*12*). Inclusion on the 303(d) list prompts further action, by which the total maximum daily loads of pollutants (often nutrients in the case of hypoxic areas) required to ameliorate conditions can be determined, and mitigation measures may be implemented (*12*).

The EPA provides recommended criteria for DO and pH in coastal waters to guide the development of state standards (*13*, *14*). Although the EPA-recommended DO criteria are based on a decade of data collection (*13*), this occurred before the establishment of the field of ocean acidification. As such, the majority of studies on which policy has been established had used nitrogen gas to establish low-DO conditions (*13*), an approach that can inflate pH values—creating unrealistic, basified conditions—and that ignores any additional acidification stress that coastal organisms may endure under hypoxia (*4*). In addition, state derivations of the recommended pH criterion can permit pH levels now known to cause harm or death to coastal organisms (*3, 15*) and can be expressed as a deviation from a naturally occurring pH range, for which there is often insufficient historical baseline data to clearly define (*15*).

DO minima allowable under state standards vary considerably, ranging as high as 6.5 mg liter^{-1} and as low as 2 mg liter^{-1}, despite the EPA guidance criteria of 2.3 mg liter^{-1} and 4.8 mg liter^{-1} for adult-juvenile survival and adult-juvenile-larval growth, respectively (*13*), evidencing state efforts to modify recommended criteria to protect the diverse marine taxa within regional ecosystems. In some states, saltwater DO criteria may be high enough (for example, Oregon, 6.5 mg liter^{-1}) to partially or entirely account for additional acidification stress. However, states with acute or chronic minima $\leq$3 mg liter^{-1} (for example, New York and Texas) may require a reevaluation that considers DO thresholds of local marine life under concurrent hypoxia and acidification stress, given that the negative effects of low DO and low pH can be more severe when experienced concomitantly (*4*). Moreover, future DO levels of 2.3 mg liter^{-1} could potentially have more severe negative effects on coastal animals relative to today owing to intensification of ocean acidification, particularly given the nonlinear depression of pH in hypoxic systems (*8*).

Despite the increased attention and research dedicated to ocean acidification over the past two decades, the EPA-recommended numeric saltwater criterion for pH has remained unchanged for more than 40 years (*14*). Revision of water-quality criteria follows solicitation of data, comment from the public, and evaluation of available information by the EPA. From 2009 to 2010, responding to concern over the effects of ocean acidification on coastal waters, the EPA considered revision of the recommended marine pH criterion and concluded that the data available regarding ocean acidification were insufficient to warrant changes to the currently recommended pH criterion (*9*). Acknowledging the importance of pH conditions to aquatic life, the EPA encouraged states to monitor and assess their local water bodies for acidification-related pH impairment (*9*, *15*).

Most coastal states (15 of 28) specify a pH minimum for coastal and/or estuarine waters identical to the limit recommended by the EPA: 6.5 pH units (*14*). In some states, the pH criterion consists solely of a permissible range of pH values (for example, Georgia, 6.0 to 8.5, and Maryland, 6.5 to 8.5). Many important coastal organisms experience deleterious physiological consequences and substantial mortality at pH values above the lower bounds of these ranges (*3*, *15*). In addition to pH minimum values, many states adopt standards with criteria that limit the divergence of pH from "natural" conditions in coastal and/or estuarine waters. Impermissible excursions from natural conditions vary by state (ranging from >0.1 to >1.0 pH units) but most commonly are >0.2 pH units, which is consistent with the EPA-recommended criterion, although it should be noted that the EPA recommends this criterion for open ocean waters (*14*). It is challenging to define natural reference conditions for pH because pH is influenced by local (direct acid deposition), regional (nutrient loading and eutrophication), and global (ocean acidification) anthropogenic processes acting and interacting over differing temporal scales, and long-term datasets reporting the temporal variability of pH with the certainty required to detect 0.1- to 0.2-pH unit deviations are scarce (*15*). The absence of explicitly defined natural reference conditions renders standards based on deviations from these conditions ineffectual.

It has been suggested that in some cases, pH is not the most biologically relevant acidification-related parameter to measure and that new criteria to address acidification should be developed for other variables, such as calcium carbonate saturation state, a measure related to the ability of some organisms to calcify (*15*). Although establishing such criteria could benefit aquatic life, such as in certain state waters with designated uses related to shellfisheries, widespread state monitoring of calcium carbonate saturation state requires additional measurements (of either total alkalinity, dissolved inorganic carbon, or CO_2 partial pressure) and is currently unrealistic for many states owing to the complexity and cost of performing accurate and precise analyses. Accordingly, until more feasible analytical methods become available, refinement of states' pH criteria is seemingly the most viable managerial approach to protect aquatic life from acidification-related impairment.

Beyond the water-quality standards effective under the CWA, several nonfederal policy approaches may help alleviate coastal hypoxia and acidification, including reducing coastal erosion, land-use changes (*9*), and/or regulating onsite septic systems. Without consideration of pH and DO together, many fisheries and important coastal resources are left more vulnerable than expected, especially given projections of future, climate change–induced reductions in ocean DO and pH. Therefore, increasing allowable DO minima to accommodate acidification stress, amending designated pH threshold values to biologically nonharmful levels, assessing the coeffects of low DO and low pH on more marine taxa to guide future criteria, and improving pH-monitoring efforts to more clearly define natural pH conditions are all appropriate approaches that would ultimately lead to the improved protection of fisheries and aquatic life. ■

REFERENCES AND NOTES

1. S. W. Nixon, *Ophelia*. **41**, 199 (1995).
2. R. J. Diaz, R. Rosenberg, *Oceanogr. Mar. Biol. Annu. Rev.* **33**, 245 (1995).
3. K. J. Kroeker, R. L. Kordas, R. N. Crim, G. G. Singh, *Ecol. Lett.* **13**, 1419 (2010).
4. C. J. Gobler, H. Baumann, *Biol. Lett.* 10.1098/rsbl.2015.0976 (2016).
5. D. Breitburg *et al.*, *Science* **359**, eaam7240 (2018).
6. IPCC, Climate Change 2014: Synthesis Report. Contribution of Working Groups I, II and III to the Fifth Assessment Report of the Intergovernmental Panel on Climate Change, Core Writing Team, R. K. Pachauri, L. A. Meyer, Eds. (IPCC, 2014); www.ipcc.ch/site/assets/uploads/2018/02/SYR_AR5_FINAL_full.pdf.
7. G. G. Waldbusser, J. E. Salisbury, *Ann. Rev. Mar. Sci.* **6**, 221 (2014).
8. W.-J. Cai *et al.*, *Nat. Geosci.* **4**, 766 (2011).
9. R. P. Kelly *et al.*, *Science* **332**, 1036 (2011).
10. GB3097-1997, Seawater Quality Standard of China (1997); www.chinesestandard.net/PDF/Sample.aspx/GB3097-1997.
11. C. O. N. A. M. A. Framework Resolution, 357/2005 of Brazil (2005); www.braziliannr.com/brazilian-environmental-legislation/conama-resolution-35705.
12. 33 U.S.C §§ 1251-1387, Federal Water Pollution Control Act As Amended Through Pub. L. No. 107-303 (2002); www.epa.gov/sites/production/files/2017-08/documents/federal-water-pollution-control-act-508full.pdf.
13. EPA, *Ambient Water Quality Criteria for Dissolved Oxygen (Saltwater): Cape Cod to Cape Hatteras* (EPA, 2000); www.epa.gov/sites/production/files/2018-10/documents/ambient-al-wqc-dissolved-oxygen-cape-code.pdf.
14. EPA, *Quality Criteria for Water* (EPA, 1976); www.epa.gov/sites/production/files/2018-10/documents/quality-criteria-water-1976.pdf.
15. S. B. Weisberg *et al.*, *Ocean Coast. Manag.* **126**, 31 (2016).

10.1126/science.aba4896

BOOKS *et al.*

Our desire to consume "natural" foods has moral and theological connotations.

PHILOSOPHY OF SCIENCE

The trouble with turning to nature

Our obsession with "natural" products and practices is a proxy for other values

By **Silvia Camporesi**

When I was pregnant, I remember pondering with my husband the pros and cons of a "natural" versus a "medicalized" birth. Should we opt for a hospital that would offer epidural anesthesia or for a clinic that would allow the birth process to unfold without intervention and without pain relief? Should we choose to breastfeed exclusively or to introduce formula early on so that we could share more equally in caring for our newborn? Should we obey nature or transcend it through medicine? In *Natural*, Alan Levinovitz shows that the framing of this final question is fundamentally misguided, because it creates an oppositional binary where one does not exist.

Natural
Alan Levinovitz
Beacon Press, 2020.
264 pp.

Levinovitz covers a wide range of case studies, from childbirth to national parks, from lab-grown meat to organic foods, from financial markets to contraception, and from alternative medicine to the use of prostheses and supplements in sports. He unravels the moral and theological connotations of the word "natural" and questions what is left of the word once it is stripped bare.

Levinovitz shows how "natural" is often used as a proxy for other values. In cases where parents refuse to vaccinate their children, for example, he asserts that these parents are simply looking for an experience of medicine that is more holistic and provides an existential explanation to illness. We should strive to realize this more-expansive vision in conventional medicine, he argues, as it could help reestablish the trust that parents looking for alternative therapies have lost.

In another example, Levinovitz reveals inconsistencies in how the term "natural" is used with regard to a variety of athletic performance advantages. Olympians such as Finnish skier Eero Mäntyranta, who had unusually high hemoglobin levels, and U.S. swimmer Michael Phelps, with his abnormally long arms and torso, had distinct advantages over other athletes, but their ability to compete was never questioned. The naturally high testosterone levels of South African middle-distance runner Caster Semenya, however, have been repeatedly cited as being unfair to competitors.

So what does "natural" mean in the context of professional sports? The book shows that there are legitimate disagreements, even between biomechanical experts, about the extent to which a natural advantage can be considered fair, but the term "natural" is usually used as a proxy for a "healthy and safe" body that does not cross some other supposedly "natural" division (for example, gender).

In another chapter, Levinovitz tackles Adam Smith's "invisible hand" and the justification of economic policies on the basis of appeals to nature. Here, he shows how something that may seem perfectly natural today, such as the practice of charging interest, was considered unnatural, even sinful, for a long time. Those who talk of Bitcoin as the evolution of "natural currency" similarly reflect our inclination to map models from nature onto economic systems—an inherently theological approach.

The idea that "natural" is used with moral or theological connotations is not new. Nearly 40 years ago, Stephen Jay Gould wrote that we cannot find answers in nature to how we should behave in our everyday lives (*1*). It is too easy to cherry-pick examples of natural behaviors in favor of, or against, any practice in which we might choose to engage. Today, Levinovitz shows that unraveling the layers of moral and theological meanings associated with the notion of "natural" is a relevant endeavor, not just for scientists, ethicists, and policy-makers but for all human beings as we try to make sense of our relationship with the world around us.

In the afterword, Levinovitz provides a reflective account of how his own attitude toward "naturalness" changed through the journey of writing the book. Although he was initially skeptical about the use of the word, he came to recognize its importance as he unpacked the different values that people ascribe to it. The take-home message? Rather than dismissing "natural" altogether, we should strive to acknowledge and explore its many facets, depending on the context. In this sense, Levinovitz's book is an important call for more nuance over simplicity, for compromise over dogmatism, and for embracing uncertainty over certainty. ■

The reviewer is at the Department of Global Health and Social Medicine, King's College London, London WC2B 4BG, UK. Email: silvia.camporesi@kcl.ac.uk

REFERENCES AND NOTES

1. S. J. Gould, *Nat. Hist.* **91**, 19 (1982).

10.1126/science.abb5404

PHOTO: ISTOCK.COM/CHARDAY PENN

NEUROSCIENCE

A history of the metaphorical brain

Analogies abound and inform our quest to understand the nervous system

By **Alex Gomez-Marin**

Physicists, biologists, psychologists, philosophers, mathematicians, and computer scientists work (sometimes together) to unravel the mysteries of how the brain, and by extension the mind, operates. This makes neuroscience a peculiar community—a wild confluence of different approaches, backgrounds, and specific interests. *The Idea of the Brain* by Matthew Cobb is a history of this struggle. Spanning approximately five centuries, the book reveals that there are many ways to think about what brains are, what they do, and their relation to the mind. Cobb's erudition and engaging writing style take readers on an enthralling journey, rich with accidental discoveries, controversies, and rejected hypotheses.

For centuries, in many traditions, the heart was considered the seat of thought and feeling. In the 17th century, things slowly started to change. The French philosopher René Descartes suggested that hydraulic automata in the brain could move "animal spirits" through the nerves, producing behavior. The Danish anatomist Nicolaus Steno proposed that the brain is a machine: To figure out how it works, we must take it apart. Gottfried Leibniz, a German polymath, protested. If one could enter the brain as one enters a mill, he argued, there would be only mechanical parts, but one would not be able to observe thoughts.

The Italian scientists Luigi Galvani and Alessandro Volta experimented with the role of electricity in animal flesh in the mid-18th century. In the 19th century, the German physicist Hermann von Helmholtz coined the term "action potential" to describe the electrical impulse transmitted down the nerves, and the brain analogy was updated: Nerves were now akin to wires, and the nervous system was conceived of as a telegraph. The Spanish anatomist Santiago Ramón y Cajal preferred a natural metaphor: "The cerebral cortex," he wrote, "is like a garden full of an infinite number of trees."

In the 20th century, American researchers Walter Pitts and Warren McCulloch proposed the first mathematical model of a neural network. Biology and technology hybridized, and the brain became a computer.

Throughout the book, Cobb stresses the productive but also pernicious role of metaphors in how we conceive of the brain. He gives the impression that theoretical speculation can and should be avoided while conducting empirical science. But without theory, how can we decide what should be observed?

In the second part of the book, Cobb reveals how much progress (however lacking in major conceptual innovations) we have made in the past 70 years, detailing the elusive quest to find the physical manifestation of memory, the many advances in brain-machine interfaces and neuromodulators, the improvement in mapping neural circuits, the invention of functional magnetic resonance imaging, and the progress made on understanding the neural correlates of consciousness. Despite our endless refinement of tools and our ability to collect massive amounts of data, many fundamental questions remain unanswered.

The book's final section, focused on the future of neuroscience, is the shortest, offering a brisk stroll through some caveats to currently accepted approaches and a sketch of alternative scenarios. Cobb acknowledges that "we may indeed be approaching the end of the computational metaphor. What is not clear, however, is what would replace it."

Cobb's goal, as explained in the book's introduction, is to navigate the many ways people have conceived of the brain. He definitely accomplishes it. However, there are topics and areas of research that I would have liked to have seen covered in greater detail, for example, brain development, the idea of embodied cognition, and the concept of distributed intelligence (as seen in ant colonies), as well as artificial intelligence. In trying to identify the author's philosophical commitments, the reader may detect a certain ambivalence: Does Cobb buy the mechanistic, reductionistic, and materialistic zeitgeist of molecular biology, for example, or not?

The path toward understanding the brain is long, winding, and littered with dead ends. In the words of the Argentinian writer Jorge Luis Borges, "The solution to the mystery is always inferior to the mystery itself." As *The Idea of the Brain* demonstrates, the mysteries of the mind may not just be stranger than we suppose; they may be stranger than we can suppose. ■

The reviewer is at the Instituto de Neurociencias (CSIC-UMH), Alicante, Spain. Email: agomezmarin@gmail.com

The Idea of the Brain: The Past and Future of Neuroscience
Matthew Cobb
Basic Books, 2020. 496 pp.

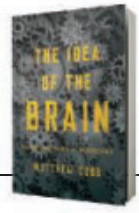

PHOTO: © MACIEK JASIK

A paralyzed individual uses a brain-computer interface to manipulate an apple with a robotic arm.

10.1126/science.abc0421

LETTERS

Insufficiently regulated contamination from the Elk Valley mines in British Columbia, Canada, threatens downstream ecosystems in both Canada and the United States.

Edited by **Jennifer Sills**

Retraction

After the publication of our Report "Current-induced strong diamagnetism in the Mott insulator Ca_2RuO_4" (*1*), new measurements performed in Kyoto by Giordano Mattoni *et al.* (*2*) revealed a serious technical artifact that affected our published data. Specifically, it became clear that a large part of the reported diamagnetic signal arose from a mechanism that we did not anticipate. This signal is attributable to localized heating of the sample holder, caused by the unavoidable Joule heating in the sample.

The published data in Figs. 1A, 1C, and 2B are affected by this artifact. The theoretical model of Fig. 3 remains valid, as it deals with the generic case in which a Mott gap is suppressed. Because the artifact affects the main experimental data, the authors unanimously agreed to retract the Research Article. For the same reason, another work on $Ca_3(Ru_{1-x}Ti_x)_2O_7$ by some of the present authors published in *Physical Review Letters* (*3*) is also being retracted (*4*).

Chanchal Sow[1], Shingo Yonezawa[1], Sota Kitamura[2,3], Takashi Oka[3,4], Kazuhiko Kuroki[5], Fumihiko Nakamura[6], Yoshiteru Maeno[1]*
[1]Department of Physics, Graduate School of Science, Kyoto University, Kyoto 606-8502, Japan. [2]Department of Physics, Graduate School of Science, University of Tokyo, Tokyo 113-0033, Japan. [3]Max Planck Institute for the Physics of Complex Systems, D-01187 Dresden, Germany. [4]Max Planck Institute for Chemical Physics of Solids, D-01187 Dresden, Germany. [5]Department of Physics, Graduate School of Science, Osaka University, Osaka 560-0043, Japan. [6]Department of Education and Creation Engineering, Kurume Institute of Technology, Fukuoka 830-0052, Japan.
*Corresponding author.
Email: maeno@scphys.kyoto-u.ac.jp

REFERENCES AND NOTES

1. C. Sow *et al*, *Science* **358** 1084 (2017).
2. G. Mattoni, S. Yonezawa, Y. Maeno, *Appl. Phys. Lett.* 10.1063/5.0006098 (2020); published online: arXiv:2004.04570 (2020).
3. C. Sow et al, *Phys. Rev. Lett.* **122**, 196602 (2019).
4. C. Sow *et al*., *Phys. Rev. Lett.* **124**, 169902 (2020).

10.1126/science.abc0469

Canada's mines pose transboundary risks

In 2019, Canada approved an extension of the deadline to start one of the world's largest copper and gold mines in the headwaters of the transboundary Unuk River (*1*). The plan for the Kerr-Sulphurets-Mitchell (KSM) mine is to dig one of the largest human-made holes on earth, erect one of the highest dams in North America, and operate water treatment for 200 years after the mine closes (*2*). Mines such as KSM pose long-term risks to downstream water quality, fish, and people (*3*). Given that mine contamination is not constrained by political boundaries, U.S., Canadian, and Indigenous governments must urgently engage in collaborative evaluation and regulation of mines in internationally shared rivers. Shortfalls in mine assessments and permitting policies should be addressed.

Mine assessments underestimate risk at high environmental cost. Contributing factors include the ecological complexity of rivers, policy shortcomings in weighing environmental risk (*4*), and profound engineering challenges posed by mountain mining. For example, insufficient evaluation of soil stability enabled the 2014 catastrophic failure of the Mount Polley tailings dam (*5*).

Furthermore, the issuance of mine permits relies on the promise of mitigations that lack field validation. Canadian industrial projects typically underdeliver on their mitigations, such as restoring fish habitat (*6*). Unverified technologies can fail, as evidenced by the 2014 fish kill downstream of Teck Resources' wastewater treatment plant (*7*).

Finally, mine assessment and permitting do not require incorporation of transparent, independent, and peer-reviewed science (*8*). For example, Teck's Elk Valley permit allows contaminant discharges up to 65 times above scientifically established protective thresholds for fish (*9*). Political borders do not block the downstream flow of this contaminated water into Montana and Idaho (*10*).

Stakes are high. Upstream Canadian mines threaten downstream economies, waters, and ways of life, even as the United States is currently weakening its own federal environmental regulations (*11*). Rather than a race to the bottom, we urge our governments to honor their mutual obligations to protect our shared transboundary waters as codified in the Boundary Waters Treaty of 1909 (*12*) and immediately collaborate on binational environmental reviews that are founded upon independent, transparent, and peer-reviewed science.

Erin K. Sexton[1]*, Christopher J. Sergeant[1,2], Jonathan W. Moore[3], Alana R. Westwood[4], David M. Chambers[5], Megan V. McPhee[2], Sonia A. Nagorski[6], Sarah L. O'Neal[7], Jill Weitz[8], Adrienne Berchtold[9], Marissa Capito[10], Christopher. A. Frissell[1,11], Jennifer Hamblen[12], F. Richard Hauer[1], Leslie A. Jones[13], Greg Knox[9], Randal Macnair[14], Rachel L. Malison[1], Vicki

PHOTO: GARTH LENZ

Marlatt[15], Jennifer McIntyre[16], Nikki Skuce[17], Diane C. Whited[1]
[1]Flathead Lake Biological Station, University of Montana, Polson, MT 59860, USA. [2]College of Fisheries and Ocean Sciences, University of Alaska Fairbanks, Juneau, AK 99801, USA. [3]Earth2Ocean Research Group, Simon Fraser University, Burnaby, BC V5A 1S6, Canada. [4]Mitacs Canadian Science Policy Fellow, Ottawa, ON K1P5A9, Canada. [5]Center for Science in Public Participation, Bozeman, MT 59715, USA. [6]Environmental Science and Geography Programs, University of Alaska Southeast, Juneau, AK 99801, USA. [7]School of Aquatic and Fishery Sciences, University of Washington, Seattle, WA 98105, USA. [8]Salmon Beyond Borders, Juneau, AK 99801, USA. [9]SkeenaWild Conservation Trust, Terrace, BC V8G 1M9, Canada. [10]Juneau, AK 99801, USA. [11]Frissell and Raven Hydrobiological and Landscape Sciences LLC, Polson, MT 59860, USA. [12]Takshanuk Watershed Council, Haines, AK 99827, USA. [13]Alaska Center for Conservation Science, University of Alaska, Anchorage, Anchorage, AK 99508, USA. [14]Wildsight, Kimberley, BC V1A 1Z6, Canada. [15]Department of Biological Sciences, Simon Fraser University, BC V5A 1S6 Canada. [16]School of the Environment, Puyallup Research and Extension Center, Washington State University, WA 98371, USA. [17]Northern Confluence Initiative, Smithers, BC V0J 2N0, Canada.
*Corresponding author.
Email: erin.sexton@umontana.edu

REFERENCES AND NOTES

1. British Columbia, Epic, KSM, Environmental Assessment Decision (2019); https://projects.eao.gov.bc.ca/p/58851156aaecd9001b81e652/project-details;currentPage=1;pageSize=10;sortBy=-datePosted;ms=1585955323365
2. H. Ghaffari *et al.*, "KSM (Kerr-Sulphurets-Mitchell) prefeasibility study update and preliminary economic assessment," Tetra Tech (2016); www.miningdataonline.com/reports/KSM_PFS_PEA_112016.pdf.
3. M. A. Palmer *et al.*, *Science* **327**, 148 (2010).
4. C. C. Murray *et al.*, *Environ. Manage.* **61**, 1062 (2018).
5. Independent Expert Engineering Investigation and Review Panel, "Report on Mount Polley Tailings Storage Facility Breach" (2015); www.mountpolleyreviewpanel.ca/.
6. J. T. Quigley, D. J. Harper, *Environ. Manage.* **37**, 336 (2006).
7. Government of Canada, "Teck Coal Limited: Conviction information for 2017-10-05" (2017); https://environmental-protection.canada.ca/offenders-registry/Home/Record?RefNumber=198.
8. A. R. Westwood *et al.*, *UBC Law Rev.* **52**, 243 (2019).
9. Teck, "Elk Valley Water Quality Plan," Teck Coal Limited (Sparwood, BC, 2014); www.teck.com/media/2015-Water-elk_valley_water_quality_plan_T3.2.3.2.pdf.
10. T. S. Presser *et al.*, "USGS measurements of dissolved and suspended particulate material selenium in Lake Koocanusa in the vicinity of Libby Dam (MT), 2015–2017 (update)" (U.S. Geological Survey data release, 2018).
11. A. Wittenberg, *Science*, 10.1126/science.aan7035 (2017).
12. The Boundary Waters Treaty of 1909 (International Joint Commission, 2016); www.ijc.org/sites/default/files/2018-07/Boundary%20Water-ENGFR.pdf.

COMPETING INTERESTS

C.A.F. is affiliated with the Department of Hydrology Salish Kootenai College, Pablo, MT 59855, USA. S.L.O. is affiliated with Agua Dulce Freshwater Consulting. A.R.W. is affiliated with Natural Resources Canada, but the views expressed herein do not in any way represent the Government of Canada or its departments or agencies.

10.1126/science.abb8819

Investments' role in ecosystem degradation

In their Review "Pervasive human-driven decline of life on Earth points to the need for transformative change" (13 December 2019, p. eaax3100), Díaz *et al.* discuss the results of the first integrated global-scale assessment report on biodiversity and ecosystem services. The authors identify extraction of resources to provide food, feed, and industrial feedstocks as the main direct driver of the observed changes in the ecosystems on which humans depend. Socioeconomic and institutional factors represent the indirect drivers. Although Díaz *et al.* mention that tax havens channel funds to support illegal fishing (*1*), they do not sufficiently emphasize the systemic role of investments in capitalist society.

Almost all provisions of food, feed, and raw materials, as well as socioeconomic and institutional changes, happen within the structural constraints and incentives of capitalism (*2*), a system based on private property, the competitive search for profit, and the reinvestment of profits. This system is extremely productive, generating enormous amounts of wealth, estimated at US$360 trillion in 2019 (*3*). However, the laws of competition demand that this wealth be reinvested somewhere to yield a return, a fact that can have striking environmental consequences. The investment decisions of a small number of financial intermediaries are responsible for substantial changes to the Amazon and boreal forests biomes (*4*). In addition, wealth is distributed very unequally (*5*). The investments of individuals with a high net worth have a disproportionately large impact on the expansion of cropland in the Global South (*6*). These considerations raise two fundamental questions: If we succeed in finding investment opportunities for the global wealth, what will the ecological consequences be? And if we fail, what will the economic consequences be? At this point, greater attention should be paid to the nexus between wealth generation, investment, and environmental degradation in terms of both research effort and policy initiatives.

M. Graziano Ceddia
Centre for Development and Environment, University of Bern, Bern, 3012 CH, Switzerland.
Email: graziano.ceddia@cde.unibe.ch

REFERENCES AND NOTES

1. V. Galaz *et al.*, *Nat. Ecol. Evol.* **2**, 1352 (2018).
2. B. Milanovic, *Capitalism, Alone: The Future of the System That Rules the World* (Harvard University Press, 2019).
3. A. Shorrocks, J. Davies, R. Lluberas, "Global wealth report 2019" (Credit Suisse, 2019); www.credit-suisse.com/about-us/en/reports-research/global-wealth-report.html.
4. V. Galaz, B. Crona, A. Dauriach, B. Scholtens, W. Steffen, *Glob. Environ. Change* **53**, 296 (2018).
5. C. Coffey, P. E. Revollo, R. Harvey, M. Lawson, "Time to Care: Unpaid and underpaid care work and the global inequality crisis" (Oxfam, 2020), p. 63.
6. M. G. Ceddia, *Nat. Sustain.*, 10.1038/s41893-020-0480-2 (2020).

10.1126/science.abb5756

Response

We agree with Ceddia that investment can play a key role in achieving the transformative change that is necessary to reverse nature's ongoing decline. In our Review, we pointed to the large impact of extractive industries, the unequal distribution of wealth associated with trade flows, and the handful of transnational corporations that control the majority of supply chains in agriculture, fishing, logging, and mining. Changing investment in these sectors can profoundly affect the future of nature.

More broadly, the impact of both public and private investment deserves more visibility (*1*, *2*). It is also important to focus on the role that public policy and public opinion (including a more holistic view of economics and quality of life) can have in shaping investment (*3*, *4*). A new economic system should build on and enhance the fabric of life rather than erode it. By rewarding actions that promote sustainability and penalizing actions that result in environmental deterioration, policies and attitudes can create powerful incentives for change in global financial and economic systems toward this vision.

Sandra Díaz*, Josef Settele, Eduardo Brondizio, Hien T. Ngo, Alexander Pfaff, Stephen Polasky, John Agard, Almut Arneth, Patricia Balvanera, Kate A. Brauman, Stuart H. M. Butchart, Kai M. A. Chan, Lucas A. Garibaldi, Kazuhito Ichii, Jianguo Liu, Suneetha M. Subramanian, Guy F. Midgley, Patricia Miloslavich, Zsolt Molnár, David Obura, Andy Purvis, Jona Razzaque, Belinda Reyers, Rinku Roy Chowdhury, Yunne-Jai Shin, Ingrid Visseren-Hamakers, Katherine J. Willis, Cynthia N. Zayas
*Corresponding author.
Email: sandra.diaz@unc.edu.ar
The list of author affiliations is available at https://science.sciencemag.org/content/366/6471/eaax3100.

REFERENCES AND NOTES

1. P. Balvanera *et al.*, in *Global Assessment Report of the Intergovernmental Science-Policy Platform on Biodiversity and Ecosystem Services*, E. S. Brondizio *et al.*, Eds. (Secretariat of the Intergovernmental Science-Policy Platform for Biodiversity and Ecosystem Services, Bonn, Germany, 2019).
2. K. A. Brauman *et al.*, in *Global Assessment Report of the Intergovernmental Science-Policy Platform on Biodiversity and Ecosystem Services*, E. S. Brondízio *et al.*, Eds. (Secretariat of the Intergovernmental Science-Policy Platform for Biodiversity and Ecosystem Services, Bonn, Germany, 2019).
3. K. M. A. Chan *et al.*, in *Global Assessment Report of the Intergovernmental Science-Policy Platform on Biodiversity and Ecosystem Services*, E. S. Brondízio *et al.*, Eds. (Secretariat of the Intergovernmental Science-Policy Platform for Biodiversity and Ecosystem Services, Bonn, Germany, 2019)
4. J. Razzaque *et al.*, in *Global Assessment Report of the Intergovernmental Science-Policy Platform on Biodiversity and Ecosystem Services*, E. S. Brondízio *et al.*, Eds. (Secretariat of the Intergovernmental Science-Policy Platform for Biodiversity and Ecosystem Services, Bonn, Germany, 2019).

10.1126/science.abb6019

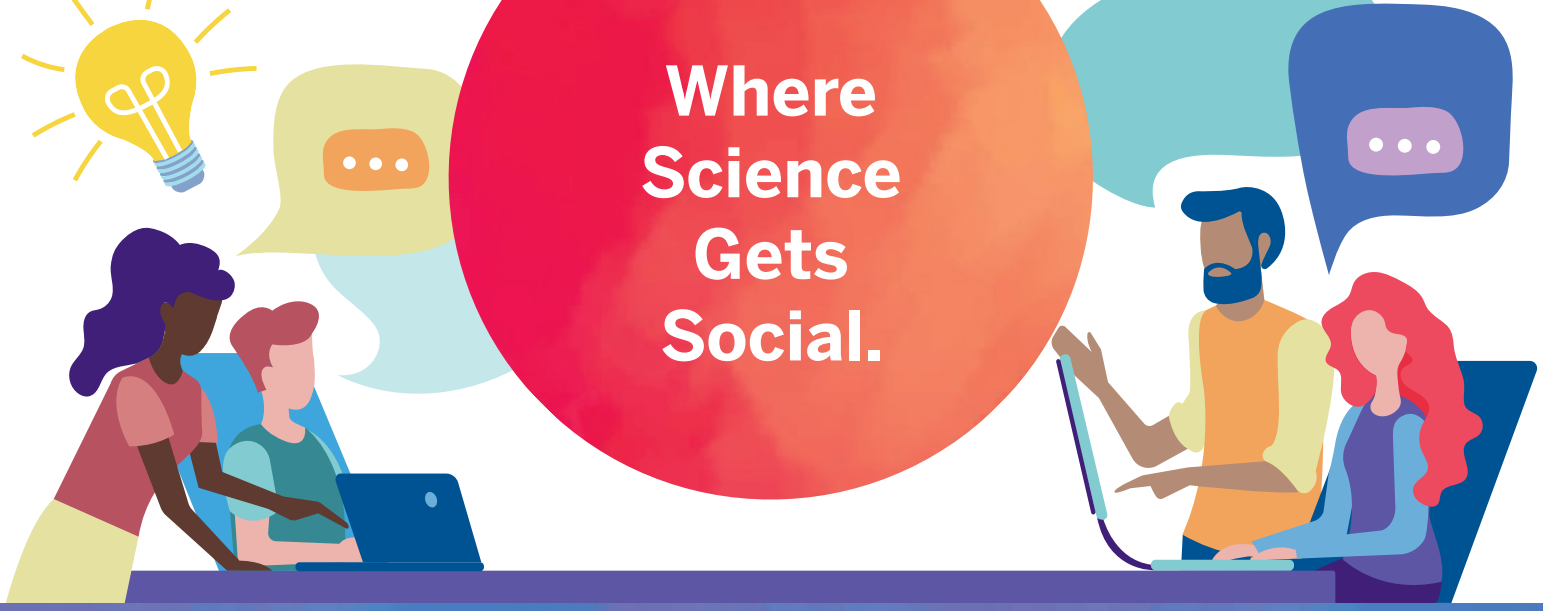

AAAS.ORG/COMMUNITY

AAAS' Member Community is a one-stop destination for scientists and STEM enthusiasts alike. It's "Where Science Gets Social": a community where facts matter, ideas are big and there's always a reason to come hang out, share, discuss and explore.

Member COMMUNITY
AAAS

AMERICAN ASSOCIATION FOR THE ADVANCEMENT OF SCIENCE

North Carolina's Cape Fear River contains high levels of several different per- and polyfluoroalkyl substances, some known to pose human health dangers.

PHOTO: NICK SANTILLO

Summit briefs policy-makers on drinking water safety

AAAS and National League of Cities address PFAS, chemicals linked to health problems

By **Adam D. Cohen**

On 7 February, the American Association for the Advancement of Science hosted a summit focused on a public health issue affecting virtually everyone in the United States.

At the day-long event, 23 municipal leaders from around the country met to share experiences and receive scientific guidance related to per- and polyfluoroalkyl substances, or PFAS. A family of approximately 4700 synthetic chemicals that are water-, heat-, and stain-resistant, PFAS are present in certain industrial machinery, consumer goods, and firefighting foams.

Though researchers have not established causal relationships between PFAS and adverse health effects, the two most studied compounds, perfluorooctanoic acid (PFOA) and perfluorooctanesulfonic acid (PFOS), are associated with increased rates of numerous ailments, including some cancers, thyroid disease, and high cholesterol. Between 2006 and 2015, American companies phased out the manufacturing of PFOA and PFOS, but it is still legal to import the chemicals in consumer products.

No federal regulations limit PFAS levels in drinking water systems, despite a 2007 study led by the Centers for Disease Control and Prevention (CDC) showing that 97% of Americans had the chemicals in their blood. Though blood levels of PFOA and PFOS have declined by more than 60% and 80%, respectively, since 1999, current measurements by the CDC continue to find PFAS "in the serum of nearly all of the people tested."

Thus, the recent meeting provided a much-needed forum for participants—mostly mayors, city council members, and water department managers—to learn from each other and hear experts' advice on testing water for the substances and removing them.

Since its launch in September 2018, the AAAS Center for Scientific Evidence in Public Issues, known as the EPI Center, has worked to deliver clear, concise, and actionable scientific evidence to policy-makers. Hosted in partnership with the National League of Cities, the meeting on drinking water safety concluded a series of three stakeholder summits organized by the EPI Center and supported by the Chan Zuckerberg Initiative.

The previous two summits—the first on natural resources, sustainability, and energy and the second on addiction, artificial intelligence, and other issues that arise in legal proceedings—were well received and led to requests from participants for follow-up sessions.

"We are not advocating for particular policy outcomes, but we are trying to help policy-makers access and understand relevant scientific evidence as they grapple with these complex problems," said Michael Fernandez, director of the EPI Center. "We understand that scientific evidence isn't the only basis on which people are making policies; we just want to make sure that they have access to the most up-to-date scientific evidence to inform their decisions."

Though scientists first discovered PFAS in the 1930s, initial understanding of their environmental persistence and potential health effects arose within the scientific community in the 1990s, and more widespread concern about drinking water contamination came only in the past decade.

While speaking to attendees at February's PFAS summit, Patricia Reyes, director of the Interstate Technology and Regulatory Council, a public-private coalition that communicates best environmental practices for states, recalled a 2016 meeting at which Environmental

Protection Agency (EPA) Administrator Gina McCarthy addressed a group of commissioners representing most states. At the time, only a few of the commissioners raised their hands to indicate that they knew what PFAS was.

"The EPA administrator stood up and said, 'I guarantee you, in 6 months, you'll all know what it is,'" Reyes said. "And then she said, 'It is also going to be the biggest environmental issue of our lifetime.'"

PFAS contain extremely strong carbon-fluorine bonds that make them crucial components of many consumer products, including nonstick pans, water-resistant food packaging, and stain-resistant carpeting. Additionally, they are the key ingredient in aqueous film-forming foams, highly efficient fire extinguishers used to fight fuel fires, most often on military bases and at airports.

"They were seen as miracle compounds," said environmental engineer Michelle Crimi while presenting at the drinking water conference. "We wanted these things."

Ironically, the same properties that make PFAS so useful in everyday items and potentially lifesaving in firefighting foams make them concentrate in animals and humans rather than break down in the environment. To prevent one of the most common pathways of exposure, municipalities must remove the compounds from drinking water before it reaches people's taps. Crimi highlighted the latest research on different "methods of attack," such as ion exchange, reverse osmosis, and a process that uses ultrasound waves to destroy PFAS.

Shaun Mulholland, city manager for Lebanon, New Hampshire, attended the summit to learn more about the science of treating PFAS-contaminated water. Though Lebanon's drinking water is clean, liquid leaching from the city's landfills contains PFAS, and Mulholland is developing a test site to remove the dangerous compounds. He appreciated receiving scientific guidance tailored to decision-makers in his position.

"They did an excellent job," Mulholland said. "I've spent quite a bit of time just researching things online. But they were able to explain it in a way that I could understand it, which was very, very helpful."

Deborah Calvert, a city council member in Minnetonka, Minnesota, came to the summit with a more intimate understanding of the havoc that PFAS can cause than most attendees. At the time of the meeting, officials had closed 6 of the 19 municipal wells in Woodbury—like Minnetonka, a Twin Cities suburb—due to PFAS contamination. They have since shuttered a seventh. The St. Paul–based 3M Company is paying to build a filtration plant that would enable the city to reopen some of the wells, in addition to the $850 million it paid in 2018 to settle an environmental-damage suit brought by the state attorney general.

At the summit, Calvert mentioned cruises on Lake Minnetonka run by a University of Minnesota extension program, during which public officials and residents learn about chemical contaminants, invasive species, and other water quality issues. She was pleased that the meeting's organizers were able to provide a forum for her and other officials to exchange such ideas.

"I wanted to know what they could do to help coalesce information for us, to share technical information more easily, which I thought they did an incredible job of doing," Calvert said. "Also, learning what are other city officials grappling with around the country; there's just no substitute for that kind of conversation."

WHAT DO YOU AND THOMAS EDISON HAVE IN COMMON?

AAAS.

By investing in AAAS you join Thomas Edison and the many distinguished individuals whose vision led to the creation of AAAS and our world-renowned journal, *Science*, more than 150 years ago.

Like Edison, you can create a legacy that will last well into the future through planned giving to AAAS. By making AAAS a beneficiary of your will, trust, retirement plan, or life insurance policy, you make a strong investment in our ability to advance science in the service of society for years to come.

To discuss your legacy planning, contact Juli Staiano, Chief Philanthropy Officer, at (202) 326-6636, or jstaiano@aaas.org, or visit **aaas.org/1848society** for more information.

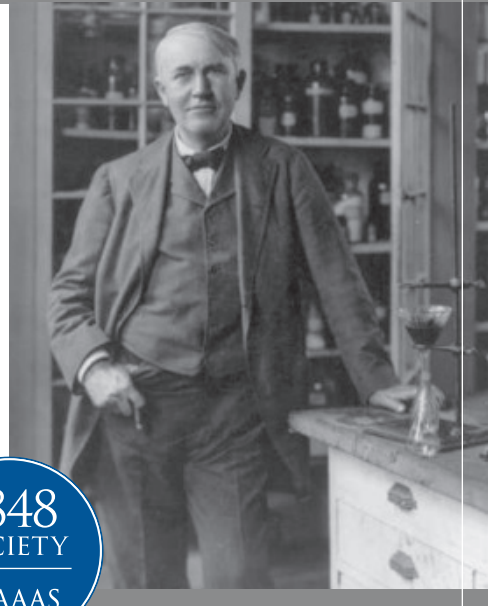

1848 SOCIETY AAAS

RESEARCH

IN *SCIENCE* JOURNALS

Edited by **Michael Funk**

Fossilized coral on the island of Niue in the South Pacific Ocean. Reefs, whether modern or ancient, are sites of high animal diversity.

PHOTO: © LAUREN CAMEO/REAMSTIME.COM

PALEONTOLOGY

Across time, but also across space

Fossils, especially those from marine systems, have long been used to estimate changes in patterns of diversity over time. However, fossils are patchy in their occurrence, so such temporal estimates generally have not included variations due to space. Such a singular examination has the potential to simplify, or even misrepresent, patterns. Close *et al*. used a spatially explicit approach to measure diversity changes in marine fossils across time and space. They found that, like modern systems, diversity varies considerably across space, with reefs increasing diversity levels. Accounting for this spatial-environmental variation will shed new light on the study of diversity over time. —SNV

Science, this issue p. 420

ATMOSPHERIC PHYSICS

Explaining super-rotation on Venus

The solid surface of Venus rotates very slowly, once every 243 days, but its thick atmosphere circles the planet in just 4 days. This phenomenon, known as super-rotation, requires a continuous input of angular momentum, from an unknown source, to overcome friction with the surface. Horinouchi *et al*. mapped the planet's winds using ultraviolet observations of Venus' clouds from the orbiting Akatsuki spacecraft (see the Perspective by Lebonnois). They incorporated these data into a global model of angular momentum transport in the atmosphere, finding that the super-rotation is maintained through thermal tides driven by solar heating. —KTS

Science, this issue p. 405; see also p. 363

RNA STRUCTURE

One guanosine determines transcript fate

Transcripts of the HIV-1 RNA genome can be either spliced and translated into viral proteins or packaged into new virions as a progeny genome. The path taken depends on whether the transcript contains one guanosine at the 5′ terminus (1G) rather than two or three (2G or 3G). Brown *et al*. used nuclear magnetic resonance spectroscopy to show that 1G transcripts adopt a dimeric structure that sequesters a terminal cap required for translation and splicing but exposes sites that bind to the HIV-1 Gag protein, which recruits the genome during viral assembly. Conversely, 2G or 3G transcripts have the cap accessible, but Gag-binding sites are sequestered. Therefore, a single guanosine acts as a conformational switch to determine the fate of HIV-1 transcripts. —VV

Science, this issue p. 413

INSECT POPULATIONS

Local drivers of decline matter

Recent studies have reported alarming declines in insect populations, but questions persist about the breadth and pattern of such declines. van Klink *et al*. compiled data from 166 long-term surveys across 1676 globally distributed sites and confirmed declines in terrestrial

insects, albeit at lower rates than some other studies have reported (see the Perspective by Dornelas and Daskalova). However, they found that freshwater insect populations have increased overall, perhaps owing to clean water efforts and climate change. Patterns of variation suggest that local-scale drivers are likely responsible for many changes in population trends, providing hope for directed conservation actions. —SNV

Science, this issue p. 417; see also p. 368

CORONAVIRUS

Outbreak to pandemic

In response to global dispersion of severe acute respiratory syndrome–coronavirus 2 (SARS-CoV-2), quarantine measures have been implemented around the world. To understand how travel and quarantine influence the dynamics of the spread of this novel human virus, Chinazzi *et al*. applied a global metapopulation disease transmission model to epidemiological data from China. They concluded that the travel quarantine introduced in Wuhan on 23 January 2020 only delayed epidemic progression by 3 to 5 days within China, but international travel restrictions did help to slow spread elsewhere in the world until mid-February. Their results suggest that early detection, hand washing, self-isolation, and household quarantine will likely be more effective than travel restrictions at mitigating this pandemic. —CA

Science, this issue p. 395

CORONAVIRUS

Targeting a key enzyme in SARS-CoV-2

Scientists across the world are working to understand severe-acute respiratory syndrome–coronavirus 2 (SARS-CoV-2), the virus that causes coronavirus disease 2019 (COVID-19). Zhang *et al.* determined the x-ray crystal structure of a key protein in the virus' life cycle: the main protease. This enzyme cuts the polyproteins translated from viral RNA to yield functional viral proteins. The authors also developed a lead compound into a potent inhibitor and obtained a structure with the inhibitor bound, work that may provide a basis for development of anticoronaviral drugs. —VV

Science, this issue p. 409

INFECTIOUS DISEASE

Understanding variable RSV severity

Almost all young children become infected with respiratory syncytial virus (RSV), but only a few progress to severe disease, and certain immune responses have been shown to be harmful. To better understand the immune signatures associated with mild or severe disease, Heinonen *et al*. performed transcriptomic and flow cytometry analysis on samples from RSV-infected children under the age of 2 with either mild or severe disease. The severe cases displayed reduced viral loads, lower induction of type I interferon, and changes in blood immune cell populations. Overall, a robust innate immune response seemed indicative of a more favorable outcome. —LP

Sci. Transl. Med. **12**, eaaw0268 (2020).

PROTEIN RADICALS

Caught in the act

Proton-coupled electron transfer (PCET) is an important process for moving electrons through proteins and requires precise positioning of suitable proton and electron carriers. Kang *et al*. determined a cryo–electron microscopy structure of the active complex formed by ribonucleotide reductase that allows for PCET between two protein subunits over a total distance of ~35 angstroms. Several interventions that stabilized the radical en route also stabilized the complex and allowed for visualization of the interface between the two subunits and the full network of residues that permit PCET. —MAF

Science, this issue p. 424

IN OTHER JOURNALS

Edited by **Caroline Ash** *and* **Jesse Smith**

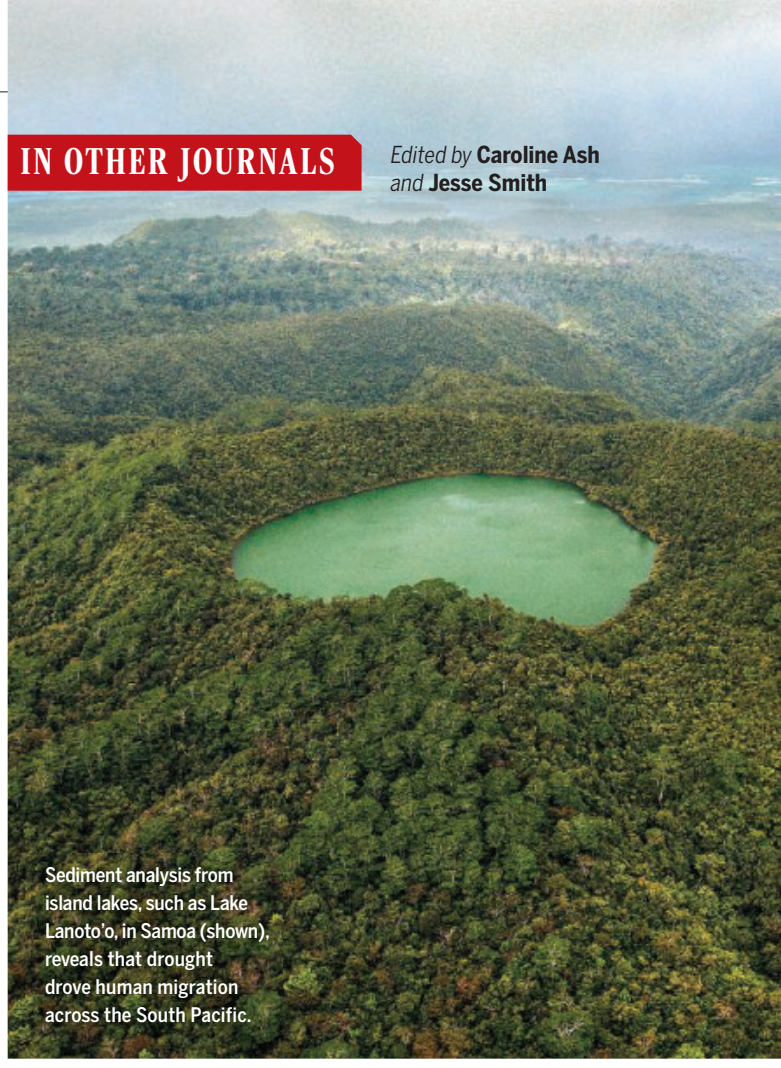

Sediment analysis from island lakes, such as Lake Lanoto'o, in Samoa (shown), reveals that drought drove human migration across the South Pacific.

PHOTO: ATMOTU IMAGES/ALAMY STOCK PHOTO

SIGNAL TRANSDUCTION

Into the heart of blood flow

The flow of blood within the heart is exactly matched to its metabolic needs and, throughout life, never runs out of energy. How is this possible? Zhao *et al.* identified a local and instantaneous feedback control system that couples metabolism in cardiac myocytes to the regulation of blood flow. Several such mechanisms exist, but these authors characterize one that depends on adenosine triphosphate (ATP)–sensitive K^+ (K_{ATP}) channels. Studies of mouse ventricular myocytes showed that as active cells depleted intracellular concentrations of ATP, K_{ATP} channels were activated. This caused an efflux of K^+, thus depolarizing the cells. Electrical coupling of the myocytes to neighboring endothelial cells and contractile pericytes and smooth muscle cells allowed a compensatory increase in blood flow. —LBR

Proc. Natl. Acad. Sci. U.S.A. **117**, 7461 (2020).

HUMAN GENETICS

Diversity in genome studies

Genome-wide association studies have been used to identify genetic variants associated with specific phenotypes. However, such studies have mostly focused on individuals of European descent. Hu *et al.* examined the genome architecture of blood lipid traits associated with heart and metabolic disease in >45,000 ancestrally diverse participants from the Population Architecture using Genomics and Epidemiology (PAGE) study. This study identified previously uncharacterized loci and variants affecting lipid metabolism in non-European populations.

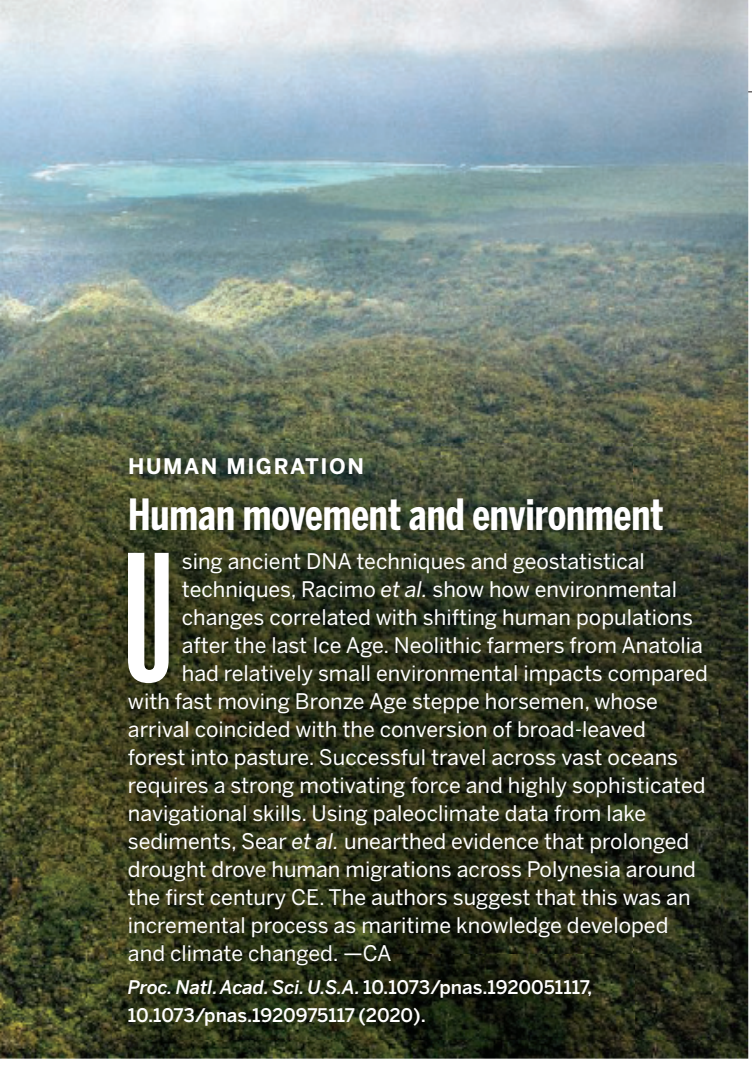

HUMAN MIGRATION

Human movement and environment

Using ancient DNA techniques and geostatistical techniques, Racimo *et al.* show how environmental changes correlated with shifting human populations after the last Ice Age. Neolithic farmers from Anatolia had relatively small environmental impacts compared with fast moving Bronze Age steppe horsemen, whose arrival coincided with the conversion of broad-leaved forest into pasture. Successful travel across vast oceans requires a strong motivating force and highly sophisticated navigational skills. Using paleoclimate data from lake sediments, Sear *et al.* unearthed evidence that prolonged drought drove human migrations across Polynesia around the first century CE. The authors suggest that this was an incremental process as maritime knowledge developed and climate changed. —CA

Proc. Natl. Acad. Sci. U.S.A. **10.1073/pnas.1920051117, 10.1073/pnas.1920975117 (2020).**

By combining these results with other cohorts, some of which were primarily composed of individuals of European descent, disease-causative variants could be mapped, the magnitude of effects in loci of Europeans was confirmed, and new variants of potential interest were identified, including a gene associated with blood lipid concentrations in individuals from non-European populations. —LMZ

PLOS Genet. **16**, e1008684 (2020).

METALLURGY

Rubbery alloys

Materials that have large and recoverable elastic strain behavior are usually polymers or other types of soft materials. Chen *et al.* discovered a superelastic NiCoFeGa alloy with virtually no hysteresis when strained. This means that the material stretches and recovers its shape in a reversible way even after thousands of cycles. The underlying microstructures allowing this behavior may be useful for developing other superelastic alloys. —BG

Nat. Mater. 10.1038/s41563-020-0645-4 (2020).

QUANTUM SECURITY

Securing quantum key distribution

The deployment of quantum technologies will be reliant on developing platforms that are mass-manufacturable and cost-effective. Quantum key distribution is a protocol that ensures secure communications between various parties within a network using shared secret keys to encrypt the communication channels. However, practical implementations with hybrid systems can leave side channels open, which compromises the security of the network. Semenenko *et al.* demonstrate a quantum-ready platform based on all the optical components being monolithically integrated on an indium-phosphide photonic chip. With the side channels to information leakage effectively closed and demonstrated secret keys exchanged at rates exceeding 1 kilobit per second over 100 kilometers, such a platform provides a promising solution for the development of secure communication over citywide quantum networks. —ISO

Optica **7**, 238 (2020).

SINGLE-USE PLASTICS

Legacy of the disposable cup

It is estimated that, as a global population, we use between 250 billion and 300 billion disposable cups annually. These cups are mostly composed of virgin tree cellulose coated with plastic and are almost never recycled. Foteinis conducted a life-cycle analysis of disposable cup use, focusing on the United Kingdom, and found that their annual carbon footprint was equivalent to that produced by the manufacture of ~11,500 midsized cars or that of 1.5 million European residents. Improved recycling could reduce these impacts by up to 40%, and reusable cups would reduce the carbon footprint threefold. Disposable cups represent only a tiny bit of our daily resource use, so these results emphasize just how large an impact our day-to-day activities have on the planet. They also show how much improvement we have the potential to make with small, seemingly inconsequential choices. —SNV

J. Clean. Prod. **255**, 120294 (2020).

CLIMATE

Separation climatology

The El Niño–Southern Oscillation (ENSO) has a large influence on temperature and precipitation across the globe, so predicting it and its impact is an important challenge. However, that has been made even more difficult by global warming, which appears to be changing the nature of ENSO. Hu *et al.* discuss how some recent El Niños have experienced a decoupling between oceanic and atmospheric temperatures. Without this coupling, the impact of central and eastern tropical Pacific warming on extratropical climate is different from that caused by El Niño events in which the ocean and atmosphere are coupled. —HJS

Geophys. Res. Lett. **47**, e2020GL087621 (2020).

Paper coffee cups are coated with plastic, are rarely recycled, and have a large carbon footprint.

PHOTO: ICEDMOCHA/SHUTTERSTOCK

REVIEW SUMMARY

PROTEOSTASIS

The integrated stress response: From mechanism to disease

Mauro Costa-Mattioli* and Peter Walter*

BACKGROUND: The integrated stress response (ISR) is an evolutionarily conserved intracellular signaling network that helps the cell, tissue, and organism to adapt to a variable environment and maintain health. In response to different environmental and pathological conditions, including protein homeostasis (proteostasis) defects, nutrient deprivation, viral infection, and oxidative stress, the ISR restores balance by reprogramming gene expression. The various stresses are sensed by four specialized kinases (PERK, GCN2, PKR and HRI) that converge on phosphorylation of a single serine on the eukaryotic translation initiation factor eIF2. eIF2 phosphorylation blocks the action of eIF2's guanine nucleotide exchange factor termed eIF2B, resulting in a general reduction in protein synthesis. Paradoxically, phosphorylation of eIF2 also triggers the translation of specific mRNAs, including key transcription factors, such as ATF4. These mRNAs contain short inhibitory upstream open reading frames in their 5′-untranslated regions that prevent translation initiation at their canonical AUGs. By tuning down general mRNA translation and up-regulating the synthesis of a few proteins that drive a new transcriptional program, the ISR aims to maintain or reestablish physiological homeostasis. However, if the stress cannot be mitigated, the ISR triggers apoptosis to eliminate the damaged cell.

ADVANCES: Our understanding of the central mechanisms that govern the ISR has advanced vastly. The ISR's central regulatory hub lies in the eIF2–eIF2B complex, which controls the formation of the eIF2•GTP•methionyl-intiator tRNA ternary complex (TC), a prerequisite for initiating new protein synthesis. Assembly of functional TC is inhibited by eIF2-P, which blocks eIF2B noncompetitively. In mammalian cells, the phosphorylation of eIF2 is a tightly regulated process. In addition to the four specialized eIF2 kinases that phosphorylate eIF2, two dedicated phosphatases antagonize this reaction. Both phosphatases contain a common catalytic core subunit, the protein phosphatase 1 (PP1), and a regulatory subunit (GADD34 or CReP), which render the phosphatase specific to eIF2. Structural and biophysical approaches have elucidated the mechanism of action of eIF2B and its modulation by ISR inhibitors and activators. Gene expression analyses have revealed complex ISR-driven reprogramming. Although it has been long recognized that, in the brain, long-term memory formation requires new protein synthesis, recent causal and convergent evidence across different species and model systems has shown that the ISR serves as a universal regulator of this process. Briefly, inhibition of the ISR enhances long-term memory formation, whereas activation of the ISR prevents it. Consistent with this notion, unbiased genome-wide association studies have identified mutations in key components of the ISR in humans with intellectual disability. Furthermore, age-related cognitive disorders are commonly associated with the activation of the ISR. Most notably, oxidative stress, misfolded proteins, and other stressors induce the ISR in several neurodegenerative disorders, including Alzheimer's disease. Recent genetic and pharmacological evidence suggest that tuning the ISR reverses cognitive dysfunction as well as neurodegeneration in a wide range of memory disorders that result from protein homeostasis defects. Thus, long-term memory deficits may primarily result as a consequence of ISR activation rather than from the particular proteostasis defects that lead to its induction. Finally, the ISR is also implicated in the pathogenesis of a plethora of other complex diseases, including cancer, diabetes, and metabolic disorders.

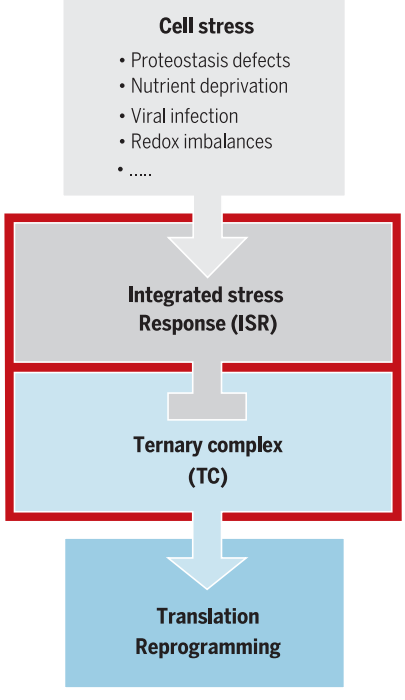

The regulatory network of the ISR. Diverse deviations from homeostasis activate the ISR. The resulting dysregulation of translation contributes to numerous diseases.

ON OUR WEBSITE

Read the full article at https://dx.doi.org/10.1126/science.aat5314

OUTLOOK: The ISR is emerging as a central regulator of protein homeostasis at both the cellular and organismal level. Mechanistically, much remains to be understood regarding additional inputs into the eIF2B–eIF2 regulatory hub controlling TC concentration, as well as the IRS's connectivity to other intracellular signaling networks. As yet, little is known about the role of the specific proteins whose synthesis is altered during acute and persistent ISR activation and how these effectors collaborate to compute the life or death decisions cells make upon ISR activation. ISR gene expression signatures and functional consequences will need to be mapped across different tissues, cell types, and developmental stages. In addition, it will be invaluable to generate additional genetic and molecular tools that permit the direct temporal and spatial manipulation of ISR pathway in specific cells and circuits to determine their function. From a medical perspective, the ISR is implicated in the etiology of several disorders, and manipulation of the ISR is emerging as a promising therapeutic avenue for the treatment of a variety of diseases. The use of innovative mouse models, patient-derived induced pluripotent stem cells, and human organoids will greatly enhance our ability to explore the ISR's clinical relevance further and help define therapeutic windows in which ISR modulation may prove beneficial. Identifying additional specific small-molecule inhibitors and activators of the ISR will offer valuable opportunities to dissect the role of the ISR pharmacologically in health and disease. Finally, discovery and mechanistic understanding of additional ISR modulators will increase the repertoire of therapeutic targets and may further enable clinical development in a wide range of age-related human diseases. ■

The list of author affiliations is available in the full article online.
*Corresponding author. Email: costamat@bcm.edu (M.C.-M.); peter@walterlab.ucsf.edu (P.W.)
Cite this article as M. Costa-Mattioli and P. Walter, *Science* 368, eaat5314 (2020). DOI: 10.1126/science.aat5314

RESEARCH ARTICLE SUMMARY

STRUCTURAL BIOLOGY

Structural basis of ER-associated protein degradation mediated by the Hrd1 ubiquitin ligase complex

Xudong Wu, Marc Siggel, Sergey Ovchinnikov, Wei Mi, Vladimir Svetlov, Evgeny Nudler, Maofu Liao, Gerhard Hummer, Tom A. Rapoport*

INTRODUCTION: Protein homeostasis in the endoplasmic reticulum (ER) is maintained by a quality control system. When a newly synthesized ER protein misfolds, it is ultimately retrotranslocated into the cytosol, polyubiquitinated, and degraded by the proteasome, a pathway referred to as ER-associated protein degradation (ERAD). ERAD alleviates cytotoxic stress imposed by protein misfolding and is implicated in numerous diseases. ERAD is found in all eukaryotic cells but is best studied for the ERAD-L pathway in *Saccharomyces cerevisiae*, which disposes of misfolded glycoproteins in the ER lumen. The glycan attached to these proteins is first trimmed by glycosidases to generate a terminal α1,6-mannose residue. This residue, together with an unfolded polypeptide segment, targets the substrate to the Hrd1 complex, which is composed of the multispanning ubiquitin ligase Hrd1 and four additional proteins (Hrd3, Der1, Usa1, and Yos9). The Hrd1 complex mediates the retrotranslocation of the polypeptide into the cytosol, where it is polyubiquitinated, extracted from the membrane by the Cdc48 adenosine triphosphatase complex, and, finally, degraded by the proteasome.

RATIONALE: The mechanism of ERAD-L remains poorly understood. Arguably the most mysterious aspect is how misfolded proteins cross the ER membrane, which normally presents a barrier to macromolecules. How ERAD-L substrates are recognized and distinguished from properly folding intermediates is also unclear. Answers to these questions require structural information on the Hrd1 complex.

RESULTS: Here, we report a structure of the active Hrd1 complex from *S. cerevisiae*, as determined by cryo–electron microscopy (cryo-EM) analysis of two subcomplexes. Our structures, biochemical data, and experiments in vivo indicate that the Hrd1 complex functions as a monomer in ERAD-L. Hrd3 and Yos9 jointly create a luminal binding site that recognizes misfolded glycoproteins. The α1,6-mannose residue binds to the mannose 6-phosphate receptor homology (MRH) domain of Yos9, and the polypeptide segment downstream of the glycan attachment site is likely accommodated in a groove of the luminal domain of Hrd3. Hrd1 and the rhomboid-like Der1 protein are linked by Usa1 on the cytosolic side of the membrane. Both Der1 and Hrd1 have lateral gates that face one another within the membrane and possess luminal and cytosolic cavities, respectively. Both proteins distort the membrane region between the lateral gates, making it much thinner than a normal phospholipid bilayer, an observation supported by molecular dynamics simulations. The structures and photocrosslinking experiments indicate that the retrotranslocation of an ERAD-L substrate is initiated by loop insertion of the polypeptide into the membrane, with one strand of the loop interacting with Der1 and the other with Hrd1.

ON OUR WEBSITE

Read the full article at https://dx.doi.org/10.1126/science.aaz2449

CONCLUSION: Our results lead to a model for the mechanism of retrotranslocation through the Hrd1 complex. The pathway across the membrane is formed by two "half-channels" corresponding to the luminal and cytosolic cavities of Der1 and Hrd1, respectively. These half-channels are juxtaposed in a thinned membrane region. The substrate inserts into the retrotranslocon as a hairpin that is hydrophilic on both sides. These features contrast with the Sec61 channel, which accepts substrates with a hydrophobic signal or transmembrane segment forming one side of the loop. This segment exits the lateral gate into the lipid environment and is not translocated, while the other side of the loop moves through the membrane in an entirely hydrophilic environment. The structural features of the retrotranslocon can facilitate movement of a fully hydrophilic substrate through a thinned and thus distorted membrane, a paradigm that may be replicated in other protein translocation systems. ■

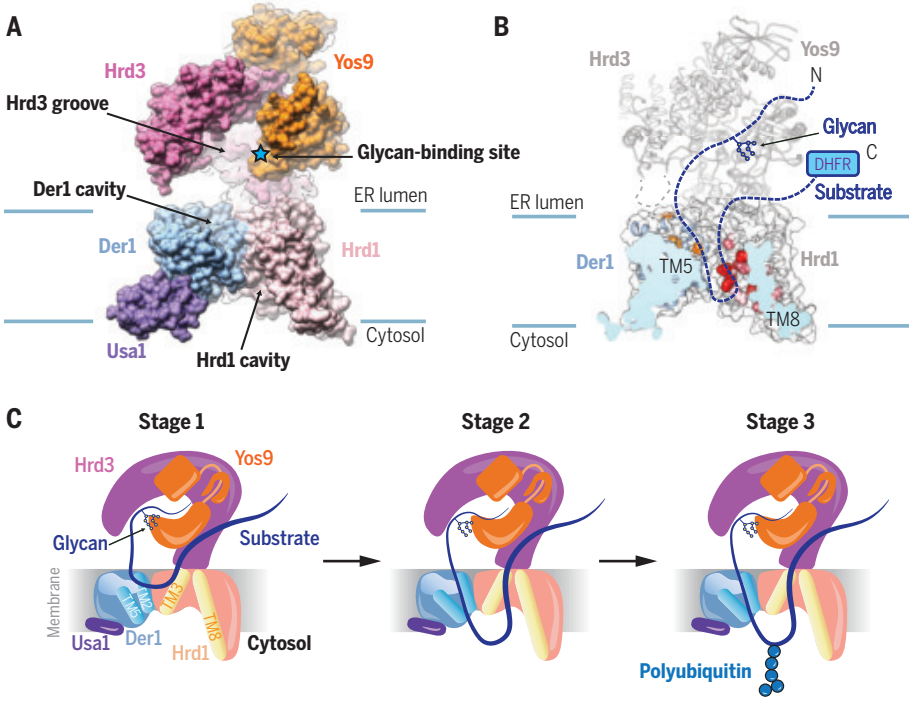

Initiation of ERAD-L revealed by cryo-EM and photocrosslinking. (**A**) Side view of a space-filling model of the Hrd1 complex, based on structures of the Hrd1~Usa1-Der1-Hrd3 and Hrd3-Yos9 subcomplexes. (**B**) Hypothetical position of a glycosylated ERAD-L substrate in the Hrd1 complex (dashed blue line). Substrate-interacting amino acid residues in Hrd1 and Der1 (red and orange, respectively) were determined by photocrosslinking. N, N terminus; C, C terminus; DHFR, dihydrofolate reductase; TM, transmembrane helix. (**C**) Model for the first three stages of retrotranslocation.

The list of author affiliations is available in the full article online.
*Corresponding author. Email: tom_rapoport@hms.harvard.edu
Cite this article as X. Wu *et al.*, *Science* 368, eaaz2449 (2020). DOI: 10.1126/science.aaz2449

RESEARCH ARTICLE SUMMARY

ULTRAFAST MICROSCOPY

Ultrafast vector imaging of plasmonic skyrmion dynamics with deep subwavelength resolution

Timothy J. Davis*, David Janoschka, Pascal Dreher, Bettina Frank, Frank-J. Meyer zu Heringdorf*, Harald Giessen*

INTRODUCTION: Topology is the study of geometric properties that are unaffected by continuous changes in shape and size. Skyrmions are examples of topological defects in vector fields. Skyrmions exhibit a characteristic vector structure. When excited by electromagnetic near fields on thin metal films, they are called plasmonic skyrmions. These fields exist at sub–100-nm scales and oscillate with periods of a few femtoseconds and thus are difficult to measure.

RATIONALE: Two-photon photoemission electron microscopy studies were previously able to image the local plasmon fields with femtosecond time resolution, but the vector information of the local electric fields was missing. Here we introduce a new technique, time-resolved vector microscopy, that enables us to compose entire movies on a subfemtosecond time scale and a 10-nm spatial scale of the electric field vectors of surface plasmon polaritons (SPPs). We use this technique to image complete time sequences of propagating surface plasmons, demonstrating their spin-momentum locking, as well as plasmonic skyrmions on atomically flat single-crystalline gold films that have been patterned using gold ion beam lithography.

RESULTS: The key technique to obtain vector information is to take two sequences of the entire process with two different probe beam polarizations. Hence, the electric field vectors will be projected onto the probing electric field by the two-photon photoemission process. The spatial dependence of the two in-plane vector components coupled with Maxwell's equations then permits the retrieval of the out-of-plane component. This allows us to unambiguously resolve all vector components of the electric field as well as their time dynamics, enabling the retrieval of the experimental time-dependent skyrmion number and indicating the periodic transformation from skyrmion number +1 to −1 and back on a time scale of a few femtoseconds. Additionally, all three magnetic field vectors of the surface can be obtained from the electric field vectors by using Maxwell's curl equation.

ON OUR WEBSITE

Read the full article at https://dx.doi.org/10.1126/science.aba6415

CONCLUSION: With our vector microscopy technique, we are able to image plasmonic spin-momentum locking and plasmonic skyrmion dynamics. In the future, other topological nanophotonic systems should be in reach as well; these include plasmonic merons or short-range skyrmions, where the dispersion of plasmons in extremely thin films is used. This research will open the door to creating linear optical features on the few-nanometer length scale. ■

The list of author affiliations is available in the full article online.
*Corresponding author. Email: timd@unimelb.edu.au (T.J.D.); meyerzh@uni-due.de (F.-J.M.z.H.); giessen@pi4.uni-stuttgart.de (H.G.)
Cite this article as T. J. Davis *et al.*, *Science* **368**, eaba6415 (2020). DOI: 10.1126/science.aba6415

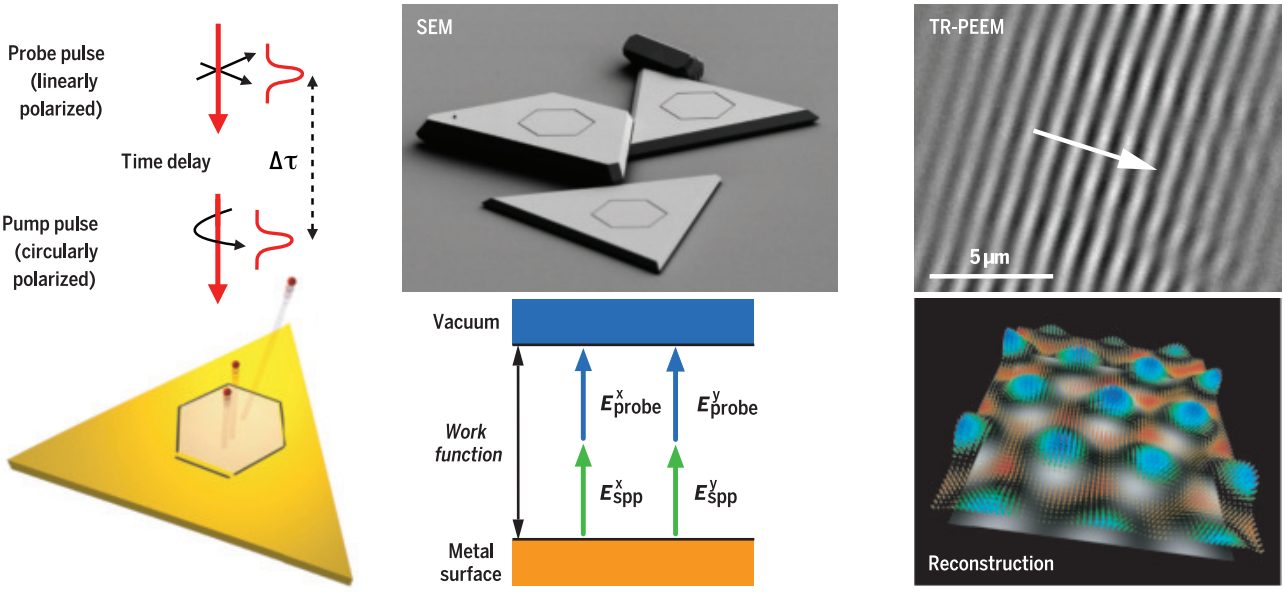

Ultrafast time-resolved vector microscopy of plasmonic skyrmions. Femtosecond laser pump-probe techniques using polarized beams combined with two-photon electron emission in an electron microscope enables the retrieval of all vector components of the electric field of propagating SPPs as a function of time. We used this technique to image the vectorial time dynamics of the plasmonic skyrmion field. Hexagons are milled into single-crystalline gold flakes via ion beam lithography. A circularly polarized femtosecond laser pulse excites surface plasmon waves on the gold flakes that interfere to create an SPP skyrmion lattice. The SPPs are detected by interference with a second laser pulse that is first polarized in the *x* direction to retrieve the E_x component of the SPP wave and then is polarized in the *y* direction to produce the E_y component. These fields are combined to obtain the characteristic in-plane pattern of the skyrmion lattice: $E_{||}$. Use of the measured field components in Maxwell's equations enables the vertical field component E_z to be calculated. From these data, we reconstruct the vector field of the SPP skyrmion and, by varying the laser pump-probe delay time ($\Delta\tau$), gain time-resolved information (top right), allowing us to create vector movies that show plasmonic spin-momentum locking and plasmonic skyrmions (bottom right). SEM, scanning electron microscopy; TR-PEEM, time-resolved photoemission electron microscopy.

RESEARCH ARTICLES

DRUG DISCOVERY

Selective targeting of BD1 and BD2 of the BET proteins in cancer and immunoinflammation

Omer Gilan[1,2]*, Inmaculada Rioja[3]*, Kathy Knezevic[1], Matthew J. Bell[3], Miriam M. Yeung[1], Nicola R. Harker[3], Enid Y. N. Lam[1,2], Chun-wa Chung[3], Paul Bamborough[3], Massimo Petretich[4], Marjeta Urh[5], Stephen J. Atkinson[3], Anna K. Bassil[3], Emma J. Roberts[3], Dane Vassiliadis[1,2], Marian L. Burr[1,2], Alex G. S. Preston[3], Christopher Wellaway[3], Thilo Werner[4], James R. Gray[3], Anne-Marie Michon[4], Thomas Gobbetti[3], Vinod Kumar[6], Peter E. Soden[3], Andrea Haynes[3], Johanna Vappiani[4], David F. Tough[3], Simon Taylor[3], Sarah-Jane Dawson[1,2,7], Marcus Bantscheff[4], Matthew Lindon[3], Gerard Drewes[4], Emmanuel H. Demont[3], Danette L. Daniels[5], Paola Grandi[4], Rab K. Prinjha[3]†‡, Mark A. Dawson[1,2,7]†‡

The two tandem bromodomains of the BET (bromodomain and extraterminal domain) proteins enable chromatin binding to facilitate transcription. Drugs that inhibit both bromodomains equally have shown efficacy in certain malignant and inflammatory conditions. To explore the individual functional contributions of the first (BD1) and second (BD2) bromodomains in biology and therapy, we developed selective BD1 and BD2 inhibitors. We found that steady-state gene expression primarily requires BD1, whereas the rapid increase of gene expression induced by inflammatory stimuli requires both BD1 and BD2 of all BET proteins. BD1 inhibitors phenocopied the effects of pan-BET inhibitors in cancer models, whereas BD2 inhibitors were predominantly effective in models of inflammatory and autoimmune disease. These insights into the differential requirement of BD1 and BD2 for the maintenance and induction of gene expression may guide future BET-targeted therapies.

The BET (bromodomain and extraterminal domain) family is composed of germ cell–specific (BRDT) and ubiquitously expressed (BRD2, BRD3, and BRD4) epigenetic reader proteins. All family members contain N-terminal tandem bromodomains, a structural feature that enables the recognition and binding to acetylated lysine residues on histones and other cellular proteins that support their function as key transcriptional regulators (*1*). After the development of first-in-class BET bromodomain inhibitors (*2*–*4*), the BET proteins have become one of the most closely studied protein families in biology. These studies have highlighted the essential role of the BET proteins in coordinating the transcription programs necessary for normal development, maintenance of oncogenic gene expression, and physiological response to injury and infection (*5*, *6*). Although preclinical studies have demonstrated the benefit of BET inhibition in a variety of nonmalignant pathologies (*3*, *7*–*10*), these inhibitors have been most widely studied in the context of cancer (*4*, *11*–*14*). On the basis of several promising preclinical studies in hematological and solid malignancies, these drugs are being evaluated in clinical trials across the world. Early results indicate that specific small-molecule inhibitors of the BET bromodomains are safe and capable of inducing complete clinical remissions; however, side effects and a short duration of clinical response have limited their broad therapeutic application (*15*, *16*).

The first generation of BET inhibitors show equal affinity for the first (BD1) and second (BD2) bromodomains of all the BET proteins and despite enormous investment and interest in the field, little is known about the functional commonalities of, and differences between, the two tandem bromodomains. Similarly, although most studies have focused on the role of BRD4 in transcriptional regulation, the individual and redundant roles of BRD2 and BRD3 have yet to be fully determined. To enable this functional dissection, we developed and characterized potent and highly selective bromodomain inhibitors of BD1 and BD2 of the BET proteins.

Development of selective BD1 and BD2 inhibitors

The helical bromodomain modules found within at least 46 human proteins (*1*) (fig. S1, A and B) share a conserved acetyl-lysine (KAc)–binding pocket. The divergent ZA and BC loops around the entrance have enabled the development of inhibitors specific to individual bromodomain families. All eight bromodomains families (fig. S1, C and D) share structural features, including a narrow ZA channel and a conserved hydrophobic Trp-Pro-Phe (WPF) shelf. First-generation inhibitors exploit these to achieve selectivity for the BET proteins over other bromodomains but show little discrimination within the BET family. The BD1 and BD2 domains form two separate subfamilies, and compounds able to bind preferentially to BD1s or BD2s have been reported (fig. S2), including two undergoing clinical investigation (RVX-208 and ABBV-744) (*17*, *18*). The disparate formats of the published data make direct comparison difficult, but our time-resolved fluorescence resonance energy transfer (TR-FRET) assays indicated that most compounds, except the recently disclosed ABBV-744, lack the potency or selectivity required to discriminate between BD1 and BD2 inhibition (fig. S3A).

To achieve a high degree of selectivity, we used structure-based design to generate compounds that interact specifically with either BD1 or BD2 of the BET proteins (Fig. 1A). Herein, GSK778 and GSK046 are referred to as iBET-BD1 and iBET-BD2, respectively. Their affinities for the individual bromodomains of the BET family were initially determined by TR-FRET (Fig. 1B, fig. S1F, and table S1). In contrast to other reported domain-selective molecules, these compounds showed little binding to bromodomains outside of the BET family (fig. S1E and table S2). Surface plasmon resonance (SPR) binding to BRD4 BD1 and BD2 confirmed their selectivity, showing that iBET-BD1 is ≥130-fold selective for BD1 and that iBET-BD2 is >300-fold selective for BD2 (fig. S4). The maintenance of this selectivity within a cellular context was verified with various orthogonal cellular assays using iBET-BD1 and iBET-BD2 (figs. S6 and S7). Together, these data demonstrate the high domain selectivity of iBET-BD1 and iBET-BD2 and their specificity over other bromodomain proteins.

Crystal structures of iBET-BD1 and iBET-BD2 with BET BD1 and/or BD2 domains revealed the molecular basis of selectivity and validated our design intent (Fig. 1, C to E; fig. S5; and table S3). Guided by the BRD2 BD1 crystal structure with I-BET151 (*19*), iBET-BD1 was designed to interact with BRD4 Asp^{144}, an aspartic acid in the BC loop of all BET BD1s, which is replaced by His in the BD2s. The x-ray structure of iBET-BD1 in BRD4 BD1 confirms that its binding mode is similar to that of I-BET151 and that the appended pyrrolidine substituent, which confers BD1 selectivity, is stabilized by a water network involving Asp^{144}

[1]Peter MacCallum Cancer Centre, Melbourne, VIC, Australia. [2]Sir Peter MacCallum Department of Oncology, University of Melbourne, Melbourne, VIC, Australia. [3]Epigenetics RU, GlaxoSmithKline Medicines Research Centre, Stevenage, UK. [4]Cellzome GmbH, Functional Genomics R&D, GlaxoSmithKline, Heidelberg, Germany. [5]Promega Corporation, Madison, WI, USA. [6]Computational Biology, GlaxoSmithKline, Collegeville, PA, USA. [7]Centre for Cancer Research, University of Melbourne, Melbourne, VIC, Australia.
*These authors contributed equally to this work.
†These authors contributed equally to this work.
‡Corresponding author. Email: mark.dawson@petermac.org (M.A.D.); rabinder.prinjha@gsk.com (R.K.P.)

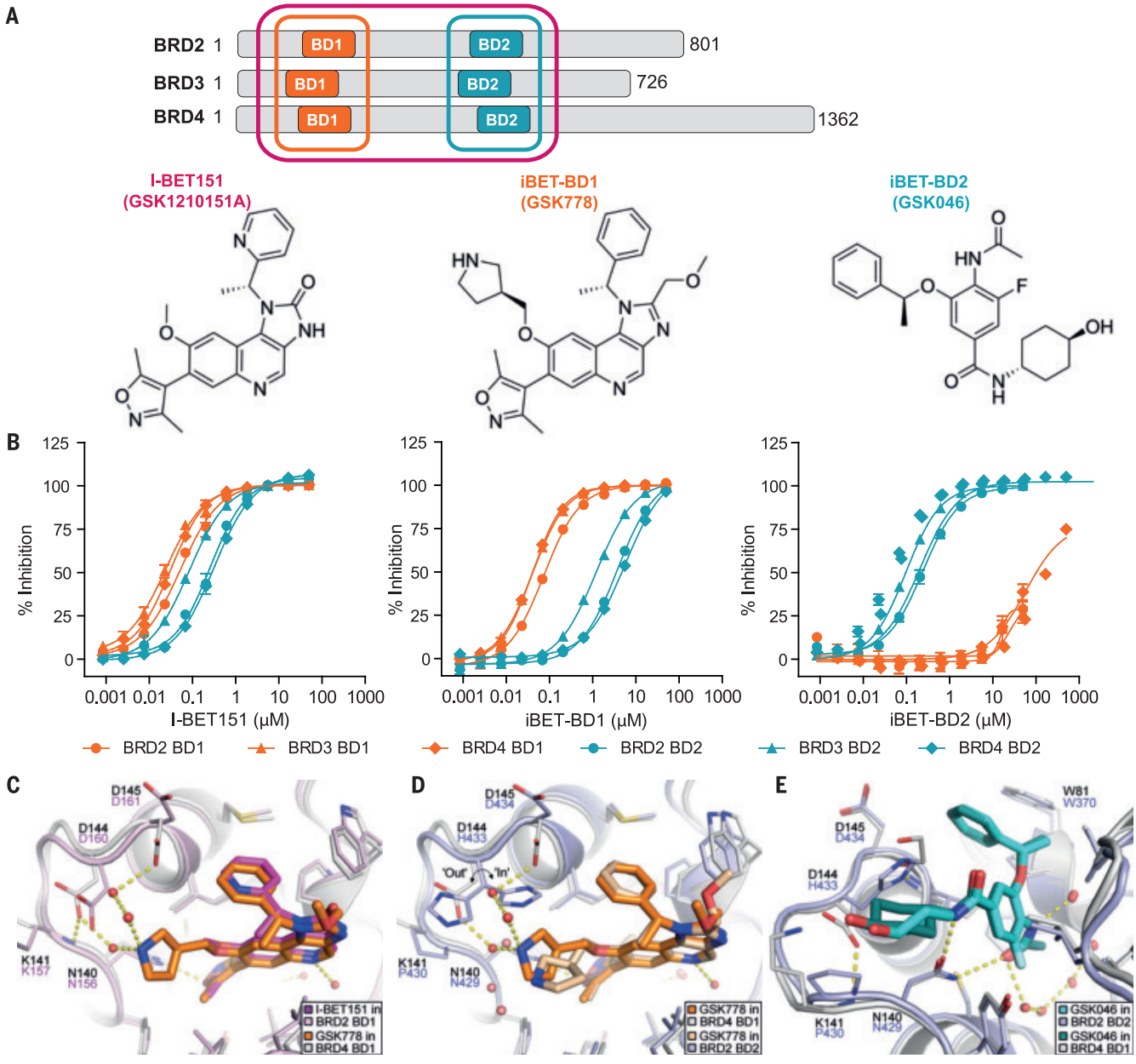

Fig. 1. Selectivity profile of I-BET151, iBET-BD1 (GSK778), and iBET-BD2 (GSK046). (**A**) Schematic of the BET bromodomain proteins and chemical structures. (**B**) Compound binding to the individual bromodomains of BD1 (orange) and BD2 (cyan) of BET tandem bromodomains in TR-FRET assays. (**C**) X-ray crystal structure of I-BET151 in BRD2 BD1 [magenta, PDB 4A1G (*19*)] superimposed on the structure of iBET-BD1 in BRD4 BD1 (orange, PDB 6SWN). (**D**) iBET-BD1 bound to BRD4 BD1 (dark orange/white, PDB 6SWN) and BRD2 BD2 (light orange/blue, PDB 6SWO), highlighting differences in the BC loop. (**E**) iBET-BD2 bound to BRD2 BD2 (light blue, PDB 6SWP) and BRD4 BD1 (cyan, PDB 6SWQ). In BRD2 BD2, the inhibitor's benzyl and cyclohexane rings pack against Pro^{430} and His^{433}, which adopts a single "in" conformation. In BRD4 BD1, iBET-BD2 makes no significant contacts with the corresponding Asp^{144} and Lys^{141} side chains, and the space occupied by the His^{433} side chain in BRD2 BD2 is filled by an ethane-1,2-diol molecule from the crystallization buffer.

and Asp^{145} (Fig. 1C). The Asp^{144} sidechain is constrained by hydrogen bonding to Lys^{141}. In the BRD2 BD2 domain, replacement of Asp^{144} by His^{433} and Lys^{141} by Pro^{430} alters the local environment, preventing formation of this water network (Fig. 1D). Asp^{144} and Lys^{141} are present in all of the BET BD1 domains and are substituted by His and Pro in all BD2 domains, explaining the selectivity of iBET-BD1 for BD1s across the entire BET family.

iBET-BD2 was optimized from a high-throughput, BD2-selective screening hit. The BRD4 BD1 and BRD2 BD2 crystal structures rationalize its BD2 selectivity (Fig. 1E). In BRD2 BD2, the benzylic WPF shelf group and cyclohexylamide of iBET-BD2 make extensive hydrophobic contacts with Pro^{430} and His^{433}. As outlined above, Pro^{430} and His^{433} are conserved in BD2 domains and replaced by Lys and Asp in BD1 domains. In BRD4 BD1, iBET-BD2 makes no contact with Lys^{141} or Asp^{144}, accounting for its BD2 selectivity across the family. Additionally, a BRD2 BD2 crystal

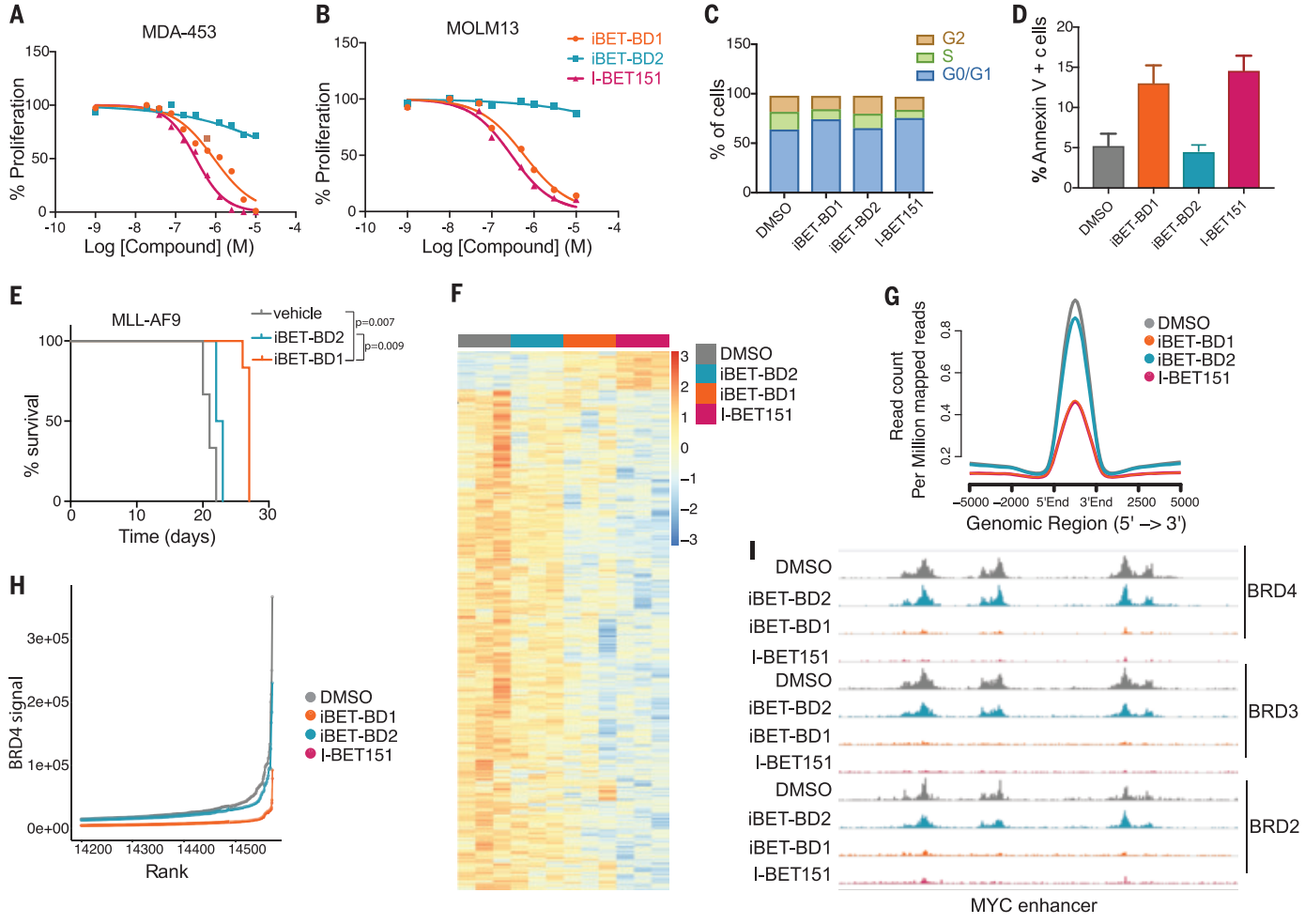

Fig. 2. BET-BD1 inhibition phenocopies pan-BET inhibition. Median inhibitory concentration (IC_{50}) assays were performed at 72 hours in MDA-453 (**A**) and MOLM-13 (**B**) cells after incubation with a range of doses of iBET-BD1, iBET-BD2, or I-BET151. Data points represent means (n = 3 cell culture replicates) plotted as a representative from 3 independent experiments. (**C**) Cell cycle analysis of MV4;11 cells treated with dimethyl sulfoxide (DMSO), I-BET151 (1000 nM), iBET-BD1 (1000 nM), or iBET-BD2 (1000 nM). (**D**) Apoptosis assay performed on MOLM13 cells treated with DMSO, I-BET151 (1000 nM), iBET-BD1 (1000 nM), or iBET-BD2 (1000 nM). (**E**) Kaplan–Meier curve of vehicle- and drug-treated C57BL/6 mice transplanted with 1×10^6 MLL-AF9 leukemic cells. Treatment commenced at day 9 with twice-daily intraperitoneal injections at 15 mg/kg of I-BET151, iBET-BD1, iBET-BD2, or vehicle (n = 6 mice per group). P values were calculated with the two-tailed log-rank test. (**F**) Heatmap of differential gene expression from SLAM-seq in THP-1 cells. Shown are the average profile of BRD4 ChIP-seq signal at typical enhancers [TEs; (**G**)] and at superenhancers (**H**) after treatment with vehicle (DMSO), I-BET151, iBET-BD1, or iBET-BD2. (**I**) Genome browser view of the MYC superenhancer in THP-1 cells showing the occupancy of BRD2, BRD3, and BRD4 after treatment with vehicle (DMSO), iBET-BD1, iBET-BD2, or I-BET151.

structure with ABBV-744, a preferential BD2 inhibitor, shows that its ethylamide group contacts His[433] and superimposes well on the iBET-BD2 cyclohexylamide moiety, suggesting that similar mechanisms account for the BD2 selectivity of both compounds (fig. S3B) (*17*).

BD1 inhibition phenocopies the effects of pan-BET inhibitors in cancer

The evolutionarily conserved tandem bromodomain structure of the BET proteins is critical for their binding to acetylated interphase and mitotic chromatin (*20*). Structural studies have demonstrated that both BD1 and BD2 preferentially engage diacetylated peptides with an optimal spacing of two amino acids (Kac-XX-Kac). Whereas BD1 favors binding to diacetylated residues on histone H4, particularly H4K5ac/K8ac, BD2 is more permissive and can accommodate a diverse range of diacetylated peptides (*1*, *20*–*22*). Subsequent biochemical studies suggested that BD1 of the BET proteins is primarily responsible for chromatin binding (*23*, *24*), and recent functional studies showed that BD1 is primarily responsible for maintaining the malignant phenotype of acute myeloid leukemia (AML) cells (*25*). Consistent with these previous studies, we found that iBET-BD1 was efficient at displacing chromatin-bound BRD4, whereas iBET-BD2 was largely ineffective (figs. S6D and S7). These findings raised the prospect that selective BD1 inhibitors may be equally effective as pan-BET inhibitors in cancer cells.

Treatment of a range of human cancer cell lines showed that iBET-BD1 has a more pronounced effect on the growth and viability of these cells (Fig. 2, A and B, and fig. S8, A to H). The effects of iBET-BD1 phenocopied the effects of the pan-BET inhibitor I-BET151 in inhibiting proliferation, inducing cell cycle arrest and apoptosis in these cells (Fig. 2, C and D, and fig. S8, I to K). Moreover, iBET-BD1

reduced the clonogenic capacity of primary human AML cells (fig. S8L). Interestingly, iBET-BD2 was less effective in all of these phenotypic assays. These findings contrast with the previously reported BD2-selective compounds RVX-208 (*18*) and ABBV-744 (*17*), and are likely due to the fact that the ability of these compounds to also engage BD1 and other bromodomain proteins in a cellular context has been markedly underappreciated (figs. S6A, S9, and S10). We next profiled the in vivo properties of the domain-selective inhibitors in mice. Despite the poorer pharmacokinetic properties of iBET-BD1 compared with iBET-BD2 (table S4), iBET-BD1 offered a superior survival advantage to iBET-BD2 in an aggressive MLL-AF9 AML model (Fig. 2E).

To examine the effects of iBET-BD1 and iBET-BD2 on transcription, we performed global nascent mRNA sequencing with SLAM-Seq (*26*). We found that the global transcriptome of iBET-BD1–treated cells resembled that of I-BET151–treated cells (Fig. 2F and fig. S11, A to D), whereas

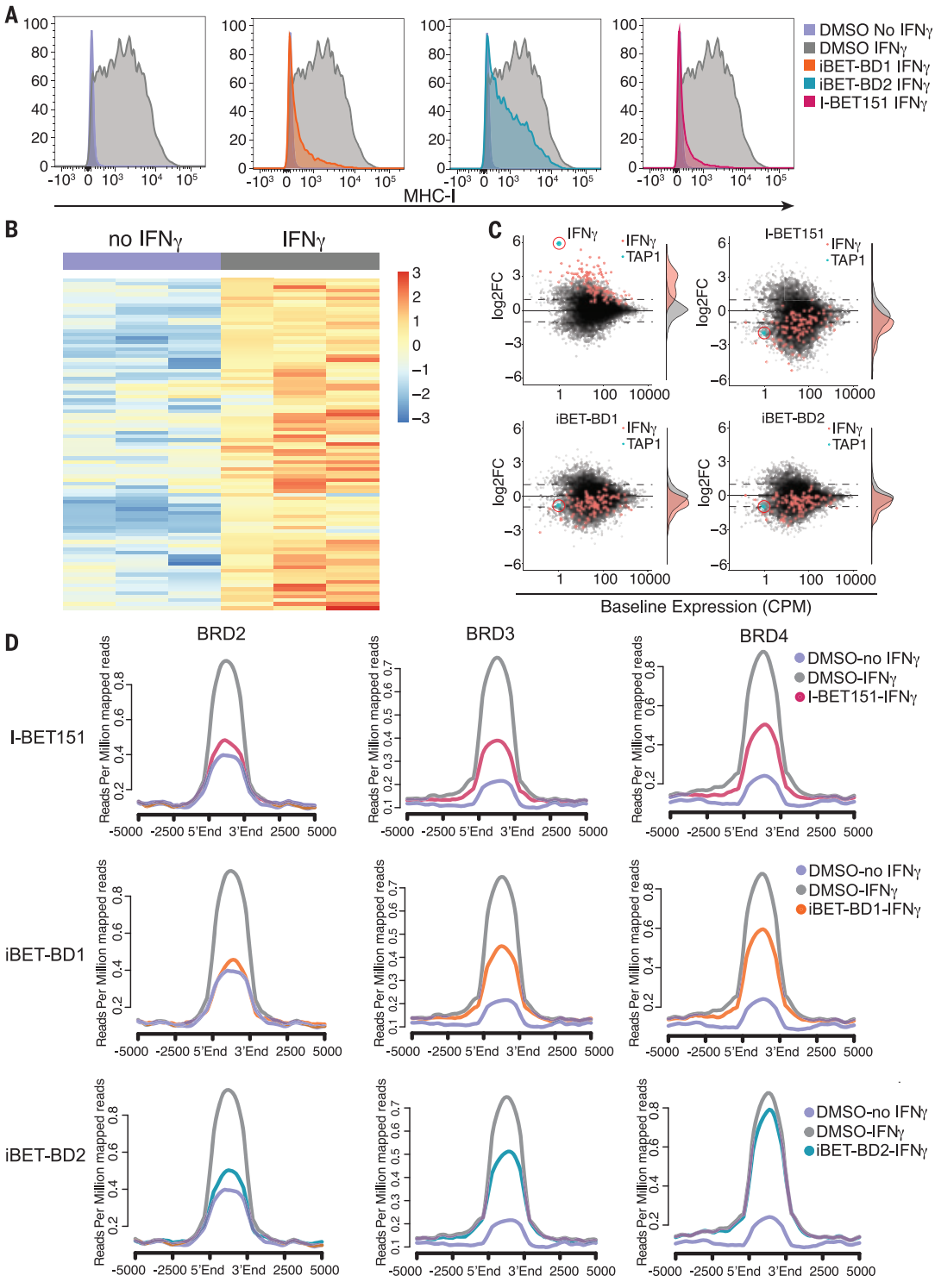

Fig. 3. BET-BD2 is required for activation of IFN-γ target genes. (**A**) Fluorescence-activated cell sorting (FACS) analysis of MHC-I expression using antibodies against HLA-A/B/C in K562 cells after stimulation with IFN-γ (10 ng/ml) and treatment with DMSO, iBET-BD1, iBET-BD2, or I-BET151 for 48 hours. (**B**) Hierarchical clustering heatmap from SLAM-seq data in K562 cells showing up-regulated genes after IFN-γ treatment for 6 hours. (**C**) Scatter plot of differential expression of all genes (gray) and genes significantly up-regulated by IFN-γ (red) in K562 cells, scatter plot, and histogram shown for DMSO, iBET-BD1, iBET-BD2, and I-BET151. (**D**) Average profile plot of BRD2, BRD3, and BRD4 at genomic loci where H3K27ac levels increased after stimulation with IFN-γ in K562 cells for 6 hours.

iBET-BD2 treatment did not induce marked transcriptional changes. Concordant with these findings, we found that iBET-BD1 displaced BRD2, BRD3, and BRD4 from chromatin as efficiently as I-BET151, whereas the binding of these proteins was largely unaltered by iBET-BD2 (Fig. 2G and fig. S11G) even at well characterized superenhancers (*27*) such as MYC (Fig. 2, H and I, and fig. S11H).

BD2 facilitates recruitment of BET proteins for the induction of gene expression

Although the role of the BET proteins in maintaining oncogenic gene expression programs continues to be an area of intense investigation, therapeutic targeting of this family of proteins has also shown efficacy in a range of nonmalignant pathologies, particularly in the context of immunoinflammation. After inflammatory stimuli such as cytokine stimulation, the BET proteins are specifically recruited to target gene loci to help facilitate the rapid induction of gene expression. To model this scenario, we stimulated K562 cells with the proinflammatory cytokine interferon-γ (IFN-γ). K562 cells lack cell surface expression of major histocompatibility complex I (MHC-I); however, these genes are transcriptionally induced by IFN-γ stimulation, leading to the cell surface expression of MHC-I and a functional readout for this pathway (*28*). Using this established model of cytokine-induced gene expression, we explored the functional effects of the domain-selective inhibitors. We found that I-BET151 inhibited the IFN-γ–induced expression of MHC-I, and both iBET-BD1 and iBET-BD2 were also effective in recapitulating this response (Fig. 3A).

To follow the molecular events associated with this phenotype, we assessed the global nascent transcriptome of the cells after stimulation with IFN-γ in the presence or absence of various BET inhibitors (Fig. 3B). We found that I-BET151, iBET-BD1, and iBET-BD2 inhibited the induction of IFN-γ–responsive transcripts, which include several components of the MHC-I antigen presentation pathway (Fig. 3C). The effects of iBET-BD2 at these genes were specific to IFN-γ stimulation, as the inhibitor did not alter the baseline expression of these transcripts (fig. S12, A to C). These data suggested that although BD2 is not essential for the chromatin binding of the BET proteins to maintain preexisting transcriptional programs, it plays a more important role in the recruitment of the BET proteins for the induction of gene expression.

In support of this possibility, chromatin immunoprecipitation sequencing (ChIP-seq) analyses showed that in the presence of I-BET151, iBET-BD1, and iBET-BD2, the BET proteins show reduced recruitment to IFN target genes after IFN-γ stimulation (Fig. 3D and fig. S12D). iBET-BD2 appeared to more prominently affect

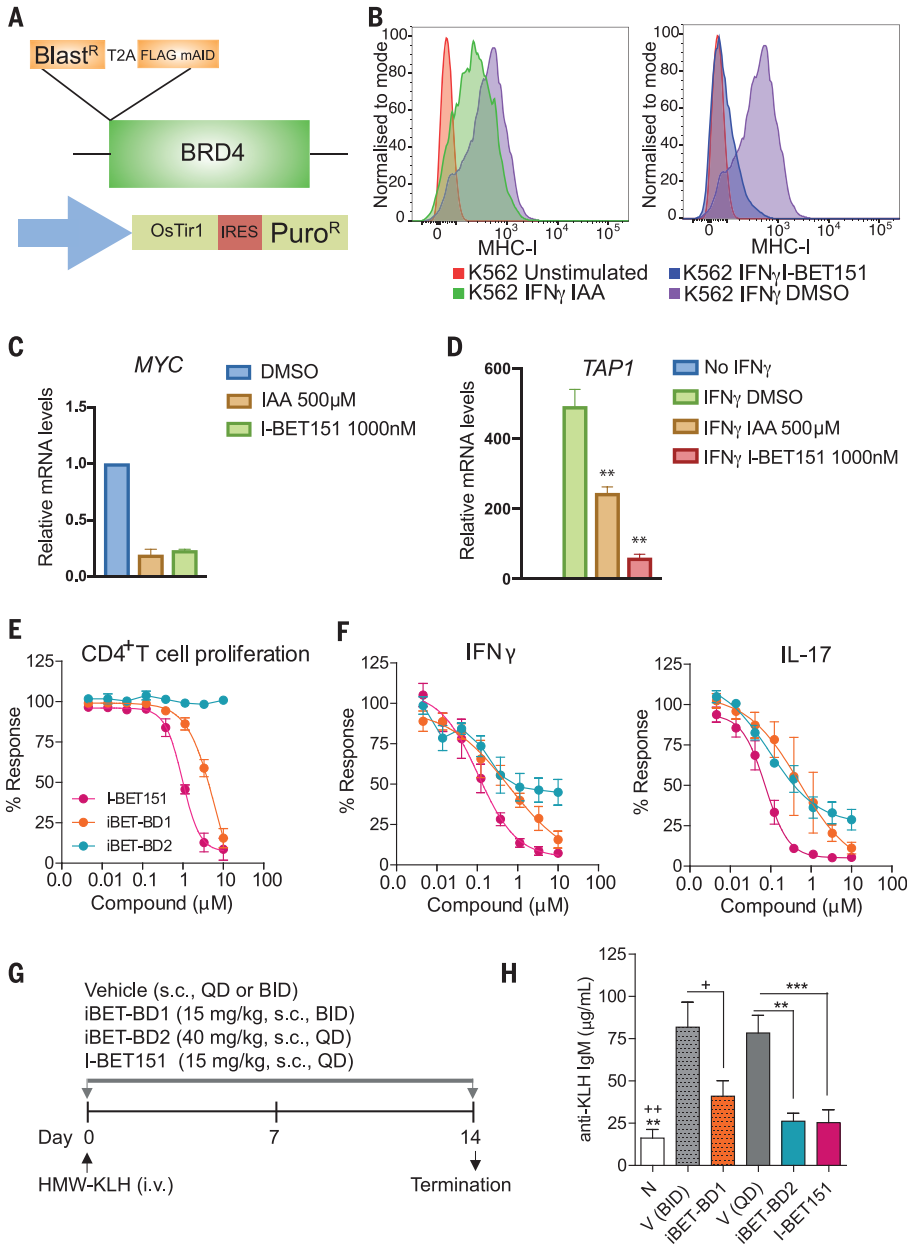

Fig. 4. iBET-BD2 has immunomodulatory activity. (**A**) Schematic of auxin-inducible degradation strategy for BRD4. Shown is Blast^R (blasticidin resistance) linked in-frame with T2A self-cleaving peptide to FLAG-mAID-BRD4. A separate viral vector was used to express the CMV promoter driving expression of OsTIR1-IRES-Puro resistance. (**B**) FACS analysis of HLA/B/C expression in K562 cells pretreated with DMSO, auxin (IAA), or I-BET151 for 6 hours, followed by stimulation with IFN-γ (10 ng/ml) for 48 hours and incubation with the compounds for 48 hours. (**C**) Quantitative reverse transcription polymerase chain reaction (qRT-PCR) analysis of MYC expression in K562 cells after treatment with I-BET151 or IAA for 6 hours. Data are shown as mean ± SD (n = 3). (**D**) qRT-PCR analysis of TAP1 expression in K562 cells before and after IFN-γ treatment (6 hours) and/or either IAA, IBET151, or DMSO (vehicle control) for 7 hours (1 hour of pretreatment). Data are shown as mean ± SD (n = 3); $^{**}P > 0.01$. (**E** and **F**) Compound effects on cellular proliferation (E) and cytokine production (F) in anti-CD3/CD28–stimulated human primary CD4$^+$ T cells. Data represent the mean ± SEM (n = 4). (**G** and **H**) Efficacy of compounds reducing KLH-induced antibody responses (IgM) in mice. N, naïve (n = 4); V, vehicle. iBET-BD1 (15 mg/kg) was given subcutaneously twice per day (BID). iBET-BD2 (40 mg/kg) and I-BET151 (15 mg/kg) were given subcutaneously four times a day (QD). Data are shown as mean ± SEM (n = 10). One-way ANOVA followed by Bonferroni's multiple-comparisons test were used to determine statistical significance compared with the respective vehicle controls ($^{***}P < 0.001$, $^{**}P < 0.005$ versus vehicle QD; $^{++}P < 0.005$, $^{+}P < 0.01$ versus vehicle BID).

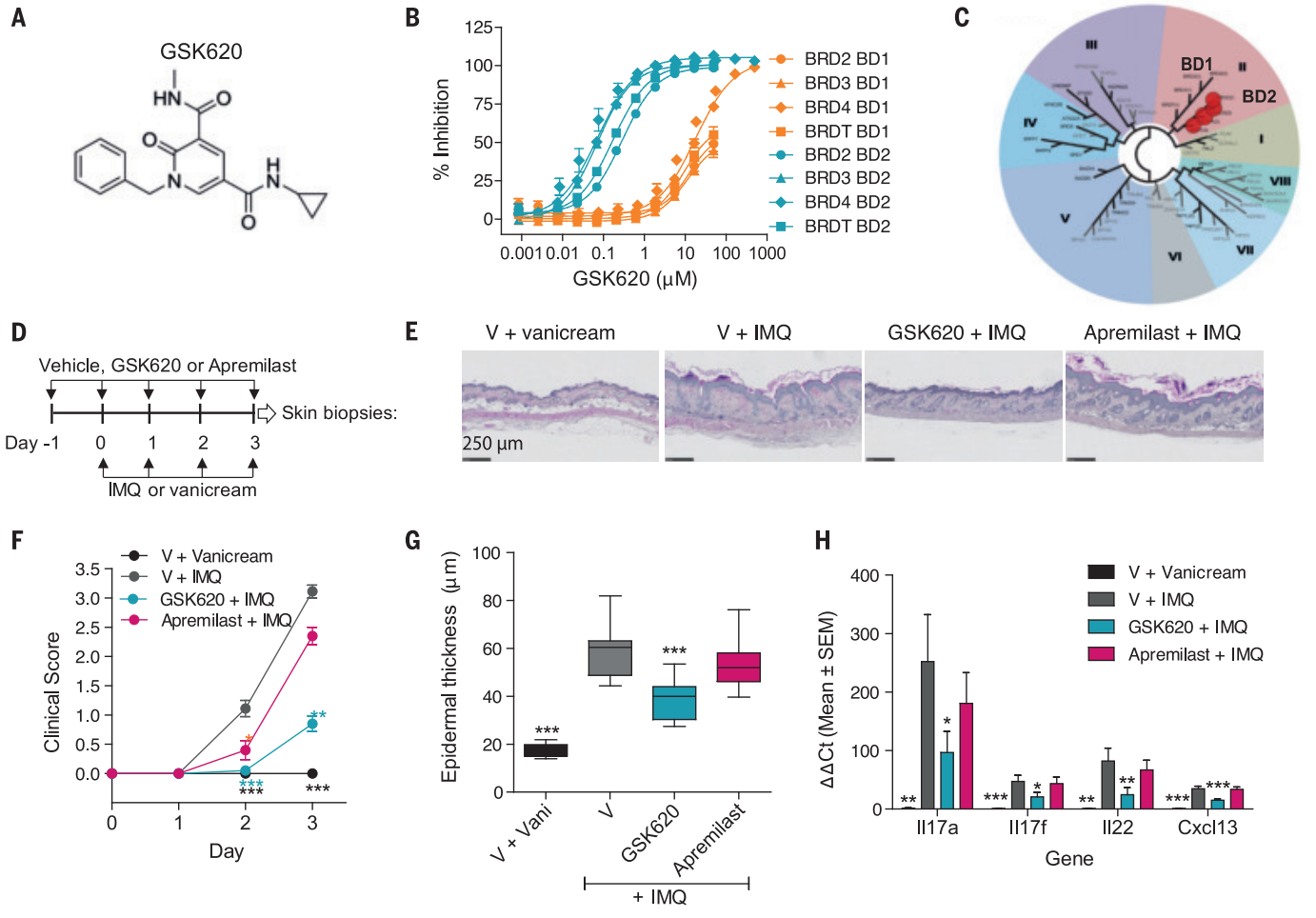

Fig. 5. GSK620 is efficacious in preclinical models of immunoinflammation. (**A**) Chemical structure of the BD2-selective BET inhibitor in vivo tool GSK620. (**B**) Compound binding to the individual tandem bromodomains [BD1 (orange) and BD2 (cyan)] of BRD2, BRD3, BRD4, and BRDT determined using TR-FRET. Data are shown as mean ± SEM (n = 12 to 21). (**C**) Phylogenetic tree of bromodomain family demonstrating preferential compound binding for the BD2 domains of the BET family of proteins using the BROMOscan bromodomain competition binding assay. Red dots represent dissociation constant (K_d) values. (**D**) Mouse IMQ-induced psoriasis study design. (**E**) Histology hematoxylin and phloxin staining of skin sections. GSK620 [20 mg/kg, orally (po), QD] reduced the psoriasis score (**F**), the epidermal thickness (**G**), and the expression levels of inflammatory genes (**H**) in skin biopsies. V, vehicle; Vani, vanicream. Apremilast was given orally at 20 mg/kg BID. Data are shown as mean ± SEM (n = 10) and were analyzed with one-way ANOVA followed by Dunnett's multiple-comparisons test (***P < 0.0001 versus V + IMQ).

the recruitment of BRD2 and BRD3 compared with BRD4 (Fig. 3D and fig. S12D). To further understand whether the findings associated with cytokine stimulation were also applicable to other cellular contexts and different stimuli that also result in gene induction, we next assessed the global transcriptome and chromatin binding of the BET proteins in THP-1 cells stimulated with phorbol 12-myristate 13-acetate (PMA), a widely used model of macrophage differentiation (*29*). Here again, we focused on the genes induced by PMA treatment (fig. S13), and although the baseline expression of these genes was not affected by iBET-BD2, treatment with iBET-BD2 prevented PMA-induced gene expression (fig. S13B). Consistent with our data in the context of cytokine stimulation, we found that iBET-BD2, like iBET-BD1 and I-BET151, prevented the PMA-induced recruitment of all of the BET proteins, and the effects of iBET-BD2 were again more pronounced against BRD2 and BRD3 (fig. S13, C to E). Moreover, these findings were replicated in a third model using anti-CD3/CD28–mediated stimulation of primary human $CD4^+$ T cells (fig. S14)

BRD4 alone is insufficient for stimulated gene expression

Although most of the literature assessing the transcriptional function of the BET proteins has focused on the coactivatory effects of BRD4, these studies have mainly examined the requirement of BRD4 to maintain preexisting transcriptional programs. Whether BRD4 alone is sufficient for rapid induction has not been thoroughly evaluated. Our data raised the prospect that in the context of stimulus-induced gene expression, all of the ubiquitously expressed BET proteins, and not just BRD4, may be required for efficient gene induction. To address this observation, we replicated the effects of a small-molecule inhibitor that rapidly and specifically impairs the function of BRD4 without affecting either BRD2 or BRD3 by using an auxin [indole acetic acid (IAA)]–inducible degron-tagging strategy to degrade endogenous BRD4 (Fig. 4A and fig. S15A). This method has been used to highlight the importance of BRD4 in maintaining established malignant gene expression programs (*26*). Similarly, we also found that specific loss of BRD4 led to an impaired proliferation and survival of cancer cell lines

that was comparable in efficacy to I-BET151 and iBET-BD1 (fig. S15B). Moreover, the changes in the established gene expression program after selective BRD4 loss are largely phenocopied by I-BET151 (fig. S15E).

Although these data confirm that BRD4 is required to maintain established oncogenic transcriptional programs, we found that selective BRD4 loss was not as effective as a pan-BET inhibitor at impairing the induction of MHC-I after IFN-γ stimulation (Fig. 4B). Although selective BRD4 loss, but not iBET-BD2 treatment, resulted in profound repression of MYC that was equivalent to the effects seen with I-BET151 or iBET-BD1 (Fig. 4C and fig. S15, C and D), it was not as effective as I-BET151 in negating IFN-γ–induced gene expression (Fig. 4D). Together, these findings suggest that whereas BRD4 may be the primary BET protein required to maintain steady-state gene expression, cooperation among all of the BET proteins is required to efficiently induce gene expression. Moreover, although BD1 of the BET proteins is sufficient to tether the BET family to chromatin and maintain gene expression, both BD1 and BD2 of all BET family members are required for the recruitment and binding to chromatin for the rapid induction of gene expression.

iBET-BD1 and iBET-BD2 have immunomodulatory activity

To further investigate the functional properties of iBET-BD1 and iBET-BD2, we used the BioMAP Diversity PLUS Panel to assess the phenotypic responses of cytokine, growth factor, and hormonal stimulation in a broad range of primary human cell–based coculture systems. These data showed that both I-BET151 and iBET-BD1 treatment resulted in a broad phenotypic profile across the entire BioMAP panel, whereas iBET-BD2 displayed a more selective phenotypic fingerprint, particularly inhibiting the production of key proinflammatory mediators, including Th17 cytokines in the B and T cell coculture system (fig. S16, A and B). These effects were subsequently confirmed in anti-CD3/CD28–stimulated human primary $CD4^+$ T cell cultures. Unlike the results after I-BET151 and iBET-BD1 treatment, in these cultures, iBET-BD2 did not affect the proliferative activity of the cells but still inhibited the production of effector cytokines, including IFN-γ, interleukin-17A (IL-17A), and IL-22 (Fig. 4, E and F, and figs. S15F and S16C). Moreover, consistent with our molecular data in THP1 cells, we again found that iBET-BD2 impaired macrophage activation after PMA stimulation, similar to the results with iBET-BD1 and I-BET151, without affecting cellular viability (fig. S15, G and H).

These functional assays in vitro raised the intriguing possibility that although iBET-BD2 was largely ineffective at impairing the proliferation and survival of cancer cells (Fig. 2 and fig. S8), it may have greater in vivo activity in an immunomodulatory context. To explore this further, we assessed the efficacy of iBET-BD1 and iBET-BD2 in a T cell–dependent immunization model (*30*). Mice were immunized with the exogenous antigen keyhole limpet hemocyanin (KLH), resulting in efficient T cell activation and the production of cytokines (IFN-γ) and T cell–dependent primary antibodies (IgM). All compounds were well tolerated (fig. S16D), and, in agreement with our molecular data and the functional in vitro assays, we found that iBET-BD2 was as effective as iBET-BD1 and I-BET151 in reducing the production of anti-KLH IgM (Fig. 4, G and H). Taken together, these data show that BD2-selective inhibition specifically affects the induction of gene expression while leaving the maintenance of established transcription programs largely unaltered. This distinction may have important clinical implications because the repression of established gene expression may be essential for the maintenance of cell identity and viability. For instance, as described previously, even low doses of pan-BET inhibitors result in the undesired effect of testicular atrophy (*31*, *32*); however, these effects are much less pronounced even with high doses of iBET-BD2 (fig. S16E).

BD2-selective inhibition ameliorates inflammatory disease in preclinical models

The ability to selectively alter induced gene expression while leaving established gene expression programs intact with iBET-BD2 raised the exciting possibility of specifically targeting pathologies initiated by an inflammatory gene expression program. To address this further, we optimized the pharmacokinetic properties of iBET-BD2 to develop GSK620 (Fig. 5, A to C, and tables S4 and S5). This compound retains the marked specificity for binding BD2 in all of the BET family of proteins (Fig. 5C and tables S1 and S2) but has significantly improved oral bioavailability compared with iBET-BD2 (table S5). We initially tested GSK620 in a collagen-induced arthritis model in rats, a commonly used model of pathologies such as rheumatoid arthritis, in which an immunological response manifests as inflammatory arthritis associated with progressive cartilaginous destruction, joint swelling, and ultimately ankylosis. In this model, GSK620 led to a significant dose-dependent inhibition of both the arthritic score and IgG1 production in response to the immunization (fig. S17, A to E). At the well-tolerated highest dose, GSK620 showed a similar level of efficacy to the pan-BET inhibitor I-BET151 and also dramatically reduced joint swelling, synovitis, cartilage damage, pannus formation, and bone resorption (fig. S17, C, F, and G).

The efficacy of BD2-selective inhibition in these immunoinflammatory models contrasts sharply with the modest effects seen in cancer models and raised the prospect that BD2-selective BET inhibition may be a valuable therapeutic strategy to specifically counter various immunoinflammatory diseases. Therefore, we next evaluated the efficacy of GSK620 in a mouse model of imiquimod (IMQ)–induced psoriasis (*33*). Although topical therapies are often used for mild psoriasis, more severe forms of the disease require systemic therapy with anti-inflammatory and immunomodulatory agents, including the phosphodiesterase 4 (PDE4) inhibitor apremilast, which has recently been approved by the U.S. Food and Drug Administration for moderate to severe psoriasis and other autoimmune diseases such as Behcet's disease (*34*). In our study, we found that GSK620 was superior to apremilast in reducing the clinical score (erythema and plaque formation) and the epidermal hyperplasia associated with the IMQ treatment (Fig. 5, D to G, and fig. S17H). Moreover, gene expression analyses from the skin of treated mice showed that GSK620 significantly reduced the expression of disease-relevant proinflammatory genes, including IL-17A, IL-17F, and IL-22 (Fig. 5H).

Finally, we tested GSK620 in a mouse model of nonalcoholic fatty liver disease (NAFLD), a widespread problem in Western society that is associated with obesity and insulin resistance and ultimately manifests in liver fibrosis and predisposes to the development of hepatocellular carcinoma. We have recently demonstrated the promising effects of nonselective BET inhibition in the STAM mouse model, which recapitulates many of the features of human NAFLD (*8*), and wanted to further evaluate whether these effects could be phenocopied with BD2-selective inhibition. We assessed the effects of treatment at two distinct time windows to evaluate its efficacy on early nonalcoholic steatohepatitis (NASH) ("NASH phase"; weeks 6 to 9; fig. S18, A to C) and during fibrosis onset ("fibrosis phase"; weeks 9 to 12) (fig. S18 D). We found that mice treated with GSK620 showed reduced steatosis, lobular inflammation, and hepatocyte ballooning compared with the vehicle-treated group (fig. S18C). Compared with telmisartan, which has shown activity in human NASH, we found that GSK620 had similar activity in reducing hepatic fibrosis in mice (fig. S18E). Moreover, GSK620 was highly effective in reducing the expression of proinflammatory and profibrotic genes in liver biopsies taken from treated animals (fig. S18F). Taken together, these data in separate models of inflammatory arthritis, psoriasis, and hepatitis demonstrate the preclinical value of specifically

modulating inducible gene expression by targeting BD2 of the BET family in immunoinflammatory pathologies.

Discussion

Despite marked progress in studying the role of the BET proteins as key transcriptional regulators, several fundamental questions about this family of proteins remain. For instance, it is largely unknown why most cells ubiquitously express three BET proteins. It is also not clear why both bromodomains in all BET proteins share such a high degree of structural conservation and show a similar preference for substrate binding (particularly diacetylated histone tails). Our data assessing the specific requirements of BD1 and BD2 in the context of maintenance or induction of gene expression have highlighted that BD1 is the primary module required to bind chromatin to maintain established gene expression programs, and that it phenocopies the effects of pan-BET inhibitors in cancer cells. Although first-generation pan-BET inhibitors can induce a complete clinical remission in some patients (*15*, *16*, *35*, *36*), these remissions are often short-lived, suggesting that these drugs will need to be combined with other conventional and targeted therapies to provide meaningful clinical outcomes. Because every cancer therapy has side effects, refining the target specificity of current BET inhibitors to focus on BD1 may maintain the observed efficacy but limit the side effects, particularly as part of combination regimes.

In contrast to the effects seen with BD1-selective inhibitors, BD2-selective inhibitors have minimal effects in altering preexisting gene expression programs because they are largely ineffective at displacing chromatin-bound BET proteins from established *cis*-regulatory elements, including superenhancers. Although BD2 inhibition is not critical to maintaining gene expression, we found that BD2 of all BET proteins is necessary after a stimulus that drives rapid gene induction. The requirement for a structurally related chromatin-binding module to facilitate the rapid recruitment and stability of the BET proteins to provide a swift and coordinated transcriptional response helps to explain why the two tandem bromodomains are not only structurally similar but were also highly conserved through evolution. We also found that efficient gene induction demands the functional integrity of all three ubiquitously expressed BET proteins, and BRD4 by itself was insufficient for optimal gene induction. These findings help to reconcile a number of previous observations. For instance, global genetic dependency analyses have clearly demonstrated that BRD4 is the only BET protein that is a pan-essential requirement in mammalian cells (*37*). BRD4 also appears to be the main BET protein required to maintain established gene expression programs (*26*), making it difficult to understand why its paralogs, BRD2 and BRD3, are also ubiquitously expressed. The BET proteins, particularly BRD2, have consistently been shown to play a critical role in mediating inflammatory responses (*38*), and mice that express a hypomorphic BRD2 allele are protected from inflammatory diseases (*39*). The first-generation BET inhibitors have been effective in a number of seemingly disparate pathologies, including heart failure (*40*), sepsis (*3*), and drug-induced nephrotoxicity (*41*). Although these pathologies appear to be unrelated, they are linked by the common requirement to mount an immediate adaptive transcriptional response after a defined insult or injury. Consistent with this, our data show that BD2-selective inhibition is efficacious in a broad range of inflammatory pathologies. They also raise the possibility that BD2 inhibition may be a useful and novel therapeutic strategy to counter the immunoinflammatory damage that results in end organ damage after infective, autoimmune, or toxic insult. Our results provide new insights to refine our therapeutic strategy and achieve greater efficacy with few side effects when targeting BET proteins in distinct pathologies such as cancer and immunoinflammation.

REFERENCES AND NOTES

1. P. Filippakopoulos *et al*., *Cell* **149**, 214–231 (2012).
2. P. Filippakopoulos *et al*., *Nature* **468**, 1067–1073 (2010).
3. E. Nicodeme *et al*., *Nature* **468**, 1119–1123 (2010).
4. M. A. Dawson *et al*., *Nature* **478**, 529–533 (2011).
5. M. A. Dawson, *Science* **355**, 1147–1152 (2017).
6. D. F. Tough, P. P. Tak, A. Tarakhovsky, R. K. Prinjha, *Nat. Rev. Drug Discov.* **15**, 835–853 (2016).
7. K. Klein *et al*., *Ann. Rheum. Dis.* **75**, 422–429 (2016).
8. S. A. Middleton *et al*., *Sci. Rep.* **8**, 17257 (2018).
9. A. Nadeem *et al*., *Pharmacol. Res.* **99**, 248–257 (2015).
10. Q. Duan *et al*., *Sci. Transl. Med.* **9**, eaah5084 (2017).
11. J. E. Delmore *et al*., *Cell* **146**, 904–917 (2011).
12. J. Zuber *et al*., *Nature* **478**, 524–528 (2011).
13. C. Y. Fong *et al*., *Nature* **525**, 538–542 (2015).
14. P. Rathert *et al*., *Nature* **525**, 543–547 (2015).
15. M. Dawson *et al*., *Blood* **130**, 1377 (2017).
16. C. Berthon *et al*., *Lancet Haematol.* **3**, e186–e195 (2016).
17. E. J. Faivre *et al*., *Nature* **578**, 306–310 (2020).
18. K. G. McLure *et al*., *PLOS ONE* **8**, e83190 (2013).
19. J. Seal *et al*., *Bioorg. Med. Chem. Lett.* **22**, 2968–2972 (2012).
20. A. Dey, F. Chitsaz, A. Abbasi, T. Misteli, K. Ozato, *Proc. Natl. Acad. Sci. U.S.A.* **100**, 8758–8763 (2003).
21. R. Gamsjaeger *et al*., *Mol. Cell. Biol.* **31**, 2632–2640 (2011).
22. J. Morinière *et al*., *Nature* **461**, 664–668 (2009).
23. M. G. J. Baud *et al*., *Science* **346**, 638–641 (2014).
24. T. C. Miller *et al*., *Nat. Commun.* **7**, 13855 (2016).
25. D. S. Tyler *et al*., *Science* **356**, 1397–1401 (2017).
26. M. Muhar *et al*., *Science* **360**, 800–805 (2018).
27. J. Shi *et al*., *Genes Dev.* **27**, 2648–2662 (2013).
28. M. L. Burr *et al*., *Cancer Cell* **36**, 385–401.e8 (2019).
29. M. Daigneault, J. A. Preston, H. M. Marriott, M. K. Whyte, D. H. Dockrell, *PLOS ONE* **5**, e8668 (2010).
30. A. Kelso, P. Groves, A. B. Troutt, M. H. Pech, *Int. Immunol.* **6**, 1515–1523 (1994).
31. M. M. Matzuk *et al*., *Cell* **150**, 673–684 (2012).
32. E. Shang, H. D. Nickerson, D. Wen, X. Wang, D. J. Wolgemuth, *Development* **134**, 3507–3515 (2007).
33. L. van der Fits *et al*., *J. Immunol.* **182**, 5836–5845 (2009).
34. G. Hatemi *et al*., *N. Engl. J. Med.* **372**, 1510–1518 (2015).
35. S. Amorim *et al*., *Lancet Haematol.* **3**, e196–e204 (2016).
36. J. Lewin *et al*., *J. Clin. Oncol.* **36**, 3007–3014 (2018).
37. A. Tsherniak *et al*., *Cell* **170**, 564–576.e16 (2017).
38. A. C. Belkina, B. S. Nikolajczyk, G. V. Denis, *J. Immunol.* **190**, 3670–3678 (2013).
39. F. Wang *et al*., *Biochem. J.* **425**, 71–85 (2009).
40. Q. Duan *et al*., *Sci. Transl. Med.* **9**, eaah5084 (2017).
41. L. Sun, J. Liu, Y. Yuan, X. Zhang, Z. Dong, *Am. J. Physiol. Renal Physiol.* **315**, F469–F478 (2018).

ACKNOWLEDGMENTS

We thank members of the Dawson laboratory and the molecular genomics and flow cytometry core facility at the Peter MacCallum Cancer Centre for helpful discussions and technical assistance, and C. Cullinane and S. Jackson for assistance with the animal experiments. **Funding:** We thank the following funders for fellowship and grant support: a CCV Dunlop fellowship and an HHMI international research scholarship to M.A.D.; a Victoria Cancer Agency fellowship to O.G. and E.Y.N.L.; CRUK to M.L.B.; and a CSL Centenary fellowship to S.J.D. Work from the Dawson laboratory is supported by grant funding from the NHMRC (1106444, 1144649, 1146192), the University of Melbourne, and the Peter MacCallum Foundation. **Author contributions:** O.G., I.R., R.K.P., and M.A.D. designed and analyzed experiments and wrote the manuscript with helpful contributions from all authors. M.M.Y., E.Y.N.L., and D.V. performed computational analyses with supervision from S.-J.D. and M.A.D. O.G., K.K., and M.L.B. performed experiments and analyzed data with supervision from M.A.D. M.J.B., N.R.H., A.K.B., E.J.R., P.E.S., and D.F.T. performed in vitro biology experiments and analyzed and interpreted data with supervision from I.R. and R.K.P. S.J.A., A.G.S.P., C.W., M.L., and E.H.D. designed and synthesized the compounds and generated and analyzed data. J.R.G., S.T., T.G., V.K., and A.H. designed and generated data from DMPK and in vivo efficacy studies. C.C. and P.B. generated crystallography and analyzed data. M.P., T.W., A.-M.M., J.V., and M.B. designed and generated data and analyzed omics experiments with supervision from G.D. and P.G. **Competing interests:** M.A.D. has been a member of advisory boards for CTX CRC, Storm Therapeutics, Celgene, and Cambridge Epigenetix. The Dawson laboratory receives research funding from CTX CRC. The following authors are employees and shareholders of GlaxoSmithKline (GSK): R.K.P., I.R., M.J.B., N.R.H., A.K.B., E.J.R., P.E.S., D.F.T., J.R.G., T.G., V.K., A.H., S.J.A., A.G.S.P., C.W., E.H.D., C.C., P.B., M.P., T.W., A.-M.M., J.V., M.B., G.D., and P.G. M.L. is an employee of Biopharmaceuticals R&D, AstraZeneca. S.T. is an employee of Pharmaron UK and holds shares at GSK. GSK and the authors S.J.A., A.G.S.P., M.L., and E.H.D. have a patent/patent application WO 2017037116 A1 related to the invention of certain compounds that are bromodomain inhibitors, including GSK620. M.U. and D.L.D. are employees of Promega. The remaining authors declare no competing financial interests. **Data and materials availability:** I-BET151, GSK778, GSK046, and GSK620 are available from R.K.P. (rabinder.prinjha@gsk.com) and I.R. (inma.5.rioja@gsk.com) under a material transfer agreement with GSK. Coordinates and structure factors have been deposited in the Protein Data Bank (PDB) with identification codes 6SWN, 6SWO, 6SWP, and 6SWQ. The RNA-seq and ChIP-seq data have been deposited to the NCBI Sequence Read Archive under accession number GSE138210.

SUPPLEMENTARY MATERIALS

science.sciencemag.org/content/368/6489/387/suppl/DC1
Materials and Methods
Figs. S1 to S18
Tables S1 to S5
Captions for Data S1 to S18
Supplementary Methods: Chemistry
References (*42*–*45*)

23 October 2019; accepted 6 March 2020
Published online 19 March 2020
10.1126/science.aaz8455

CORONAVIRUS

The effect of travel restrictions on the spread of the 2019 novel coronavirus (COVID-19) outbreak

Matteo Chinazzi[1], Jessica T. Davis[1], Marco Ajelli[2], Corrado Gioannini[3], Maria Litvinova[3], Stefano Merler[2], Ana Pastore y Piontti[1], Kunpeng Mu[1], Luca Rossi[3], Kaiyuan Sun[4], Cécile Viboud[4], Xinyue Xiong[1], Hongjie Yu[5], M. Elizabeth Halloran[6,7], Ira M. Longini Jr.[8]*, Alessandro Vespignani[1,3]*

Motivated by the rapid spread of coronavirus disease 2019 (COVID-19) in mainland China, we use a global metapopulation disease transmission model to project the impact of travel limitations on the national and international spread of the epidemic. The model is calibrated on the basis of internationally reported cases and shows that, at the start of the travel ban from Wuhan on 23 January 2020, most Chinese cities had already received many infected travelers. The travel quarantine of Wuhan delayed the overall epidemic progression by only 3 to 5 days in mainland China but had a more marked effect on the international scale, where case importations were reduced by nearly 80% until mid-February. Modeling results also indicate that sustained 90% travel restrictions to and from mainland China only modestly affect the epidemic trajectory unless combined with a 50% or higher reduction of transmission in the community.

QQ group: 970508760

Beginning in December 2019, Chinese health authorities have been closely monitoring a cluster of pneumonia cases in the city of Wuhan in Hubei province, China. The pathogen that causes the viral pneumonia in affected individuals is the newly recognized coronavirus known as severe acute respiratory syndrome–coronavirus 2 (SARS-CoV-2) (*1*). As of 3 March 2020, 80,151 cases (*2*) have been detected and confirmed in mainland China. Internationally, more than 10,566 additional cases have been detected and confirmed in 72 countries (*3*). In this work, we model both the domestic and international spread of the novel coronavirus disease 2019 (COVID-19) epidemic. We estimate the effects of the travel ban implemented in Wuhan and the international travel restrictions adopted by several countries in early February 2020.

To model the international spread of the COVID-19 outbreak, we used the global epidemic and mobility model (GLEAM), an individual-based, stochastic, and spatial epidemic model (*4*–*7*). GLEAM uses a metapopulation network approach integrated with real-world data where the world is divided into subpopulations centered around major transportation hubs (usually airports). The subpopulations are connected by the flux of individuals traveling daily among them. The model includes more than 3200 subpopulations in roughly 200 different countries and territories. The airline transportation data encompass daily origin-destination traffic flows from the Official Aviation Guide (OAG) and International Air Transport Association (IATA) databases (updated in 2019), whereas ground mobility flows are derived from the analysis and modeling of data collected from the statistics offices of 30 countries on five continents (*5*). Mobility variations in mainland China were derived from Baidu location-based services (LBS). Within each subpopulation, the human-to-human transmission of COVID-19 is modeled by using a compartmental representation of the disease in which individuals can occupy one of the following states: susceptible, latent, infectious, and removed. Susceptible individuals can acquire the virus through contacts with individuals in the infectious category and can subsequently become latent (i.e., infected but not yet able to transmit the infection). Latent individuals progress to the infectious stage at a rate inversely proportional to the latent period (which we assume to have the same duration as the incubation period), and infectious individuals progress to the removed stage at a rate inversely proportional to the infectious period. The sum of the mean latent and infectious periods defines the generation time. Removed individuals are those who can no longer infect others (i.e., they are isolated, hospitalized, have recovered, or have died).

The model generates an ensemble of possible epidemic scenarios described by the number of newly generated infections, time of disease arrival in each subpopulation, and number of traveling infection carriers. We assume a starting date of the epidemic that falls between 15 November 2019 and 1 December 2019, with 40 infections caused by zoonotic exposure (*8*–*11*). The transmission dynamic is calibrated by using an approximate Bayesian computation approach (*12*) to estimate the posterior distribution of the basic reproductive number R_0 by exploring the likelihood of importation of COVID-19 infections to international locations (*13*). We assume that the overall global detection of imported infections can be as low as 40% (*14*, *15*). Data on importation of cases were obtained from available published line lists (*16*, *17*).

We performed a sensitivity analysis by considering different combinations of average latent and infectious periods, detection rates, initial conditions, and a generation time (T_g) ranging from 6 to 11 days on the basis of plausible ranges from the SARS epidemic and recent analysis of COVID-19 data (*16*, *18*–*23*). Details and sensitivity analysis on all parameters are reported in the supplementary materials (*12*). Here we report the results for T_g = 7.5 days (*20*). The obtained posterior distribution provides an average R_0 = 2.57 [90% confidence interval (CI): 2.37 to 2.78] and a doubling time of T_d = 4.2 days (90% CI: 3.8 to 4.7 days). The obtained values are in the same range as previous analyses based on early COVID-19 data (*9*, *20*, *24*–*26*). Although the calibration obtained for different generation times provides different posterior distributions for R_0, in the early stages of the epidemic the prevalence of infections and case importations is determined by the epidemic growth rate, and the obtained results (*12*) are consistent with those reported here.

Wuhan travel ban

On 22 January 2020, the projected median number of infections with no travel restrictions for mainland China, excluding Wuhan, was 7474 (90% CI: 3529 to 16,142). The overwhelming majority of infections were in Wuhan with a median number of 117,584 (90% CI: 62,468 to 199,581). To analyze the effect of the travel ban from Wuhan, we implemented long-range travel restrictions beginning on 23 January (airport shutdown). Furthermore, we modeled mobility limitations within mainland China by using de-identified and aggregated domestic population movement data between Chinese provinces for February 2020, as derived from Baidu LBS (*12*).

Initially, we assumed no changes in transmissibility and disease dynamics (the status quo scenario). The model output shows no noticeable differences in the epidemic trajectory of Wuhan but a delay of ~3 days for other locations in mainland China (Fig. 1A). The overall reduction of infections in mainland

[1]Laboratory for the Modeling of Biological and Socio-technical Systems, Northeastern University, Boston, MA, USA. [2]Bruno Kessler Foundation, Trento, Italy. [3]ISI Foundation, Turin, Italy. [4]Fogarty International Center, NIH, Bethesda, MD, USA. [5]School of Public Health, Fudan University, Key Laboratory of Public Health Safety, Ministry of Education, Shanghai, China. [6]Fred Hutchinson Cancer Research Center, Seattle, WA, USA. [7]Department of Biostatistics, University of Washington, Seattle, WA, USA. [8]Department of Biostatistics, College of Public Health and Health Professions, University of Florida, Gainesville, FL, USA.
*Corresponding author. Email: a.vespignani@northeastern.edu (A.V.); ilongini@ufl.edu (I.M.L.)

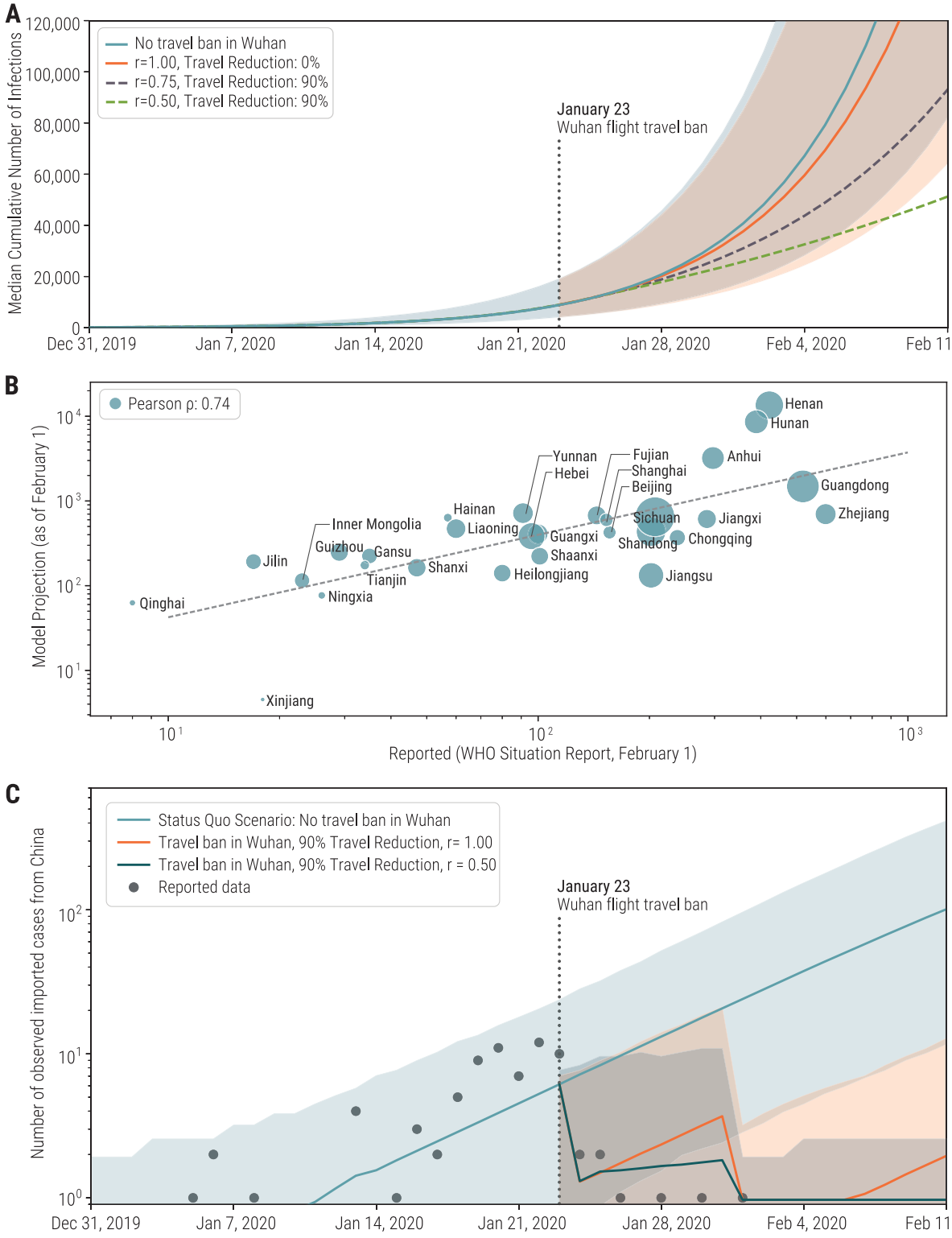

Fig. 1. Effect of the Wuhan travel ban on the COVID-19 epidemic. (**A**) Trajectory of the COVID-19 epidemic in Chinese locations (excluding Wuhan) under the ban on travel to and from Wuhan as of 23 January 2020. Trajectories are also plotted for scenarios with relative transmissibility reduction *r* and international travel restrictions. Lines represent median cumulative number of infections; shaded areas represent 90% reference ranges. (**B**) Correlation between the number of cases reported in each province by the WHO situation report and model projections on 1 February 2020 (no provinces were reporting zero cases by this date). Circle size is proportional to the population size in each province. (**C**) Projections of the average detected number of daily international case importations for different modeling scenarios. Shaded areas represent 99% reference ranges. We report the observed data of international case importations with a travel history from China, classified by arrival date. We also report scenarios with relative transmissibility reduction *r*. Data points after 23 January 2020 were used for out-of-sample validation and were not used in the model calibration.

China, excluding Wuhan, was close to 10% by 31 January 2020, with a relative reduction of infections across specific locations ranging from 1 to 58% (Fig. 2). With a doubling time of 4 to 5 days, this level of reduction corresponds to only a modest delay (1 to 6 days) of the epidemic trajectory in mainland China. These results are in agreement with estimates from the combination of epidemiological and human mobility data (*27*). The model clearly indicates that, as of 23 January 2020, the epidemic was seeded in several locations across mainland China. As an independent validation test, we assessed the cumulative number of cases in mainland China provinces through 1 February 2020 (Fig. 1B), as reported from the official World Health Organization (WHO) situation report (*28*), and compared these results with model projections. The model projections are highly correlated with the observed data (Pearson's correlation coefficient = 0.74, $P < 0.00001$), although, as expected, we found that there are significantly fewer reported cases than projected (Fig. 1B). If we assume that the number of reported cases in the WHO situation report and in the simulation are related through a simple binomial stochastic sampling process, we find that the median ascertainment rate of detecting an infected individual in mainland China is 24.4% (interquartile range: 12.7 to 35.8%). In other words, the modeling results suggest that, in mainland China, only one in four infections is detected and confirmed.

Relative risk of case importation

The model also allows us to estimate the number of case importations in international locations from mainland China. In Fig. 1C, we report the mean number of total international importation events in a fully status quo scenario as opposed to a travel ban. We find a 77% reduction in cases imported from mainland China to other countries as a result of the Wuhan travel ban in early February. Although the number of cases imported internationally decreases markedly at first, it picks up again in the following weeks with importation from locations in mainland China. The model indicates that, after the travel restrictions in Wuhan are implemented on 23 January, the five origin cities with the highest rates of international case importations are Shanghai, Beijing, Shenzhen, Guangzhou, and Kunming. Similarly, the model can rank countries across the world according to the relative risk of importing cases from mainland China. More precisely, the relative risk is defined for each country Y as the relative probability $P(Y)$ that a single infected individual travels from an area affected by the epidemic to that specific destination Y. In other words, given the occurrence of one exported case, $P(Y)$ is the relative probability that the disease carrier will appear in location Y, with respect to any other possible location. This risk depends on the travel flow from cities in mainland China to other countries and the disease prevalence in those cities. Notably, the traffic flows used in the model are origin-destination data that do not depend on traveling routes (i.e., a proxy for the actual mobility demand across cities). Figure 3 illustrates how the cities with the most COVID-19 cases in mainland China contribute to the relative risk of the 20 countries that are most susceptible to case importation, both before and after implementation of the Wuhan travel ban . In particular, before the travel ban, ≈86% of the internationally imported cases originated from Wuhan. After the travel ban, the top 10 contributors to the relative risk—of

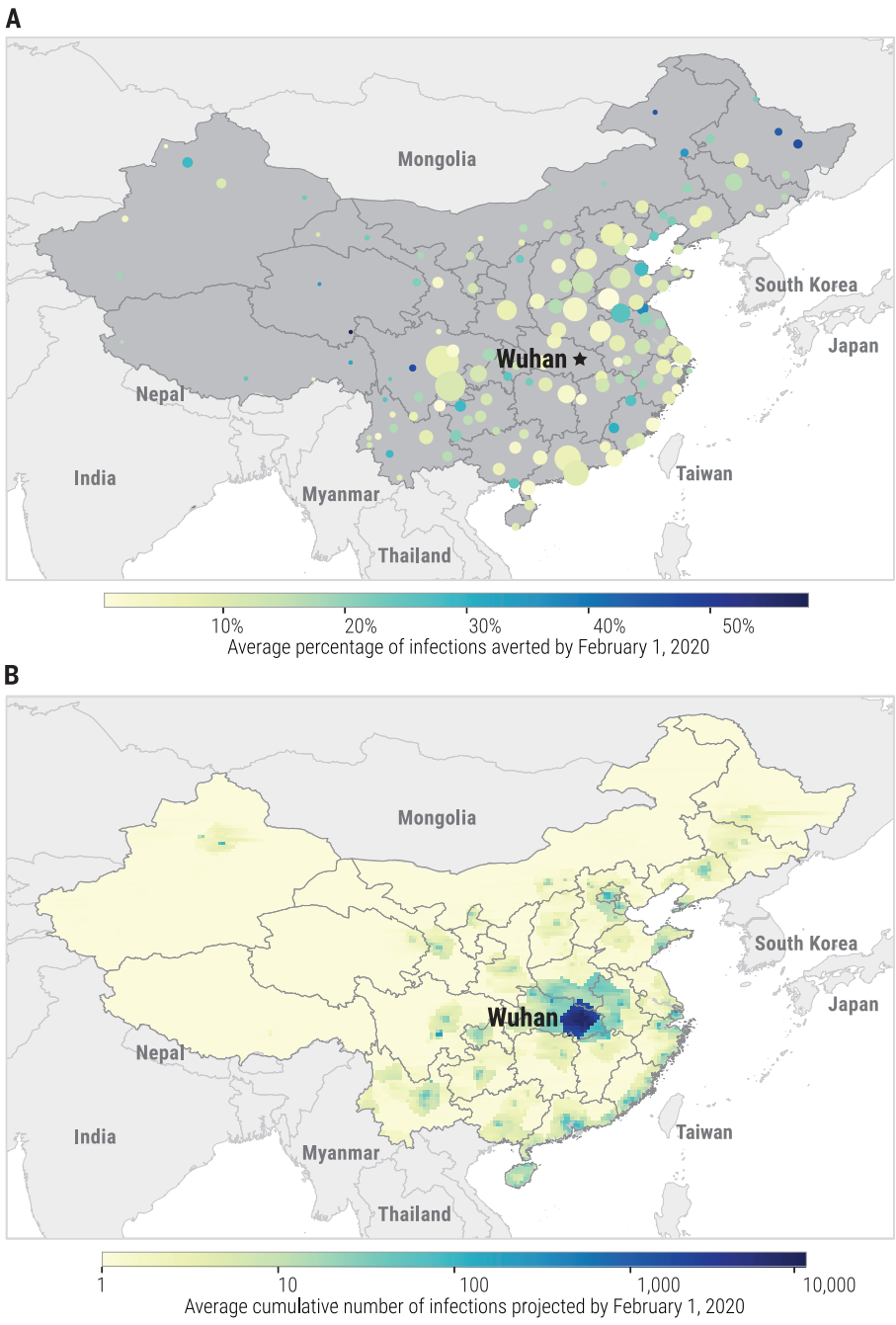

Fig. 2. Effects of Wuhan travel ban on COVID-19 incidence across mainland China. (**A**) Relative incidence reduction as of 1 February 2020. Circle color represents the relative reduction in the number of infections, whereas circle size corresponds to population. (**B**) Projected cumulative number of infections by the same date, after implementation of travel restrictions in Wuhan. A resolution of 0.25° by 0.25° geographical cells was used in the model.

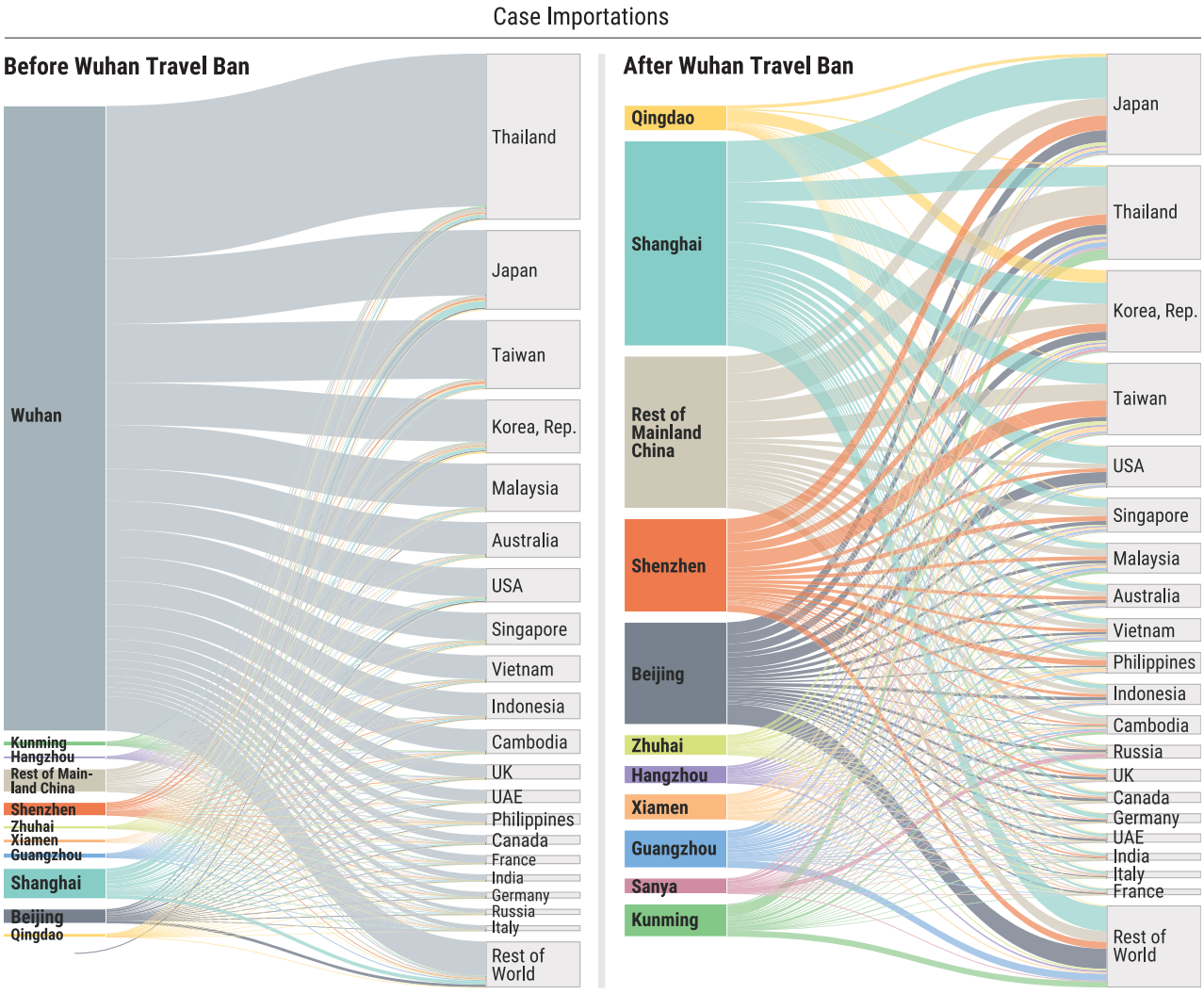

Fig. 3. Relative risk of case importation. Contribution to the relative risk of importation from the 10 Chinese cities with the highest rates of disease (plus the rest of mainland China) until 22 January 2020 (**left**) and after the Wuhan travel ban from 23 January to 1 March 2020 (**right**). The listed countries are the 20 countries at greatest risk of case importation. Flows are proportional to the relative probability that a single imported case will travel from a given origin to a specific destination.

which the top three are Shanghai (28.1%), Beijing (14%), and Shenzhen (12.8%)—accounted for at least ≈80% of the internationally imported cases. The countries most at risk of importation after the implementation of the Wuhan travel ban are Japan (11% pre-ban, 13.9% post-ban), Thailand (22.8% pre-ban, 13% post-ban), the Republic of Korea (7.4% pre-ban, 11.3% post-ban), Taiwan (9.5% pre-ban, 10% post-ban), and the United States (4.7% pre-ban, 5.7% post-ban).

International travel restrictions and transmissibility reduction

Starting in early February 2020, 59 airline companies suspended or limited flights to mainland China, and several countries—including the United States, Russia, Australia, and Italy—have imposed government-issued travel restrictions (*29*–*34*). It is difficult to calculate exactly the level of traffic reduction imposed by these measures. For this reason, we analyzed two major scenarios in which international travel restrictions produce a 40 and 90% overall traffic reduction to and from mainland China. A relative reduction of transmissibility could be achieved through early detection and isolation of cases, as well as behavioral changes and awareness of the disease in the population. Along with travel reductions, we considered three scenarios pertaining to disease transmissibility: (i) a status quo situation with the same transmissibility as that from the model calibration through 23 January 2020; (ii) a moderate relative reduction of the original transmissibility (25%), corresponding to a transmissibility dampening factor of r = 0.75; and (iii) a strong reduction (50%) of the original transmissibility (r = 0.50). In Fig. 4, we show the combined effects of the travel and transmissibility reductions on the epidemic incidence in mainland China and the number of exported cases to other countries.

The simulated scenarios reveal that even in the case of 90% travel reductions (Fig. 4D), if transmissibility is not reduced (r = 1), the epidemic in mainland China would be delayed for no more than 2 weeks. The model projects that, in the status quo scenario, the peak of the epidemic in mainland China will be reached in late April to early May 2020. Notably, in the absence of transmissibility reductions, the epidemic would peak in Wuhan during the first week of March. The number of infections imported in other countries (Fig. 4, A to C) was initially affected by a 10-fold reduction, but by 1 March, when there is no transmissibility reduction

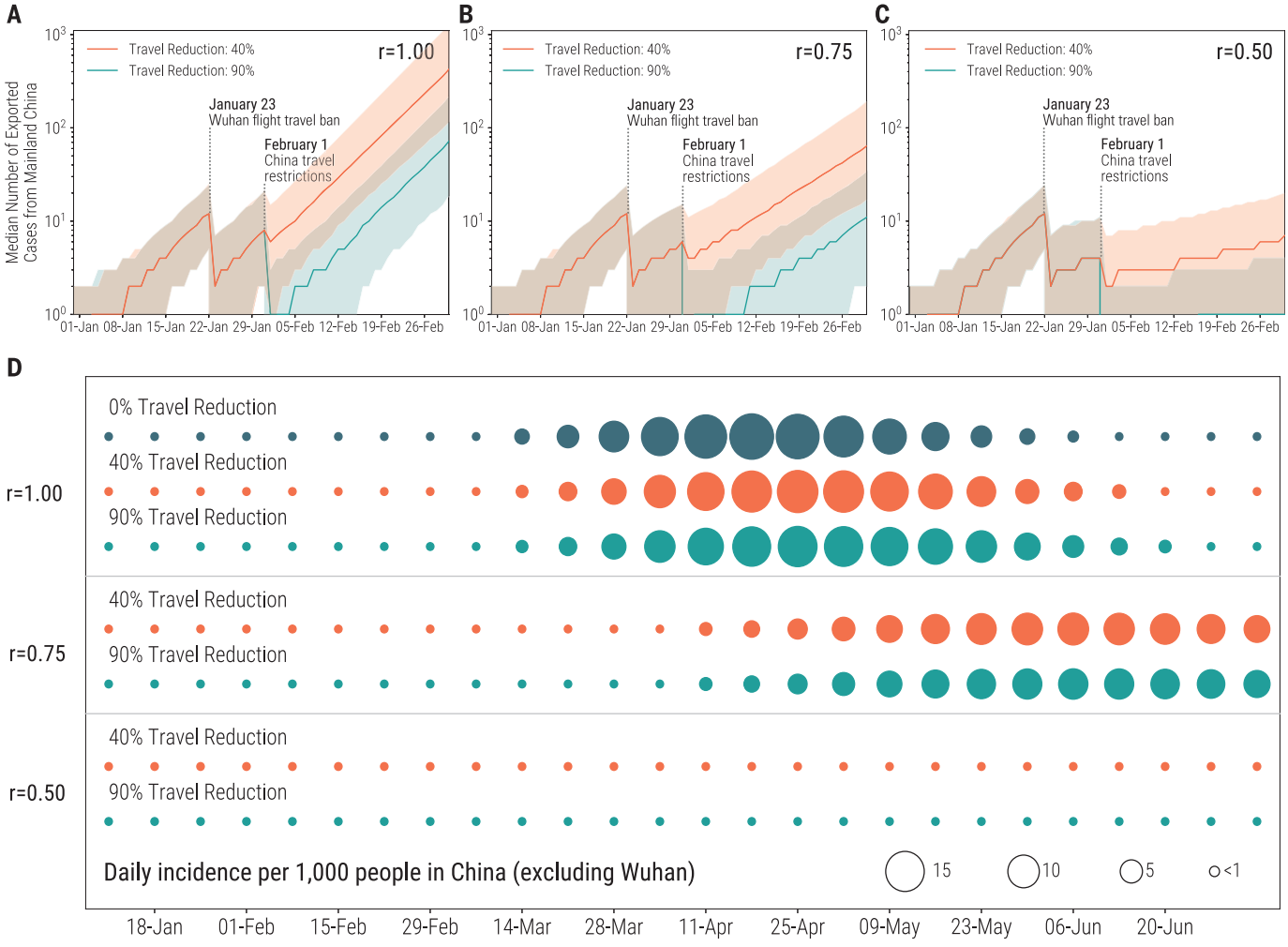

Fig. 4. Combined effects of travel and transmissibility reductions on the epidemic. (**A**) Median total number of imported infections from mainland China with no transmissibility reduction and travel reductions of 40 and 90%. (**B**) Same as (A) for the moderate transmissibility reduction scenario (r = 0.75). (**C**) Same as (A) for the strong transmissibility reduction scenario (r = 0.5). Shaded areas represent 90% CIs. (**D**) Disease incidence in mainland China, excluding Wuhan, for the scenarios plotted in (A) to (C).

(r = 1), we would again see 170 and 35 detected cases per day for the 40 and 90% travel restrictions scenarios, respectively. However, the concurrent presence of both travel and transmissibility reductions produces a much larger synergistic effect that becomes visible by delaying both the epidemic activity in mainland China and the number of internationally imported infections. In the moderate transmissibility reduction scenarios (r = 0.75), the epidemic peak is delayed to late June 2020, and the total number of international infection importations by 1 March is 26 cases per day for the 40% scenario and 5 per day for the 90% scenario. Even more restrictive travel limitations (>90%) would extend the period during which the importation of infections is greatly reduced. Strong transmissibility reduction (r = 0.5) along with travel restrictions would delay the epidemic growth in mainland China such that the daily incidence rate would never surpass 1 infection per 1000 people and the number of imported infections at international destinations would always be in the single-digit range. The effect of transmissibility reduction on the short-term epidemic curve in mainland China is also visible (Fig. 1A): There is a pronounced reduction in the number of infections by 22 February 2020, with respect to the status quo epidemic curve. We also report the estimated number of detected international importations, as determined by the model in the strong transmissibility reduction scenario (Fig. 1C). The results are consistent with the data collected from the travel history of international imported cases after 23 January 2020 (*16*, *17*). Similar results are obtained by assuming that the transmissibility reduction interventions successfully reduce the reproductive number below the epidemic threshold in the second half of February, as data from mainland China seem to suggest (*28*).

Notably, many infected individuals from mainland China have not been detected and have potentially dispersed to international locations. By 1 February 2020, in the strong transmissibility reduction scenario, the model estimates 101 (90% CI: 50 to 173) importation events, with one or more potential infections that could seed multiple epidemic outbreaks across the world, potentially leading to the international expansion of the COVID-19 epidemic. This finding is consistent with the emergence of COVID-19 outbreaks in countries such as Italy, the Republic of Korea, and Iran in the second half of February 2020.

Our analysis, as with all modeling exercises, has several limitations and requires certain assumptions. The model parameters, such as generation time and incubation period, are

chosen on the basis of early data associated with the COVID-19 outbreak and prior knowledge of SARS and Middle East respiratory syndrome (MERS) coronavirus epidemiology. Although the model is stable to variations in these parameters, more information on the key characteristic of the disease would considerably reduce uncertainties. At this stage, the transmission and mobility model does not account for heterogeneities due to age differences in susceptibility and contact patterns. The model calibration does not consider correlations among importations (family travel) and assumes that travel probabilities are homogeneous across all individuals in the catchment area of each transportation hub. We were not able to find reliable data on the effectiveness of containment measures (e.g., body temperature screening for passengers on flights departing from Wuhan International Airport) in mainland China before 23 January, so this information is not included in the model. In the travel restriction scenario, we assume long-term enforcement of individual mobility restrictions (travel was restricted until the end of June 2020), but this policy may not be feasible or sustainable for such a long period.

Discussion

The analysis of the COVID-19 outbreak and the modeling assessment of the effects of travel limitations could be beneficial to national and international agencies for public health response planning. We show that, by 23 January 2020, the epidemic had already spread to other cities within mainland China. The travel quarantine around Wuhan has only modestly delayed the spread of disease to other areas of mainland China. This finding is consistent with the results of separate studies on the diffusion of SARS-CoV-2 in mainland China (*27*, *35*, *36*). The model indicates that although the Wuhan travel ban was initially effective at reducing international case importations, the number of imported cases outside mainland China will continue to grow after 2 to 3 weeks. Furthermore, the modeling study shows that additional travel limitations (up to 90% of traffic) have only a modest effect unless paired with public health interventions and behavioral changes that can facilitate a considerable reduction in disease transmissibility (*37*). The model also indicates that, despite the strong restrictions on travel to and from mainland China since 23 January 2020, many individuals exposed to SARS-CoV-2 have been traveling internationally without being detected. Moving forward, we expect that travel restrictions to COVID-19–affected areas will have modest effects and that transmission reduction interventions will provide the greatest benefit for mitigating the epidemic. Our results provide data with potential uses for the definition of optimized containment schemes and mitigation policies, including the local and international dimensions of the COVID-19 epidemic.

REFERENCES AND NOTES

1. World Health Organization (WHO), "Novel Coronavirus – China" (WHO, 2020); www.who.int/csr/don/12-january-2020-novel-coronavirus-china/en/.
2. The Center for Systems Science and Engineering at Johns Hopkins University, Coronavirus COVID-19 Global Cases (2020); www.arcgis.com/apps/opsdashboard/index.html#/bda7594740fd40299423467b48e9ecf6.
3. WHO, "Coronavirus disease 2019 (COVID-19): Situation Report – 43" (WHO, 2020); www.who.int/docs/default-source/coronaviruse/situation-reports/20200303-sitrep-43-covid-19.pdf?sfvrsn=2c21c09c_2.
4. D. Balcan *et al*., *Proc. Natl. Acad. Sci. U.S.A.* **106**, 21484–21489 (2009).
5. D. Balcan *et al*., *J. Comput. Sci.* **1**, 132–145 (2010).
6. M. F. Gomes *et al*., *PLOS Curr.* 10.1371/currents.outbreaks.cd818f63d40e24aef769dda7df9e0da5 (2014).
7. Q. Zhang *et al*., *Proc. Natl. Acad. Sci. U.S.A.* **114**, E4334–E4343 (2017).
8. A. Rambaut, "Preliminary phylogenetic analysis of 11 nCoV2019 genomes, 2020-01-19" (2020); http://virological.org/t/preliminary-phylogenetic-analysis-of-11-ncov2019-genomes-2020-01-19/329.
9. N. Imai *et al*., "Report 3: Transmissibility of 2019-nCoV" (Imperial College London, 2020); www.imperial.ac.uk/mrc-global-infectious-disease-analysis/covid-19/report-3-transmissibility-of-covid-19/.
10. K. Anderson, "Clock and TMRCA based on 27 genomes" (2020); http://virological.org/t/clock-and-tmrca-based-on-27-genomes/347.
11. T. Bedford *et al*., "Genomic analysis of nCoV spread. Situation report 2020-01-23" (2020); https://nextstrain.org/narratives/ncov/sit-rep/2020-01-23.
12. See supplementary materials.
13. M. Sunnåker *et al*., *PLOS Comput. Biol.* **9**, e1002803 (2013).
14. R. Niehus, P. M. De Salazar, A. Taylor, M. Lipsitch, medRxiv 2020.02.13.20022707 [Preprint]. 18 February 2020.
15. P. M. De Salazar, R. Niehus, A. Taylor, C. O. Buckee, M. Lipsitch, medRxiv 2020.02.04.20020495 [Preprint]. 11 February 2020.
16. K. Sun, J. Chen, C. Viboud, *Lancet Digital Health* **2**, e201–e208 (2020).
17. F. Pinotti *et al*., medRxiv 2020.02.24.20027326 [Preprint]. 25 February 2020.
18. J. A. Backer, D. Klinkenberg, J. Wallinga, *Euro Surveill.* **25**, 2000062 (2020).
19. C. Huang *et al*., *Lancet* **395**, 497–506 (2020).
20. Q. Li *et al*., *N. Engl. J. Med.* **382**, 1199–1207 (2020).
21. M. Lipsitch *et al*., *Science* **300**, 1966–1970 (2003).
22. S. Riley *et al*., *Science* **300**, 1961–1966 (2003).
23. M. Kraemer, D. Pigott, "Epidemiological Data from the nCoV-2019 Outbreak: Early Descriptions from Publicly Available Data" (2020); http://virological.org/t/epidemiological-data-from-the-ncov-2019-outbreak-early-descriptions-from-publicly-available-data/337.
24. J. Riou, C. L. Althaus, *Euro Surveill.* **25**, 4 (2020).
25. S. Zhao *et al*., *Int. J. Infect. Dis.* **92**, 214–217 (2020).
26. J. M. Read, J. R. E. Bridgen, D. A. T. Cummings, A. Ho, C. P. Jewell, medRxiv 2020.01.23.20018549 [Preprint]. 28 January 2020.
27. H. Tian *et al*., medRxiv 2020.01.30.20019844 [Preprint]. 10 March 2020.
28. WHO, "Novel Coronavirus (2019-nCoV): Situation Report - 12" (WHO, 2020); www.who.int/docs/default-source/coronaviruse/situation-reports/20200201-sitrep-12-ncov.pdf?sfvrsn=273c5d35_2.
29. New York Times, "North Korea Bans Foreign Tourists Over Coronavirus, Tour Operator Says" (2020); www.nytimes.com/2020/01/21/world/asia/coronavirus-china-north-korea-tourism-ban.html.
30. Channel News Asia (CNA), "Scoot cancels flights to China's Wuhan over virus outbreak" (2020); www.channelnewsasia.com/news/singapore/wuhan-virus-scoot-cancels-flights-mtr-train-12309076.
31. Toui tre News, "Vietnam aviation authority ceases all flights to and from coronavirus-stricken Wuhan" (2020); https://tuoitrenews.vn/news/business/20200124/vietnam-aviation-authority-ceases-all-flights-to-and-from-coronavirusstricken-wuhan/52707.html.
32. Reuters, "Russia ramps up controls, shuts China border crossings over virus fears" (2020); www.reuters.com/article/us-china-health-russia-border/russian-regions-in-far-east-close-border-with-china-amid-coronavirus-fears-tass-idUSKBN1ZR0TU.
33. Center for Disease Control (CDC), "Global COVID-19 Pandemic Notice" (CDC, 2020); https://wwwnc.cdc.gov/travel/notices/warning/novel-coronavirus-china.
34. The Australian, "Travelers from China to be denied entry to Australia" (2020); www.theaustralian.com.au/nation/travellers-from-china-to-be-denied-entry-into-australia/news-story/7b7619d44af78dd7395a934e22b52997.
35. J. T. Wu, K. Leung, G. M. Leung, *Lancet* **395**, 689–697 (2020).
36. Z. Du *et al*., *Emerg. Infect. Dis.* 10.3201/eid2605.200146 (2020).
37. J. M. Drake, S. K. Chew, S. Ma, *PLOS ONE* **1**, e20 (2006).
38. M. Chinazzi, mobs-lab/COVID-19: The effect of travel restrictions on the spread of the 2019 novel coronavirus (COVID-19) outbreak, Version 001, Zenodo (2020); http://doi.org/10.5281/zenodo.3697201.

ACKNOWLEDGMENTS

Funding: M.E.H. acknowledges the support of the MIDAS-U54GM111274. S.M. and M.A. acknowledge support from the EU H2020 MOOD project. C.G. and L.R. acknowledge support from the EU H2020 Icarus project. M.C. and A.V. acknowledge support from Google Cloud Healthcare and Life Sciences Solutions via the GCP research credits program. The findings and conclusions in this study are those of the authors and do not necessarily represent the official position of the funding agencies, the National Institutes of Health, or the U.S. Department of Health and Human Services. **Author contributions:** M.C. and A.V. designed the research; M.C., J.T.D., M.A., C.G., M.L., S.M., A.P.yP., K.M., L.R., K.S., C.V., X.X., H.Y., M.E.H., I.M.L., and A.V. performed the research; M.C., J.T.D., A.P.yP., K.M., and A.V. analyzed the data; and M.C., J.T.D., M.A., C.G., M.L., S.M., A.P.yP., K.M., L.R., K.S., C.V., X.X., H.Y., M.E.H., I.M.L., and A.V. wrote and edited the paper. **Competing interests:** M.E.H. reports grants from the National Institute of General Medical Sciences during the conduct of the study; A.V. reports grants and personal fees from Metabiota, Inc., outside of the submitted work; M.C. and A.P.yP. report grants from Metabiota, Inc., outside of the submitted work; H.Y. reports grants from Glaxosmithkline (China) Investment Co., Ltd., Yichang HEC Changjiang Pharmaceutical Co., Ltd, Sanofi Pasteur, and Shanghai Roche Pharmaceuticals Company, outside of the submitted work. The authors declare no other relationships or activities that could appear to have influenced the submitted work. **Data and materials availability:** Proprietary airline data are commercially available from OAG and IATA databases. All other data that support the plots within this paper and other findings of this study are available at https://github.com/mobs-lab/COVID-19/blob/master/README.md (*38*). The GLEAM model is publicly available at www.gleamviz.org/. This work is licensed under a Creative Commons Attribution 4.0 International (CC BY 4.0) license, which permits unrestricted use, distribution, and reproduction in any medium, provided the original work is properly cited. To view a copy of this license, visit https://creativecommons.org/licenses/by/4.0/. This license does not apply to figures/photos/artwork or other content included in the article that is credited to a third party; obtain authorization from the rights holder before using such material.

SUPPLEMENTARY MATERIALS

science.sciencemag.org/content/368/6489/395/suppl/DC1
Material and Methods
Figs. S1 and S2
Table S1
References (*39*–*110*)
MDAR Reproducibility Checklist

20 January 2020; resubmitted 7 February 2020
Accepted 5 March 2020
Published online 6 March 2020
10.1126/science.aba9757

POLIOVIRUS

Evolving epidemiology of poliovirus serotype 2 following withdrawal of the serotype 2 oral poliovirus vaccine

G. R. Macklin[1,2]*, K. M. O'Reilly[1], N. C. Grassly[3], W. J. Edmunds[1], O. Mach[2], R. Santhana Gopala Krishnan[2], A. Voorman[4], J. F. Vertefeuille[5], J. Abdelwahab[6], N. Gumede[7], A. Goel[2], S. Sosler[8], J. Sever[9], A. S. Bandyopadhyay[4], M. A. Pallansch[5], R. Nandy[6], P. Mkanda[7], O. M. Diop[2], R. W. Sutter[2,5]

Although there have been no cases of serotype 2 wild poliovirus for more than 20 years, transmission of serotype 2 vaccine-derived poliovirus (VDPV2) and associated paralytic cases in several continents represent a threat to eradication. The withdrawal of the serotype 2 component of oral poliovirus vaccine (OPV2) was implemented in April 2016 to stop VDPV2 emergence and secure eradication of all serotype 2 poliovirus. Globally, children born after this date have limited immunity to prevent transmission. Using a statistical model, we estimated the emergence date and source of VDPV2s detected between May 2016 and November 2019. Outbreak response campaigns with monovalent OPV2 are the only available method to induce immunity to prevent transmission. Yet our analysis shows that using monovalent OPV2 is generating more paralytic VDPV2 outbreaks with the potential for establishing endemic transmission. A novel OPV2, for which two candidates are currently in clinical trials, is urgently required, together with a contingency strategy if this vaccine does not materialize or perform as anticipated.

Ever since the oral poliovirus vaccine (OPV) was first identified in 2000 as the source of a paralytic poliomyelitis outbreak, vaccine-derived polioviruses (VDPVs) have been a known obstacle to achieving polio eradication (*1*, *2*). Despite the global withdrawal of the serotype 2 component of OPV (OPV2), paralytic poliomyelitis cases associated with serotype 2 VDPV (VDPV2) have been reported in expanding global geographies. This is important because there is now a global cohort of children without immunity against serotype 2 that would prevent transmission, which could result in established endemicity of the virus. The inactivated poliovirus vaccine (IPV) can protect against paralysis but provides limited intestinal immunity to stop transmission (*3*). Therefore, the method to control VDPV2 transmission is through vaccination campaigns with monovalent OPV2 (mOPV2) (*4*). However, any use of mOPV2 carries the risk of seeding more VDPV2 (*5*).

After the eradication of serotype 2 wild poliovirus (WPV), vaccination continued with OPV2 as part of the trivalent vaccine (tOPV, containing serotypes 1, 2, and 3) (fig. S1), resulting in periodic outbreaks of VDPV2 (as well as VDPV1 and VDPV3) and cases of vaccine-associated paralytic poliomyelitis (VAPP) (*6*). This is because the attenuated virus strains contained in OPV can mutate and reacquire factors associated with causing paralytic disease and transmission (*7*). Populations with low immunization coverage are particularly at risk of spread (*7*). Once the eradication of serotype 2 WPV was certified, it was decided to withdraw the OPV2 to prevent paralysis caused by type 2 poliovirus (fig. S1) (*6*). In April 2016, the Global Polio Eradication Initiative (GPEI) coordinated a globally synchronized switch from tOPV to bivalent OPV (bOPV, containing serotypes 1 and 3) in all routine and supplemental immunization activities, commonly referred to as "the Switch" (fig. S1) (*8*). As a risk mitigation strategy, countries began to introduce a dose of IPV into routine immunization schedules to protect against paralysis from serotype 2 poliovirus (*9*). However, an estimated 143 million children have not received IPV since April 2016 because of supply shortages (43 million) and poor routine immunization coverage (100 million) (*10*).

It was predicted that after the Switch, circulation of serotype 2 polioviruses would steadily disappear. Some VDPV2 outbreaks were expected, largely from prior widespread tOPV use in immunization campaigns (approximately 1.5 billion doses in the 12 months before the Switch) (*11*, *12*). The response to any outbreaks was to conduct campaigns with mOPV2 from a finite global stockpile of vaccine (*4*). Although the virus disappeared from most geographies, eradication did not occur (*13*). More recently, outbreaks of VDPV2 have been increasing in frequency and geographic spread (Fig. 1). At present, WHO classifies circulating VDPV2 (cVDPV2) outbreaks as Public Health Emergencies of International Concern (*14*). Here, we investigated the epidemiology and source of VDPV2 outbreaks through a retrospective analysis of poliovirus surveillance and mOPV2 campaign data between 1 May 2016 and 1 November 2019.

We obtained data on virus isolates from acute flaccid paralysis (AFP) cases and environmental samples through the surveillance network of the Global Polio Laboratory Network (GPLN) on 1 November 2019. We estimated the date of seeding interval (i.e., 95% confidence intervals for the date that the infectious OPV dose was administered) on the basis of the date of detection and the number of nucleotides divergent from the OPV2 virus in the viral protein 1 (*VP1*) gene (see supplementary materials). We assumed that the first *VP1* mutation is instantaneous and that each subsequent mutation follows an average rate, previously estimated at 1.14×10^{-2} nucleotides per site per year, that corresponds to one nucleotide change observed after approximately 35 days (*15*). The time to each independent mutation was modeled using an exponential distribution, and the sum of waiting times as an Erlang distribution (see supplementary materials).

Global VDPV2 detections and source

Between 1 May 2016 and 1 November 2019, the GPLN had detected 859 isolates of VDPV2 across 26 countries, including 325 cases of AFP (Fig. 1). The AFP cases had a median age of 1.75 years (range 0.2 to 12 years), and 27.0% of cases reported receiving no previous polio vaccine doses.

We calculated that 65.5% (548/837) of sequenced VDPV2 viruses detected since April 2016 had a ≥90% probability of being seeded after the Switch (Fig. 2A). For isolates with a ≥90% probability of being seeded after the Switch, we identified whether a mOPV2 campaign was conducted within the same geographic region during the estimated seeding interval. We found that the source of 71.5% (392/548) of these isolates was consistent with mOPV2 outbreak response campaigns conducted within the country of emergence and that the source of 24.6% (135/548) was consistent with mOPV2 campaigns conducted within a neighboring country (Fig. 2B).

Circulating VDPV2 (cVDPV2) outbreaks

VDPV2 emergences are classified as cVDPV2 when there is evidence of person-to-person transmission (isolates are genetically linked to a previously detected isolate), or as ambiguous VDPV2 (aVDPV2) events, when there is no evidence of transmission and after ruling out primary immunodeficiency in infected individuals (*16*, *17*).

[1]Centre of Mathematical Modelling of Infectious Diseases, London School of Hygiene and Tropical Medicine, London, UK. [2]Polio Eradication, World Health Organization, Geneva, Switzerland. [3]Department of Infectious Disease Epidemiology, Imperial College London, London, UK. [4]Bill and Melinda Gates Foundation, Seattle, WA, USA. [5]Centers for Disease Control and Prevention (CDC), Atlanta, GA, USA. [6]United Nations Children's Fund (UNICEF), New York, NY, USA. [7]Regional Office for Africa, World Health Organization, Brazzaville, Congo. [8]Gavi (the Vaccine Alliance), Geneva, Switzerland. [9]Rotary International, Evanston, IL, USA.
*Corresponding author. Email: mackling@who.int

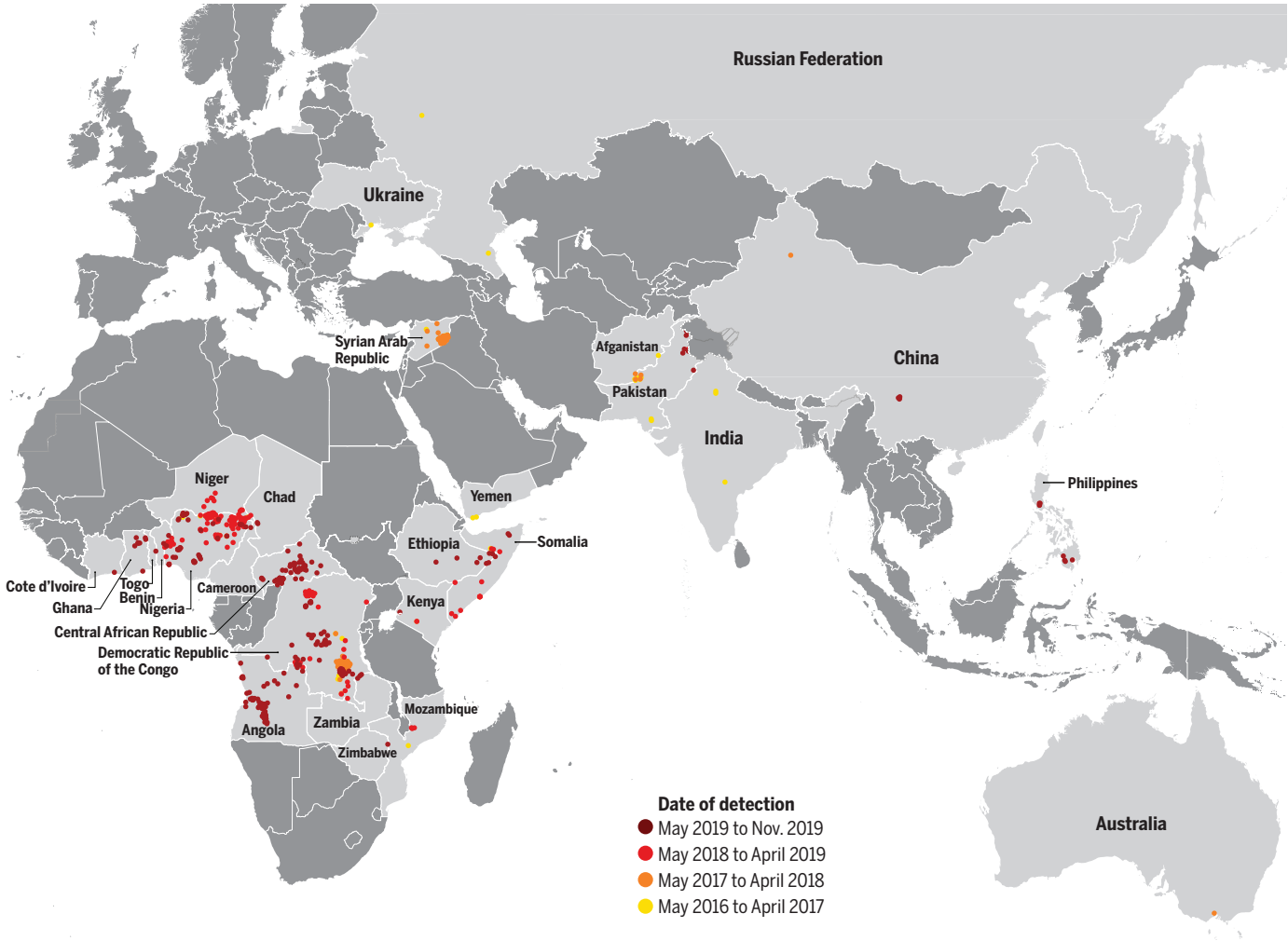

Fig. 1. Geographic location of vaccine-derived poliovirus serotype 2 (VDPV2) isolates detected between 1 May 2016 and 1 November 2019. The color of points illustrates the date of isolate detection. Data are as of 1 November 2019.

We identified 62 aVDPV2 events and 41 independent cVDPV2 outbreaks that have occurred since the Switch (Fig. 3 and table S1). The 41 cVDPV2 outbreaks emerged in Angola (n = 7), Central African Republic (n = 6), China (n = 1), Democratic Republic of the Congo (DRC) (n = 10), Mozambique (n = 1), Nigeria (n = 9), Pakistan (n = 3), Philippines (n = 1), Somalia (n = 1), Syrian Arab Republic (Syria) (n = 1), and Zambia (n = 1). International spread of cVDPV2s has led to transmission in Benin, Cameroon, Chad, Côte d'Ivoire, Ethiopia, Ghana, Kenya, and Togo. The countries where these outbreaks occur are mainly characterized by suboptimal health systems with low routine immunization coverage, inaccessible or active conflict-affected areas, and low sanitation and hygiene (table S1).

A total of 126 post-Switch mOPV2 campaigns have been conducted in response to these outbreaks, using more than 300 million doses of the mOPV2 vaccine (table S2), primarily in Nigeria (59%) and DRC (15%). These campaigns are consistent with seeding 27 of 41 outbreaks (table S2).

Evolving situation over time

In the first year after the Switch (May 2016 to April 2017), our analysis shows that there were six cVDPV2 outbreaks, seeded before (n = 5) or close to the time of the Switch (n = 1), likely through immunization with tOPV (Fig. 3 and table S1). This was consistent with the predictions made, including from mathematical modeling groups (*11*, *18*). These outbreaks, which occurred in Nigeria (n = 2), DRC (n = 2), Pakistan (n = 1), and Syria (n = 1), were rapidly controlled through mOPV2 use (table S1) (*19*).

Interestingly, we observed that no virus was detected later than 6 months after the Switch in the American, European, and South-East Asian regions of WHO: No cVDPV2 outbreaks occurred, and the rare detection of aVDPV2 in the first 6 months in these regions was limited, likely because of generally high pre-Switch intestinal mucosal immunity, good sanitation standards, and post-Switch IPV use (*13*, *20*).

In the second year after the Switch (May 2017 to April 2018), five more outbreaks emerged (table S1). We calculate that one of these was seeded before the Switch and that the other four were seeded after the Switch (Fig. 2). In two of these outbreaks (SOM-BAN-1 and NIE-JIG-1 emergences), failure to control the virus has resulted in spread across national borders to establish transmission in neighboring countries: from Somalia to Kenya and Ethiopia and from Nigeria to Niger, Cameroon, Ghana, Benin, Chad, Togo, and Côte d'Ivoire (table S1). These two outbreaks, which have not yet been controlled, are the longest in duration, with transmission detected for periods of 22 and 21 months, respectively (table S1).

In the third and fourth years after the Switch (May 2018 to November 2019), it was expected (and planned) that there would be a substantial reduction in the number of outbreaks (*18*). However, we demonstrate that the

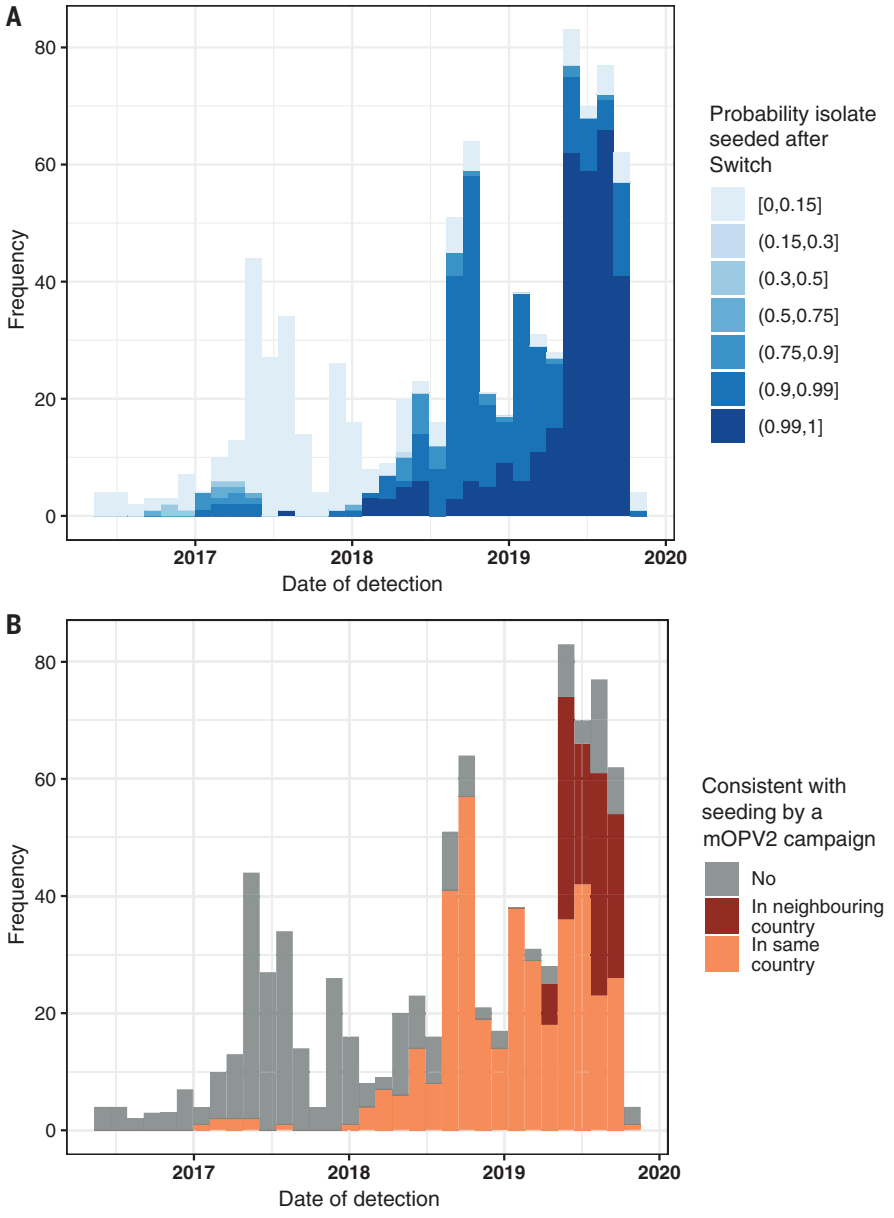

Fig. 2. Incidence of vaccine-derived poliovirus serotype 2 (VDPV2) isolates detected between 1 May 2016 and 1 November 2019. (**A**) The probability that isolate was seeded after the Switch (1 May 2016) was calculated according to the 95% confidence intervals of the estimated seeding date, estimated by the number of nucleotides of divergence from the poliovirus vaccine strain, in the viral protein 1 gene of the position, assuming a model for the mutation rate (see supplementary materials). (**B**) For all isolates with >0.9 probability of post-Switch seeding, the color demonstrates whether there was a corresponding mOPV2 campaign within estimated dates of seeding and the same or adjacent country.

highest frequency of outbreaks has been in this period: 10 outbreaks emerged between May 2018 and April 2019 and 20 in the period from May 2019 to November 2019 alone. Our analysis shows that all except one of these emergences were seeded after the Switch (Fig. 1).

There has been a shift in epidemiology observed over this period, characterized by the emergence of several cVDPV2s in 2019 with low nucleotide divergence in geographies without preceding mOPV2 use (Fig. 3). There have been six cVDPV outbreaks in the Central African Republic and seven in Angola (table S1), which are consistent with seeding from mOPV2 responses in the neighboring DRC. Additionally, two low-divergence cVDPV2s have emerged in Pakistan, a country where mOPV2 had not been used in outbreak response for more than 1 year prior to the estimated seeding date. Ongoing investigations are exploring hypotheses of outbreak source, including multiple international importations from mOPV2-using areas and inadvertent mOPV2/tOPV use. However, established transmission of cVDPV2 now exists in these populations, and as such, the geographic scope of detections is expanding rapidly (Fig. 2).

The detection of two highly divergent cVDPV2s in China and the Philippines in 2019 confirms transmission in the Western Pacific Region of WHO (table S1). In the Philippines, the cVDPV2 was first detected in an AFP case in June 2019 with a 64-nucleotide divergence from OPV2, which suggests that the virus was seeded in 2014 (Fig. 3). Subsequently, an individual with primary immunodeficiency was detected excreting virus genetically linked to the outbreak; however, the role of this case in the outbreak is not clear. It seems unlikely that the virus would circulate undetected for 5 years, although serotype 2 poliovirus is thought to have approximately 2000 infections for every paralytic case, yet these examples emphasize the need for continuing high-quality surveillance and expanding environmental surveillance (*21*).

Using logistic regression, we demonstrate the probability that a new VDPV2 emergence (i) was seeded after the Switch, is increasing over time (regression coefficient = 1.99, $P < 0.001$, intercept = −1.66); and (ii) establishes person-to-person transmission, is increasing over time (regression coefficient = 0.88, $P < 0.001$, intercept = −2.27).

At this juncture, we show that polio eradication is battling both the new emergences of cVDPV outbreaks seeded after the Switch—largely through mOPV2 use in response to outbreaks—and outbreaks seeded before the Switch that had delayed detection. In 2019, we have observed the largest numbers of outbreaks and countries experiencing cVDPV2 transmission to date. We conclude that the GPEI is in a paradoxical situation: On one hand, it is not currently possible to control the outbreaks without inducing intestinal mucosal immunity through mOPV2 use, but on the other hand, the use of mOPV2 is generating VDPV2. The risk of VDPV2 circulation is increasing over time as the immunity of the global population rapidly decreases (*5*).

Policy perspective

Since the Switch more than 4 years ago, the epidemiology of serotype 2 poliovirus has developed in directions that were neither expected nor planned. This has policy implications for polio. Although the Switch has largely eliminated the incidence of serotype 2 VAPP and immunodeficiency-related VDPV cases, it has not achieved the major objective—that is, the eradication of the last serotype 2 polioviruses (those originating from the oral poliovirus vaccine) in all populations. The question remains as to what the GPEI should do next.

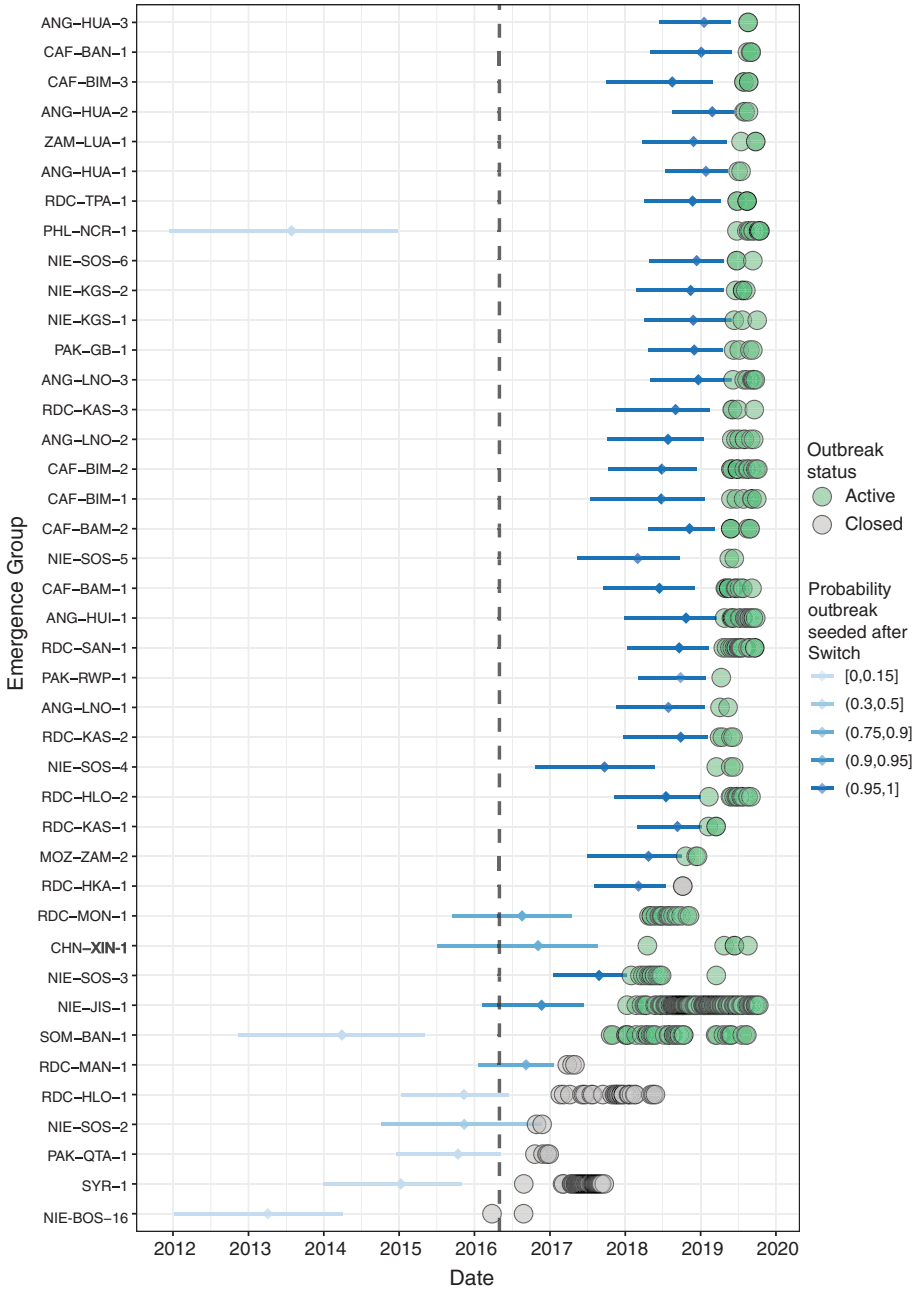

Fig. 3. Timeline of circulating VDPV2 outbreaks reported between 1 May 2016 and 1 November 2019, ordered by the date of first isolate detection. The estimated seeding date (i.e., the date that an infectious OPV dose was administered) and 95% confidence intervals are given by horizontal bars, colored by the probability that the date of seeding was after the Switch on 1 May 2016 (dashed black line denotes date of Switch). Detected virus isolates are shown by colored circles, with the color indicating whether the outbreak is assumed to be active (detection within previous 12 months) or closed (no detection in previous 12 months). Data are as of 1 November 2019. NIE-BOS-16: This outbreak was genetically linked to a cVDPV2 emergence originating in Chad in 2012.

In 2010, the GPEI initiated the development of two candidates for serotype 2 novel oral poliovirus vaccine (nOPV2), which are currently completing phase II clinical trials (*21*). The nOPV2s are designed to provide intestinal immunity similar to that of the current OPV while being more genetically stable. Therefore, the major advantage of nOPV2 use in outbreak control would be a lower risk of seeding new VDPV2 (and cVDPV2 outbreaks). In 2020, there are efforts to rapidly accelerate the clinical development of one candidate for this vaccine and pursue World Health Organization regulatory approval though the Emergency Use Listing procedure (*22*).

A strategy for the response to cVDPV2s has been developed for 2020–2021. In the time before nOPV2 is available, the approach is to conduct enhanced outbreak response campaigns with the current mOPV2 to contain cVDPV2 spread. Capacity to conduct aggressive, rapid, and high-quality campaigns is essential: Persistent delays and pockets of low coverage will continually hinder the impact of outbreak responses with any vaccine, whether the nOPV2 or mOPV2. Strengthening routine administration of IPV and strategic vaccination with remaining available IPV doses (to ensure that missed children in areas at high risk are reached) will be used as a paralysis prevention method.

When the nOPV2 vaccine becomes available in sufficient quantities, it will be rolled out to eventually replace mOPV2 in outbreak response. In the situation that nOPV2 does not materialize or perform as anticipated, or incurs substantial delays, the GPEI would have to implement a contingency plan (under preparation). The reintroduction of preventive vaccination with mOPV2 or tOPV, either through preventive campaigns or routine immunization, would have to be considered. However, this approach would require quantities of mOPV2 or tOPV doses that are currently not available.

It is critical that cVDPV2 outbreaks be managed as national public health emergencies in line with the declaration of a Public Health Emergency of International Concern by WHO (*14*). All GPEI partners, member state governments, and agencies must fully operationalize their emergency frameworks to prevent the reestablishment of endemic transmission of serotype 2 poliovirus in the form of cVDPV2. It remains clear that OPV removal is essential to stop all cases of paralytic poliomyelitis. However, the epidemiology that has evolved since OPV2 removal has implications for existing strategies outlined for total OPV cessation, which need urgent attention (*23*).

REFERENCES AND NOTES

1. O. Kew *et al.*, *Science* **296**, 356–359 (2002).
2. P. E. Fine, G. Oblapenko, R. W. Sutter, *Bull. World Health Organ.* **82**, 47–52 (2004).
3. G. R. Macklin *et al.*, *Lancet Infect. Dis.* **19**, 1121–1128 (2019).
4. Global Polio Eradication Initiative, *Standard Operating Procedures: Responding to a Poliovirus Event or Outbreak* (2019); http://polioeradication.org/wp-content/uploads/2016/07/sop-polio-outbreak-response-version-20193101.pdf.
5. K. A. McCarthy, G. Chabot-Couture, M. Famulare, H. M. Lyons, L. D. Mercer, *BMC Med.* **15**, 175 (2017).
6. Centers for Disease Control and Prevention, *MMWR Morb. Mortal. Wkly. Rep.* **50**, 222–224 (2001).
7. O. M. Kew, R. W. Sutter, E. M. de Gourville, W. R. Dowdle, M. A. Pallansch, *Annu. Rev. Microbiol.* **59**, 587–635 (2005).
8. L. M. Hampton *et al.*, *MMWR Morb. Mortal. Wkly. Rep.* **65**, 934–938 (2016).
9. *Wkly. Epidemiol. Rec.* **88**, 1–16 (2013).

10. S. Zipursky *et al.*, *J. Infect. Dis.* **216** (suppl. 1), S15–S23 (2017).
11. M. Pons-Salort *et al.*, *PLOS Pathog.* **12**, e1005728 (2016).
12. R. J. Duintjer Tebbens, M. A. Pallansch, S. G. F. Wassilak, S. L. Cochi, K. M. Thompson, *BMC Infect. Dis.* **16**, 137 (2016).
13. I. M. Blake *et al.*, *N. Engl. J. Med.* **379**, 834–845 (2018).
14. J. Zarocostas, *Lancet* **392**, 2425 (2018).
15. C. C. Burns *et al.*, *J. Virol.* **87**, 4907–4922 (2013).
16. Global Polio Eradication Initiative, *Classification and Reporting of Vaccine-Derived Polioviruses (VDPV)* (2016); http://polioeradication.org/wp-content/uploads/2016/09/Reporting-and-Classification-of-VDPVs_Aug2016_EN.pdf.
17. G. Macklin *et al.*, *Front. Immunol.* **8**, 1103 (2017).
18. K. M. Thompson, R. J. Duintjer Tebbens, *J. Infect. Dis.* **210** (suppl. 1), S475–S484 (2014).
19. C. Mbaeyi *et al.*, *MMWR Morb. Mortal. Wkly. Rep.* **67**, 690–694 (2018).
20. O. M. Kew *et al.*, *Bull. World Health Organ.* **82**, 16–23 (2004).
21. N. Nathanson, O. M. Kew, *Am. J. Epidemiol.* **172**, 1213–1229 (2010).
22. World Health Organisation, *Emergency Use Listing Procedure, Version 9* (January 2020); https://extranet.who.int/prequal/sites/default/files/documents/EUL_Procedure_Jan2020.pdf.
23. Global Polio Eradication Initiative, *Polio Post-Certification Strategy* (2018); http://polioeradication.org/wp-content/uploads/2018/04/polio-post-certification-strategy-20180424-2.pdf.

ACKNOWLEDGMENTS

This article was submitted on behalf of the Strategy Committee of the Global Polio Eradication Initiative (GPEI). Members of the committee include M. Zaffran (World Health Organization), J. Wenger (Bill & Melinda Gates Foundation), R. Martin (Centers for Disease Control and Prevention), A. Iyer (UNICEF), A. Nguyen (Gavi, the Vaccine Alliance), and C. Pandak (Rotary International). We acknowledge the personnel at the 144 laboratories of the WHO Global Polio Laboratory Network (GPLN) in all six WHO regions, as well as personnel from Virus Isolation, Intratypic Differentiation, and Sequencing Laboratories, for providing the data used in this study. We also acknowledge the contribution of discussions with the Institute for Disease Modelling and Kid Risk Inc. The results and conclusions in this article are those of the authors and do not necessarily represent the official position or policies of the U.S. Centers for Disease Control and Prevention. **Funding:** Supported by a Ph.D. scholarship from the UK Medical Research Council and funding from the Bill and Melinda Gates Foundation (OPP1191821) and WHO. N.C.G. acknowledges joint Centre funding from the UK Medical Research Council and Department for International Development. **Author contributions:** G.R.M.: conceptualization, methodology, formal analysis, visualization, writing (original draft), project administration. K.M.O.: methodology, validation, writing (original draft), supervision. N.C.G.: methodology, writing (original draft), supervision. W.J.E.: conceptualization, writing (review and editing). O.M.: writing (original draft), supervision. R.S.G.K.: data curation, visualization. A.V.: methodology, writing (review and editing). J.F.V., J.A., S.S., J.S., A.S.B., and R.N.: writing (review and editing). N.G. and M.A.P.: investigation, resources, writing (review and editing). A.G.: data curation. P.M. and O.M.D.: investigation, resources. R.W.S.: conceptualization, writing (original draft), supervision. **Competing interests:** The authors declare no competing interests. **Data and materials availability:** Data used in this study are the property of the individual countries and are available on the Polio Information System (PolIS), https://extranet.who.int/polis/. Data access was provided through the Global Polio Eradication Initiative Data Sharing Agreement.

SUPPLEMENTARY MATERIALS

science.sciencemag.org/content/368/6489/401/suppl/DC1
Materials and Methods
Tables S1 and S2
Figs. S1 and S2
References (*24*–*26*)

6 January 2020; accepted 11 March 2020
Published online 19 March 2020
10.1126/science.aba1238

REPORTS

ATMOSPHERIC PHYSICS

How waves and turbulence maintain the super-rotation of Venus' atmosphere

Takeshi Horinouchi[1,2]*, Yoshi-Yuki Hayashi[3], Shigeto Watanabe[4], Manabu Yamada[5], Atsushi Yamazaki[2], Toru Kouyama[6], Makoto Taguchi[7], Tetsuya Fukuhara[7], Masahiro Takagi[8], Kazunori Ogohara[9], Shin-ya Murakami[2], Javier Peralta[2], Sanjay S. Limaye[10], Takeshi Imamura[11], Masato Nakamura[2,12], Takao M. Sato[4], Takehiko Satoh[2,12]

Venus has a thick atmosphere that rotates 60 times as fast as the surface, a phenomenon known as super-rotation. We use data obtained from the orbiting Akatsuki spacecraft to investigate how the super-rotation is maintained in the cloud layer, where the rotation speed is highest. A thermally induced latitudinal-vertical circulation acts to homogenize the distribution of the angular momentum around the rotational axis. Maintaining the super-rotation requires this to be counteracted by atmospheric waves and turbulence. Among those effects, thermal tides transport the angular momentum, which maintains the rotation peak, near the cloud top at low latitudes. Other planetary-scale waves and large-scale turbulence act in the opposite direction. We suggest that hydrodynamic instabilities adjust the angular-momentum distribution at mid-latitudes.

The thick atmosphere of Venus rotates at speeds up to 60 times those of the slow planetary rotation; the surface rotates westwards with a period of 243 days (throughout this paper, day refers to Earth days). The mechanism responsible for this super-rotation (SR) remains unclear (*1*, *2*), partly because of insufficient observational evidence for hypothesis testing.

SR may also occur in tidally locked exoplanets—those that always face the same way toward their host star and are therefore heated only on one side. Zonal (east-west) flow around the rotation axis, including SR, can transport heat from the dayside to the nightside of those exoplanets (*3*).

SR cannot occur unless the atmospheric angular momentum with respect to the rotational axis (hereinafter, AM) is transported by axially asymmetric flows (eddies) such as waves and turbulence. Without these, AM (per unit mass) is homogenized by the latitudinal-vertical circulation (meridional circulation) induced by the pole-equator temperature difference (*4*). Estimates of the AM transport from observations have been attempted by tracking features in images of the cloud top (65 to 70 km in altitude) obtained by the Mariner 10 (*5*) and Pioneer Venus Orbiter (*6*, *7*) spacecraft; however, the sampling proved insufficient both in space and in time.

Simulations using atmospheric general circulation models have generated SR (*8*–*15*); these simulations indicate that SR is realized by AM transport via tidal (*9*, *11*, *13*, *14*) and other waves (*8*, *10*–*15*). Some of these waves arise from hydrodynamic instabilities [such as the barotropic (*10*, *12*–*14*), baroclinic (*12*, *13*, *15*), and Rossby-Kelvin instabilities (*14*)] and turbulent eddies (*15*). The relative contributions of each of these effects to SR differ between models.

The AM budget can be described by the following equation, which in meteorology is known as the transformed Eulerian mean equation

$$\frac{\partial M}{\partial t} = -\boldsymbol{v}^r \cdot \nabla + \rho_0^{-1} \nabla \cdot \boldsymbol{F}$$

where M is the zonal-mean (i.e., averaged along latitudinal circles) AM per unit mass, which is negative when westward, as in SR; $\boldsymbol{F}$ is (minus) the AM flux, called the Eliassen-Palm flux; $\boldsymbol{v}^r \equiv (0, v^r, w^r)$ represents the mean meridional circulation velocities and is called the residual circulation; v^r is the northward velocity; and w^r is the westward velocity (*16*). The equation above indicates that, at steady state, AM transport by eddies (the $\rho_0^{-1} \nabla \cdot \boldsymbol{F}$ term) and AM transport by the mean meridional circulation (the $-\boldsymbol{v}^r \cdot \nabla M$ term) compensate each other. On Venus, $|M|$ reaches its maximum around the cloud-top altitude near the equator (*17*, *18*). Maintenance of

[1]Faculty of Environmental Earth Science, Hokkaido University, Sapporo, Japan. [2]Institute of Space and Astronautical Science, Japan Aerospace Exploration Agency, Sagamihara, Japan. [3]Department of Planetology and Center for Planetary Science, Kobe University, Kobe, Japan. [4]Space Information Center, Hokkaido Information University, Ebetsu, Japan. [5]Planetary Exploration Research Center, Chiba Institute of Technology, Narashino, Japan. [6]Artificial Intelligence Research Center, National Institute of Advanced Industrial Science and Technology, Tokyo, Japan. [7]College of Science, Rikkyo University, Tokyo, Japan. [8]Faculty of Science, Kyoto Sangyo University, Kyoto, Japan. [9]School of Engineering, University of Shiga Prefecture, Hikone, Japan. [10]Space Science and Engineering Center, University of Wisconsin–Madison, Madison, WI, USA. [11]Graduate School of Frontier Sciences, The University of Tokyo, Kashiwa, Japan. [12]Department of Space and Astronautical Science, School of Physical Sciences, The Graduate University for Advanced Studies (SOKENDAI), Tokyo, Japan.
***Corresponding author. Email: horinout@ees.hokudai.ac.jp**

this maximum requires eddy AM transport to that region.

We begin by examining the mean meridional circulation and its effects. To determine the circulation directly from wind observations is difficult even for Earth's atmosphere. For Venus, the most credible estimates are provided by observations of solar and thermal radiations, from which we constructed a model (*16*). The resulting w^r and v^r indicate an upwelling of a few millimeters per second in the equatorial upper cloud layer and a poleward flow of ~1 m s^{-1} at around the mid-latitude cloud top, respectively (Fig. 1).

We introduce an idealized zonal wind (eastward velocity component) structure into the model (*16*). The upwelling in the equatorial cloud layer acts to decelerate the SR by ~1 m s^{-1} day^{-1} at the AM peak around the equatorial cloud top (Fig. 1C), which must be compensated by eddy acceleration.

At mid-to-high latitudes, negative (or positive) acceleration occurs through the $-\boldsymbol{v}^r \cdot \nabla M$ term above (or below) ~65 km (Fig. 1C). We expect that hydrodynamic instabilities inevitably induced by the circulation (*19*, *20*) compensate for these accelerations (*16*) (fig. S2), so we infer that the AM distribution at mid-to-high latitudes can be formed more-or-less spontaneously.

We provide further constraints using data from the Akatsuki spacecraft orbiting Venus. We analyzed observations taken between December 2015 and December 2018, divided into five subperiods, starting 7 December 2015, 21 September 2016, 21 April 2017, 1 December 2017, and 16 June 2018 (ending on 7 December 2018). Using a cloud-tracking method with quality control (*21*, *22*), we derived wind estimates using Akatsuki's Ultraviolet Imager (UVI) (*23*) at the wavelengths of 365 and 283 nm. We derived horizontal velocities near the cloud top over regions of about 1000 km by 1000 km with a time resolution of 4 hours (*16*) (uncertainties shown in fig. S3A). The 283-nm results capture winds at slightly higher altitudes than the 365-nm results, presumably by a few kilometers (*24*).

The meridional component of the Eliassen-Palm flux F_y is likely dominated by the $f_{yv} \equiv -\langle u^* v^* \rangle \cos\varphi$ term (*16*), where u and v are zonal and meridional (south-to-north) winds, respectively, and the angle brackets and asterisks represent zonal mean and the deviation from it, respectively. We employ a coordinate system based on local time τ_L, latitude φ, and time t, where τ_L is defined by assigning 0 to 24 hours to longitudes relative to the antisolar point. Temporally averaged winds in this system $(\bar{u}, \bar{v})$ consist of zonal and temporal mean winds (u_0, v_0) and the flow associated with the thermal tides (u_t, v_t). The mean winds from the 3 years are shown in fig. S3.

We estimated (u_t, v_t) by subtracting the model estimated (u_0, v_0) from the observationally derived $(\bar{u}, \bar{v})$ for each of the UVI image subperiods (*16*). The resulting tidal AM flux, $\langle u_t v_t \rangle \cos\varphi$, is shown in Fig. 2A. It is positive (negative) in the northern (southern) hemisphere, which indicates equatorward transport of westward AM in both hemispheres. The consistency between our results for different subperiods (Fig. 2A) demonstrates the robustness of our estimation. The tidal meridional AM flux convergence acts to accelerate the SR between 20°S and 20°N, reaching peak values around −0.6 (−0.9) m s^{-1} day^{-1} for the 365-nm (283-nm) case, which indicates the acceleration of westward SR (Fig. 2C). The estimates depend on u_0 and v_0; we performed a sensitivity study (*16*) (figs. S9 and S10) to verify the robustness of the estimates, although some uncertainty remains (*16*). Thermal tide carries eastward AM, so our result is consistent with the action-reaction law on the tide generation by solar heating, which is stronger at lower latitudes.

We next examine the AM transport by transient motions other than thermal tides. We use $(u', v') \equiv (u - \tilde{u}, v - \tilde{v})$, where $(\tilde{u}, \tilde{v})$ are the averages of (u, v) over ±15 days at fixed τ_L and φ. Figure 2B shows the AM flux $\overline{\langle u'v' \rangle} \cos\varphi$ (solid lines) after the effects of the correlation between the errors in u' and v' have been subtracted using the error covariance (*16*) (fig. S5). Prior to subtraction, the error covariance enhanced the AM flux by a factor of 1.5. However, this effect is very small (*16*) for $\overline{\langle u^\# v^\# \rangle} \cos\varphi$, where $(u^\#, v^\#)$ is (u', v') smoothed by daily averaging, which is time averaging over each day at fixed τ_L and φ. The UVI was typically operated for 16 hours each day, so the daily averaging smooths winds over several thousand kilometers in longitude because of the SR.

The derived AM flux (Fig. 2B) is opposite to that provided by the thermal tides (Fig. 2A). The consistency between subperiods again indicates the robustness of our method. Unlike the tidal case, both wavelengths produce quantitatively consistent results, which suggests a deceleration of the SR that is weaker than the tidal acceleration (Fig. 2C). The AM flux computed with $(u^\#, v^\#)$ (Fig. 2B) is slightly weaker than that computed with (u', v'), which suggests that a small fraction of the AM flux resides at high frequencies (periods shorter than 2 days) or, equivalently, at small scales.

Next, we consider the nature of transient disturbances and their roles in the AM transport. Figure 3A presents an example of the spatial distribution of wind disturbances using $(u^\#, v^\#)$ and the absolute vorticity computed with $(u^\# + \tilde{u}, v^\# + \tilde{v})$, constructed by shifting by 90° per day, approximating the advection by SR; more examples are shown in figs. S6 and S7. The smooth transition over adjacent days indicates that overall temporal evolution is slow. The distribution of $u^\#$ suggests the dominance of variability at zonal wave number

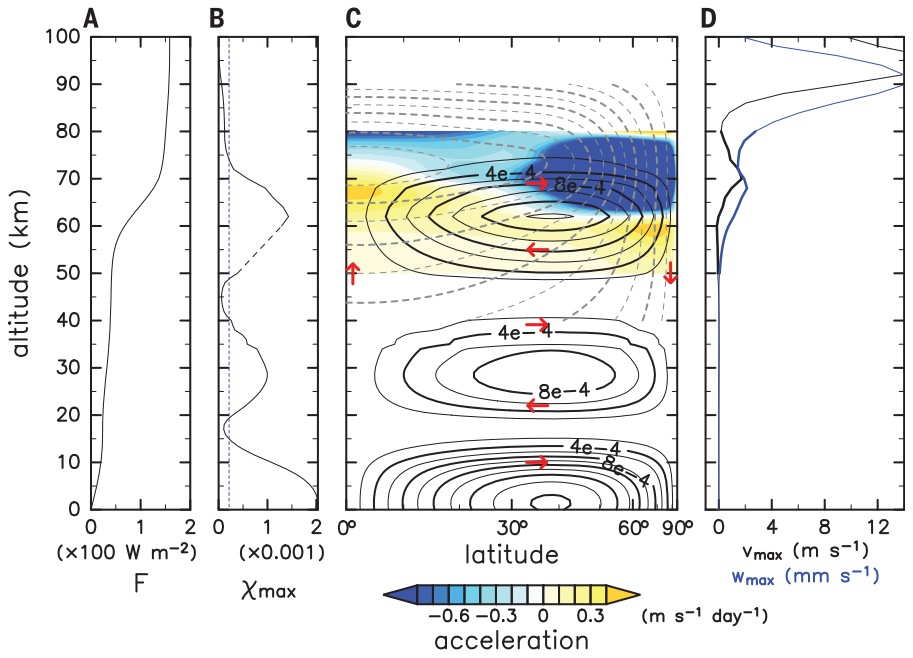

Fig. 1. Idealized model calculation of the meridional circulation derived from solar heating and the advective acceleration of idealized zonal AM. (**A**) Global-mean downward solar flux (F). (**B**) The mass stream function χ derived from the solar heating at φ_{max} = 38.2°. The dashed line indicates interpolation and the blue dotted line indicates the value at 74 km. (**C**) Hemispheric structure of χ (black contours; flow directions are indicated schematically by red arrows); idealized M between 40 and 90 km (gray dashed contours); and advective zonal acceleration $-(a \cos\varphi)^{-1} \boldsymbol{v}^r \cdot \nabla M$ between 50 and 80 km (color shading). (**D**) v^r at φ_{max} (black line) and w^r at the equator (blue line). Thicker lines highlight values between 50 and 80 km.

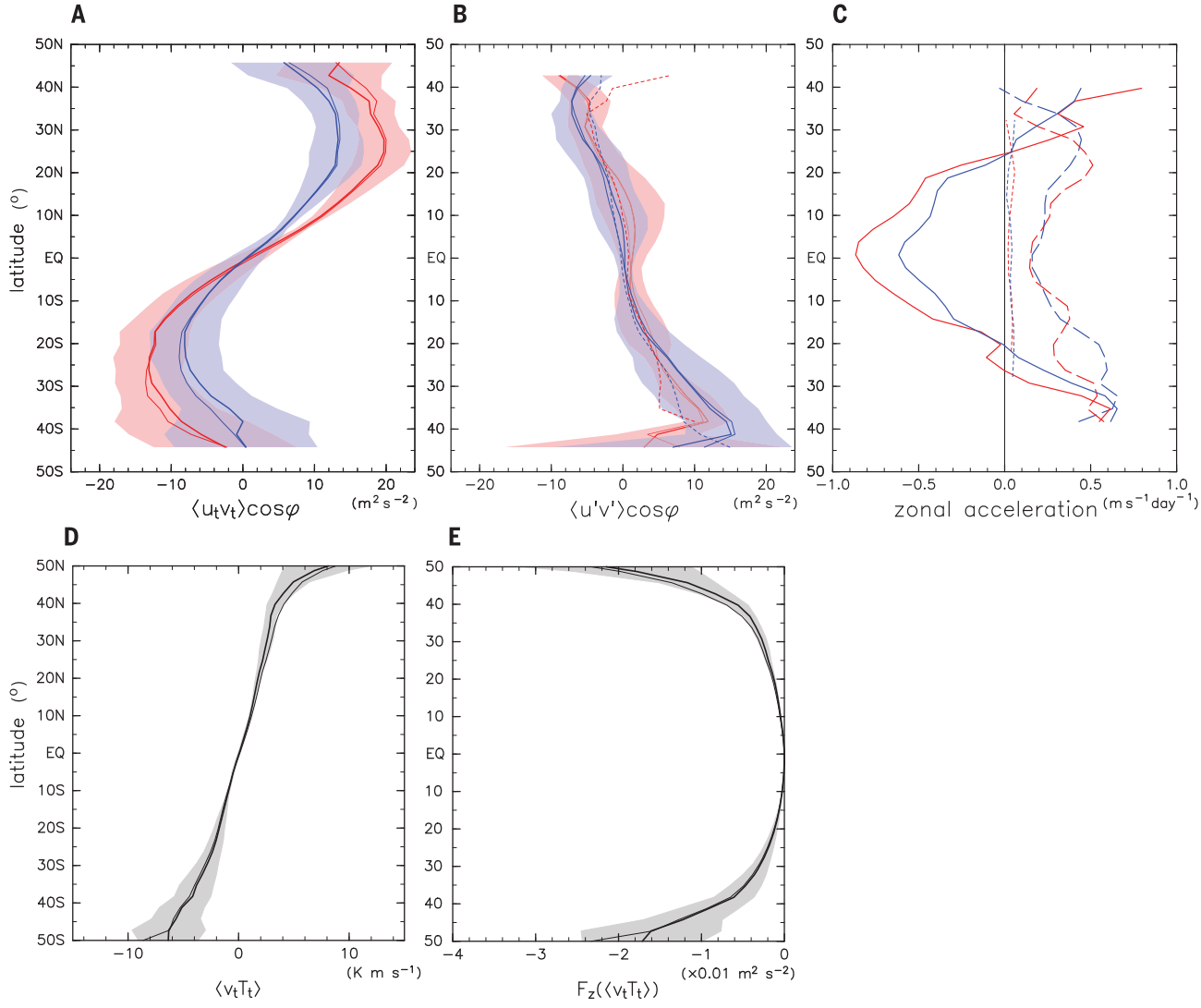

Fig. 2. Meridional AM flux and its divergence due to thermal tide and transient disturbances at the cloud top and tidal heat flux. (**A**) Mean tidal flux (thick lines: red, from 283-nm images; blue, from 365-nm images) obtained by averaging $\langle u_t v_t \rangle \cos\varphi$ for the second to fifth subperiods; the first subperiod was excluded because the local time coverage was too narrow to estimate u_0. Shaded areas indicate the standard deviation among subperiods. Thin solid lines are like the solid lines but were obtained without subperiod division. (**B**) As in (A) but for transient disturbances, $\overline{\langle u'v' \rangle} \cos\varphi$, from the five subperiods. Biases arising from the error covariance between u' and v' have been subtracted. Dotted lines are as the thin solid lines, except they are obtained from daily-mean winds ($u^{\#}$, $v^{\#}$). (**C**) Zonal acceleration by the meridional AM flux convergence by thermal tides ($-\frac{\partial \langle u_t v_t \rangle \cos^2\varphi}{a \cos^2\varphi \, \partial\varphi}$; solid lines) and transient disturbances ($-\frac{\partial \langle u'v' \rangle \cos^2\varphi}{a \cos^2\varphi \, \partial\varphi}$; dashed lines) based on the thin solid lines in (A) and (B). Dotted lines are the same, but for Rossby waves obtained from the co-spectra after a 1:2:1 smoothing with latitude. Colors are as in (A). (**D**) Mean tidal heat flux by diurnal tides obtained by averaging $\langle v_t T_t \rangle_1$ for the five subperiods with v_t at 365 nm (thick solid line). Shaded areas indicate the standard deviation among subperiods. Thin solid line was obtained without subperiod division. (**E**) As in (D) but for $f_{zT1} \equiv \zeta_a S^{-1} \langle v_t T_t \rangle_1 \cos\varphi$ (using absolute vorticity ζ_a in fig. S3B and the stability $S = 8 \times 10^{-3}$ K m^{-1}).

(the wave number along the longitude direction in radians) equal to 1—i.e., a single wave extending over latitudinal circles—which is consistent with Rossby waves (*25*, *26*). We derived power spectra of $u^{\#}$ (Fig. 3B), which reach a maximum at a frequency of around 0.2 day^{-1}, corresponding to a ground-based period of 5.2 days. The sign of the imaginary part of cross-spectrum (fig. S8C) that arises from quadrature-phase lags is also consistent with a Rossby wave structure. A secondary spectral peak appears in Fig. 3B at 0.24 day^{-1} (corresponding to a ground-based period of 4 days), which is consistent with Kelvin waves (*25*, *26*). The equivalent signal in $v^{\#}$ away from the equator (fig. S8B) indicates a distortion that is absent in pure Kelvin waves.

In addition to the waves, turbulence-like motion is apparent in Fig. 3A (and fig. S6). The nonmonotonic change of absolute vorticity with latitudes around 30°N indicates overturning motion to generate turbulence. Meandering (often cross-equatorial) flows prevail near the equator where the directions of absolute-vorticity gradients vary substantially, which is difficult to explain with simple superpositions of Rossby waves. These flows are also unlike gravity waves. Therefore, we conclude that some portion of the transient wind disturbances are due to horizontal turbulence.

The real part of the cross-spectrum (co-spectrum) of $u^{\#}$ and $v^{\#}$ decomposes their correlation along frequencies (Fig. 3C). The signs at different frequencies almost always agree at latitudes poleward of 20°N and 20°S. The co-spectrum of two random signals has an equal probability to be positive or negative, so this agreement cannot be explained by coincidence or by noise. From the co-spectra, we

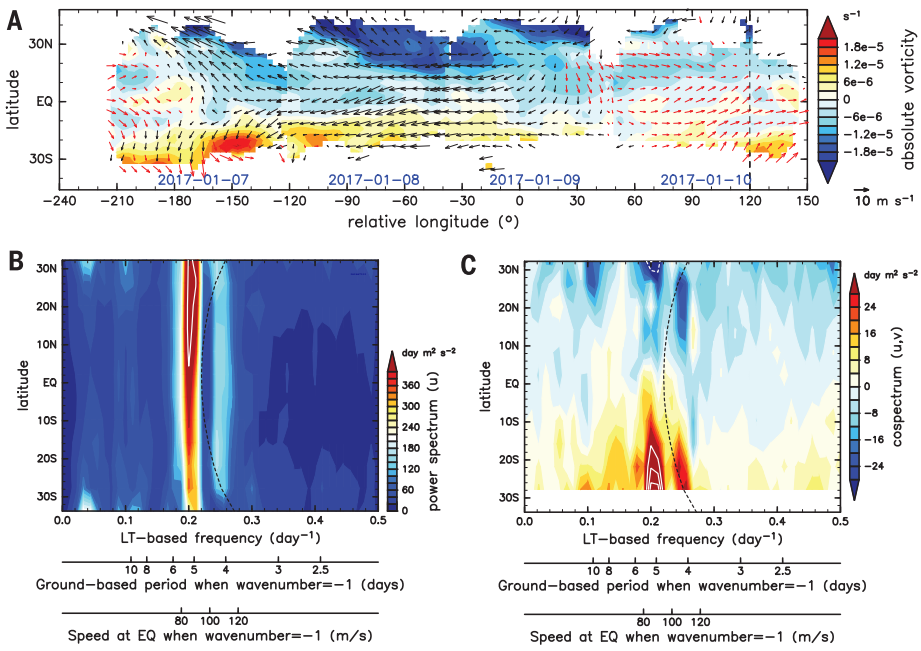

Fig. 3. Example wind disturbances (365 nm) and corresponding spectra. (**A**) Daily-mean transient winds ($u^{\#}$, $v^{\#}$) (arrows; red if $u^{\#} > 0$) and absolute vorticity (colored shading) for the period 7 to 10 January 2017, overlaid by shifting 90° per day. (**B**) Power spectra of $u^{\#}$ obtained from the second to the fourth subperiods (colored shading; the white contour is at 500 $m^2\ s^{-2}$ day). Frequency is for observers at fixed local time (LT), τ_L; the corresponding ground-based period (days) and zonal propagation speed at the equator (EQ) when the disturbances have zonal wave number 1 and move westwards (negative wave number) are shown on the abscissa. (**C**) Same as in (B) but for co-spectra between $u^{\#}$ and $v^{\#}$ (white contours are at an interval of 20 $m^2\ s^{-2}$ day).

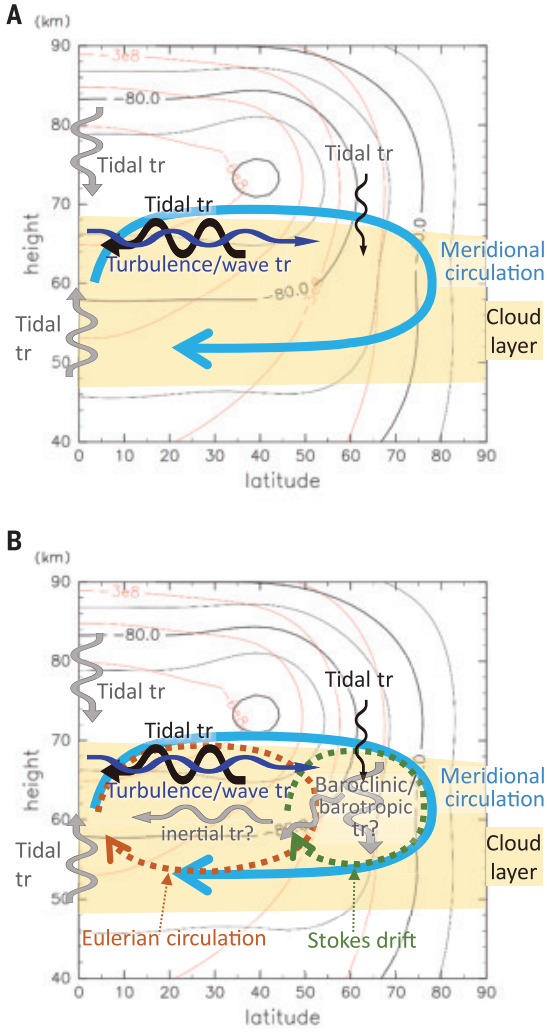

Fig. 4. Schematic illustration of the suggested AM balance in the cloud layer of Venus. (**A**) Processes quantified or estimated in this study. (**B**) Same as (A) with our suggested interpretation overlain. Wavy arrows indicate eddy transport of SR's negative AM; those labeled with "tr" represent transport processes that we quantified (black, blue) or estimated (gray), and those with "tr?" in (B) represent suggested transport processes. Their widths crudely represent their relative contributions to the AM transport. The cyan curved arrow shows the mean meridional circulation that acts to homogenize the AM. The dotted curved arrows are expected contributions to the circulation (*16*). The background shows the cloud layer (pale orange shading), idealized distributions of $\langle u \rangle$ (black contours; meters per second), and M (red contours; square meters per second).

computed the contribution of the Rossby-wave periods (frequencies 0.1888 to 0.2222 day^{-1}) to the meridional AM flux (Fig. 2C). This is only a small fraction of the AM transport, at least between 30°S and 30°N. The contribution of the Kelvin waves is even smaller. We therefore suggest that horizontal turbulence at broad frequency (together with waves) collectively decelerates the SR. This idea opposes the earlier expectation that turbulent AM transport accelerates SR, which is required in the so-called classical Gierasch-Rossow-Williams mechanism in which AM transport by meridional circulation and AM transport by turbulence balance one another (*1*, *27*, *28*).

We further investigate the vertical component of $\boldsymbol{F}$, $F_z \propto f_{zw} + f_{zT}$, where f_{zw} and f_{zT} are terms proportional to $\langle u^* w^* \rangle$ and $\langle v^* T^* \rangle$, respectively (*16*); here, w is vertical velocity. We estimated the meridional heat flux by the diurnal (i.e., zonal wave number 1) components of the thermal tides (diurnal tides), $\langle v_t T_t \rangle_1 \propto f_{zT}$, by using the brightness temperature obtained from Akatsuki's Longwave Infrared Camera (LIR) (*16*). This shows that the tidal heat flux is poleward (Fig. 2D). The diurnal tides are dominated by a Rossby wave at mid-to-high latitudes (*29*). Theoretically, the F_z component of a Rossby wave is dominated by f_{zT}, so its estimation (Fig. 2E) indicates that the wave transports negative AM downward. Its typical magnitude is 1×10^{-2} $m^2\ s^{-2}$ at midlatitudes. This indicates that its effect on SR is minor because the expected acceleration is ~0.1 m s^{-1} day^{-1} (this value follows if the vertical convergence of f_{zT} due to tidal excitation occurs over a height scale of 10 km).

The entire semidiurnal (i.e., zonal wave number 2) components of the thermal tides (semidiurnal

tides) and the low-latitude portion of the diurnal tides are dominated by gravity waves (*29*). They are expected to transport AM to its upgradient to accelerate the SR (*9*, *30*). Observational estimations of F_z associated with gravity waves are not available because it is dominated by f_{zw}, and thus includes vertical velocity. We instead performed an order-of-magnitude estimation (*16*), finding that the acceleration associated with $\frac{\partial F_z}{\partial z}$ is likely ~1 m s^{-1} day^{-1} or smaller. Therefore, the tidal vertical AM transport can contribute to the acceleration of SR at low latitudes by an amount similar to the contribution of the horizontal transport.

The Akatsuki data have allowed us to estimate the horizontal AM transport by thermal tides, planetary-scale Rossby waves, and other transient disturbances. The thermal tides transport westward (super-rotating) AM equatorward, contributing to the maintenance of the SR against the homogenization by the meridional circulation. The other motions act in the opposite direction at low latitudes. We also estimated vertical AM transport by thermal tides. The AM balance that governs the maintenance of the SR in the cloud layer is schematically illustrated in Fig. 4. We suggest that the SR maintenance mechanism is a version of the nonclassical Gierasch-Rossow-Williams scenario (*1*), which extends the classical one to include AM transport by tidal waves.

REFERENCES AND NOTES

1. A. Sánchez-Lavega, S. Lebonnois, T. Imamura, P. Read, D. Luz, *Space Sci. Rev.* **212**, 1541–1616 (2017).
2. P. L. Read, S. Lebonnois, *Annu. Rev. Earth Planet. Sci.* **46**, 175–202 (2018).
3. A. P. Showman, L. M. Polvani, *Astrophys. J.* **738**, 71 (2011).
4. R. Hide, *J. Atmos. Sci.* **26**, 841–853 (1969).
5. S. S. Limaye, V. E. Suomi, *J. Atmos. Sci.* **38**, 1220–1235 (1981).
6. W. B. Rossow, A. D. del Genio, T. Eichler, *J. Atmos. Sci.* **47**, 2053–2084 (1990).
7. S. S. Limaye, *J. Geophys. Res.* **112**, E04S09 (2007).
8. M. Yamamoto, M. Takahashi, *J. Atmos. Sci.* **60**, 561–574 (2003).
9. M. Takagi, Y. Matsuda, *J. Geophys. Res.* **112**, D09112 (2007).
10. C. Lee, S. R. Lewis, P. L. Read, *J. Geophys. Res.* **112**, E04S11 (2007).
11. S. Lebonnois *et al.*, *J. Geophys. Res.* **115**, E06006 (2010).
12. N. Sugimoto, M. Takagi, Y. Matsuda, *Geophys. Res. Lett.* **41**, 7461–7467 (2014).
13. S. Lebonnois, N. Sugimoto, G. Gilli, *Icarus* **278**, 38–51 (2016).
14. J. M. Mendonça, P. L. Read, *Planet. Space Sci.* **134**, 1–18 (2016).
15. N. Sugimoto, M. Takagi, Y. Matsuda, *Geophys. Res. Lett.* **46**, 1776–1784 (2019).
16. Materials and methods are available as supplementary materials.
17. G. Schubert *et al.*, *J. Geophys. Res.* **85**, 8007–8025 (1980).
18. V. V. Kerzhanovich, S. S. Limaye, *Adv. Space Res.* **5**, 59–83 (1985).
19. S. I. Iga, Y. Matsuda, *J. Atmos. Sci.* **62**, 2514–2527 (2005).
20. M. Takagi, Y. Matsuda, *Geophys. Res. Lett.* **33**, L14807 (2006).
21. S. Ikegawa, T. Horinouchi, *Icarus* **271**, 98–119 (2016).
22. T. Horinouchi *et al.*, *Meas. Sci. Technol.* **28**, 085301 (2017).
23. A. Yamazaki *et al.*, *Earth Planets Space* **70**, 23 (2018).
24. T. Horinouchi *et al.*, *Earth Planets Space* **70**, 10 (2018).
25. T. Kouyama, T. Imamura, M. Nakamura, T. Satoh, Y. Futaana, *J. Geophys. Res.* **118**, 37–46 (2013).
26. M. Imai *et al.*, *J. Geophys. Res. Planets* **124**, 2635–2659 (2019).
27. P. J. Gierasch, *J. Atmos. Sci.* **32**, 1038–1044 (1975).
28. W. B. Rossow, G. P. Williams, *J. Atmos. Sci.* **36**, 377–389 (1979).
29. T. Kouyama *et al.*, *Geophys. Res. Lett.* **46**, 9457–9465 (2019).
30. M. Newman, C. Leovy, *Science* **257**, 647–650 (1992).
31. S. Murakami *et al.*, Venus Climate Orbiter Akatsuki UVI Longitude-Latitude Map Data, v1.0, JAXA Data Archives and Transmission System (2018); http://doi.org/10.17597/isas.darts/vco-00016.
32. S. Murakami *et al.*, Venus Climate Orbiter Akatsuki LIR Longitude-Latitude Map Data, v1.0, JAXA Data Archives and Transmission System (2018); http://doi.org/10.17597/isas.darts/vco-00019.
33. S. Murakami *et al.*, Venus Climate Orbiter Akatsuki IR2 Longitude-Latitude Map Data, v1.0, JAXA Data Archives and Transmission System (2018); http://doi.org/10.17597/isas.darts/vco-00018.

ACKNOWLEDGMENTS

We thank numerous colleagues who supported the Akatsuki project and three anonymous reviewers who provided comments that helped improve this paper. **Funding:** This study was supported by the Japanese Society for Promotion of Science grants-in-aid 16H02231, 16H02225, 19H05605, and 19K14789 and by NASA grant NNX16AC79G. J.P. acknowledges the Japan Aerospace Exploration Agency's International Top Young Fellowship. **Author contributions:** T.H. derived the wind estimations, conducted analysis, produced the figures, and wrote the text. K.O., S.M., M.Tak., T.K., and T.H. developed the cloud-tracking program. Y.-Y.H., J.P., S.S.L., and T.S. contributed to the interpretation. S.W., M.Y., and A.Y. calibrated the UVI radiance. T.K., M.Tag., and T.F. derived the temperatures using Akatsuki's LIR. K.O. and M.Tak. refined the geographic data mapping. T.M.S., T.S., T.I., S.M., and M.N. coordinated Akatsuki's observations and processed the original data. **Competing interests:** The authors declare no competing interests. **Data and materials availability:** The Akatsuki data are available at (*31*–*33*). The data derived in this paper, including the cloud tracking results and the results shown in the figures, are available at https://darts.isas.jaxa.jp/pub/akatsuki/paper/Horinouchi_2020/ and in table S1.

SUPPLEMENTARY MATERIAL

science.sciencemag.org/content/368/6489/405/suppl/DC1
Materials and Methods
Supplementary Text
Figs. S1 to S11
Table S1
References (*34*–*56*)

11 September 2019; accepted 27 March 2020
10.1126/science.aaz4439

CORONAVIRUS

Crystal structure of SARS-CoV-2 main protease provides a basis for design of improved α-ketoamide inhibitors

Linlin Zhang[1,2], Daizong Lin[1,3], Xinyuanyuan Sun[1,2], Ute Curth[4], Christian Drosten[5], Lucie Sauerhering[6,7], Stephan Becker[6,7], Katharina Rox[8,9], Rolf Hilgenfeld[1,2]*

The coronavirus disease 2019 (COVID-19) pandemic caused by severe acute respiratory syndrome–coronavirus 2 (SARS-CoV-2) is a global health emergency. An attractive drug target among coronaviruses is the main protease (M^{pro}, also called $3CL^{pro}$) because of its essential role in processing the polyproteins that are translated from the viral RNA. We report the x-ray structures of the unliganded SARS-CoV-2 M^{pro} and its complex with an α-ketoamide inhibitor. This was derived from a previously designed inhibitor but with the P3-P2 amide bond incorporated into a pyridone ring to enhance the half-life of the compound in plasma. On the basis of the unliganded structure, we developed the lead compound into a potent inhibitor of the SARS-CoV-2 M^{pro}. The pharmacokinetic characterization of the optimized inhibitor reveals a pronounced lung tropism and suitability for administration by the inhalative route.

In December 2019, a new coronavirus caused an outbreak of pulmonary disease in the city of Wuhan, the capital of Hubei province in China, and has since spread globally (*1*, *2*). The virus has been named severe acute respiratory syndrome–coronavirus 2 (SARS-CoV-2) (*3*) because the RNA genome is about 82% identical to that of the SARS coronavirus (SARS-CoV); both viruses belong to clade b of the genus *Betacoronavirus* (*1*, *2*). The disease caused by SARS-CoV-2 is called coronavirus disease 2019 (COVID-19). Whereas at the beginning of the outbreak, cases were connected to the Huanan seafood and animal market in Wuhan, efficient human-to-human transmission led to exponential growth in the number of cases. On 11 March 2020, the World Health Organization (WHO) declared the outbreak a pandemic. As of 9 April, there were >1,500,000 cumulative cases globally, with a ~5.9% case fatality rate.

One of the best-characterized drug targets among coronaviruses is the main protease (M^{pro}, also called $3CL^{pro}$) (*4*). Along with the papain-like protease(s), this enzyme is essential for processing the polyproteins that are

[1]Institute of Biochemistry, Center for Structural and Cell Biology in Medicine, University of Lübeck, 23562 Lübeck, Germany. [2]German Center for Infection Research (DZIF), Hamburg-Lübeck-Borstel-Riems Site, University of Lübeck, 23562 Lübeck, Germany. [3]Changchun Discovery Sciences Ltd., 789 Shunda Road, Changchun, Jilin 130012, China. [4]Institute for Biophysical Chemistry, Hannover Medical School, 30625 Hannover, Germany. [5]Institute of Virology, Charité Universitätsmedizin Berlin, 10117 Berlin, Germany. [6]Institute of Virology, University of Marburg, 35043 Marburg, Germany. [7]German Center for Infection Research (DZIF), Marburg-Gießen-Langen Site, University of Marburg, 35043 Marburg, Germany. [8]Department of Chemical Biology, Helmholtz Center for Infection Research (HZI), 38124 Braunschweig, Germany. [9]German Center for Infection Research (DZIF), Hannover-Braunschweig Site, Helmholtz Center for Infection Research, 38124 Braunschweig, Germany.
***Corresponding author. Email: rolf.hilgenfeld@uni-luebeck.de**

translated from the viral RNA (*5*). The M^{pro} operates at no fewer than 11 cleavage sites on the large polyprotein 1ab (replicase 1ab, ~790 kDa); the recognition sequence at most sites is Leu-Gln↓(Ser, Ala, Gly) (↓ marks the cleavage site). Inhibiting the activity of this enzyme would block viral replication. Because no human proteases with a similar cleavage specificity are known, such inhibitors are unlikely to be toxic.

Previously, we designed and synthesized peptidomimetic α-ketoamides as broad-spectrum inhibitors of the main proteases of betacoronaviruses and alphacoronaviruses as well as the 3C proteases of enteroviruses (*6*). The best of these compounds (**11r**; Fig. 1) showed an half-maximal effective concentration (EC_{50}) of 400 pM against Middle East respiratory syndrome–coronavirus (MERS-CoV) in Huh7 cells as well as low-μM EC_{50} values against SARS-CoV and a whole range of enteroviruses in various cell lines, although the antiviral activity seemed to depend to a great extent on the cell type used in the experiments (*6*). To improve the half-life of the compound in plasma, we modified **11r** by hiding the P3-P2 amide bond within a pyridone ring (Fig. 1, green ovals) in the expectation that this might prevent cellular proteases from accessing this bond and cleaving it. Further, to increase the solubility of the compound in plasma and to reduce its binding to plasma proteins, we replaced the hydrophobic cinnamoyl moiety by the somewhat less hydrophobic Boc group (Fig. 1, red ovals) to give **13a** (see scheme S1 for synthesis).

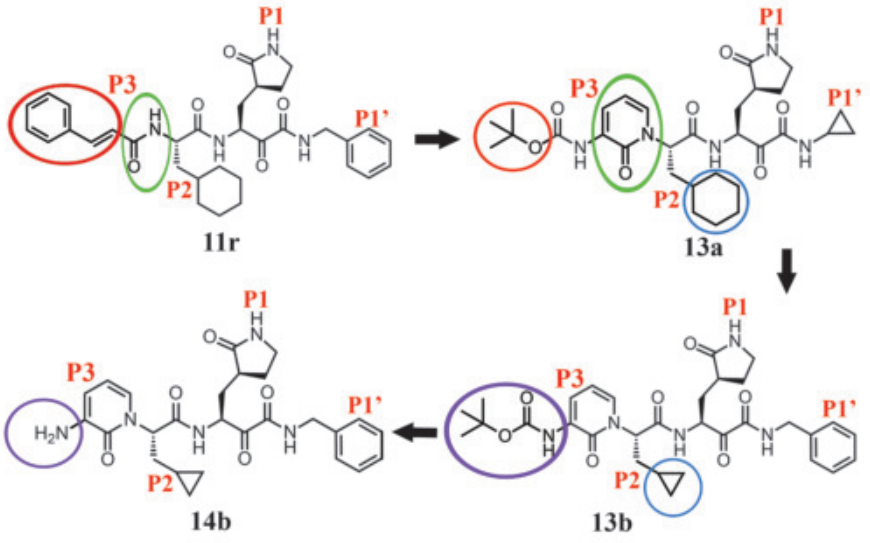

Fig. 1. Chemical structures of α-ketoamide inhibitors 11r, 13a, 13b, and 14b. Colored ovals and circles highlight the modifications from one development step to the next (see text).

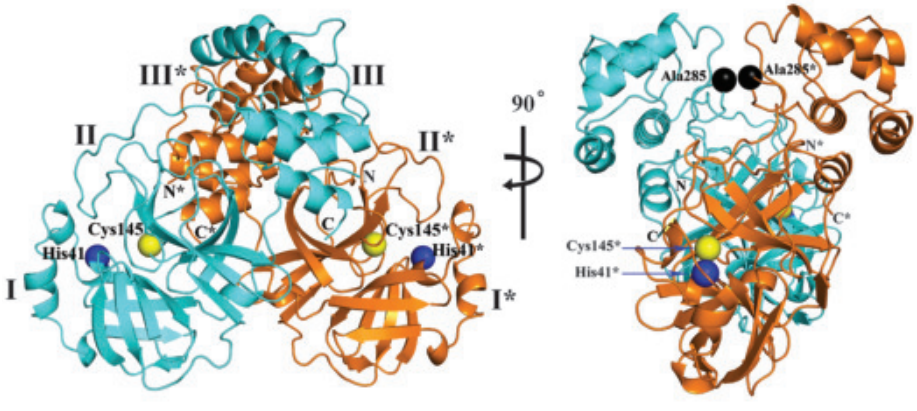

Fig. 2. Three-dimensional structure of SARS-CoV-2 M^{pro} in two different views. One protomer of the dimer is shown in light blue, the other one in orange. Domains are labeled by Roman numerals. Amino acid residues of the catalytic site are indicated as yellow spheres for Cys^{145} and blue spheres for His^{41}. Asterisks mark residues from protomer B (orange). Black spheres indicate the positions of Ala^{285} for each of the two domains III (see text). Chain termini are labeled N and C for molecule A (light blue) and N* and C* for molecule B (orange).

To examine whether the introduced pyridone ring is compatible with the three-dimensional structure of the target, we determined the crystal structure, at 1.75 Å resolution, of the M^{pro} of SARS-CoV-2 (Fig. 2). The three-dimensional structure is highly similar to that of the SARS-CoV M^{pro}, as expected from the 96% sequence identity (see fig. S8); the root mean square deviation between the two free-enzyme structures is 0.53 Å for all Cα positions [comparison between SARS-CoV-2 M^{pro} structure and SARS-CoV M^{pro}, PDB entry 2BX4 (*7*)]. The chymotrypsin-like and picornavirus 3C protease–like domains I and II (residues 10 to 99 and 100 to 182, respectively) are six-stranded antiparallel β barrels that harbor the substrate-binding site between them. Domain III (residues 198 to 303), a globular cluster of five helices, is involved in regulating the dimerization of the M^{pro}, mainly through a salt-bridge interaction between Glu^{290} of one protomer and Arg^{4} of the other (*8*). The tight dimer formed by SARS-CoV-2 M^{pro} has a contact interface of ~1394 $Å^2$, predominantly between domain II of molecule A and the NH_2-terminal residues ("N-finger") of molecule B, with the two molecules oriented perpendicular to one another (Fig. 2). Dimerization of the enzyme is necessary for catalytic activity, because the N-finger of each of the two protomers interacts with Glu^{166} of the other protomer and thereby helps shape the S1 pocket of the substrate-binding site (*9*). To reach this interaction site, the N-finger is squeezed in between domains II and III of the parent monomer and domain II of the other monomer.

Interestingly, in the SARS-CoV but not in the SARS-CoV-2 M^{pro} dimer, there is a polar interaction between the two domains III involving a 2.60-Å hydrogen bond between the side-chain hydroxyl groups of residue Thr^{285} of each protomer, supported by a hydrophobic contact between the side chain of Ile^{286} and Thr^{285} Cγ2. In SARS-CoV-2, the threonine is replaced by alanine (indicated by the black spheres in Fig. 2) and the isoleucine by leucine (fig. S8). It was previously shown that replacing Ser^{284}, Thr^{285}, and Ile^{286} by alanine residues in SARS-CoV M^{pro} leads to enhancement of the catalytic activity of the protease by a factor of 3.6, concomitant with a slightly closer packing of the two domains III of the dimer against one another (*10*). This was accompanied by changes in enzyme dynamics that transmit the effect of the mutation to the catalytic center. Indeed, the Thr^{285} → Ala replacement observed in the SARS-CoV-2 M^{pro} also allows the two domains III to approach each other more closely (the distance between

the Cα atoms of residues 285 in molecules A and B is 6.77 Å in SARS-CoV M^{pro} and 5.21 Å in SARS-CoV-2 M^{pro}, and the distance between the centers of mass of the two domains III shrinks from 33.4 Å to 32.1 Å). However, the catalytic efficiency of SARS-CoV-2 M^{pro} is only slightly higher, if at all [turnover number (k_{cat})/Michaelis constant (K_m) = 3426.1 ± 416.9 s^{-1} M^{-1}] than that of SARS-CoV M^{pro} (k_{cat}/K_m = 3011.3 ± 294.6 s^{-1} M^{-1}). Further, the estimated dissociation constant of dimerization is the same (~2.5 μM) for the two enzymes, as determined by analytical ultracentrifugation (fig. S10).

We used this crystal structure to dock the α-ketoamide **13a**; this suggested that the pyridone ring might have some steric clash with the side chain of Gln^{189}. However, in our previous work (*6*), we had found Gln^{189} to be quite flexible, and therefore we went ahead with **13a** as a lead. The plasma half-life of this compound in mice was increased by a factor of ~3 relative to **11r** (from 0.3 hours to 1.0 hours), the in vitro kinetic plasma solubility was improved by a factor of ~19 (from 6 μM for **11r** to 112 μM for **13a**), and the thermodynamic solubility increased by a factor of ~13 (from 41 μM to 530 μM). Binding to mouse plasma protein was reduced from 99% to 97% [many drugs have plasma protein binding of >90% (*11*)]. However, relative to **11r** (IC_{50} = 0.18 ± 0.02 μM), the structural modification led to some loss of inhibitory activity against the main protease of SARS-CoV-2 (IC_{50} = 2.39 ± 0.63 μM) as well as the 3C proteases ($3C^{pro}$) of enteroviruses. **11r** was designed for broad-spectrum activity, with the P2 cyclohexyl moiety intended to fill a pocket in the enterovirus $3C^{pro}$. The S2 pocket of the betacoronavirus M^{pro} (Fig. 3) features substantial plasticity, enabling it to adapt to the shape of smaller inhibitor moieties (*6*). To enhance the antiviral activity against betacoronaviruses of clade b (SARS-CoV-2 and SARS-CoV), we sacrificed the goal of broad-spectrum activity and replaced the P2 cyclohexyl moiety of **13a** by the smaller cyclopropyl in **13b** (Fig. 1, blue circles). Here, we present x-ray crystal structures in two different crystal forms, at 1.95 and 2.20 Å resolution, of the complex between α-ketoamide **13b** and the M^{pro} of SARS-CoV-2. One structure is in space group *C*2 (Fig. 3), where both protomers of the M^{pro} dimer are bound by crystal symmetry to have identical conformations; the other is in space group $P2_12_12_1$, where the two protomers are independent of each other and free to adopt different conformations. Indeed, we find that in the latter crystal structure, the key residue Glu^{166} adopts an inactive conformation in protomer B (as evidenced by its distance from His^{172} and the lack of H-bonding interaction with the P1 moiety of the inhibitor), even though compound **13b** is bound in the same mode as in molecule A. This phenomenon has also been observed with the SARS-CoV M^{pro} (*12*) and is consistent with the half-site activity described for this enzyme (*13*). In all copies of the inhibited SARS-CoV-2 M^{pro}, the inhibitor binds to the shallow substrate-binding site at the surface of each protomer, between domains I and II (Fig. 3).

Through the nucleophilic attack of the catalytic Cys^{145} onto the α-keto group of the inhibitor, a thiohemiketal is formed in a reversible reaction. This is clearly reflected in the electron density (Fig. 3, inset); the stereochemistry of this chiral moiety is *S* in all copies of compound **13b** in these structures. The oxyanion (or hydroxyl) group of this thiohemiketal is stabilized by a hydrogen bond from His^{41}, whereas the amide oxygen of **13b** accepts a hydrogen bond from the main-chain amides

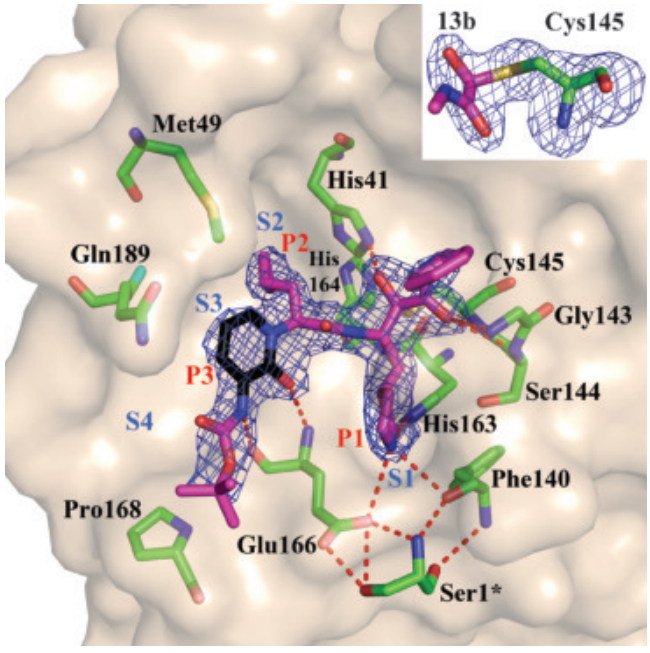

Fig. 3. Compound 13b in the substrate-binding cleft located between domains I and II of the M^{pro} in the monoclinic crystal form (space group *C*2). $F_{obs} - F_{calc}$ density is shown for the inhibitor (contouring level 3σ). Carbon atoms of the inhibitor are magenta, except in the pyridone ring, which is black; oxygen atoms are red, nitrogens blue, and sulfur yellow. Light blue symbols S*n* (*n* = 1, 2, 3...) indicate the canonical binding pockets for moieties P*n* (*n* = 1, 2, 3...) (red symbols) of the peptidomimetic inhibitor. Hydrogen bonds are indicated by dashed red lines. Note the interaction between Ser^{1*}, the N-terminal residue of molecule B, and Glu^{166} of molecule A, which is essential for keeping the S1 pocket in the correct shape and the enzyme in the active conformation. Inset: Thiohemiketal formed by the nucleophilic attack of the catalytic cysteine onto the α-carbon of the inhibitor. The stereochemistry of the α-carbon is *S*. $F_{obs} - F_{calc}$ density (contoured at 3σ) is shown in blue. See fig. S9 for more details.

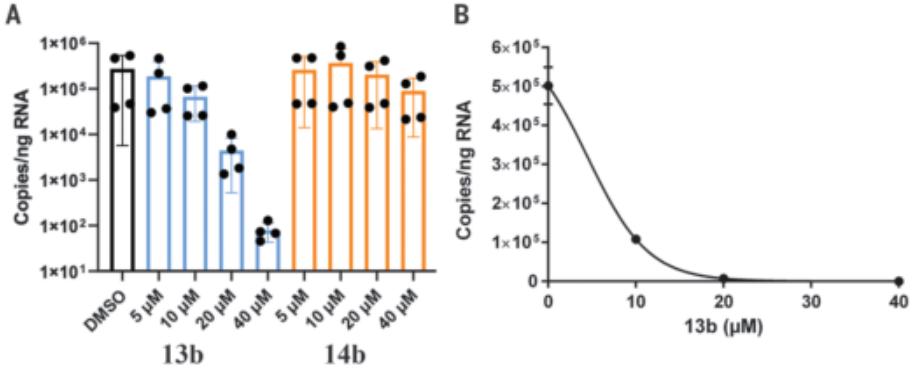

Fig. 4. Compound 13b inhibits SARS-CoV-2 replication in human Calu-3 lung cells. (**A**) Calu-3 cells were infected with SARS-CoV-2 using a multiplicity of infection (MOI) of 0.05. Varying amounts (5, 10, 20, or 40 μM) of **13b** (blue bars) or **14b** (orange bars) were added. DMSO was used as vehicle control (black bar). Total RNA was isolated from cell lysates, and viral RNA content was analyzed by quantitative polymerase chain reaction. Data are means ± SD of two biological experiments with two technical replicates each. (**B**) For the estimation of the EC_{50} value of compound **13b** against SARS-CoV-2, a dose-response curve was prepared (GraphPad).

of Gly[143], Cys[145], and partly Ser[144], which form the canonical "oxyanion hole" of the cysteine protease. It is an advantage of the α-ketoamides that their warhead can interact with the catalytic center of the target proteases through two hydrogen-bonding interactions (*6*) rather than only one, as with other warheads such as aldehydes (*14*) or Michael acceptors (*15*).

The P1 γ-lactam moiety, designed as a glutamine surrogate (*15*, *16*), is deeply embedded in the S1 pocket of the protease, where the lactam nitrogen donates a three-center (bifurcated) hydrogen bond to the main-chain oxygen of Phe[140] (3.20/3.10/3.28 Å; values for the structure in space group $C2$/space group $P2_12_12_1$ molecule A/space group $P2_12_12_1$ molecule B) and to the Glu[166] carboxylate [3.35/3.33/(3.55) Å], and the carbonyl oxygen accepts a 2.57/2.51/2.81 Å hydrogen bond from the imidazole of His[163]. The P2 cyclopropyl methyl moiety fits snugly into the S2 subsite, which has shrunk by 28 Å^3 relative to the complex between compound **13a** with P2 = cyclohexyl methyl and the SARS-CoV M^{pro} (*17*). The pyridone in the P3-P2 position of the inhibitor occupies the space normally filled by the substrate's main chain; its carbonyl oxygen accepts a 2.89/2.99/3.00 Å hydrogen bond from the main-chain amide of residue Glu[166]. Further, the P3 amide donates a 2.83/2.96/2.87 Å hydrogen bond to the main-chain oxygen of Glu[166]. Embedded within the pyridone, the P2 nitrogen can no longer donate a hydrogen bond to the protein (the H-bond prevented from forming would connect the P2 nitrogen and the side-chain oxygen of Gln[189]; these two atoms are highlighted in fig. S9). However, our previous crystal structures showed that the P2 main-chain amide of the linear α-ketoamides does not make a hydrogen bond with the protein in all cases, so this interaction does not seem to be critical (*6*). The protecting Boc group on P3 does not occupy the canonical S4 site of the protease [in contrast to the protecting groups of other inhibitors in complex with the SARS-CoV M^{pro} (*18*)] but is located near Pro[168] (3.81/4.17/3.65 Å) (Fig. 3); as a result of this interaction, the latter residue moves outward by more than 2 Å (relative to the structure of the free enzyme). This contact explains why removing the Boc group as in compound **14b** (Fig. 1, purple ovals) weakens the inhibitory potency of this compound by a factor of ~2. Interestingly, there is a space between the pyridone ring of **13b**, the main chain of residue Thr[190], and the side chain of Gln[189] (smallest distance: 3.6 Å), which is filled by a dimethyl sulfoxide (DMSO) molecule in the $C2$ crystal structure and a water molecule in the $P2_12_12_1$ structure. This suggests that P3 moieties more bulky than pyridone may be accepted here.

Compound **13b** inhibits the purified recombinant SARS-CoV-2 M^{pro} with IC_{50} = 0.67 ± 0.18 μM. The corresponding IC_{50} values for inhibition of the SARS-CoV M^{pro} and the MERS-CoV M^{pro} are 0.90 ± 0.29 μM and 0.58 ± 0.22 μM, respectively. In a SARS-CoV replicon (*19*), RNA replication is inhibited with EC_{50} = 1.75 ± 0.25 μM. In human Calu-3 cells infected with SARS-CoV-2, an EC_{50} of 4 to 5 μM was observed, whereas compound **14b** lacking the Boc group was almost inactive (Fig. 4). This suggests that the hydrophobic and bulky Boc group is necessary to cross the cellular membrane and that an even more hydrophobic moiety might be advantageous here, although this may again lead to increased plasma protein binding, as observed for the cinnamoyl-containing **11r**.

To assess the absorption-distribution-metabolism-excretion (ADME) properties of the pyridone-containing α-ketoamides, we first investigated compound **13a**. Metabolic stability in mouse and human microsomes was good, with intrinsic clearance rates Cl_{int_mouse} = 32.0 μl min^{-1} (mg protein)$^{-1}$ and Cl_{int_human} = 21.0 μl min^{-1} (mg protein)$^{-1}$. This means that after 30 min, ~80% and 60% (for mouse and human, respectively) of residual compound remained metabolically stable. Pharmacokinetic studies in CD-1 mice using the subcutaneous route at 20 mg/kg showed that **13a** stayed in plasma for up to 4 hours but was excreted via urine for up to 24 hours. The maximum plasma concentration (C_{max}) was determined at 334.5 ng ml^{-1} and the mean residence time was ~1.6 hours. Although **13a** seemed to be cleared very rapidly from plasma, at 24 hours it was found at 135 ng/g tissue in the lung and at 52.7 ng ml^{-1} in bronchioalveolar lavage fluid (BALF), which suggests that it was mainly distributed to tissue. Next, we investigated **13b** for its pharmacokinetic properties in CD-1 mice using the subcutaneous route as well, but at 3 mg kg^{-1}. The ADME parameters of **13b** were similar to those of **13a**; in addition, binding to human plasma proteins was found to be 90%. The C_{max} of **13b** was determined at 126.2 ng ml^{-1}. This is around 37% of the C_{max} detected for **13a**, although the **13b** dosage was lower by a factor of ~7. The mean residence time for **13b** was extended to 2.7 hours and the plasma half-life in mice was 1.8 hours. In addition, **13b** showed a less rapid clearance relative to **13a** (table S3). During the pharmacokinetic study with **13b**, we monitored its lung tissue levels. After 4 hours, **13b** was still found at ~13 ng g^{-1} in lung tissue. This lung tropism of **13a** and **13b** is beneficial given that COVID-19 affects the lungs. In addition to subcutaneous administration, **13b** was nebulized using an inhalation device at 3 mg kg^{-1}. After 24 hours, **13b** was found at 33 ng g^{-1} in lung tissue. Inhalation was tolerated well and mice did not show any adverse effects, which suggests that direct administration of the compound to the lungs would be possible. Given these favorable pharmacokinetic results, our study provides a useful framework for the development of the pyridone-containing inhibitors toward anticoronaviral drugs.

REFERENCES AND NOTES

1. P. Zhou *et al*., *Nature* **579**, 270–273 (2020).
2. F. Wu *et al*., *Nature* **579**, 265–269 (2020).
3. A. E. Gorbalenya *et al*., *Nat. Microbiol.* **5**, 536–544 (2020).
4. K. Anand, J. Ziebuhr, P. Wadhwani, J. R. Mesters, R. Hilgenfeld, *Science* **300**, 1763–1767 (2003).
5. R. Hilgenfeld, *FEBS J.* **281**, 4085–4096 (2014).
6. L. Zhang *et al*., *J. Med. Chem.* acs.jmedchem.9b01828 (2020).
7. J. Tan *et al*., *J. Mol. Biol.* **354**, 25–40 (2005).
8. J. Shi, J. Song, *FEBS J.* **273**, 1035–1045 (2006).
9. K. Anand *et al*., *EMBO J.* **21**, 3213–3224 (2002).
10. L. Lim, J. Shi, Y. Mu, J. Song, *PLOS ONE* **9**, e101941 (2014).
11. N. A. Kratochwil, W. Huber, F. Müller, M. Kansy, P. R. Gerber, *Biochem. Pharmacol.* **64**, 1355–1374 (2002).
12. H. Yang *et al*., *Proc. Natl. Acad. Sci. U.S.A.* **100**, 13190–13195 (2003).
13. H. Chen *et al*., *J. Biol. Chem.* **281**, 13894–13898 (2006).
14. L. Zhu *et al*., *Antiviral Res.* **92**, 204–212 (2011).
15. J. Tan *et al*., *J. Virol.* **87**, 4339–4351 (2013).
16. P. S. Dragovich *et al*., *Bioorg. Med. Chem.* **7**, 589–598 (1999).
17. L. Zhang, D. Lin, R. Hilgenfeld, Crystal structure of the complex resulting from the reaction between the SARS-CoV main protease and tert-butyl (1-((S)-3-cyclohexyl-1-(((S)-4-(cyclopropylamino)-3,4-dioxo-1-((S)-2-oxopyrrolidin-3-yl) butan-2-yl) amino)-1-oxopropan-2-yl)-2-oxo-1,2-dihydropyridin-3-yl)carbamate, PDB ID 6Y7M (2020).
18. L. Zhu, R. Hilgenfeld, Crystal structure of SARS coronavirus main protease complexed with an alpha, beta-unsaturated ethyl ester inhibitor SG85, PDB ID 3TNT (2012).
19. Y. Kusov, J. Tan, E. Alvarez, L. Enjuanes, R. Hilgenfeld, *Virology* **484**, 313–322 (2015).

ACKNOWLEDGMENTS

We thank Y. Kusov and G. Hansen, as well as A. Aljnabi, for determining the inhibitory activities of compounds in a SARS-CoV replicon and against recombinant MERS-CoV M^{pro}, respectively; T. Biet for recording ^{13}C NMR spectra; A. Ahlers, J. Schreiber, and L. Litz for excellent technical assistance; K. Chen for continuous organizational support; and the staff at beamline 14.2 of BESSY II, Berlin, Germany, for help with diffraction data collection. **Funding:** We thank the German Center for Infection Research (DZIF) for financial support (projects TTU01, grant 8011801806, and TTU09, grant 8004709710). **Author contributions:** Conceptualization: L.Z., D.L., R.H.; investigation: L.Z., D.L., X.S., U.C., L.S., S.B., K.R., R.H.; contribution of research materials: C.D.; writing (original draft preparation): R.H., D.L., K.R.; writing (review and editing): L.Z., D.L., U.C., L.S., K.R., R.H.; visualization: L.Z., L.S.; supervision: R.H.; funding acquisition: R.H., S.B., K.R. **Competing interests:** The University of Lübeck has filed a patent application covering compounds **13a** and **13b** as well as related compounds with a pyridone structure in the P3-P2 position, with L.Z., D.L., and R.H. as inventors. **Data and materials availability:** Crystallographic coordinates and structure factors are available from the PDB under accession codes 6Y2E (unliganded M^{pro}), 6Y2F (complex with **13b** in space group $C2$), and 6Y2G (complex with **13b** in space group $P2_12_12_1$). The plasmid encoding the SARS-CoV-2 M^{pro} is freely available. The available amounts of inhibitors are limited.

SUPPLEMENTARY MATERIALS

science.sciencemag.org/content/368/6489/409/suppl/DCI
Materials and Methods
Supplementary Text
Scheme S1
Figs. S1 to S10
Tables S1 to S3
References (*20*–*42*)

17 February 2020; accepted 18 March 2020
Published online 20 March 2020
10.1126/science.abb3405

RNA STRUCTURE

Structural basis for transcriptional start site control of HIV-1 RNA fate

Joshua D. Brown[1], Siarhei Kharytonchyk[2], Issac Chaudry[1], Aishwarya S. Iyer[1], Hannah Carter[1], Ghazal Becker[1], Yash Desai[1], Lindsay Glang[1], Seung H. Choi[1], Karndeep Singh[1], Michael W. Lopresti[1], Matthew Orellana[1], Tatiana Rodriguez[1], Ubiomo Oboh[1], Jana Hijji[1], Frances Grace Ghinger[1], Kailan Stewart[1], Dillion Francis[1], Bryce Edwards[1], Patrick Chen[1], David A. Case[3], Alice Telesnitsky[2]*, Michael F. Summers[1]*

Heterogeneous transcriptional start site usage by HIV-1 produces 5′-capped RNAs beginning with one, two, or three 5′-guanosines (^{Cap}1G, ^{Cap}2G, or ^{Cap}3G, respectively) that are either selected for packaging as genomes (^{Cap}1G) or retained in cells as translatable messenger RNAs (mRNAs) (^{Cap}2G and ^{Cap}3G). To understand how 5′-guanosine number influences fate, we probed the structures of capped HIV-1 leader RNAs by deuterium-edited nuclear magnetic resonance. The ^{Cap}1G transcript adopts a dimeric multihairpin structure that sequesters the cap, inhibits interactions with eukaryotic translation initiation factor 4E, and resists decapping. The ^{Cap}2G and ^{Cap}3G transcripts adopt an alternate structure with an elongated central helix, exposed splice donor residues, and an accessible cap. Extensive remodeling, achieved at the energetic cost of a G-C base pair, explains how a single 5′-guanosine modifies the function of a ~9-kilobase HIV-1 transcript.

All viral constituents required for HIV-1 replication are encoded within a single integrated proviral DNA and expressed using a single promoter (*1*). Diversification of transcript function is achieved primarily by splicing, which produces mRNAs encoding the viral envelope and accessory proteins, and by regulated frameshifting during translation of unspliced transcripts to produce the Gag and Gag-Pol polyproteins. Some unspliced transcripts do not function as mRNAs but are instead selected for packaging into assembling virions as progeny genomes (gRNA). Genomes are packaged as dimers (*2*–*4*), a requirement for strand transfer–mediated recombination during reverse transcription (*5*). Dimerization, packaging, and other RNA-dependent functions required for viral replication are mediated by conserved elements within the HIV-1 5′-leader (*1*, *6*–*8*), and there is considerable evidence that transcript structure and function are established by the dimerization state of the leader (*2*–*4*). Although dimerization could be modulated by a riboswitch-like mechanism (*8*–*10*), recent studies indicate that dimerization and function are instead controlled at the level of transcription by heterogeneous start site usage (*11*, *12*).

The HIV-1 promoter contains three sequential guanosines that can function as the transcription initiation site (U3-R junction) (Fig. 1A). Cells infected with the laboratory-adapted NL4-3 strain of HIV-1 (subtype B; HIV-1_{NL4-3}) utilize all three start sites to express transcripts containing one, two, or three 5′-guanosines (1G, 2G, or 3G, respectively). Most of these RNAs (~90%) are transcribed with 1G or 3G 5′-ends (*11*, *12*), consistent with a predominant "twinning" transcription initiation mechanism (*12*). Like eukaryotic mRNAs, HIV-1 transcripts are cotranscriptionally capped by a 5′,5′-triphosphate–linked 7-methylguanosine (Fig. 1A) (*13*–*16*). Capping is important for RNA splicing, nuclear export, translation, and metabolic stability (*17*). 5′-Capped 1G transcripts (^{Cap}1G) preferentially form dimers in vitro (*12*) and are selectively packaged into assembling virions in infection assays (*11*, *12*), whereas those containing two or three guanosines (^{Cap}2G and ^{Cap}3G) preferentially form monomers and are retained in cells and enriched on polysomes (*12*).

To understand how transcriptional addition of as few as one or two 5′-guanosines modulates RNA dimerization and fate, we probed the structures of ^{Cap}1G, ^{Cap}2G, and ^{Cap}3G HIV-1 leader RNAs by deuterium (^{2}H)–edited nuclear magnetic resonance (NMR) and examined their abilities to interact with cellular proteins important for RNA processing and metabolic stability. Studies focused on the MAL strain of HIV-1, which is widely distributed among humans (M group subtype A; HIV-1_{MAL}) (*18*). The HIV-1_{MAL} leader contains a dimer-promoting GUGCAC palindrome and adopts a monomer-dimer equilibrium insensitive to the presence of the cognate NC protein (*19*) (fig. S1). Cultured 293T cells were transiently transfected with an HIV-1 vector containing the first 368 nucleotides of HIV-1_{MAL} followed by the NL4-3 strain *gag/pol* sequence (MAL-GPP-pA), and 5′-end sequences of cellular and virion-associated RNA transcripts were determined by RNase

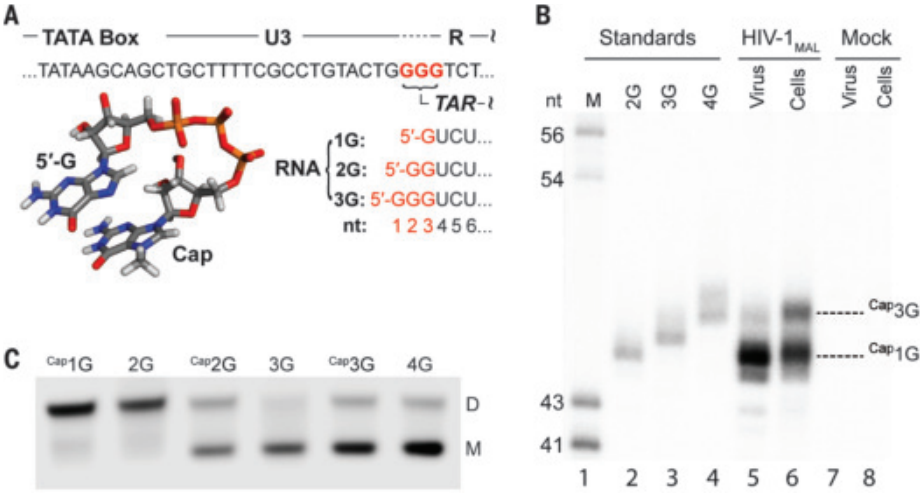

Fig. 1. Heterogeneous transcriptional start site usage modulates HIV-1_{MAL} RNA dimerization and function. (**A**) Three guanines (red) can serve as alternative transcription start sites. Transcripts are cotranscriptionally capped by 7-methylguanosine. (**B**) 5′ ends of cellular and virion RNAs expressed from transiently transfected HIV-1 MAL-GPP-pA analyzed by RNase protection. Lane 1: molecular size standards. Lanes 2 to 4: HIV-1_{MAL} RNA standards; 2G, 3G and 4G protected products served as mobility standards for ^{Cap}1G, ^{Cap}2G, and ^{Cap}3G ends, respectively. Lanes 5 and 6: protected fragments from RNA samples harvested from 293T cells transfected with the HIV-1 derivative MAL-GPP-pA (lane 6) and from virus produced by these cells (lane 5). Lanes 7 and 8: protected fragments from RNA samples harvested from mock-transfected 293T cells (lane 8) and from media produced by these cells (lane 7). (**C**) Full-length leader RNAs (L^{371}) that begin with a single capped guanosine or two noncapped guanosines favor the dimer, whereas RNAs with an additional 5′-guanosine or cap favor the monomer. nt, nucleotides.

[1]Howard Hughes Medical Institute and Department of Chemistry and Biochemistry, University of Maryland Baltimore County, 1000 Hilltop Circle, Baltimore, MD 21250, USA. [2]Department of Microbiology and Immunology, University of Michigan Medical School, Ann Arbor, MI 48109-5620, USA. [3]Department of Chemistry and Chemical Biology and BioMaPS Institute, Rutgers University, 610 Taylor Road, Piscataway, NJ 08854-8087, USA.
*Corresponding author. Email: summers@hhmi.umbc.edu (M.F.S.); ateles@umich.edu (A.T.)

protection assays (*12*). Of the three potential 5′-ends encoded by the provirus, only ^{Cap}1G and ^{Cap}3G RNAs were detected (Fig. 1, A and B). ^{Cap}1G transcripts were enriched in virions produced from MAL-GPP-pA–transfected cells (>95%), whereas ^{Cap}3G transcripts were retained in cells during virus replication (Fig. 1B). As observed for HIV-1_{NL4-3} RNAs, in vitro–transcribed HIV-1_{MAL} ^{Cap}1G 5′-leader RNAs (^{Cap}1G-L) preferentially formed dimers in vitro under physiological-like conditions [PI buffer (10 mM phosphate, 1 mM Mg^{2+}, 122 mM K^{+}; pH 7.4)], whereas ^{Cap}3G-L (and ^{Cap}2G-L) preferentially formed monomers (Fig. 1C). These findings confirm that HIV-1 subtypes A and B encode 5′-leaders with similar start site–dependent dimerization propensities and gRNA versus mRNA control.

The secondary structure of the dimeric HIV-1_{MAL} ^{Cap}1G leader [capped residue G3 through G359 [^{Cap}1G-L^{359}]$_2$; 232 kDa] was probed by ^{2}H-edited NMR. Sequential and long-range adenosine-H2–detected nuclear Overhauser effects (NOEs), which are diagnostic of RNA secondary structure (*20*) and can be used for larger RNAs (*8*, *21*), were detected for leader constructs prepared with the following nucleotide-specific ^{2}H labeling schemes (superscripts denote sites of protonation; all other sites are deuterated, e.g., A^{2r} indicates adenosines protonated at C2 and ribose carbons): A^{2r}, $A^{2r}G^{r}$, $A^{2r}U^{r}$, $A^{2}G^{r}$, and $A^{2}U^{r}$. NMR assignments were corroborated by comparisons with spectra obtained for fragment RNAs (fig. S2) and by database ^{1}H-NMR chemical shift analyses (*22*). Adenosine-H2 NOEs were assigned for stretches of residues within most of the expected secondary structures of [^{Cap}1G-L^{359}]$_2$, including those in the transcriptional activation (TAR), primer binding (PBS), dimerization (DIS), packaging (Ψ), and cleavage and polyadenylation site [poly(A)] elements (Fig. 2, A and B) (*8*, *21*). Well-resolved NOEs for A111 and A351 confirmed the presence of the U5:AUG helix that pairs upstream sequences with those flanking the *gag* start codon (Fig. 2B and fig. S3) (*23*).

NOEs between the Cap methyl group and protons of G3 and G103 were detected for the intact dimeric leader, suggesting that the Cap is sandwiched between these residues (Fig. 2C). Similar spectra were obtained for a truncated portion of the leader comprising the TAR and poly(A) hairpins and the U5:AUG helix (^{Cap}1G-L^{TPUA}) (Fig. 2, C and D, and fig S4). The improved sensitivity and spectral resolution obtainable for the smaller ^{Cap}1G-L^{TPUA} construct (42 kDa) were sufficient for three-dimensional (3D) structural studies (table S1 and fig. S4). Residues G103, Cap, and G3 are sequentially stacked, as are residues C55, C56, and C57, leading to an overall end-to-end stacking of the TAR and poly(A) hairpins (Fig. 2E and fig. S4). The structure juxtaposes the Cap

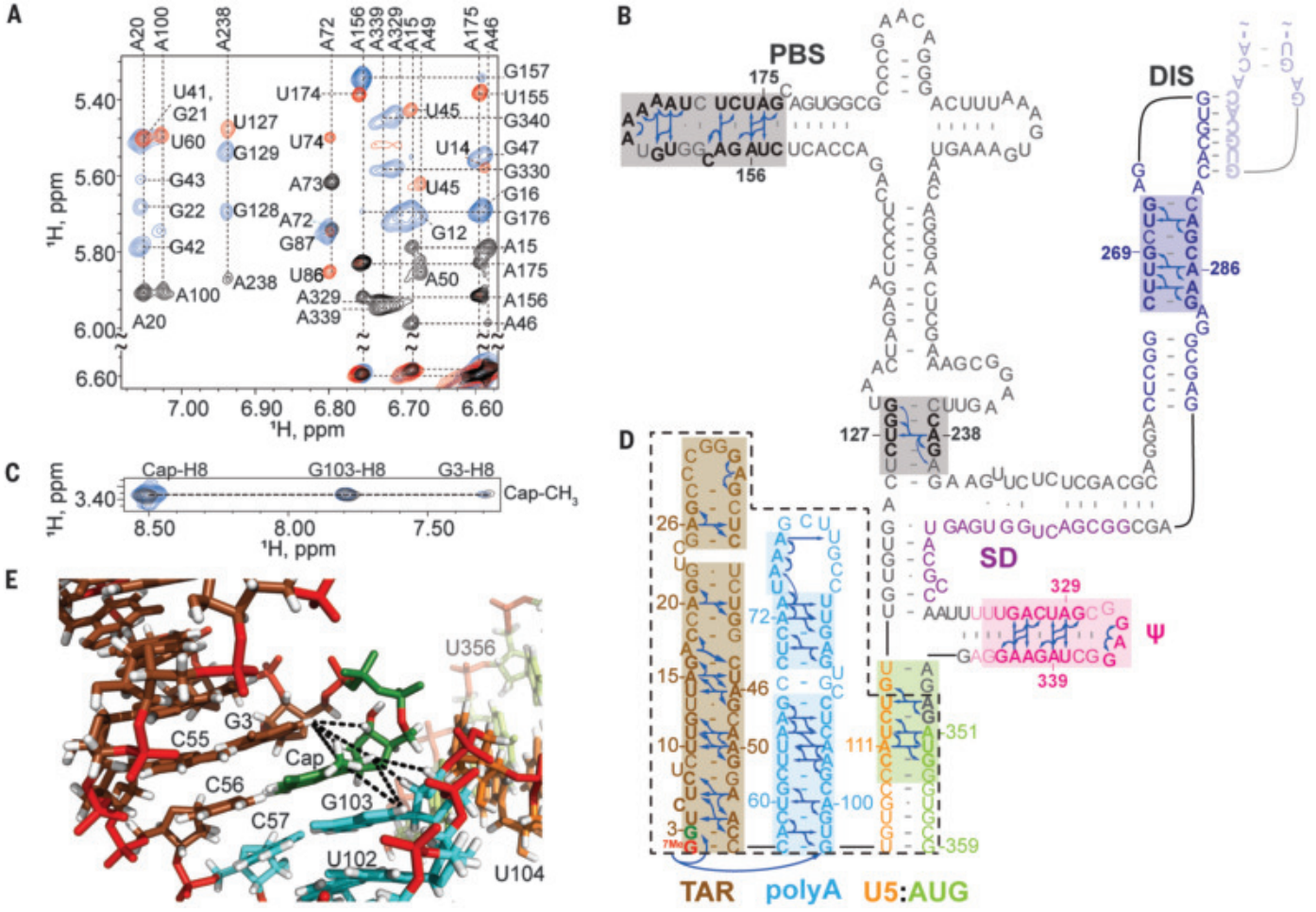

Fig. 2. NMR and structural findings for the dimeric ^{Cap}1G form of the HIV-1_{MAL} leader. (**A**) Portions of 2D NOE spectra for ^{2}H-labeled [^{Cap}1G-L^{359}]$_2$ samples (A^{2r}, black; $A^{2}U^{r}$, red; $A^{2}G^{r}$, blue). (**B**) Assigned A-H2 NOEs and deduced secondary structure; discrete functional elements differentiated by color and intermolecular "kissing" interactions are denoted as shaded residues. (**C**) Portions of 2D NOE spectra showing similarities of Cap-CH_3 to Cap-H8, G3, and G108 NOEs observed for G^{8}-[^{Cap}1G-L^{359}]$_2$ (blue), and truncated leader fragment ^{Cap}1G-L^{TPUA} (black). (**D**) (dashed black lines). (**E**) Portion of the ^{Cap}1G-L^{TPUA} NMR structure showing Cap NOEs (dashed lines) indicative of end-to-end stacking of the TAR (brown) and poly(A) (cyan) helices.

and C56 bases in a manner consistent with Cap:C56 base pairing.

NMR studies were also conducted with monomeric 2G and 3G leader RNAs. Nuclear Overhauser effect spectroscopy (NOESY) spectra obtained for noncapped 3G-L^{371} (Fig. 3A) and capped ^{Cap}2G-L^{371} and ^{Cap}3G-L^{371} (Fig. 3, B to E) RNAs exhibited similar cross-peak patterns indicative of a common structure, with residues of AUG forming a hairpin rather than the U5:AUG helix observed in the dimer (*8*). NOE patterns for TAR, Ψ, and a portion of PBS were similar to those observed for [^{Cap}1G-L^{359}]$_2$, indicating that these substructures exist in both the monomeric and dimeric forms of the leader (figs. S5 and S6). Long-range A58-H2 NOEs to G1 (but not G103) ribose protons were observed [confirmed by using a sample in which only the G1 guanosine and adenosines were protonated (Fig. 3A)], indicating that the lower portion of the poly(A) hairpin was remodeled (*12*). In addition, signals diagnostic of the DIS hairpin in the [^{Cap}1G-L^{359}]$_2$ RNA were absent in the 3G-L^{371} NOESY spectra. ^{1}H-NMR chemical shifts of the H2 and H8 protons of adenosines A65, A66, A72, A73, and A75 to A77 were also different from those observed for [^{Cap}1G-L^{359}]$_2$, and none of these adenosines exhibited long-range NOEs (fig. S6A). However, adenosine residues in the downstream portion of poly(A) exhibited long-range NOEs and chemical shifts indicative of base pairing with residues of DIS (Fig. 3B). Similar NMR results were obtained for ^{Cap}3G-L^{371} (Fig. 3, C and E) and ^{Cap}2G-L^{371} (Fig. 3D). The capped RNAs exhibited additional NOEs between A58-H2 and the Cap methyl and ribose protons (Fig. 3, D and E). The NMR data are consistent with a secondary structure that is substantially remodeled relative to that of the dimeric [^{Cap}1G-L^{359}]$_2$ leader, with residues of TAR, SD, Ψ, and AUG adopting independently folded hairpin structures (Fig. 3F) and residues of poly(A), U5, and DIS forming an elongated helix (Fig. 3F).

No sequential NOEs between the Cap and G1 residues were detected in spectra obtained for the intact ^{Cap}3G-L^{371} or ^{Cap}2G-L^{371} leader RNAs. Spectra with improved sensitivity and resolution were obtained for constructs corresponding to the lower portion of the capped TAR hairpin (^{Cap}2G-TAR^m in Fig. 3D and ^{Cap}3G-TAR^m in Fig. 3, E and G). NMR chemical shifts and NOE patterns were similar to those observed for analogous residues in ^{Cap}3G-L^{371} and indicated that the Cap residue does not stack with G1 or G2 and is disordered (Fig. 3H and fig. S7).

The NMR data suggest that structural remodeling of the capped 2G and 3G RNAs relative to the capped 1G leader is a consequence of a single additional base pair (Cap:C57 in ^{Cap}2G-L or G1:C57 in ^{Cap}3G-L). Consistent with this hypothesis, replacement of C57 by G in ^{Cap}1G-L^{371} to ablate the base pair at the terminus of the poly(A) helix (C57:G103) (Fig. 2B) shifted the monomer-dimer equilibrium to the monomer (Fig. 4A), and compensatory substitution of G103 to C reverted the equilibrium toward dimer (Fig. 4A). This indicates that structural remodeling is achieved at an energetic cost equivalent to a single G-C base pair (~3 to 5 kcal/mol) (*24*). The compensatory mutant did not fully recapitulate the dimerization properties of the wild-type sequence, suggesting that the C57:G103 base pair, which is conserved in 99% of deposited sequences with reported full-length 5′ untranslated regions (see the supplementary materials), is important both for stabilizing the dimeric form of the ^{Cap}1G transcripts and enabling

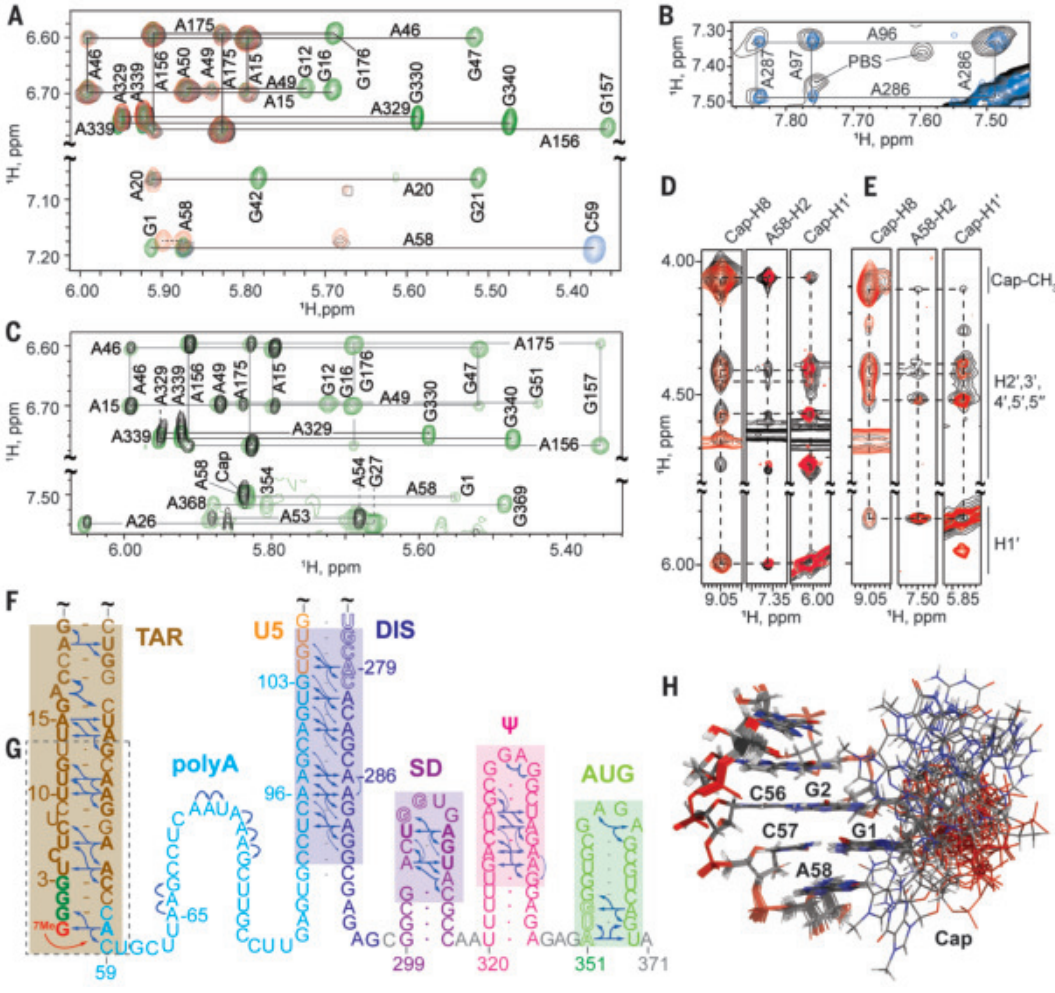

Fig. 3. NMR and structural findings for the monomeric ^{Cap}3G, ^{Cap}2G, and 3G forms of the HIV-1$_{MAL}$ leader. (**A** to **F**) Portions of 2D NOE spectra [(A) to (E)] used to make the secondary-structure assignments shown in (F). (A) Noncapped 3G-L^{371} spectra (A^H, black; A^{2r}G^r, green; A^{2r}C^r, blue; G1^{H}A^{2r}, red); G1 is the only protonated guanosine in the G1^{H}A^{2r}-labeled sample, enabling unambiguous assignment of A58-H2 NOEs to G1. (B) NOE spectra for A$^{2'-Cap}$3G-L^{371} (black) showing A-H2 to A-H2 NOEs of the extended poly(A)-DIS helix matches a noncapped analog lacking the PBS loop (A^{2r}G^r-4G-L$^{371-\Delta PBS}$, blue; see fig. S5). (C) ^{Cap}3G-L^{371} spectra (A^H, black; A^{2r}G^r, green) showing that the Cap is in close proximity to A58. (**G**) Comparison of 2D NOE spectra for A$^{2'-Cap}$2G-L^{371} (black) (D) and TAR fragment ^{Cap}2G-TAR^m (G) (red), showing NOEs between the Cap and A58. (E) Similar Cap-to-A58 NOEs were observed for ^{Cap}3G-L^{371} (black) and a ^{Cap}3G-TAR^m RNA (red). (**H**) Portion of the NMR structure of ^{Cap}3G-TAR^m, showing the disordered cap residue.

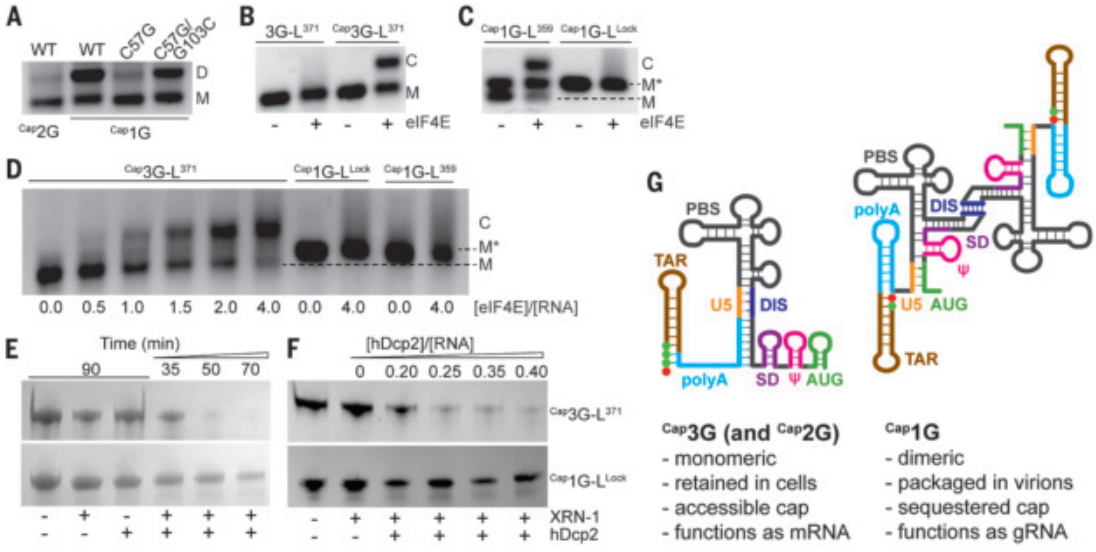

Fig. 4. Influence of 5′-guanosine number on RNA function. (**A**) Disruption of a single base pair (C57-G103) by C57→G mutagenesis disrupts ^{Cap}1G-L^{371} dimerization. Compensatory G103C substitution substantially restores dimerization. (**B**) eIF4E binds ^{Cap}3G-L^{371} (C denotes the eIF4E:RNA complex), but not the noncapped RNA. (**C**) At low ionic strength, eIF4E binds the M conformer of ^{Cap}1G-L^{359}, but not M* or the ^{Cap}1G-L^{Lock} construct. (**D**) Similar results were obtained in PI buffer. (**E** and **F**) The 5′-RNA exonuclease (XRN-1) and decapping enzyme (hDcp2) are independently unable to degrade ^{Cap}1G or ^{Cap}3G leader RNAs. In the presence of both enzymes, the ^{Cap}1G-L^{Lock} resists degradation over time (E) and with increasing hDcp2 (F) compared to the cap-exposed ^{Cap}3G-L^{371} leader. (**G**) Mechanism for transcriptional control of HIV-1 RNA function. Capped RNAs containing two or three 5′-guanosines (green dots) adopt a monomeric structure that exposes the cap (red dot) and enables RNA processing and metabolism, whereas those with a single capped G adopt a cap-sequestered conformation that promotes dimerization and packaging.

remodeling through C57:Cap or C57:G3 base pairing in the ^{Cap}2G and ^{Cap}3G transcripts, respectively.

Because the cap is exposed in monomeric ^{Cap}2G and ^{Cap}3G leader RNAs and sequestered between the TAR and poly(A) helices in the dimeric ^{Cap}1G leader, we examined the abilities of these RNAs to interact with two cellular cap binding proteins: the eukaryotic translation initiation factor 4E (eIF4E) and the human decapping enzyme hDcp2. eIF4E initiates recruitment and assembly of the eukaryotic translation machinery (*25*), and cap recognition and removal by hDcp2 is required for 5′-exonucleolytic mRNA turnover (*26*). Native agarose gel shift experiments revealed that eIF4E binds the ^{Cap}2G and ^{Cap}3G leader RNAs with affinities (K_d ~ 0.7 μM) similar to that of a single capped guanosine (K_d = 1.44 μM) (*25*) (results for noncapped 3G-L^{371} and ^{Cap}3G-L^{371} are shown in Fig. 4B). ^{Cap}1G-L titrations were also conducted under nonphysiological low–ionic-strength conditions that favor the monomer (10 mM NaCl, no Mg^{+2}). Under these conditions, ^{Cap}1G-L^{359} adopts two monomeric conformations that are resolvable on Tris-borate gels, M and M* (Fig. 4C and fig. S8). The M conformer exhibits gel mobility similar to that of the cap-exposed ^{Cap}3G-L monomer, whereas M* exhibits mobility of a cap-sequestered ^{Cap}1G-L^{359} mutant engineered to form a monomer while retaining the secondary structure of the dimer [DIS residues A273 to A281 mutated to GAGA to prevent dimerization (*27*); ^{Cap}1G-L^{Lock}) (Fig. 4C and figs. S2 and S8]. Titration of ^{Cap}1G-L^{359} with eIF4E resulted in a mobility shift for the cap-exposed M conformer, but not for the cap-sequestered M* species, even at (twofold) excess molar ratios of eIF4E (Fig. 4C). ^{Cap}1G-L^{Lock} was likewise unable to bind eIF4E (Fig. 4C). Differential eIF4E binding between ^{Cap}3G-L^{371} and ^{Cap}1G-L was also observed in PI buffers (Fig. 4D). The capped 1G leader also exhibited reduced sensitivity to hDcp2-dependent 5′-exonuclease digestion compared to the capped 3G leader RNA (Fig. 4, E and F). These findings indicate that cap-binding proteins important for mRNA translation and processing bind efficiently to monomeric, cap-exposed forms of the leader but not to the cap-sequestered ^{Cap}1G dimer.

Our findings support a structure-based mechanism for diversification of HIV-1 transcript function by heterogeneous transcriptional start site usage (Fig. 4G). Analogous to riboswitches, which undergo structural remodeling and functional activation upon binding of small exogenous ligands (*28*), the structure and function of HIV-1 transcripts are controlled by transcriptional addition of one or two 5′-guanosines. Transcripts that begin with a single 5′-capped guanosine adopt a dimeric branched multihelical structure that promotes dimerization and exposes Gag binding sites while simultaneously sequestering the 5′ cap, the major splice donor site, and the translational start site. Cap sequestration is likely to inhibit both translation and splicing, as both processes depend on initial interactions with cap-binding proteins (*29*) and may also inhibit decapping-dependent 5′-exonuclease–dependent degradation of the gRNA during cytoplasmic transport and particle assembly. Subgenomic flaviviral RNAs are similarly protected from exonuclease digestion by structural sequestration of 5′-nucleotides (*30*). HIV-1 transcripts that contain additional 5′-guanosines adopt an alternate structure that inhibits dimerization (*12*), sequesters Gag-binding sites (*8*), and exposes the cap, the major splice donor site, the *gag* start codon, and unstructured residues immediately downstream of the TAR hairpin. Cap exposure enables eIF4E binding, and the unstructured poly(A) residues immediately downstream of the TAR hairpin could facilitate eIF4E-dependent association of additional factors required for splicing and translation (*31*). A genome-wide study of mammalian promoter architecture by cap analysis of gene expression revealed that twinned transcriptional start sites comprise a substantial subset of mammalian promoters (*32*, *33*). Start site–dependent modulation of transcript structure and cap exposure could serve as a general mechanism for expanding cellular RNA function.

REFERENCES AND NOTES

1. J. M. Coffin, S. H. Hughes, H. E. Varmus, *Retroviruses* (Cold Spring Harbor Laboratory Press, 1997).
2. V. D'Souza, M. F. Summers, *Nat. Rev. Microbiol.* **3**, 643–655 (2005).
3. K. Lu, X. Heng, M. F. Summers, *J. Mol. Biol.* **410**, 609–633 (2011).
4. M. Kuzembayeva, K. Dilley, L. Sardo, W.-S. Hu, *Virology* **454-455**, 362–370 (2014).
5. A. Onafuwa-Nuga, A. Telesnitsky, *Microbiol. Mol. Biol. Rev.* **73**, 451–480 (2009).
6. A. M. Lever, *Adv. Pharmacol.* **55**, 1–32 (2007).
7. T. E. M. Abbink, M. Ooms, P. C. J. Haasnoot, B. Berkhout, *Biochemistry* **44**, 9058–9066 (2005).
8. K. Lu *et al*., *Science* **334**, 242–245 (2011).
9. J.-L. Darlix, C. Gabus, M.-T. Nugeyre, F. Clavel, F. Barré-Sinoussi, *J. Mol. Biol.* **216**, 689–699 (1990).

10. M. Ooms, H. Huthoff, R. Russell, C. Liang, B. Berkhout, *J. Virol.* **78**, 10814–10819 (2004).
11. T. Masuda *et al*., *Sci. Rep.* **5**, 17680 (2015).
12. S. Kharytonchyk *et al*., *Proc. Natl. Acad. Sci. U.S.A.* **113**, 13378–13383 (2016).
13. Y. L. Chiu, E. Coronel, C. K. Ho, S. Shuman, T. M. Rana, *J. Biol. Chem.* **276**, 12959–12966 (2001).
14. M. Zhou *et al*., *Proc. Natl. Acad. Sci. U.S.A.* **100**, 12666–12671 (2003).
15. T. M. Menees, B. Müller, H. G. Kräusslich, *AIDS Res. Hum. Retroviruses* **23**, 1042–1048 (2007).
16. A. Sharma, A. Yilmaz, K. Marsh, A. Cochrane, K. Boris-Lawrie, *PLOS Pathog.* **8**, e1002612 (2012).
17. A. Ramanathan, G. B. Robb, S. H. Chan, *Nucleic Acids Res.* **44**, 7511–7526 (2016).
18. M. Alizon, S. Wain-Hobson, L. Montagnier, P. Sonigo, *Cell* **46**, 63–74 (1986).
19. T. Tran *et al*., *Retrovirology* **12**, 83 (2015).
20. K. Wüthrich, *NMR of Proteins and Nucleic Acids* (Wiley, 1986).
21. X. Heng *et al*., *J. Mol. Biol.* **417**, 224–239 (2012).
22. J. D. Brown, M. F. Summers, B. A. Johnson, *J. Biomol. NMR* **63**, 39–52 (2015).
23. T. E. M. Abbink, B. Berkhout, *J. Biol. Chem.* **278**, 11601–11611 (2003).
24. T. Xia *et al*., *Biochemistry* **37**, 14719–14735 (1998).
25. A. C. Gingras, B. Raught, N. Sonenberg, *Annu. Rev. Biochem.* **68**, 913–963 (1999).
26. Z. Wang, X. Jiao, A. Carr-Schmid, M. Kiledjian, *Proc. Natl. Acad. Sci. U.S.A.* **99**, 12663–12668 (2002).
27. S. C. Keane *et al*., *Science* **348**, 917–921 (2015).
28. A. Serganov, E. Nudler, *Cell* **152**, 17–24 (2013).
29. J. D. Lewis, E. Izaurflde, *Eur. J. Biochem.* **247**, 461–469 (1997).
30. B. M. Akiyama *et al*., *Science* **354**, 1148–1152 (2016).
31. I. Boeras *et al*., *Sci. Rep.* **7**, 6902 (2017).
32. P. Carninci *et al*., *Nat. Genet.* **38**, 626–635 (2006).
33. M. C. Frith *et al*., *Genome Res.* **18**, 1–12 (2008).

ACKNOWLEDGMENTS

We thank HHMI staff at UMBC for technical assistance, C. Burnett (University of Michigan Medical School) for help with manuscript preparation, and R. Sprangers (University of Regensburg, Germany) for helpful suggestions. **Funding:** This research was supported by research grants from the National Institutes of Health (NIAID 8R01 AI50498 to M.F.S. and A.T., NIAID U54 AI150470 to A.T. and D.A.C.). J.D.B. was supported by NIH predoctoral fellowship F31 GM123803; M.L., K. Singh, M.O., T.R., and F.G.G. were supported by an NIGMS grant for enhancing minority access to research careers (MARC U*STAR 2T34 GM008663); M.O. and T.R. were supported by an HHMI undergraduate education grant; A.S.I., M.L., K. Singh, M.O., T.R., and F.G.G. were supported by the Meyerhoff Scholars Program at UMBC. **Author contributions:** M.F.S. and A.T. supervised and raised financial support for the studies. M.F.S. and J.D.B. conceived the study and designed the NMR and in vitro experiments. J.D.B., A.S.I., H.C., Y.D., L.G., S.H.C., M.W.L., I.C., K. Singh, M.O., T.R., U.O., J.H., F.G.G., K. Stewart, G.B., D.F., B.E., and P.C. prepared RNA samples, conducted in vitro and NMR experiments, and helped with NMR data analysis; A.T. and S.K. designed and conducted the virology experiments; D.A.C. developed the amber force field for the RNA Cap and provided advising for amber calculations; M.F.S., J.D.B., A.T., and S.K. wrote the manuscript, with contributions from all coauthors. **Competing interests:** The authors declare no competing interests. **Data and materials availability:** Depositions for ^{Cap}1G-L^{TPUA} and ^{Cap}3G-TAR^{m} structures include atomic coordinates (PDB ID 6VU1 and 6VVJ, respectively) and NMR chemical shifts and restraints for structure calculations (BMRB ID 30723 and 30724, respectively).

SUPPLEMENTARY MATERIALS

science.sciencemag.org/content/368/6489/413/suppl/DC1
Material and Methods
Figs. S1 to S8
Table S1
References (*34*–*54*)

9 October 2019; accepted 24 March 2020
10.1126/science.aaz7959

INSECT POPULATIONS

Meta-analysis reveals declines in terrestrial but increases in freshwater insect abundances

Roel van Klink[1,2,3]*, Diana E. Bowler[1,4,5], Konstantin B. Gongalsky[6,7], Ann B. Swengel[8], Alessandro Gentile[1], Jonathan M. Chase[1,9]

Recent case studies showing substantial declines of insect abundances have raised alarm, but how widespread such patterns are remains unclear. We compiled data from 166 long-term surveys of insect assemblages across 1676 sites to investigate trends in insect abundances over time. Overall, we found considerable variation in trends even among adjacent sites but an average decline of terrestrial insect abundance by ~9% per decade and an increase of freshwater insect abundance by ~11% per decade. Both patterns were largely driven by strong trends in North America and some European regions. We found some associations with potential drivers (e.g., land-use drivers), and trends in protected areas tended to be weaker. Our findings provide a more nuanced view of spatiotemporal patterns of insect abundance trends than previously suggested.

Insects are the most ubiquitous and diverse animals on the planet (*1*–*3*), providing multiple critical ecosystem services (e.g., pollination and decomposition) and disservices (e.g., damaging crops and spreading disease) (*4*). Although population declines of many species have been previously documented (*5*–*7*), recent case studies showing drastic declines in the total biomass or abundance of entire insect assemblages (*8*–*11*) have caused a surge of interest in the plight of insects (*12*, *13*). Despite the attention from the media, policy-makers, and scientists, it remains unclear whether such declines are widespread across realms and among geographic regions. Here, we compiled as many openly available long-term (10+ years) standardized monitoring surveys of assemblages of insects and arachnids (for brevity, hereafter collectively referred to as "insects") as we could find (*14*). We used the amassed data to evaluate changes in total insect abundance and biomass, as well as the geographic distribution of such changes. Our dataset included 1676 sites from 166 studies spread over 41 countries (Fig. 1; see table S1 for a list of studies). Among these, 130 datasets reported only changes in insect abundances (i.e., number of individuals) in an assemblage, 13 datasets reported only the biomass of all insects in an assemblage, and 23 datasets reported both metrics. The data spanned from 1925 to 2018, with a median start year of 1986 and a median time span of 20 years. Because our main focus was on the temporal trend of changes within assemblages (i.e., time series of total biomass or abundance), we could combine data with different sampling methods, spatial scales, and metrics into one analysis.

Across all studies, there was great variation in trends even among geographically adjacent sites (Fig. 1). We analyzed the data using a hierarchical Bayesian model accounting for variation at the study, study area, and site level (*14*). From this, we inferred strong evidence for a mean trend when the posterior probability of the estimate was larger or smaller than zero with at least 95% certainty. Likewise, we inferred moderate or weak evidence for a mean trend when the posterior probability differed from zero with 90 or 80% certainty, respectively, and interpreted no evidence for a directional trend for probabilities <80%. Overall, we found strong evidence for a decline of terrestrial insects, which we estimated to be 0.92% per year (Fig. 2A and table S2), amounting to −8.81% per decade. By contrast, we found a 1.08% annual increase for freshwater insects, equaling +11.33% per decade (Fig. 2A). The mean trend estimates of insect abundance and biomass were similar (Fig. 2A) but differed in strength of evidence because of the lower data availability for biomass (table S2). The positive trends in the freshwater realm may partially counter the negative terrestrial trends, because a model combining both realms showed no evidence for a directional trend (Fig. 2A). However, because fresh water represents only 2.4% of the earth's terrestrial surface (*15*, *16*), such a combined model is likely to be a poor representation of trends in total insect numbers at any spatial scale.

The strongest evidence for declines in terrestrial insect assemblages was found in North America (Fig. 2B), but also in some European regions (fig. S1). The exclusion of all North American data thus tempered the overall decline (mean trend without North America:

[1]German Centre for Integrative Biodiversity Research (iDiv) Halle-Jena-Leipzig, 04103 Leipzig, Germany. [2]Leipzig University, 04109 Leipzig, Germany. [3]WBBS Foundation, 9409 TV, Loon, Netherlands. [4]Institute of Biodiversity, Friedrich Schiller University Jena, 07743 Jena, Germany. [5]Helmholtz Centre for Environmental Research (UFZ), 04318 Leipzig, Germany. [6]A.N. Severtsov Institute of Ecology and Evolution, Russian Academy of Sciences, Moscow 119071, Russia. [7]M.V. Lomonosov Moscow State University, Moscow 119991, Russia. [8]Independent researcher. [9]Department of Computer Science, Martin Luther University-Halle Wittenberg, 06099 Halle (Saale), Germany.
***Corresponding author. Email: Roel.klink@idiv.de**

−0.49% per year), but there was still weak evidence for a negative mean trend. When estimating the trends in different climatic zones, we found strong evidence for directional trends in both realms in the temperate zone, as well as in Mediterranean and desert climates (drylands; Fig. 2C and table S2). We found no evidence for directional trends in other continents or climatic zones, where the data were much sparser (Fig. 2, B and C, and table S2). The increasing trend for the freshwater insects, particularly in the temperate zone, is consistent with recent analyses from these regions (*17*–*19*) and may at least partially reflect recovery from past degradation [e.g., the Clean Water Act and similar legislation (*20*–*23*)]. Other causes of this increase may have been climatic warming (*24*) and an enhanced productivity caused by nutrient inputs (*25*, *26*).

We tested whether these temporal trends changed over time by running the same model for progressively shorter timespans: since 1960, 1970, 1980, 1990, 2000, and 2005 (Fig. 3). No consistent temporal changes in trends were visible at the global level. However, in Europe, the mean slope estimate for the terrestrial insects became more negative over time and was steepest since 2005. By contrast, the overall negative trends for terrestrial insects in North America have tempered and were no longer negative since 2000. For freshwater insects, the trends became more positive in Europe and North America, as well as in Asia, where the overall increase was steepest since 1990, coinciding with the collapse of the Soviet Union and its heavy industries (*27*, *28*). Trends in the other continents seem relatively unchanged over time.

We evaluated associations of the observed trends in insect abundances with commonly hypothesized anthropogenic drivers, including land-use change and climate change (*10*, *11*, *29*). First, we found that the trends in protected areas were weaker than those in unprotected areas (Fig. 4), although there was still a moderate negative trend in terrestrial protected areas. This difference suggests a possible association between insect trends and land-use change. To evaluate this further, we used Geographic Information System (GIS) layers to extract urban and cropland cover surrounding the sampling sites at local (only available since 1992) and landscape (full period) scales (*14*). We found moderate evidence for a negative relationship

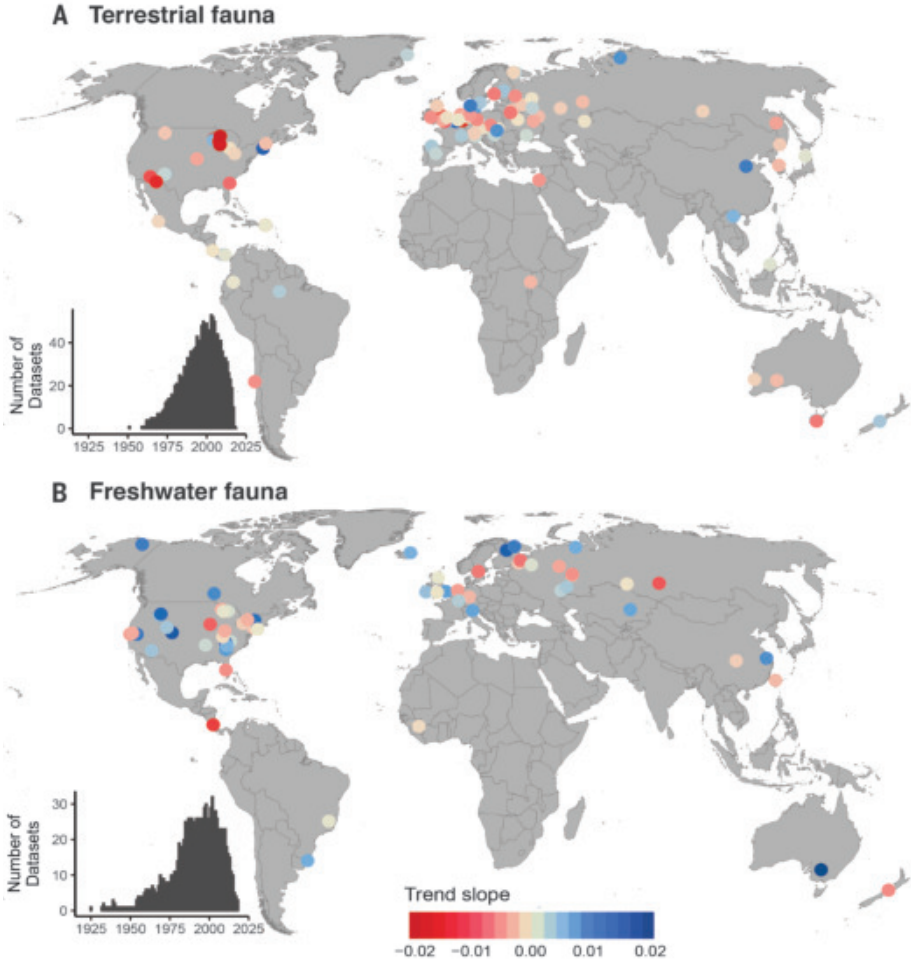

Fig. 1. Trend estimates of long-term changes in insect assemblage size, measured as insect abundance or biomass, of the 166 studies. Shown are trend estimates for terrestrial (**A**) and freshwater (**B**) fauna. The trend estimates of the individual studies were derived from the random effects of the hierarchical Bayesian model with only year as an explanatory variable. The insets show histograms of the number of datasets with at least one data point for each year.

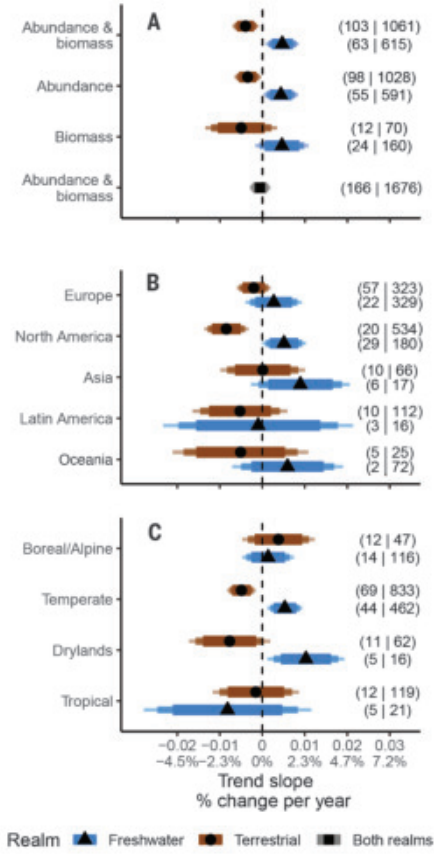

Fig. 2. Trend estimates (±80, 90, and 95% credible intervals). Shown are the trend estimates in insect abundance and biomass (**A**) at different continents (**B**) and climatic zones (**C**). Mean estimates are represented by symbols, with the error bars representing the three levels of credible intervals. The percentages below the *x*-axis indicate the annual change in insect abundance corresponding with the estimated slope. The bracketed numbers indicate the number of studies and the number of sites underlying each estimate, respectively. The continents are ordered by data availability, but Africa was omitted because of the wide credible intervals of its two studies (terrestrial: −8.93 to +18.34%; freshwater: −16.56 to +10.12% per year). Ecoregions are ordered from north to south from the Northern Hemisphere perspective.

between terrestrial insect abundance trends and landscape-scale urbanization (figs. S3 and S4a), potentially explained by habitat loss and light and/or chemical pollution associated with urbanization (*30*). By contrast, insect abundance trends were positively associated with crop cover at the local (but not landscape) scale in both realms (fig. S3). Specifically, in the terrestrial realm, temporal trends became less negative with increasing crop cover (fig. S4f), consistent with a high-profile case study (*10*). One explanation for this could be that areas with high crop cover tended to remain relatively stable over the study period (only 0.5% of the sites were converted into cropland) relative to land cover change in noncrop areas (3.8% of sites experienced other land-use change). In the freshwater realm, the trends became more positive with increasing crop cover (fig. S4), which could be because agricultural practices have become less detrimental to water quality than they were in the past. Finally, we calculated the relative change in temperature and precipitation over the sampling period at local and regional scales for each site (*14*) to test for a potential role of climate change, but found no evidence for any associations at either scale (figs. S3 and S5).

Although our data compilation has a large geographic and taxonomic scope, there are clear limitations to our analysis, so we remain cautious about generalizing these patterns. First, the trends were highly variable locally but also varied across regions, climatic zones, and time periods. Second, the strong trends in North America had a strong influence on the mean trend estimates. Finally, the manual exclusion of 14 datasets qualified as outliers [for more details, see (*14*)] provided strongly tempered trend estimates (terrestrial: −0.66%; freshwater: +0.34% per year), although there was still strong evidence for a decline for the terrestrial fauna. As with most data compilations of this kind, our data sources were not representatively spread across the world. Most data originated from temperate North America and Europe, but even here there was an underrepresentation of intensively modified sites (high urban or crop cover) compared with their global distribution (fig. S6). Likewise, protected areas were overrepresented in our dataset (34% of the sites) relative to the percentage of the terrestrial surface currently under protection (15%) (*31*). This means that locations where human land use is most intensive, and thus where the strongest effects on insect trends might be expected, were underrepresented. To infer broader patterns across the ecosystems of the world and for more comprehensive tests of human pressures, more data are needed from these underrepresented regions experiencing both low and high environmental change.

Our estimate of a 0.92% decline per year for terrestrial insects is 6-fold smaller than those of recent high-profile case studies [e.g., 3 to 6% loss per year (*10*, *11*), which were included in our analysis]. Nevertheless, our more synthetic estimate translates to an average loss of 8.81% per decade in terrestrial ecosystems. Such a decline is concerning given the critical role that insects play in food webs and ecosystem services and may contribute to other changes such as the declines observed for some insectivorous bird populations (*32*–*34*). At the same time, we found an average increase in freshwater insect abundances that might, at least partially, reflect improvements in water quality. This, in combination with our finding that trends were weaker in protected areas, suggests that appropriate habitat protection and restoration may be effective strategies for mitigating changes in insect assemblages.

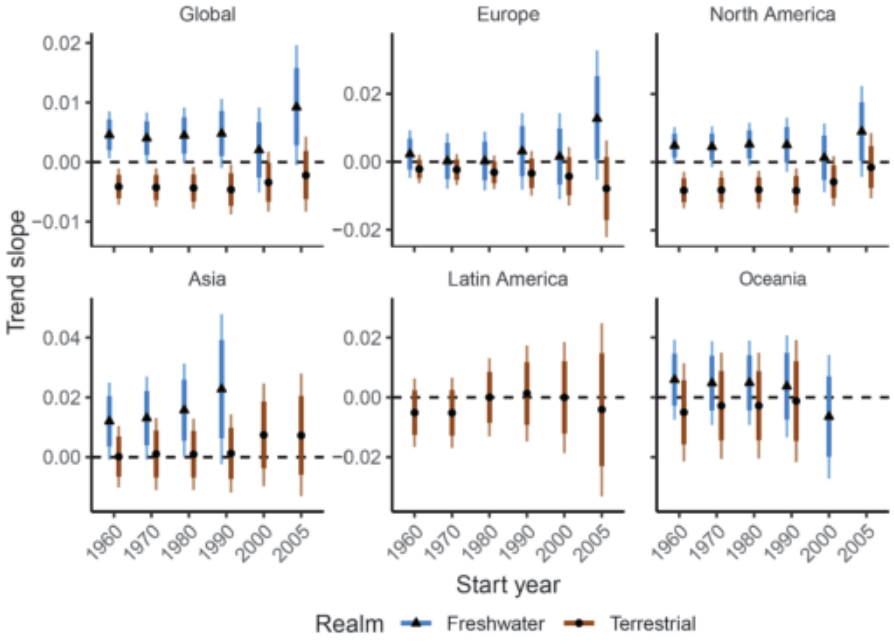

Fig. 3. Trend estimates (±80 and 95% credible intervals) for progressively shorter time periods since 1960. Each time slice included data until the last sampling date but excluded any sites spanning <9 years within the time slice. Only estimates with at least four datasets or 20 sites are shown. The continents are ordered by data availability. Annotation is as in Fig. 2.

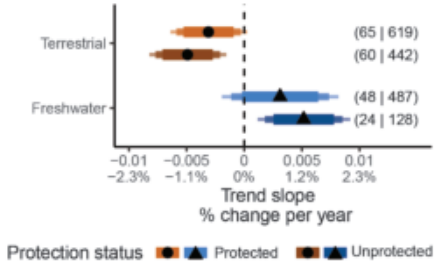

Fig. 4. Trend estimates (±80, 90, and 95% credible intervals) for terrestrial and freshwater insects inside and outside of protected areas. Bracketed numbers indicate the number of studies and number of sites underlying each estimate. Annotation is as in Fig. 2.

REFERENCES AND NOTES

1. A. D. Chapman, *Numbers of Living Species in Australia and the World* (Toowoomba, ed. 2, 2009).
2. N. E. Stork, *Annu. Rev. Entomol.* **63**, 31–45 (2018).
3. C. W. Sabrosky, *Syst. Zool.* **2**, 31–36 (1953).
4. E. O. Wilson, *Conserv. Biol.* **1**, 344–346 (1987).
5. J. A. Thomas *et al.*, *Science* **303**, 1879–1881 (2004).
6. M. L. Forister, J. P. Jahner, K. L. Casner, J. S. Wilson, A. M. Shapiro, *Ecology* **92**, 2222–2235 (2011).
7. A. Valtonen *et al.*, *J. Anim. Ecol.* **86**, 730–738 (2017).
8. R. Dirzo *et al.*, *Science* **345**, 401–406 (2014).
9. S. Schuch, K. Wesche, M. Schaefer, *Biol. Conserv.* **149**, 75–83 (2012).
10. C. A. Hallmann *et al.*, *PLOS ONE* **12**, e0185809 (2017).
11. B. C. Lister, A. Garcia, *Proc. Natl. Acad. Sci. U.S.A.* **115**, E10397–E10406 (2018).
12. G. Vogel, *Science* **356**, 576–579 (2017).
13. B. Jarvis, The insect apocalypse is here: What does it mean for the rest of life on Earth? *The New York Times Magazine*, 27 November 2018, pp. 41–48.
14. See the supplementary materials.
15. B. Lehner, P. Döll, *J. Hydrol.* **296**, 1–22 (2004).
16. G. H. Allen, T. Pavelsky, *Science* **361**, 585–588 (2018).
17. A. J. van Strien *et al.*, *Biol. Conserv.* **200**, 44–50 (2016).

18. I. Rochlin, A. Faraji, D. V. Ninivaggi, C. M. Barker, A. M. Kilpatrick, . *Nat. Commun.* **7**, 13604 (2016).
19. C. L. Outhwaite, R. D. Gregory, R. E. Chandler, B. Collen, N. J. B. Isaac, *Nat. Ecol. Evol.* **4**, 384–392 (2020).
20. D. A. Keiser, J. S. Shapiro, *Q. J. Econ.* **134**, 349–396 (2019).
21. H. F. V. Braaten *et al.*, *Environ. Sci. Technol.* **53**, 1834–1843 (2019).
22. F. Bouraoui, B. Grizzetti, *Sci. Total Environ.* **409**, 4899–4916 (2011).
23. P. Bigus, M. Tobiszewski, J. Namieśnik, *Mar. Pollut. Bull.* **78**, 26–42 (2014).
24. V. Lencioni, *Sci. Total Environ.* **622-623**, 563–575 (2018).
25. Y. Cai, Y. Lu, Z. Gong, *J. Freshwat. Ecol.* **30**, 157–168 (2015).
26. K. Slavik *et al.*, *Ecology* **85**, 939–954 (2004).
27. R. D. Robarts, A. V. Zhulidov, D. F. Pavlov, *Aquat. Sci.* **75**, 27–38 (2013).
28. L. A. Henry, V. Douhovnikoff, *Annu. Rev. Environ. Resour.* **33**, 437–460 (2008).
29. J. C. Habel, M. J. Samways, T. Schmitt, *Biodivers. Conserv.* **28**, 1343–1360 (2019).
30. K. Perris, *Ecology of Urban Environments* (Wiley-Blackwell, 2016).
31. UNEP-WCMC, IUCN, NGS, *Protected Planet Report 2018* (2018); https://livereport.protectedplanet.net/.
32. C. A. Hallmann, R. P. B. Foppen, C. A. M. van Turnhout, H. de Kroon, E. Jongejans, *Nature* **511**, 341–343 (2014).
33. K. V. Rosenberg *et al.*, *Science* **366**, 120–124 (2019).
34. D. E. Bowler, H. Heldbjerg, A. D. Fox, M. de Jong, K. Böhning-Gaese, *Conserv. Biol.* **33**, 1120–1130 (2019).
35. R. van Klink, D. E. Bowler, Code for: Meta-analysis reveals declines in terrestrial but increases in freshwater insect abundances, Zenodo (2020); https://doi.org/10.5281/zenodo.3691682.
36. R. van Klink *et al.*, A global database of long-term changes in insect assemblages, Knowledge Network for Biocomplexity (KNB) (2020); https://doi.org/10.5063/F11V5C9V.

ACKNOWLEDGMENTS

We thank R. Vermeulen (WBBS foundation), S. Swengel, M. Driessen, J. Owen, F. Gilbert, T. Wepprich, A. M. Kilpatrick, Butterfly Monitoring Israel, S. Schuch, and the Smithsonian Institution for making data freely available to us. Data from the Greenland Ecosystem Monitoring Programme were provided by the Department of Bioscience, Aarhus University, Denmark. The ECN data were supplied by the Natural Environment Research Council (UK). We also thank N. Naderi, S. Blowes, P. Keil, A. T. Clark, S. D. Jurburg, and M. Winter for help with data extraction, statistical advice, figure formatting, and commenting on earlier versions of the manuscript.
Funding: R.v.K., J.M.C., D.E.B., and A.G. were supported by the German Centre for Integrative Biodiversity Research (iDiv) Halle-Jena-Leipzig and its synthesis center (sDiv), funded by the German Research Foundation (FZT 118). K.B.G. was supported by the Russian Foundation for Basic Research (19-05-00245). Some of the data analyzed here were collected using NSF grants to the LTER Network (NSF06-20443, 8811906, 9411976, 0080529, 0217774, DEB-0423704, DEB-1633026, DEB-1637685, DEB-1256696, DEB-0832652, DEB-0936498, DEB-1832016, DEB-0620652 DEB-1234162, OCE-9982133, OCE-0620959, OCE-1237140, and OCE-1832178). **Author contributions:** R.v.K. and J.M.C. conceived the study. R.v.K. and K.B.G. performed the literature search. A.G., D.E.B., and A.B.S. collected data. R.v.K. and D.E.B. analyzed the data. R.v.K. and J.M.C. wrote the first version of the manuscript, and all authors substantially edited the text.
Competing interests: The authors declare no competing interests.
Data and materials availability: The data frames used for the analyses are available as data S1 and S2 in the supplementary materials, excluding datasets with access licenses that precluded distribution of a derived product. Links to these datasets, and all other publicly available datasets, are provided in table S1. All code for this analysis is available on GitHub (https://github.com/roelvanklink/Final-insect-abundance-changes) and is archived on Zenodo (*35*). The underlying database, including extended metadata, is available on KNB (*36*).

SUPPLEMENTARY MATERIALS

science.sciencemag.org/content/368/6489/417/suppl/DC1
Materials and Methods
Figs. S1 to S7
Tables S1 and S2
External Data S1 and S2
References (*37*–*206*)

10 May 2019; accepted 3 March 2020
10.1126/science.aax9931

PALEONTOLOGY

The spatial structure of Phanerozoic marine animal diversity

R. A. Close[1]*, R. B. J. Benson[2], E. E. Saupe[2], M. E. Clapham[3], R. J. Butler[1]

The global fossil record of marine animals has fueled long-standing debates about diversity change through time and the drivers of this change. However, the fossil record is not truly global. It varies considerably in geographic scope and in the sampling of environments among intervals of geological time. We account for this variability using a spatially explicit approach to quantify regional-scale diversity through the Phanerozoic. Among-region variation in diversity is comparable to variation through time, and much of this is explained by environmental factors, particularly the extent of reefs. By contrast, influential hypotheses of diversity change through time, including sustained long-term increases, have little explanatory power. Modeling the spatial structure of the fossil record transforms interpretations of Phanerozoic diversity patterns and their macroevolutionary explanations. This necessitates a refocus of deep-time diversification studies.

The fossil record of Phanerozoic marine biodiversity has long been a model system for understanding animal diversification through deep time (*1*–*6*). Numerous hypotheses have been proposed to explain these patterns. Some invoke long-term environmental change (*7*–*9*) or tectonic drivers (*10*), whereas others emphasize time-dependent processes, ranging from unconstrained, exponential diversification (*3*, *11*) to diversity-dependent diversification constrained by biotic interactions (*2*, *5*, *12*). Inferred diversity patterns may also reflect the structure of the fossil record, including geological factors, such as rock amount (*13*) and lithification trends (*4*), or research practices, such as sampling variation resulting from worker interest or taxonomic culture (*4*, *5*). However, there is little consensus about the relative importance of the many factors invoked by these hypotheses (*3*–*5*, *7*, *10*, *13*, *14*).

We argue that the spatial structure of the fossil record is one of the most influential factors affecting interpretations of diversity dynamics in deep time. Previous studies have acknowledged this problem but have not explicitly corrected for it (*4*, *6*). The global fossil record, as currently documented, is not truly global (*4*, *15*–*17*), and there is substantial variation through geological time in the numbers, sizes, and locations of spatial regions from which fossils have been reported. Therefore, nominally global diversity estimates among intervals of geological time derive from different points on their respective species-area curves, which introduces a confounding source of variation. Controlling for sampling intensity alone does not address this (*18*); 50 to 60% of the changes in global sampling-standardized genus richness can be explained simply by changes in the geographic spread of fossil localities (Fig. 1, C and E). This correlation is unlikely to be driven by changes in habitable area because changes in shallow–marine sediment extent are not correlated with either global fossil taxon counts or the spatial extent of the global fossil record (Fig. 1, E and F, and fig. S1; data sources for environmental covariates are listed in table S1). Moreover, diversity levels are controlled by factors that have nonrandom spatial distributions [e.g., latitude and environment (*19*)], but most studies of diversity drivers through time have not explicitly accounted for the spatial distributions of important environmental factors, such as the development of reefs (*20*) or epeiric seaways (*9*).

We present a spatially explicit framework to estimate regional-scale diversity patterns through the Phanerozoic and their relationship to time and environment. We standardized the geographic scale of the analysis by drawing sets of fossil localities that represent regions of near-uniform spatial extent. This procedure was repeated at several different spatial scales. We then conducted spatiotemporally explicit tests of the influence on inferred diversity of time-dependent processes, local environmental factors, rock record and sampling variables, and research practices. We analyzed fossil occurrence data from the Paleobiology Database (*21*), consisting of 396,815 occurrences of 22,855 marine animal genera. Our spatial subsampling algorithm identifies all nested sets of adjacent fossil localities using their paleocoordinates (*22*). From this, we extracted regions with minimum-spanning tree (MST) lengths (*6*) of ~1500, 2000, 2500, 3000, and 3500 km. We estimated genus richness for each

[1]School of Geography, Earth and Environmental Sciences, University of Birmingham, Edgbaston, Birmingham B15 2TT, UK. [2]Department of Earth Sciences, University of Oxford, Oxford OX1 3AN, UK. [3]Department of Earth and Planetary Sciences, UC Santa Cruz, Santa Cruz, CA 95064, USA.
*Corresponding author. Email: roger.close@gmail.com

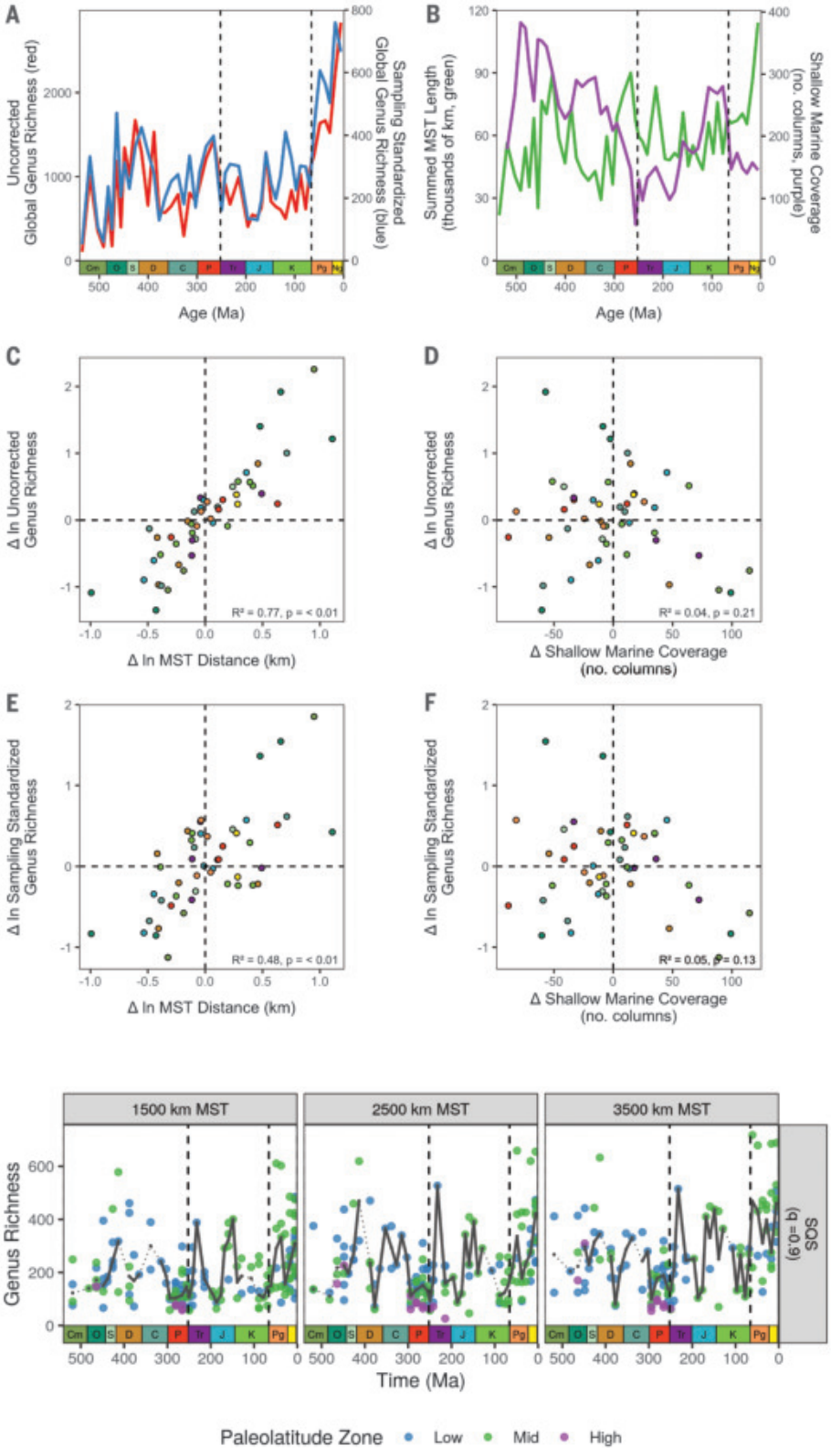
A
Uncorrected Global Genus Richness (red)
Sampling Standardized Global Genus Richness (blue)
Age (Ma)
B
Summed MST Length (thousands of km, green)
Shallow Marine Coverage (no. columns, purple)
Age (Ma)
C
Δ ln Uncorrected Genus Richness
R² = 0.77, p = < 0.01
Δ ln MST Distance (km)
D
Δ ln Uncorrected Genus Richness
R² = 0.04, p = 0.21
Δ Shallow Marine Coverage (no. columns)
E
Δ ln Sampling Standardized Genus Richness
R² = 0.48, p = < 0.01
Δ ln MST Distance (km)
F
Δ ln Sampling Standardized Genus Richness
R² = 0.05, p = 0.13
Δ Shallow Marine Coverage (no. columns)

Fig. 1. Correlations between changes in Phanerozoic marine animal diversity (Eumetazoa excluding Tetrapoda) and changes in spatial sampling and habitable area. (**A**) Uncorrected and sampling standardized [SQS (*5*), quorum = 0.7] global genus richness per bin. Cm, Cambrian; O, Ordovician; S, Silurian; D, Devonian; C, Carboniferous; P, Permian; Tr, Triassic; J, Jurassic; K, Cretaceous; Pg, Paleogene; Ng, Neogene. (**B**) Spatial sampling (summed MST length in kilometers) and habitable area [shallow marine coverage; number of (no.) columns]. (**C**) Relationship between spatial sampling and uncorrected genus richness per interval. R^2, coefficient of determination. (**D**) Relationship between habitable area (shallow marine coverage, no. columns) and uncorrected genus richness per interval. (**E**) Relationship between spatial sampling and sampling-standardized (SQS, quorum = 0.7) genus richness per interval. (**F**) Relationship between habitable area (shallow marine coverage, no. columns) and sampling-standardized (SQS, quorum = 0.7) genus richness per interval. All variables are first-differenced. R^2 and P values derive from linear model fits. For information about variables, see table S1. Colors of points in (C) to (F) match the colors of geological periods in (A) and (B).

Fig. 2. Spatially standardized diversity patterns for 1500, 2500, and 3500-km MST lengths. Genus richness estimated using SQS (*5*) [quorum (q) = 0.9]. Black lines and points indicate bin-level medians.

spatial region using shareholder quorum subsampling (SQS) (*5*), alongside additional information such as spatial statistics (e.g., counts of occupied grid cells) and local environmental parameters (*22*).

Spatially standardized diversity estimates vary considerably across the globe within each time interval (Fig. 2), which is masked in global diversity curves. We find that diversity varies at least as much across spatial regions within intervals as it does through time (fig. S2). Our spatial-standardization procedure greatly diminishes a Permian peak in diversity that was present in global curves, which resulted from the broad spatial extent

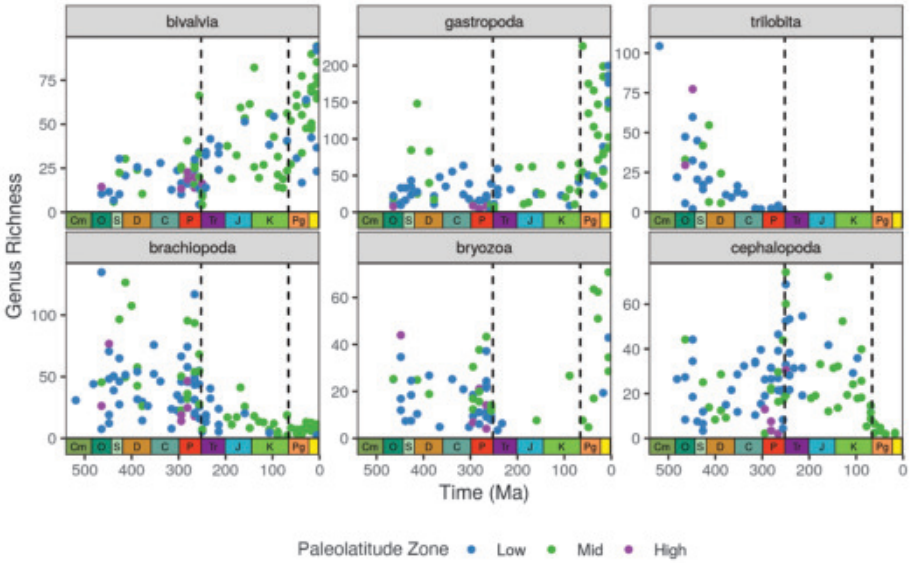

Fig. 3. Spatially standardized genus richness patterns for selected groups of marine invertebrates at 2000-km MST length. Richness estimated using SQS (*5*) (quorum = 0.8).

of Permian fossil localities in the Paleobiology Database (Fig. 1A and figs. S3 and S4). Furthermore, the sustained Mesozoic–Cenozoic global increase in diversity, a seminal feature of global diversity curves (*2*, *23*–*25*), is transformed into a much more modest, stepwise increase across the Cretaceous–Paleogene (K/Pg) boundary (Fig. 2 and fig. S5). However, in agreement with existing sampling-standardized global curves (*5*, *6*, *24*), regional diversity is higher on average from the Ordovician to the early Devonian and in the Cenozoic, and it is lower on average in the late Paleozoic and early Mesozoic.

Low paleolatitudes (±0° to 30°) are best represented during the Paleozoic, whereas mid-paleolatitudes (±30° to 60°) are better represented during the Mesozoic to the Cenozoic, partly because of continental drift (fossil-record sampling is most intense in North America and Europe, and landmasses, on average, migrated northward over this interval). Low-paleolatitude diversity in the Paleozoic is similar to that of the Neogene (Fig. 2). Mid-paleolatitude diversity is lower than average in the Permian and higher than average in the Cenozoic. High paleolatitudes (±60° to 90°) are only informative for a handful of Paleozoic bins and consistently have low diversity. Results vary only slightly across different spatial-standardization criteria (*22*) (Fig. 2).

Major groups of marine invertebrates show pronounced variation in diversity through the Phanerozoic (Fig. 3), displaying patterns that generally mirror their respective global curves. Bivalves show a pattern of sustained increase through the Phanerozoic (*5*, *26*) but with increasing variance among spatial regions through time. Brachiopods show a very different pattern than that of bivalves (*5*), with clear evidence of a marked decrease in average diversity across the Permian–Triassic (P/T) boundary. Cephalopods, by contrast, show evidence of higher diversity in the immediate aftermath of the P/T, which is consistent with global patterns observed in ammonoids (*27*). Gastropod diversity remained relatively stable across the Paleozoic-Mesozoic, but it experienced a sharp fourfold increase in diversity across the K/Pg [compared with a latest Cretaceous increase in global curves (*5*)]; this appears to be the main driver of the modest stepwise increase across the K/Pg within marine animals as a whole.

We used linear mixed-effects models to assess the roles of selected environmental, sampling, and biotic variables as drivers of diversity change through time and space, evaluated with Akaike's information criterion and model averaging (*22*). We modeled temporal autocorrelation using a continuous-time first-order autoregressive correlation structure (*22*). Exploratory analyses suggested that explanations for diversity change through time may differ between low and mid-paleolatitudes, which were therefore modeled separately. Insufficient data were available for high paleolatitudes. Our explanatory variables comprise several broad categories (table S1), including local environmental variables, shallow–marine sediment extent, temporal variables [including exponential diversification through time (*3*, *14*) and categorical variables describing equilibrial diversification phases (*2*) and short-term postextinction decreases], and variables related to research activity (including sampling variables and modern continental region identity). Modern continental region identity was specified as a random effect to control for geographic variation in research practices (e.g., taxonomic splitters versus lumpers) and to permit us to model time series autocorrelation (*22*).

The model selection procedure is relatively more decisive for mid- than for low paleolatitudes, with fewer models in the confidence set (models receiving an evidence ratio of ≤8; fig. S6 and tables S2 and S3) and higher average goodness of fit (table S4). Models incorporating a subset of our explanatory variables receive the strongest support for most spatial extents (table S3). Elevated mid-paleolatitude diversity is robustly associated with the proportion of reefal localities and with counts of references associated with spatial regions (reflecting either research or literature interest, high diversity driving high reference counts, or both; Fig. 4 and figs. S5, S7, and S8). There is also evidence that shallow–marine sediment extent is positively associated with diversity (Fig. 4). Marginal coefficients of modern continental regions show that Europe has higher diversity than other regions, perhaps because of variation in research or taxonomic practices (fig. S9). At low paleolatitudes, shallow–marine sediment extent, lithology counts, and reference counts are important at many spatial scales (Fig. 4 and fig. S8). Overall, however, at low latitudes, no single combination of explanatory variables is consistently important across all scales (table S2). An alternate set of model comparisons including continental fragmentation index (*10*) does not recover a prominent role for that variable (see "Sensitivity Analyses" in the supplementary materials).

Shallow–marine sediment extent, a proxy for global variation in shallow–marine habitat area (*28*), is positively related to the diversity of regional-scale assemblages (Fig. 4). This is consistent with the hypothesis that some changes in marine diversity were driven by factors associated with sea level, potentially via species-area effects (*7*, *9*). We also recover strong evidence that reefs are loci of high diversity (Fig. 4). This mirrors the present-day pattern in which reefs are biodiversity hotspots, hosting a disproportionate fraction of marine species (*29*). Therefore, both the flooding of continental interiors and the expansion and contraction of reefs are likely to drive changes in true global diversity.

Only one temporal variable is included consistently in the best-ranked models that explain marine animal diversity: a parameter differentiating pre-Cenozoic intervals from the Cenozoic (especially at mid-latitudes; Fig. 4, fig. S8, and tables S2 and S3). This indicates that there was, on average, approximately twofold greater diversity during the Cenozoic compared with earlier intervals (fig. S10).

No explanatory power can be attributed to the passage of continuous time [age in millions

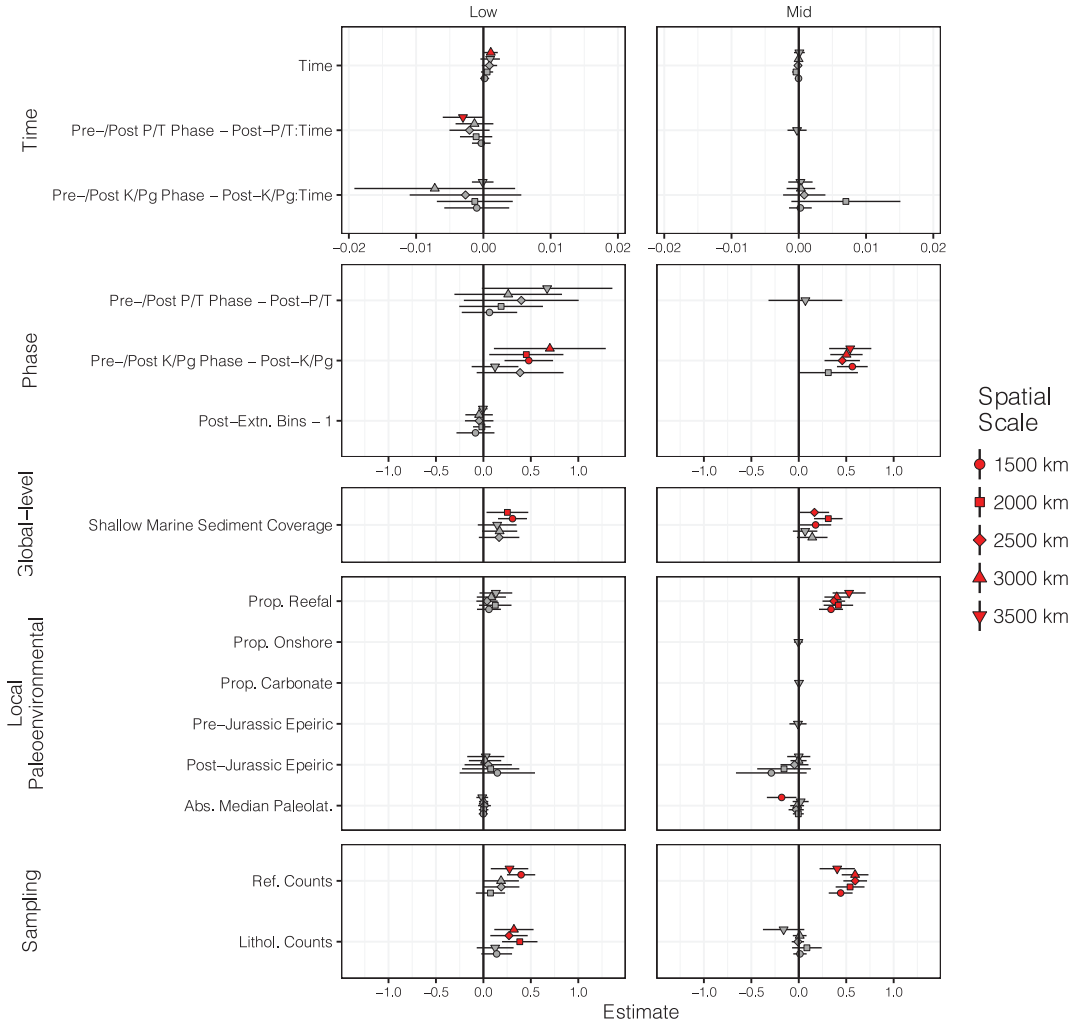

Fig. 4. Model-averaged parameter estimates for coefficients at low and mid-paleolatitudes. Models were fitted to spatially standardized diversity estimates using SQS (quorum = 0.9). See table S1 for descriptions of explanatory variables. Confidence intervals represent interquartile ranges. Red points signify estimates that do not overlap with zero; gray points indicate points that do. Extn., extinction; Prop., proportion; Abs., absolute; Paleolat., paleolatitude; Ref., reference; Lithol., lithology.

of years (Ma)]. Model-averaged parameter estimates for the coefficient of time, which represents the net long-term diversification rate, are not significantly different from zero at either mid- (−0.000994 to 0.000891) or low (−0.000493 to 0.00246) paleolatitudes at any spatial scale (Fig. 4). This indicates a lack of support for the hypothesis of sustained exponential background diversification (*3*, *14*). Regressions of diversity solely as a function of time within individual pre-Cenozoic and Cenozoic diversification phases are also nonsignificant (fig. S11). Furthermore, we do not find evidence for low diversity immediately after mass extinction events at the time scale of our analysis (bin durations averaging 11 Ma), which suggests that the postextinction recovery of regional diversity has generally been rapid.

In contrast to the lack of secular temporal trends in Phanerozoic marine animals, individual groups show marked variation in diversity through time (Fig. 3). Ecological limits imposed by finite resources such as energy and space (*30*) provide one intuitive explanation for why highly dynamic patterns within individual groups sum to produce highly constrained net diversity in marine animals throughout the Phanerozoic (with the exception of a stepwise increase in the early Cenozoic). Zero-sum dynamics could result from direct biotic competition between specific groups or more diffuse competition among multiple clades (*26*) but could also arise via chance.

Patterns of global diversity through time have been the focus of seminal studies in paleobiology, and the implications of these patterns for macroevolutionary theory have long been debated (*2*–*5*, *11*, *14*, *24*, *25*). Our spatially explicit analysis provides a different conception, in which the variation in regional diversity is partitioned between time- and environment-dependent explanations. Diversity varies by several orders of magnitude among marine environments on Earth today (*19*), and we find that it has done so for much of the Phanerozoic. In contrast, we find little evidence for sustained increases in diversity through time. We also cast doubt on the prospect of directly estimating variation in true global diversity based on current knowledge of the fossil record. These observations urge scrutiny of the focus on time and time-varying climate or Earth system parameters in global fossil record studies (*2*, *7*, *8*, *10*). Nevertheless, the importance of local environment as a driver of regional diversity indicates that variation in summed global diversity might ultimately result from shifts in Earth's climate and tectonic state. By unmasking the spatial component of variation in diversity—hitherto obscured by global

curves—our approach raises intriguing possibilities for the fossil record to shed light on the historic drivers of biological diversity on Earth.

REFERENCES AND NOTES

1. D. M. Raup, J. J. Sepkoski Jr., *Science* **215**, 1501–1503 (1982).
2. J. J. Sepkoski Jr., *Paleobiology* **10**, 246–267 (1984).
3. M. J. Benton, B. C. Emerson, *Palaeontology* **50**, 23–40 (2007).
4. J. Alroy *et al*., *Science* **321**, 97–100 (2008).
5. J. Alroy, *Science* **329**, 1191–1194 (2010).
6. J. Alroy, *Palaeontology* **53**, 1211–1235 (2010).
7. B. Hannisdal, S. E. Peters, *Science* **334**, 1121–1124 (2011).
8. P. J. Mayhew, M. A. Bell, T. G. Benton, A. J. McGowan, *Proc. Natl. Acad. Sci. U.S.A.* **109**, 15141–15145 (2012).
9. S. E. Peters, *Paleobiology* **33**, 165–181 (2007).
10. A. Zaffos, S. Finnegan, S. E. Peters, *Proc. Natl. Acad. Sci. U.S.A.* **114**, 5653–5658 (2017).
11. J. W. Valentine, *Palaeontology* **12**, 684–709 (1969).
12. J. Alroy, *Proc. Natl. Acad. Sci. U.S.A.* **105**, 11536–11542 (2008).
13. A. B. Smith, A. J. McGowan, *Palaeontology* **50**, 765–774 (2007).
14. S. M. Stanley, *Paleobiology* **33**, 1–55 (2007).
15. G. J. Vermeij, L. R. Leighton, *Paleobiology* **29**, 3–7 (2003).
16. A. J. McGowan, A. B. Smith, *Paleobiology* **34**, 80–103 (2008).
17. D. A. Vilhena, A. B. Smith, *PLOS ONE* **8**, e74470 (2013).
18. R. A. Close, S. W. Evers, J. Alroy, R. J. Butler, *Methods Ecol. Evol.* **9**, 1386–1400 (2018).
19. A. G. Fischer, *Evolution* **14**, 64–81 (1960).
20. W. Kiessling, C. Simpson, M. Foote, *Science* **327**, 196–198 (2010).
21. The Paleobiology Database; https://paleobiodb.org.
22. For further details, see supplementary materials.
23. M. E. Patzkowsky, *Annu. Rev. Earth Planet. Sci.* **45**, 471–495 (2017).
24. A. M. Bush, R. K. Bambach, *Geology* **43**, 979–982 (2015).
25. A. M. Bush, G. Hunt, R. K. Bambach, *Proc. Natl. Acad. Sci. U.S.A.* **113**, 14073–14078 (2016).
26. A. I. Miller, J. J. Sepkoski Jr., *Paleobiology* **14**, 364–369 (1988).
27. A. Brayard *et al*., *Science* **325**, 1118–1121 (2009).
28. S. E. Peters, J. M. Husson, *Geology* **45**, 323–326 (2017).
29. M. L. Reaka-Kudla, in *Biodiversity II: Understanding and Protecting Our Biological Resources*, M. L. Reaka-Kudla, D. E. Wilson, E. O. Wilson, Eds. (Joseph Henry Press, 1997), pp. 83–108.
30. D. L. Rabosky, A. H. Hurlbert, *Am. Nat.* **185**, 572–583 (2015).

ACKNOWLEDGMENTS

We thank all contributors to the Paleobiology Database and two anonymous reviewers for providing insightful and constructive comments. This is Paleobiology Database official publication 364. **Funding:** This research was funded by the European Union's Horizon 2020 research and innovation program under grant agreement 637483 (ERC Starting Grant TERRA to R.J.B.). **Author contributions:** R.A.C., R.B.J.B., and R.J.B. conceived the study. M.E.C. contributed to the dataset. R.A.C. designed and conducted the analyses and made the figures. R.A.C. and R.B.J.B. wrote the manuscript. All authors provided critical feedback on the text. **Competing interests:** The authors declare no competing interests. **Data and materials availability:** The fossil occurrence data used in this study were downloaded from the Paleobiology Database (paleobiodb.org) and are available, together with all analysis scripts, in data S1.

SUPPLEMENTARY MATERIALS

science.sciencemag.org/content/368/6489/420/suppl/DC1
Materials and Methods
Figs. S1 to S19
Tables S1 to S8
References (*31*–*63*)
MDAR Reproducibility Checklist
Data S1

22 July 2019; accepted 9 March 2020
10.1126/science.aay8309

PROTEIN RADICALS

Structure of a trapped radical transfer pathway within a ribonucleotide reductase holocomplex

Gyunghoon Kang[1,2], Alexander T. Taguchi[3]*, JoAnne Stubbe[2,3]†, Catherine L. Drennan[1,2,3]†

Ribonucleotide reductases (RNRs) are a diverse family of enzymes that are alone capable of generating 2′-deoxynucleotides de novo and are thus critical in DNA biosynthesis and repair. The nucleotide reduction reaction in all RNRs requires the generation of a transient active site thiyl radical, and in class I RNRs, this process involves a long-range radical transfer between two subunits, α and β. Because of the transient subunit association, an atomic resolution structure of an active α2β2 RNR complex has been elusive. We used a doubly substituted β2, E52Q/(2,3,5)-trifluorotyrosine122-β2, to trap wild-type α2 in a long-lived α2β2 complex. We report the structure of this complex by means of cryo–electron microscopy to 3.6-angstrom resolution, allowing for structural visualization of a 32-angstrom-long radical transfer pathway that affords RNR activity.

Ribonucleotide reductases (RNRs) convert ribonucleotides into deoxyribonucleotides and generate the deoxyribonucleotide pools needed for DNA biosynthesis and repair (Fig. 1A and fig. S1). Because of these activities, RNRs are drug targets, with several U.S. Food and Drug Administration–approved RNR inhibitors used clinically in the treatment of various forms of cancer (*1*). For all RNR classes, catalysis entails formation of a protein-based thiyl radical species in the active site (*2*). In the case of the prototypic class Ia RNR from *Escherichia coli*, the generation of this thiyl radical species occurs on the α2 subunit (C439α•) and involves a long-range radical transfer from the β2 subunit's diferric-tyrosyl radical cofactor (Y122β•) (Fig. 1B) (*3*). The distance that radical species must travel has been estimated to be an incredibly long 35 to 40 Å, according to both pulsed electron-electron double resonance (PELDOR) spectroscopy (*4*) and a docking model of an α2β2 complex that was based on shape complementarity of the separate α2 and β2 crystal structures (Fig. 1C and fig. S2A) (*5*). This radical transfer, which is proposed to occur through a series of reversible proton-coupled electron transfer (PCET) steps, does not involve typical electron-transfer cofactors but instead requires a series of conserved aromatic amino acids (Fig. 1B) (*2*, *3*, *5*, *6*). Key residue Y356β has never been structurally visualized; this residue is located on the C-terminal β-tail (residues 341β to 375β), which is disordered in all β2 structures. The goal of this study is to provide a structure of the active α2β2 state of an RNR that has the critical β-tail ordered and the intact PCET pathway visualized.

There are two main reasons why obtaining such a structure has eluded researchers. First, the α2-β2 interaction that affords thiyl radical generation is transient, with a dissociation rate constant (k_{off}) for β2 from α2 of greater than 60 s^{-1} (*7*). The PCET pathway is intact during the radical transfer process; however, after the return of the radical to β2, the PCET pathway disassembles. Second, the active α2β2 state is in equilibrium with an inactive α4β4 state (*8*). The shifting of this equilibrium between active and inactive states is responsible for regulating RNR activity in response to deoxyribonucleotide levels in *E. coli* (fig. S2B) (*8*). For these two reasons, the structure of the active form of RNR has been elusive, requiring some means of trapping the active state to slow subunit dissociation and limit oligomeric state change.

We succeeded in trapping the active state of RNR by using a previously studied doubly substituted E52Q/(2,3,5)-trifluorotyrosine122(F_3Y122)-β2 (*9*) with wild-type α2 in the presence of substrate guanosine diphosphate (GDP) and specificity effector thymidine triphosphate (TTP) (Fig. 1D). The overall resolution is 3.6 Å, with local resolution ranging from ~3.3 Å within the core of the protein complex to 5.5 Å on the α2 surface (fig. S3 and table S1). Regions of highest resolution show clear density for side chains (fig. S4). We further demonstrate that this RNR construct is active: It is capable of forming product [1 equivalent of deoxyguanosine diphosphate (dGDP) per dimer], and it forms a pathway radical (Y356•) in a kinetically competent manner (fig. S5). This structure addresses key questions about RNR and about biological PCET, including (i) how PCET residues are arranged with respect to each other and to possible proton acceptors and donors, (ii) the molecular basis for the conversion of a disordered stretch of 20 amino acids into an ordered PCET pathway, (iii) why the PCET pathway disassembles after every round of

[1]Howard Hughes Medical Institute, Massachusetts Institute of Technology, Cambridge MA, USA. [2]Department of Biology, Massachusetts Institute of Technology, Cambridge MA, USA. [3]Department of Chemistry, Massachusetts Institute of Technology, Cambridge MA, USA.
*Present address: RubrYc Therapeutics, San Carlos CA, USA.
†Corresponding author. Email: stubbe@mit.edu (J.S.); cdrennan@mit.edu (C.L.D.)

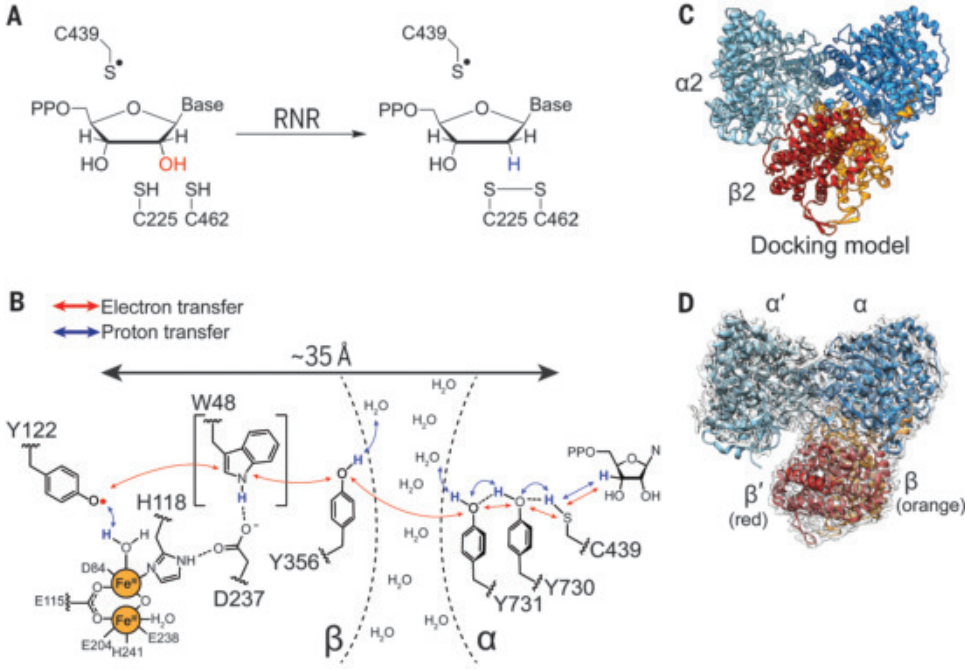

Fig. 1. RNR catalysis requires formation of a transient thiyl radical species. (**A**) Radical-based reduction of ribonucleoside diphosphates by class Ia RNR. Reducing equivalents are provided by a pair of active-site cysteines that are oxidized concomitant with product formation. The resulting disulfide is rereduced by means of disulfide exchange, with reduced nicotinamide adenine dinucleotide phosphate (NADPH) as the ultimate source of electrons (*27*). (**B**) Proposed proton-coupled electron transfer pathway that results in the transient oxidation of C439-α by Y122•-β. The direct involvement of W48 in the pathway is uncertain. (**C**) Symmetric "docking model" of 260-kDa α2β2 complex that was based on shape complementarity of the individual α2 and β2 crystal structures (*5*). α2 is shown in light and dark blue, and β2 is shown in red and orange. (**D**) 3.6-Å resolution cryo-EM map of an asymmetric, active RNR trapped by using a doubly substituted E52Q/(2,3,5)-trifluorotyrosine122(F_3Y122)-β2 with wild-type α2 in the presence of substrate GDP and specificity effector TTP. Model colors are as in (C), with cryo-EM density shown in transparent gray. (Single-letter abbreviations for the amino acid residues are as follows: A, Ala; C, Cys; D, Asp; E, Glu; F, Phe; G, Gly; H, His; I, Ile; K, Lys; L, Leu; M, Met; N, Asn; P, Pro; Q, Gln; R, Arg; S, Ser; T, Thr; V, Val; W, Trp; and Y, Tyr.)

turnover, (iv) the factors that trigger pathway disassembly and assembly, and (v) to what degree the structure of an active RNR state looks like the docking model.

The first striking observation from our structure is that unlike the *E. coli* RNR symmetric docking model (Fig. 1C), the cryo–electron microscopy (cryo-EM) structure of the α2β2 complex is asymmetric (Fig. 1D). The α2-β2 interface is formed primarily between one α monomer and β2 and minimal interaction with the other α monomer (hereafter referred to as α′) (Fig. 1D). This positioning of subunits precludes the simultaneous formation of two radical translocation pathways, which is consistent with prior evidence for half-sites reactivity such as the observation that one equivalent of the cancer drug gemcitabine diphosphate inactivates both α monomers (*10*). We now see that only one α subunit can turn over at a time. Additionally, this finding of asymmetry is consistent with previous structural snapshots of class Ib RNRs (*11*, *12*), the first of which is a structure that is best described as β2 dangling off of one α monomer (fig. S2C) (*11*).

We are able to visualize all residues of the elusive β-tail, including Y356 and the ~20 residues within the ~35-residue-long β-tail (residues 341 to 375) that have been disordered in previous structures (Fig. 2A). Consistent with complex asymmetry, the tail of the other β monomer (hereafter referred to as β′) is only resolved up to residue 341 (of 375). The ordered β-tail extends far into the active site cavity in α, coming into direct van der Waals contact with

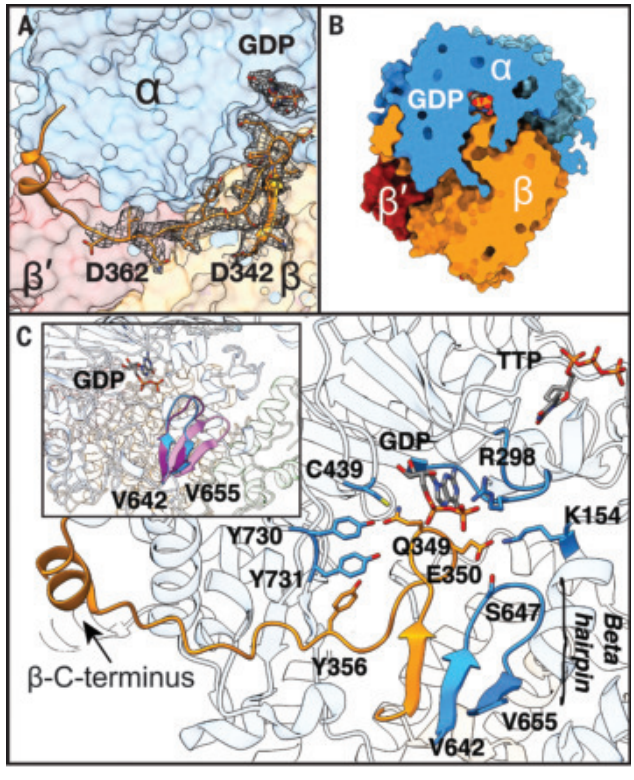

Fig. 2. Fully visualized β-tail extends deep into the α active site. (**A**) Missing β residues 342 to 362 modeled into cryo-EM density (gray mesh, threshold set to 0.0249). (**B**) Slice through space-filling representation, showing tight packing between subunits, which blocks solvent accessibility. (**C**) β–C terminus extends up to substrate-binding site in α. Regions of α that contact β-tail are displayed. Substrate GDP and effector TTP are shown in sticks, separated by the specificity loop, labeled at position R298. (Inset) β-hairpin of α shifts 5 Å toward the active site upon substrate and effector binding and the ordering of the specificity loop. Three α2 structures were aligned to highlight movement of this β-hairpin: substrate-free α2 [pink, PDB 2R1R (*14*)], substrate-effector–bound α2 from inhibited α4β4 [purple, PDB 5CNV (*13*)], and substrate-bound α2 from our structure of active α2β2 (blue).

substrate before making a sharp turn and extending back toward the β subunit and finally looping around to a groove on the side of α (Fig. 2A and fig. S6). This observation immediately allows us to answer the question of why the PCET pathway disassembles after every round of turnover: The β-tail completely sequesters the active site so that product dissociation

would necessitate β departure (Fig. 2B and fig. S7).

Additionally, this structure suggests how the binding of substrate-effector pairs could facilitate β-tail binding and PCET pathway assembly (substrate-effector pair explanation is provided in fig. S1); the β-tail binding pocket simply does not exist as a pocket in the absence of substrate. Substrate itself forms the top of the pocket (Fig. 2, B and C), and the right side of the pocket is formed by a β-hairpin from the α subunit that is known to swing in toward the active site when substrate-effector pairs are bound (Fig. 2C) (*13*, *14*). Although we do not fully understand why this β-hairpin is swung-in in the presence of cognate substrate-effector pairs, our *E. coli* RNR structures bound with all four of these pairs [cytidine diphosphate/deoxyadenosine triphosphate (CDP/dATP), uridine diphosphate (UDP)/dATP, GDP/TTP, and adenosine diphosphate/deoxyguanosine triphosphate (ADP/dGTP)] (*13*) show this swung-in position of the β-hairpin, whereas substrate-free or effector-free structures do not. In this cryo-EM structure, we observed the same recognition mode for GDP/TTP as was described before (fig. S8) (*13*) and again found a swung-in β-hairpin (Fig. 2C). Residues 643α to 647α of this hairpin run parallel to residues 343 to 346 of the β subunit, forming a miniature β-sheet and securing β in position for radical transfer (Fig. 2C and fig. S9).

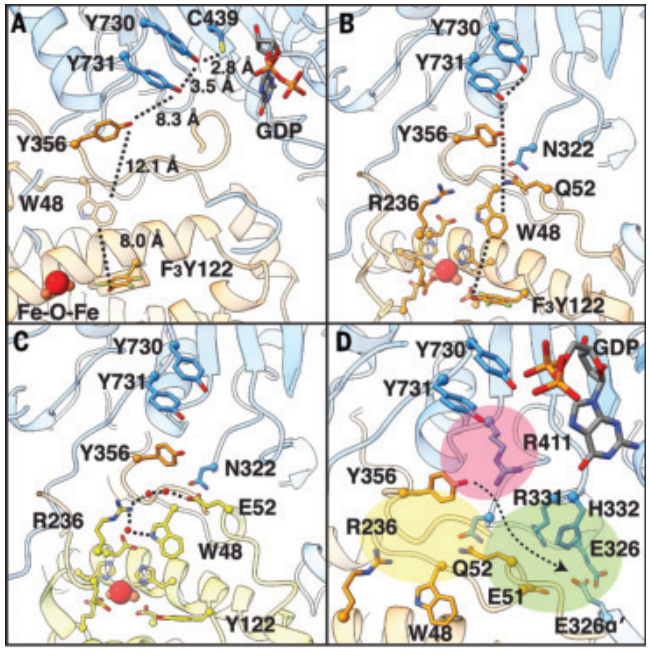

Fig. 3. The interface region of the α2β2 complex. (**A**) Key residues that are involved in PCET, including Y356, are shown with distances between them in angstroms. W48 is shown in partial transparency because of uncertainty regarding its direct participation in PCET. Colors are as in Fig. 1C. (**B**) Positioning of Q52 of β with respect to PCET pathway (dashed lines). The Q52 side chain is 2.5 Å from the side chain of N322, 6.9 Å from the side chain hydroxyl of PCET residue Y356, and 5.2 Å from the C4 position of the indole ring of W48 in β. (**C**) Superimposition of higher-resolution structure of β [yellow, PDB 5CI4 (*32*)] onto the cryo-EM structure (fig. S10) shows that E52β connects the diiron site to α residue N322 by way of a hydrogen-bonding network (dashed lines) that involves several waters (red spheres). (**D**) Regions surrounding E/Q52 are very polar. We suggest that residues and water molecules in the yellow and pink highlighted regions are involved in proton transfer and that the residues in the green region provide the route for proton release to solvent. The dashed arrow indicates the direction toward bulk solvent.

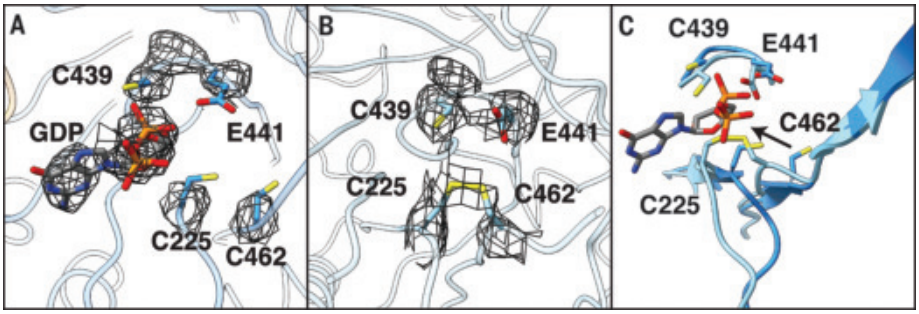

Fig. 4. The active sites of α and α′ are structurally different. (**A**) In α, density (shown in mesh) indicates the presence of substrate GDP and the absence of a disulfide between C225 and C462. Catalytic residues C439 and E441 are shown for context. (**B**) In α′, density for GDP is absent, and density indicative of a disulfide is present. (**C**) A ~3-Å shift of Cα of both C225 and C462 toward C439 and E441 within the active site of α′ is consistent with a disulfide between C225 and C462, suggesting a post-turnover state. The arrow represents the directionality of this movement between α and α′. The density thresholds for the cryo-EM maps in (A) and (B) were set to the same level (0.0384).

Further stabilization of the β-tail in its α binding pocket is derived from side chains of β-residues Q349β and E350β (Fig. 2C, fig. S9, and table S2). Q349β contacts PCET residue Y730α, and E350β contacts K154α near the effector binding site and S647α of the β-hairpin. E350β is known to play a critical role in catalysis (*15*, *16*) and in PCET gating (*17*), and we can now propose why this is the case. E350β appears to act as a latch, stabilizing the β-tail and thus the PCET pathway when substrate-effector pairs are bound and the active site is ready for catalysis. The β-hairpin is also present in class II RNR and shifts inward upon adenosylcobalamin binding to secure this cofactor in position for thiyl radical formation (*18*). Its conservation in class I RNRs was thought to be a vestige but now appears to be playing an analogous role, but with a different radical-cofactor. In both cases, this β-hairpin secures the cofactor for thiyl radical generation, which for class II RNR involves positioning adenosylcobalamin for a ~3.5-Å direct radical transfer to Cys and for class Ia RNR involves positioning a PCET pathway for a ~35-Å remote radical transfer.

The full PCET pathway is structurally resolved in our structure, revealing the position of Y356β relative to the other key residues along the PCET pathway (Fig. 3A) and showing that the radical-transfer distance is extraordinarily long. The total distance from the hydroxyl group of F_3Y122 in β to the thiyl group of C439 in α is 32.4 Å, close to the estimated 35 to 40 Å (*4*, *5*). Several features of this pathway immediately stand out, including the position of W48β directly in between Y122β and Y356β (Fig. 3A). W48β's role in PCET (if any) has been enigmatic because substitution of this residue inactivates RNR at a step before PCET—that is, cofactor formation (*19*). Seeing W48β's location, positioned at the edge of the β subunit just before Y356β, prompts us to propose that this residue plays a role in gating PCET to prevent radical loss when the β-tail is not ready to receive a radical species. Such a role will be hard to test experimentally but could be probed computationally.

Also noteworthy are the differences in distances between PCET residues in β and those in α (Fig. 3A). PCET residues in α are 2.8 to 3.5 Å apart, and side chains of Y730α and Y731α are stacked, which is consistent with

colinear transfer of an electron and a proton as suggested experimentally (*20*, *21*). By contrast, PCET residues in β are 8.0 to 12.1 Å apart, and the side chain of Y356β is not stacked with the other PCET residues. These latter distances are consistent with orthogonal electron and proton transfer (*22*) as well as with electron-transfer distances observed between cofactors within other enzymes (*23*).

Despite PCET requiring proton donors and acceptors, key PCET residue Y356β does not make direct contact with any side chains that could act as proton donor-acceptor. Y356β is, however, surrounded by polar residues that could make through-water contacts (Fig. 3). Water molecules have been implicated in orthogonal proton transfer on the basis of spectroscopic studies (*24*–*26*), including the proton transfer to Y122β by a water molecule on Fe1, which has been proposed to initiate forward PCET (Fig. 1B) (*22*). Polar residues of note along the PCET pathway include E52β (Q52β in this structure), which sits at the nexus of three polar-residue regions (Fig. 3D, yellow, pink, and green). In particular, Q52β is located directly at the α2-β2 interface, where it contacts α residue N322 (Fig. 3B), which in turn is adjacent to Y356β and R411α. The latter residue has been shown to affect the conformational flexibility of PCET residue Y731α (Fig. 3D, pink) (*26*). Additionally, E52β was previously shown to be part of a protracted hydrogen-bonding network that extends all the way into the core of the β2 subunit to the diiron cluster (*9*) (Fig. 3, C and D, yellow; and fig. S10), and last, this structure shows that Q52β is next to a loop containing E326 from both α and α′ in a region of the structure that leads to bulk solvent (Fig. 3D, green). Whereas α makes the vast majority of interactions with β, α′ does help form this part of the α-β interface. Overall, we speculate that E52β's essential function (*9*) is related to the proton transfer component of PCET, and we posit that residues and water molecules in Fig. 3D, the yellow and pink highlighted regions, will be involved in proton transfer, with the residues in the Fig. 3D green region providing the route for proton release to solvent.

Thus far, we have focused on α-β interaction, but the α′ structure is also worthy of comment. From the biochemical analyses of these RNR constructs (fig. S5) (*9*), we know that the α2β2 becomes trapped after a single turnover event—that is, after one α subunit generates product. Consistent with these biochemistry results, α′ appears to be the subunit that underwent turnover, whereas α appears to be the one that is in the preturnover state (Fig. 4). Briefly, the active site of α (Fig. 4A and fig. S11A) has clear density for a nucleoside diphosphate and no evidence of a disulfide between C225 and C462, the two redox-active cysteines that become oxidized concomitant with turnover (*27*). By contrast, α′ (Fig. 4B and fig. S11B) has no observable density in the active site corresponding to substrate or product, and the C225-C462 pair has density suggestive of a disulfide, indicating that nucleotide reduction and dithiol oxidation have occurred.

The oxidation of the C225-C462 cysteine pair is accompanied by a ~3-Å shift of Cα of both C225 and C462 toward the thiyl radical–forming C439 (Fig. 4C). This movement mirrors that observed in previous α2 crystal structures with reduced (*13*) and oxidized (*14*) cysteine residues (fig. S11, C and D). The disulfide generated by catalysis physically occludes the active site (Fig. 4B), likely facilitating product release. However, our structural data show that product cannot leave when the PCET pathway is intact because its exit is blocked (Fig. 2B). Thus, a possible molecular mechanism for PCET pathway dissolution involves disulfide formation "pushing" on product, and product pushing on β, causing β to swing from α′ to α (fig. S12). The displacement of β from α′ also appears necessary for the rereduction of the active site disulfide, which is completely buried when the PCET pathway is intact. We observed that α′ still has its specificity effector bound, indicating that product loss is not necessarily coupled with that of the substrate-specificity effector.

These structural views of α and α′ provide insight into both PCET pathway assembly and disassembly, respectively, suggesting how substrate binding could serve to create the PCET pathway pocket and how turnover (cysteine oxidation) could send a molecular push that enables pathway disassembly. The elegance of this molecular design has not escaped our attention, with one binding event or catalytic step triggering the next, guiding this enzyme through a series of elaborate conformational rearrangements that produce the requisite deoxynucleotide levels for DNA biosynthesis and repair.

The structure of the α2β2 active complex presented here is the culmination of decades of biochemical and structural studies (fig. S13) (*3*, *7*–*9*, *28*–*31*) and provides a powerful example of the utility of unnatural amino acids for trapping transient protein-protein complexes. It also provides an illustration of the benefit of cryo-EM for studying transient enzyme complexes. Use of the doubly substituted β2 slowed complex dissociation to the minute time scale of cryo-EM grid generation but not to the hour-day time scale that crystallization requires. Without the resolution revolution that the cryo-EM field is experiencing, this work would not have been possible. These resulting structural data will serve as a launching point toward answering other long-sought-after questions about both biological PCET and RNR.

REFERENCES AND NOTES

1. Y. Aye, M. Li, M. J. Long, R. S. Weiss, *Oncogene* **34**, 2011–2021 (2015).
2. S. Licht, G. J. Gerfen, J. Stubbe, *Science* **271**, 477–481 (1996).
3. E. C. Minnihan, D. G. Nocera, J. Stubbe, *Acc. Chem. Res.* **46**, 2524–2535 (2013).
4. M. R. Seyedsayamdost, C. T. Chan, V. Mugnaini, J. Stubbe, M. Bennati, *J. Am. Chem. Soc.* **129**, 15748–15749 (2007).
5. U. Uhlin, H. Eklund, *Nature* **370**, 533–539 (1994).
6. P. Nordlund, B. M. Sjöberg, H. Eklund, *Nature* **345**, 593–598 (1990).
7. E. C. Minnihan *et al.*, *Proc. Natl. Acad. Sci. U.S.A.* **110**, 3835–3840 (2013).
8. N. Ando *et al.*, *Proc. Natl. Acad. Sci. U.S.A.* **108**, 21046–21051 (2011).
9. Q. Lin *et al.*, *J. Biol. Chem.* **292**, 9229–9239 (2017).
10. E. Artin *et al.*, *Biochemistry* **48**, 11622–11629 (2009).
11. M. Uppsten, M. Färnegårdh, V. Domkin, U. Uhlin, *J. Mol. Biol.* **359**, 365–377 (2006).
12. W. C. Thomas *et al.*, *Nat. Commun.* **10**, 2653 (2019).
13. C. M. Zimanyi, P. Y. Chen, G. Kang, M. A. Funk, C. L. Drennan, *eLife* **5**, e07141 (2016).
14. M. Eriksson *et al.*, *Structure* **5**, 1077–1092 (1997).
15. I. Climent, B. M. Sjöberg, C. Y. Huang, *Biochemistry* **31**, 4801–4807 (1992).
16. K. Ravichandran *et al.*, *Biochemistry* **56**, 856–868 (2017).
17. B. L. Greene, J. Stubbe, D. G. Nocera, *J. Am. Chem. Soc.* **140**, 15744–15752 (2018).
18. M. D. Sintchak, G. Arjara, B. A. Kellogg, J. Stubbe, C. L. Drennan, *Nat. Struct. Biol.* **9**, 293–300 (2002).
19. J. M. Bollinger *et al.*, *J. Am. Chem. Soc.* **116**, 8024–8032 (1994).
20. T. Argirević, C. Riplinger, J. Stubbe, F. Neese, M. Bennati, *J. Am. Chem. Soc.* **134**, 17661–17670 (2012).
21. T. U. Nick *et al.*, *J. Am. Chem. Soc.* **137**, 289–298 (2015).
22. B. Wörsdörfer *et al.*, *J. Am. Chem. Soc.* **135**, 8585–8593 (2013).
23. S. Y. Reece, D. G. Nocera, *Annu. Rev. Biochem.* **78**, 673–699 (2009).
24. T. U. Nick, K. R. Ravichandran, J. Stubbe, M. Kasanmascheff, M. Bennati, *Biochemistry* **56**, 3647–3656 (2017).
25. B. L. Greene, A. T. Taguchi, J. Stubbe, D. G. Nocera, *J. Am. Chem. Soc.* **139**, 16657–16665 (2017).
26. M. Kasanmascheff, W. Lee, T. U. Nick, J. Stubbe, M. Bennati, *Chem. Sci.* **7**, 2170–2178 (2016).
27. S. S. Mao *et al.*, *Biochemistry* **31**, 9733–9743 (1992).
28. K. Yokoyama, U. Uhlin, J. Stubbe, *J. Am. Chem. Soc.* **132**, 15368–15379 (2010).
29. S. P. Salowe, M. A. Ator, J. Stubbe, *Biochemistry* **26**, 3408–3416 (1987).
30. K. R. Ravichandran, E. C. Minnihan, Y. Wei, D. G. Nocera, J. Stubbe, *J. Am. Chem. Soc.* **137**, 14387–14395 (2015).
31. M. Bennati *et al.*, *J. Am. Chem. Soc.* **127**, 15014–15015 (2005).

ACKNOWLEDGMENTS

We thank E. J. Brignole for his invaluable advice in preparing our samples for cryo-EM data collection and subsequent data processing, A. Kim for performing the activity assays and radical quantifications, and Q. Lin for providing the E52Q/F_3Y122-β2 protein that was essential for the success of this study. Cryo-EM data were collected at the University of Massachussetts Medical School Worcester Cryo-EM Facility, with the help of K. Song and C. Xu. **Funding:** This work was supported by the National Institutes of Health grants R35 GM126982 (to C.L.D), R01 GM29595 (to J.S.), and F32 GM123596 (A.T.T.) and by a David H. Koch Graduate Fellowship to G.K.; C.L.D. is a Howard Hughes Medical Institute investigator. **Author contributions:** G.K. and A.T.T. performed sample optimization for cryo-EM sample preparation. G.K. collected and processed the cryo-EM data and built and refined the structure. G.K., J.S., and C.L.D. wrote the manuscript. J.S. and C.L.D. supervised the research and led project conceptualization. **Competing interests:** The authors declare no competing interests. **Data and materials availability:** Atomic coordinates and cryo-EM map of the reported structure have been deposited to the Protein Data Bank (accession code 6W4X) and Electron Microscopy Data Bank (accession code EMD-21540), respectively.

SUPPLEMENTARY MATERIALS

science.sciencemag.org/content/368/6489/424/suppl/DC1
Materials and Methods
Figs. S1 to S14
Tables S1 to S4
References (*32*–*47*)

22 December 2019; accepted 16 March 2020
Published online 26 March 2020
10.1126/science.aba6794

STRUCTURAL BIOLOGY

Determination of the melanocortin-4 receptor structure identifies Ca^{2+} as a cofactor for ligand binding

Jing Yu[1,2,3], Luis E. Gimenez[4], Ciria C. Hernandez[4], Yiran Wu[1], Ariel H. Wein[5], Gye Won Han[5], Kyle McClary[5], Sanraj R. Mittal[5], Kylie Burdsall[5], Benjamin Stauch[5], Lijie Wu[1], Sophia N. Stevens[1], Alys Peisley[4], Savannah Y. Williams[4], Valerie Chen[6], Glenn L. Millhauser[6], Suwen Zhao[1,2], Roger D. Cone[4,7]*, Raymond C. Stevens[1,2,5]*

The melanocortin-4 receptor (MC4R) is involved in energy homeostasis and is an important drug target for syndromic obesity. We report the structure of the antagonist SHU9119-bound human MC4R at 2.8-angstrom resolution. Ca^{2+} is identified as a cofactor that is complexed with residues from both the receptor and peptide ligand. Extracellular Ca^{2+} increases the affinity and potency of the endogenous agonist α-melanocyte–stimulating hormone at the MC4R by 37- and 600-fold, respectively. The ability of the MC4R crystallized construct to couple to ion channel Kir7.1, while lacking cyclic adenosine monophosphate stimulation, highlights a heterotrimeric GTP-binding protein (G protein)–independent mechanism for this signaling modality. MC4R is revealed as a structurally divergent G protein–coupled receptor (GPCR), with more similarity to lipidic GPCRs than to the homologous peptidic GPCRs.

The melanocortin-4 receptor (MC4R) plays a central role in the control of energy homeostasis (*1*–*3*). As such, it is a prime therapeutic target for the treatment of syndromic and dietary obesity (*4*). MC4R is expressed in the hypothalamus, brainstem, and elsewhere in the nervous system, where it serves to coordinate food intake and energy expenditure (*1*, *5*). For example, a wide variety of heterozygous loss-of-function mutations, including those reducing heterotrimeric stimulatory G protein (G_s) coupling such as $I102^{2.62}T$ and $M218^{5.54}T$ [superscripts denote Ballesteros-Weinstein numbers (*6*)] in the receptor cause a morbid early-onset obesity syndrome (*7*, *8*), whereas gain-of-function mutations that increase receptor activity are associated with leanness (*9*). MC4R is something of a pharmacological enigma in that it exhibits a number of unusual properties, including (i) a gene dosage effect rarely seen with heterotrimeric GTP-binding protein (G protein)–coupled receptors (GPCRs) (*2*); (ii) regulation by both an endogenous agonist peptide [the tridecapeptide α-melanocyte–stimulating hormone (α-MSH)] and an endogenous antagonist or biased agonist called agouti-related protein (AgRP) (*10*, *11*); (iii) regulation by the cognate modulator melanocortin-2 receptor (MC2R) accessory protein 2 (*12*); and (iv) the ability to couple to the ion channel Kir7.1 independently of G proteins (*13*). Perhaps for this reason, drug development has been particularly challenging. The receptor is the target of the peptide drug setmelanotide, a synthetic cyclic α-MSH ligand that has been successful in the treatment of rare cases of monogenic and syndromic obesity (*14*, *15*) but not dietary obesity (*16*). More-potent small molecule and peptide MC4R agonists have failed clinical trials for common dietary obesity because of a target-mediated pressor response (*17*, *18*), which setmelanotide appears to lack. Approaches to drug development that target MC4R will thus require insight into these unusual properties of the MC4R.

GPCRs can bind a wide variety of extracellular ligands including physiological cations (*19*–*22*). Biological and pharmacological studies have previously implicated both Zn^{2+} (*23*) and Ca^{2+} (*24*, *25*) in the function of multiple members of the melanocortin receptor family. Whereas a structural and stabilization role for the Na^+-binding site has been described in high-resolution class A GPCR structures (*22*), a structural and functional role of cation interactions with the transmembrane domains of GPCRs is poorly understood. Here, we report the structure of the human MC4R bound to the melanocortin antagonist SHU9119 at 2.75-Å resolution (Fig. 1, A to C; fig. S1; and table S1) and show that Ca^{2+} is a critical cofactor for binding and function of the endogenous agonist α-MSH.

The final stabilized MC4R construct for crystallization was engineered by first introducing the following mutations into the MC4R wild-type sequence (Fig. 2A, C1 construct):

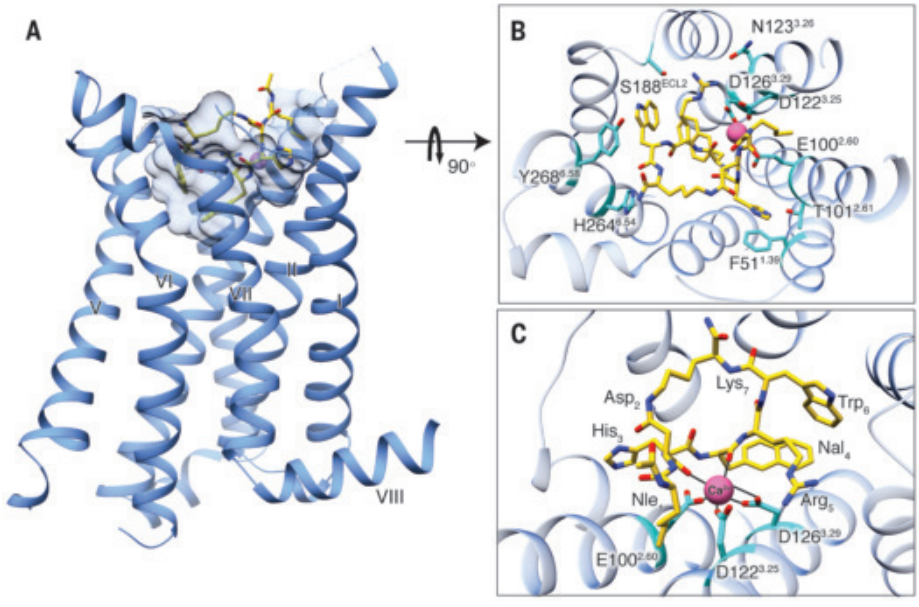

Fig. 1. Structure of SHU9119-bound MC4R. (**A**) Side view of the crystal structure of the MC4R-SHU9119 complex. MC4R is shown in blue ribbons, SHU9119 in gold sticks. Shape of the binding pocket cut off at 4.7 Å is shown by light-blue semitransparent surface model. (**B**) Structure viewed from the extracellular side shows the interaction network between MC4R, SHU9119, and the metal ion. The interaction residues on MC4R are shown in cyan. (**C**) Expanded view of the metal ion–binding site. The interactions between the metal ion, MC4R, and SHU9119 are represented by solid black lines.

[1]iHuman Institute, ShanghaiTech University, Pudong, Shanghai 201210, China. [2]School of Life Science and Technology, ShanghaiTech University, Shanghai 201210, China. [3]CAS Center for Excellence in Molecular Cell Science, Shanghai Institute of Biochemistry and Cell Biology, Chinese Academy of Sciences; University of Chinese Academy of Sciences, Shanghai 200031, China. [4]Life Sciences Institute, University of Michigan, Ann Arbor, MI 48109, USA. [5]Departments of Biological Sciences and Chemistry, Bridge Institute, USC Michelson Center for Convergent Bioscience, University of Southern California, Los Angeles, CA 90089, USA. [6]Department of Chemistry and Biochemistry, University of California Santa Cruz, Santa Cruz, CA 95064, USA. [7]Department of Molecular and Integrative Physiology, School of Medicine, University of Michigan, Ann Arbor, MI 48109, USA.
*Corresponding author. Email: rcone@umich.edu (R.D.C.); stevens@shanghaitech.edu.cn (R.C.S.)

E49$^{1.37}$V, N97$^{2.57}$L, S99$^{2.59}$F (*26*, *27*), S131$^{3.34}$A, and D298$^{7.49}$N (Fig. 2A, C2 construct). To further stabilize the receptor, we truncated N-terminal residues 1 to 15 (Fig. 2A, C3 construct) and C-terminal residues 321 to 332 (Fig. 2A, C4 construct). Last, the sequence of a portion (residues 218 to 413) of *Pyrococcus abyssi* glycogen synthase (PGS) was inserted into the receptor's third intracellular loop (ICL3) from residues H222 to R236 (Fig. 2A, C5 construct). As a result, a melting temperature of 75°C was achieved.

The MC4R-SHU9119 complex shows a classical seven-transmembrane helical bundle with a small orthosteric binding pocket containing SHU9119 and a metal ion with strong electron density, suggesting the presence of a divalent cation (Fig. 1A and fig. S2, A and B). The metal ion is coordinated by two main-chain carbonyl oxygen atoms in SHU9119 (located at Asp_2 and Nal_4; position numbers for SHU9119 residues are labeled as subscripts) and three negatively charged residues in the MC4R (E100$^{2.60}$, D122$^{3.25}$, and D126$^{3.29}$). Direct ligand interactions with the receptor include one salt bridge (Arg_5 to D126$^{3.29}$), multiple hydrogen bonds (His_3 to T101$^{2.61}$; Nal_4 main-chain amide nitrogen atom to E100$^{2.60}$; Arg_5 to N123$^{3.26}$ and S188^{ECL2}; Trp_6 to S188^{ECL2} main-chain carbonyl oxygen atom; and Trp_6 main-chain carbonyl oxygen atom to H264$^{6.54}$), and two π-π interactions (His_3 to F51$^{1.39}$ and Trp_6 to Y268$^{6.58}$) (Fig. 1, B and C, and fig. S2, A to C). The hydrophobic interactions of SHU9119 with MC4R are very expansive, because all the transmembrane helices plus the N terminus and extracellular loop 2 (ECL2) regions are involved (Fig. 1B and fig. S2C).

In vitro mutagenesis studies previously suggested a role for some of these residues in ligand binding (E100$^{2.60}$, D122$^{3.25}$, D126$^{3.29}$ and H264$^{6.54}$, and Y268$^{6.58}$) (*28*, *29*). A classification system was previously proposed (*30*) to sort obesity-associated MC4R mutations into functional classes characterized by loss of expression (class I), disrupted trafficking to the plasma membrane (class II), decreased binding affinity (class III), defective coupling to $G\alpha_s$ (class IV mutants), and obesity-associated mutations with no apparent defect (class V). As expected, some class III and IV mutants, defective in ligand binding and receptor activation, respectively, map to the ligand-binding pocket and helix VII–switch region (Fig. 3A). By contrast, class II mutants primarily defective in cellular trafficking appear to localize to a previously uncharacterized receptor domain (Fig. 3B). Class V mutants, which are associated with syndromic obesity yet exhibit normal ligand binding and $G\alpha_s$ coupling, are largely excluded from the ligand-binding pocket and helix VII switch, as would be expected (Fig. 3C), and may also be highlighting a previously uncharacterized receptor domain. It was also reported that L133$^{3.36}$ plays a role in defining the antagonist nature of SHU9119 (*31*) on MC4R, and we see an apparent interaction between this residue and the unnatural amino acid Nal_4 in SHU9119.

Notably, MC4R is structurally distinct from any reported GPCR. We compared MC4R with structures of all class A GPCRs in the inactive state by calculating the root-mean-square

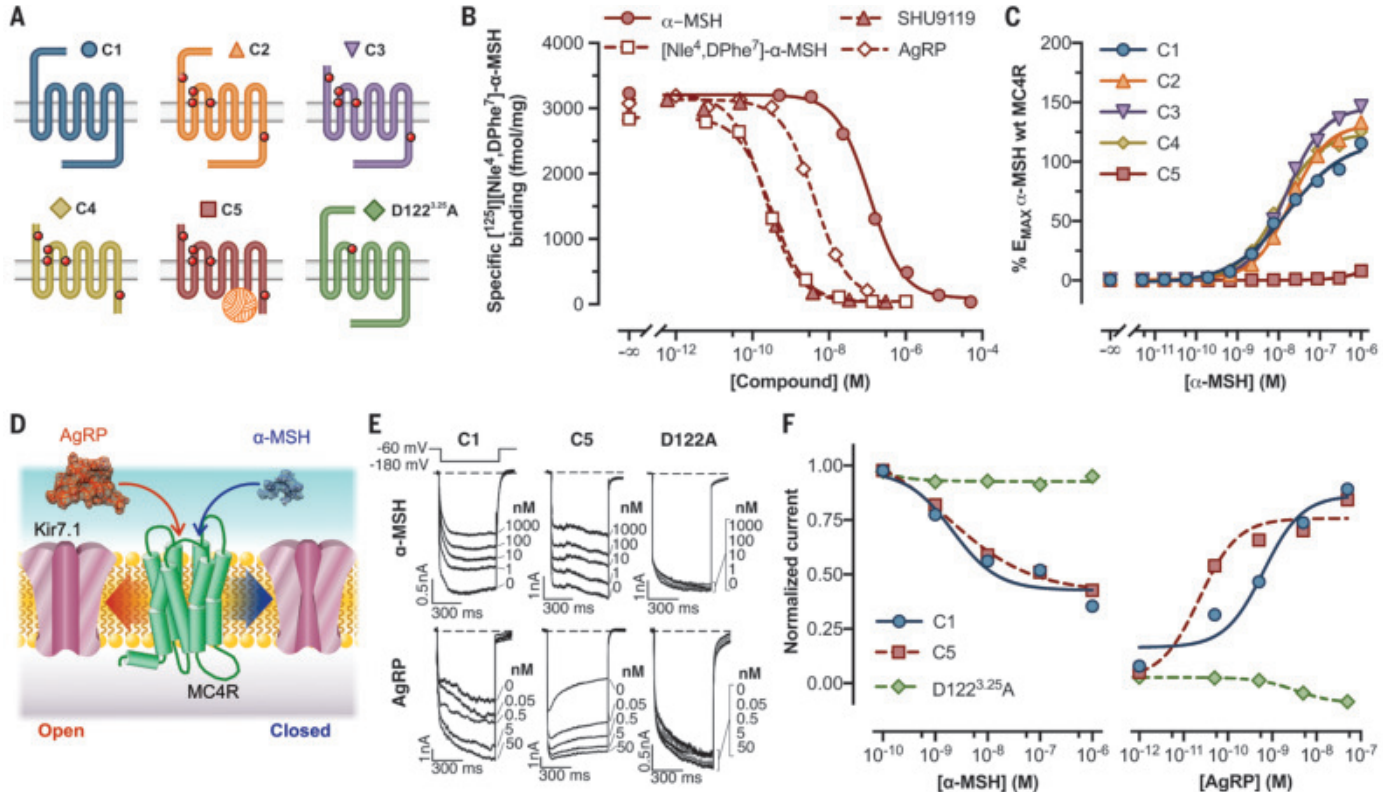

Fig. 2. Pharmacological characterization of MC4R constructs with thermostabilizing mutations, N- and C-terminal deletions, and PGS fusion. (**A**) Modifications introduced to the human MC4R sequence and color key used in the other panels. (**B**) Competition binding of indicated compounds against 80 pM ^{125}I-NDP-MSH to C5. (**C**) Live-cell α-MSH concentration-response curves for cAMP production in cells transfected with constructs C1 to C5. E_{MAX}, Maximum effect; wt, wild-type. (**D**) Diagram depicting G protein–independent Kir7.1 modulation by MC4R in the presence of α-MSH or AgRP. (**E**) Representative inwardly rectifying Kir7.1 currents elicited by hyperpolarizing the membrane to −180 mV from a holding voltage of −60 mV from cells coexpressing the channel and indicated constructs (tagged wild-type receptor construct C1 and engineered crystallized receptor construct C5). (**F**) Concentration-response curves for α-MSH and AgRP in HEK293 cells cotransfected as labeled. In (B) and (C), data points represent the mean ± standard error from a representative experiment with six to 12 replicates. Data from (E) and (F) correspond to an ensemble of three to seven different patched cells per compound concentration. All data behind (B), (C), (E), and (F) are provided in data file S1.

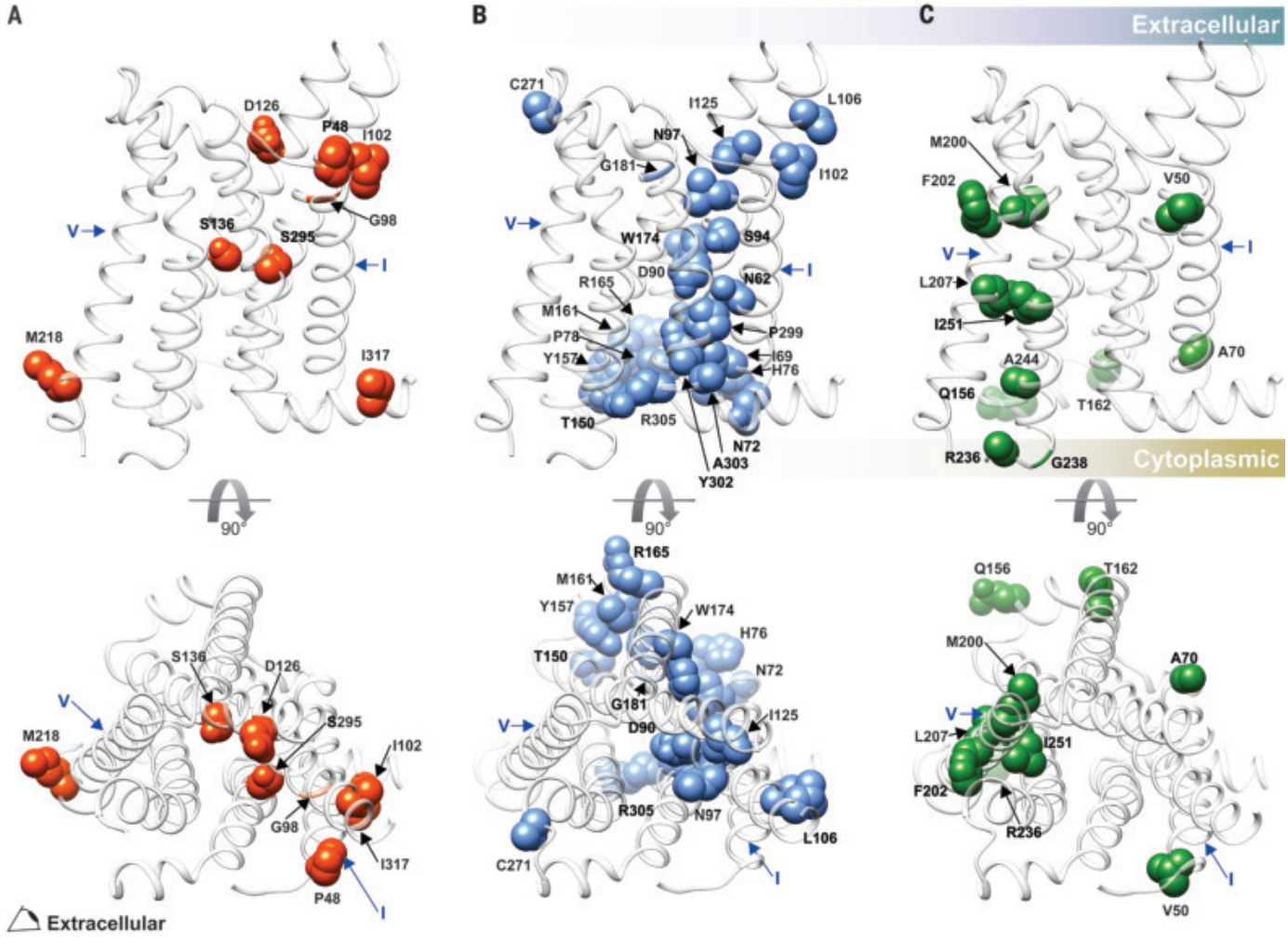

Fig. 3. Distribution of functionally characterized mutations associated with syndromic obesity on the MC4R structure. (**A**) Location of class III and IV mutations, functionally characterized as defective in ligand binding, or $G\alpha_s$ coupling, respectively. (**B**) Location of class II mutations, functionally characterized as primarily defective in trafficking. (**C**) Location of class V mutations, associated with syndromic obesity, but with normal ligand binding and $G\alpha_s$ coupling. Mutants shown here represent the subset of mutants for which we found validating functional data in the primary literature. The complete list of obesity-associated MC4R mutations and associated references from which the mutations here were derived may be found at www.mc4r.org.uk. Recently reported mutations impacting β-arrestin recruitment (9) were not included, because mutations impacting trafficking and coupling to $G\alpha_s$ also generally decrease β-arrestin recruitment. The models are shown as side views or as projections viewed from the extracellular side. Helices I and V are labeled as indicated for each model.

deviation (RMSD) of Cα atoms in the transmembrane regions. The smallest RMSD of any GPCR (excluding MC4R) to a receptor outside its subfamily is lower than 2.0 Å, whereas for MC4R, the lowest value still exceeds 2.2 Å when compared with the closest lysophosphatidic acid receptor 1 (table S2). The structural divergence between MC4R and other reported GPCR structures results primarily from its distinctive structural features, such as the very short ECL2, a missing conserved disulfide bond that usually connects ECL2 to helix III in other class A GPCRs (*32*), a distinctly outward position of helix V compared with those of other GPCRs, and the presence of nonconserved residues, including $G^{2.58}$, $D^{3.25}$, and $H^{5.50}$.

We completed a thorough pharmacological characterization of the stepwise receptor modifications (Fig. 2A, receptor forms C2 through C5) that were required to produce a crystallizable form of MC4R, as compared with the wild-type receptor (C1). All mutated constructs (C2 through C5) appear to have a favored cell-surface expression over the wild-type form, with the thermostabilizing point mutations (C2) and the deletion of the amino terminus (C3) eliciting the highest expression levels, as assessed by means of experiments with surface enzyme-linked immunosorbent assay (ELISA) (fig. S3A). The deletion of 12 C-terminal amino acids (C4) and the addition of a PGS sequence in ICL3 (C5) both showed decreased expression when compared with constructs C2 and C3 (fig. S3A). Saturation-binding studies of [^{125}I][Nle^4,DPhe^7]-α-MSH (^{125}I-NDP-MSH) (fig. S3B), a high-affinity synthetic ligand related to α-MSH, demonstrate that the crystallized form of the receptor (C5), in line with the cell-surface ELISA experiments, has a total expression level 10 times higher than that of the wild type (C1) and binds the ligand with a dissociation constant (K_d) (377 pM) similar to that of the untagged wild-type receptor (235 pM) (table S3). Competition-binding studies performed using ^{125}I-NDP-MSH at a concentration near the K_d value for this ligand demonstrate that α-MSH, AgRP, SHU9119, and [Nle^4,DPhe^7]-α-MSH (NDP-MSH) bind C5 (Fig. 2B and table S4) with a rank order of affinity similar to that

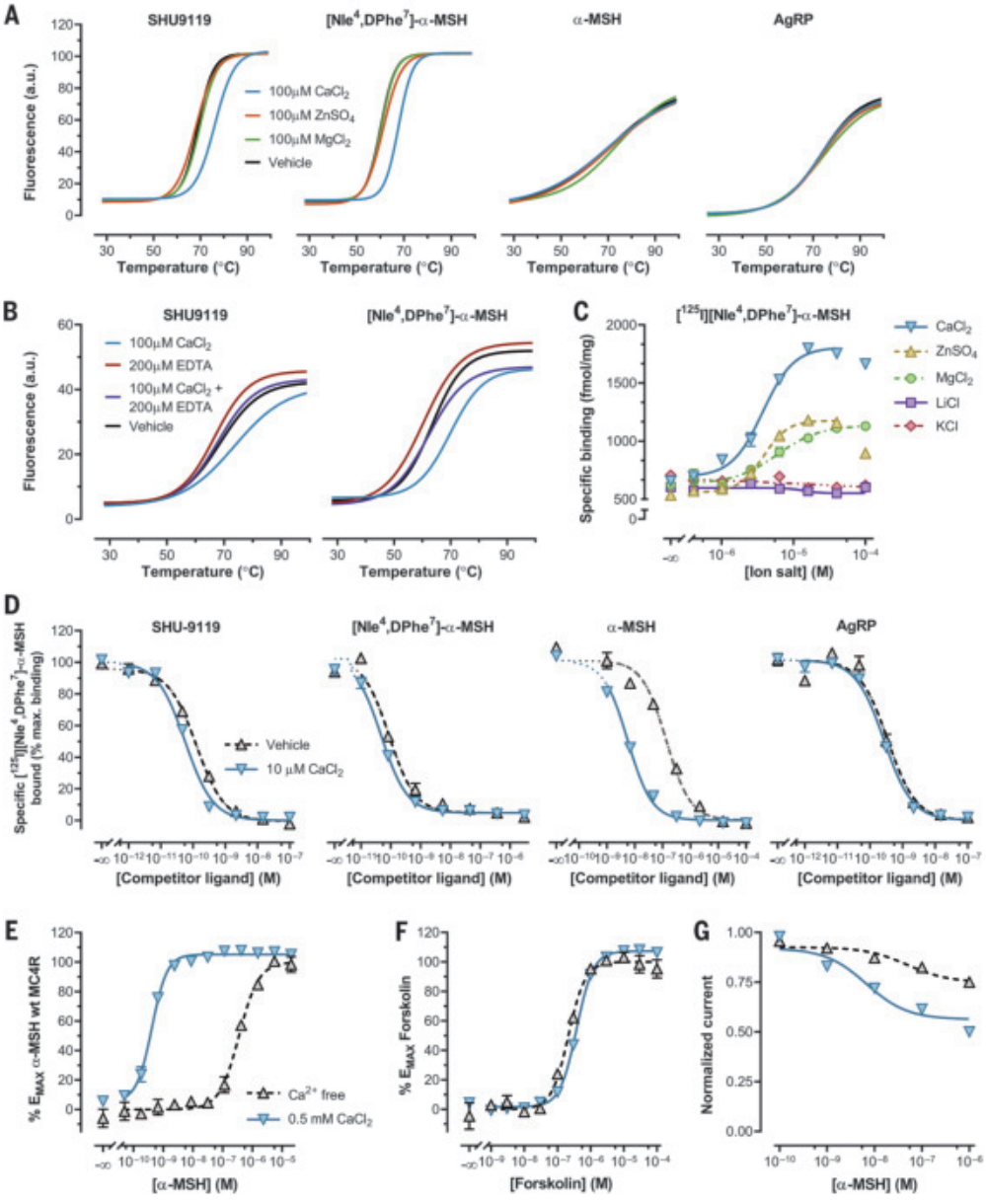

Fig. 4. Ca^{2+} affects receptor stability and modulates the binding and activation of MC4R coupling by α-MSH. (**A**) Thiol-*N*-[4-(7-diethylamino-4-methyl-3-coumarinyl)phenyl] maleimide (CPM) dye–based thermostability assays of SHU9119, NDP-MSH, α-MSH, or $AgRP_{(83–132)}$ were performed in the presence of the indicated salts at a concentration of 100 μM. (**B**) CPM dye–based thermostability assays of SHU9119 or NDP-MSH were performed in the presence of 100 μM $CaCl_2$ and/or 200 μM EDTA. a.u., arbitrary units. (**C**) Effect of different metal ions on the binding of 80 pM ^{125}I-NDP-MSH to wild-type MC4R stably expressed in HEK293 cells. (**D**) Competition binding of SHU9119, NDP-MSH, the endogenous ligand α-MSH, or the endogenous antagonist $AgRP_{(83–132)}$ against 80 pM ^{125}I-NDP-MSH in the presence or absence of 10 μM $CaCl_2$ [using the same source of MC4R as in (C)]. max., maximum. (**E** and **F**) Effect of 0.5 mM $CaCl_2$ on the concentration-response curves of α-MSH using MC4R-C1 transfected cells (E) or forskolin using untransfected HEK293 cells (F). (**G**) Effect of 0.5 mM $CaCl_2$ on α-MSH–induced Kir7.1 channel closure. Data points on (C) through (G) represent the mean ± standard error for four [(E) and (F)] to six replicates [(C) and (D)] from two independent experiments for each condition. In (G), each data point represents the aggregate of 10 to 15 individually patched cells for each agonist concentration. All data behind (C) through (G) are provided in data file S1.

seen at the wild-type receptor (data not shown). Last, using a cyclic adenosine monophosphate (cAMP)–based assay to examine coupling of C1 through C5 to $G\alpha_s$, we determined that the potency for the native agonist α-MSH and the synthetic and native antagonists SHU9119 and AgRP are nearly identical at receptors C1 to C4 (Fig. 2C; fig. S3, C and D; and table S5). As expected, the introduction of the PGS fragment into ICL3 completely blocked coupling to $G\alpha_s$ (Fig. 2C; fig. S3, C and D; and table S5).

A recent study found that regulation of the firing activity of MC4R-expressing neurons in the paraventricular nucleus of the hypothalamus could be mediated by ligand-induced coupling of the MC4R to close (by means of α-MSH) or open (by means of AgRP) the inward rectifying potassium channel Kir7.1 (Fig. 2D) (*13*). These pharmacological data suggested that neither event required G proteins. Whereas receptor construct C5 did not couple to $G\alpha_s$, whole cell–patch voltage-clamp studies using human embryonic kidney (HEK) 293 cells cotransfected with both Kir7.1 and either C1 or C5 forms of MC4R showed that the crystallized receptor form (C5) exhibits α-MSH– and AgRP-regulated coupling to Kir7.1 channels with concentration-response curves comparable (α-MSH) or even left-shifted (AgRP) relative to the wild-type (C1) receptor (Fig. 2, E and F; and table S6). We next compared concentration-response curves of Kir7.1 current inhibition and activation by α-MSH and AgRP (Fig. 2, E and F) for cells cotransfected with an MC4R mutant ($D122^{3.25}A$), previously shown to lack high-affinity ligand binding, as a result of what we have shown (Fig. 1C) to be a critical electrostatic interaction for ligand binding (*28*). We confirmed the defective cAMP stimulation (fig. S3E) and found that this mutation completely abolished coupling of MC4R to the Kir7.1 channel (Fig. 2, E and F; and table S6), demonstrating the ligand dependence of this interaction.

The most notable feature of the MC4R-SHU9119 structure is the metal ion bound to both MC4R and SHU9119 (Fig. 1, B and C; and fig. S2). This is consistent with the necessary crystallization conditions requiring 50 to 100 mM $CaCl_2$. To investigate the structural data suggesting the presence of Ca^{2+}, a series of thermal stability assays were set up to analyze the effects of different divalent cations on MC4R stability. We measured the thermal stability of the MC4R in complex with different MC4R ligands such as SHU9119,

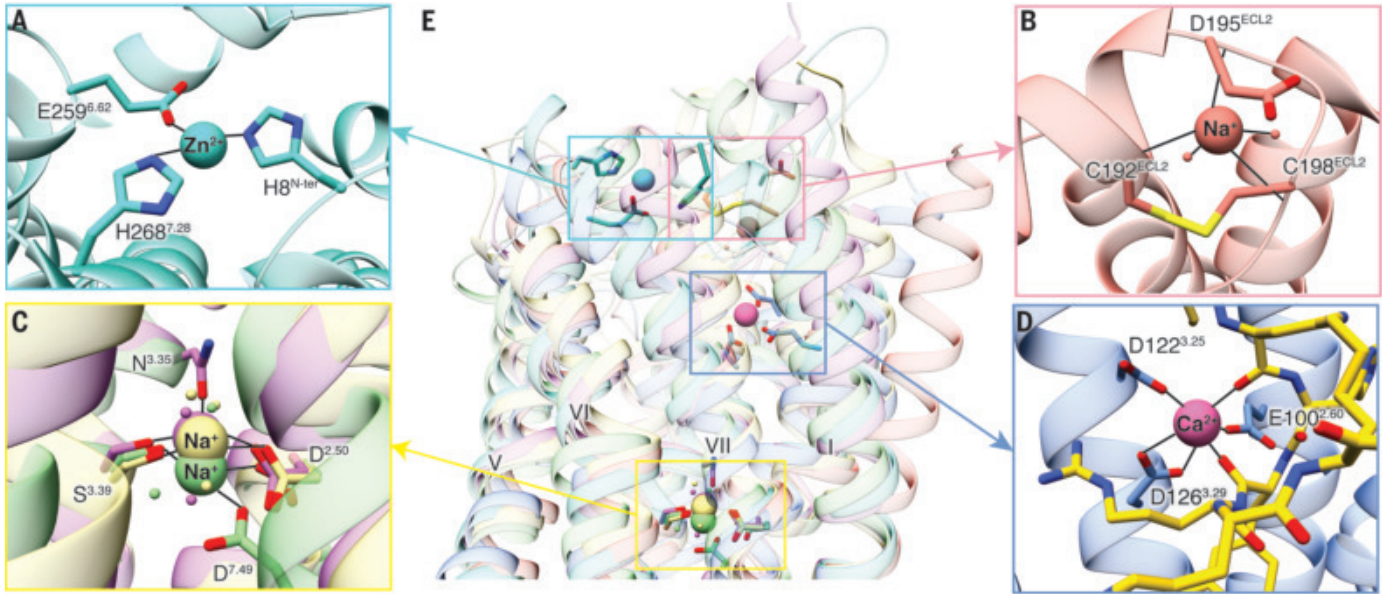

Fig. 5. Ca^{2+}-binding site of MC4R and comparison with other known GPCR cation-binding sites. (**A**) Zn^{2+} ion–binding site is located at the extracellular side of PAFR (PDB ID 5ZKQ, turquoise). Residues are shown in turquoise. (**B**) Extracellular binding site of Na^+ on β_1AR (PDB ID 4BVN, salmon) is located at the extracellular loops. (**C**) Conserved Na^+-binding site in most class A GPCRs including $D^{2.50}$ and $S^{3.39}$ (A_{2A}AR, PDB ID 4EIY, khaki). Both proteinase-activated receptor 1 (PAR1, PDB ID 3VW7, light green) and δ-type opioid receptor (DOR, PDB ID 4N6H, orchid) have an additional interaction residue, $D^{7.49}$ and $N^{3.35}$, respectively. (**D**) Binding site for Ca^{2+} in the MC4R is surrounded by residues from helices II and III and by carbonyl oxygens from the ligand, near the extracellular face. Ca^{2+} is shown as a pink sphere. The peptide ligand is represented as gold sticks. (**E**) Superposition of MC4R, PAFR, β_1AR, A_{2A}AR, PAR1, and DOR shows the comparison of known cation-binding sites. All coordinate bonds are shown in solid black lines.

NDP-MSH, α-MSH, and AgRP, in response to Ca^{2+}, Mg^{2+}, and Zn^{2+}. Only Ca^{2+} increased the thermal stability of MC4R-SHU9119 or MC4R-NDP-MSH, and the temperature decreased to the same value as the vehicle when the receptor sample was further incubated with EDTA (Fig. 4, A and B). We also performed inductively coupled plasma atomic emission spectroscopy with an aliquot of the same protein preparation (5.25 mg/ml) used for crystallization. The reported concentrations for Zn^{2+} and Mg^{2+} in this experiment were 0.21 mg/liter and <0.01 mg/liter to trace amounts, respectively, as opposed to 1.26 mg/liter for calcium, which is 100-fold higher than the concentration of Mg^{2+}. Further confirmation came from radioligand-binding experiments conducted to evaluate the effects of monovalent and divalent cations on the binding of ^{125}I-NDP-MSH to the MC4R (Fig. 4C and table S7). In concert with the structural data and effects on thermostability, Ca^{2+} was most effective at increasing ligand binding to the MC4R, with a median effective concentration (EC_{50}) of 3.7 μM (table S7). Using a competition-binding assay on wild-type receptor, we next examined the effect of 10 μM Ca^{2+} on the affinity of native and synthetic ligands. Ca^{2+} only marginally lowered the inhibition constant (K_i) values of SHU9119, AgRP, and NDP-MSH. By contrast, Ca^{2+} caused a 37-fold increase in the binding affinity of the native agonist α-MSH, lowering the K_i value from 64 to 1.7 nM (Fig. 4D and table S8). Similar results were seen when α-MSH competition-binding experiments were performed using receptor constructs C1 and C5 with K_i fold shifts of ~28 and ~99, respectively, confirming that despite the introduction of thermostabilizing mutations, N- and C-terminal truncations, and insertion of the PGS sequence, the C5 crystallization construction retains an enhanced shift toward a high-affinity state for the endogenous agonist (fig. S4 and table S9) in the presence of Ca^{2+}.

Perhaps of more importance is that the increased affinity of α-MSH for MC4R in the presence of Ca^{2+} translates into an exceedingly increased agonist potency for adenylyl cyclase stimulation and cAMP production. We found that the cAMP-level response profile for α-MSH was shifted to the left by ~600-fold, a very large effect for a sub-millimolar concentration of Ca^{2+} (Fig. 4E and table S10). Non–receptor-mediated activation of adenylyl cyclase with forskolin shows no Ca^{2+} dependence (Fig. 4F and table S10), confirming the specific role for Ca^{2+} in α-MSH–mediated MC4R stimulation. Furthermore, the importance of Ca^{2+} in MC4R function was not limited to $G\alpha_s$-elicited signaling, as we observed a left fold shift of 7.25 for the endogenous agonist in Kir7.1-MC4R–coupling dose-response experiments (Fig. 4G and table S10).

These data may help explain the unusual biological observations on the importance of extracellular Ca^{2+} for signaling of melanocortin receptors MC1R and MC2R in cells and tissues (*24*, *25*, *33*). For example, early studies demonstrated that among multiple hormones that regulate the $G\alpha_s$-mediated activation of adenylyl cyclase in adipocytes, only adrenocorticotropic hormone (ACTH) was dependent on Ca^{2+} (*24*), suggesting that Ca^{2+} may be a cofactor for ACTH binding to MC2R. Similarly, a study on the MC1R in melanocytes showed that the prolonged induction of pigmentation by NDP-MSH was Ca^{2+} dependent (*34*).

Modulation of GPCR function by physiologic cations, such as the regulation of the MC1R and MC4R by Zn^{2+} (*23*), has attracted some recent attention. Although Zn^{2+} is proposed to act as a positive allosteric modulator and weak partial agonist at the MC4R, no binding was noted in our biochemical studies. However, a binding site for Zn^{2+} coordinated by two histidine residues and one glutamic acid was recently revealed in the platelet-activating-factor receptor (PAFR) (Fig. 5A) (*35*). A role of Na^+ in the negative allosteric modulation of class A GPCRs was demonstrated at a structural and functional level when the high-resolution crystal structure of the A_{2A} adenosine receptor (A_{2A}AR) was solved (*22*). As the development of technology on membrane protein crystallography has advanced, more high-resolution structures have reported the conserved Na^+-binding site (*21*, *36*), which is mostly formed by $D^{2.50}$, $N^{3.35}$, $S^{3.39}$, $N^{7.45}$,

and N/D$^{7.49}$ (Fig. 5C). Studies on the β_1-adrenoceptor (β_1AR) reported a previously unknown Na^+-binding site located on an extracellular site coordinated by one aspartic acid, two cysteine residues, and two water molecules (Fig. 5B) (*37*). As shown in the superimposed comparison of known cation-binding sites (Fig. 5E), Ca^{2+} acts as a cofactor for ligand binding to the MC4R, occupying a different site that overlaps the MC4R orthosteric binding pocket and interacts with both the peptide ligand SHU9119 and MC4R (Fig. 5D). Our findings provide evidence supporting a different function for extracellular cations on GPCR regulation, where aside from allosteric modulators, they act as cofactors for ligand binding at the orthosteric site. Furthermore, Ca^{2+} acts in a biased fashion, regulating the affinity for the endogenous agonist α-MSH but not the endogenous inverse agonist AgRP.

MC4R has drawn much attention not only because it is the most common target of mutations causing monogenic obesity but also because it remains an important drug target for other forms of obesity as well (*14*, *15*). The features of the MC4R structure that are critical for ligand binding have evolved to allow regulation by two unrelated endogenous ligands: the linear tridecapeptide agonist α-MSH, which activates MC4R and leads to reduced appetite, and the 50–amino acid cystine-knot antagonist or biased agonist AgRP, which leads to increased food intake. We hypothesize that Ca^{2+} stabilizes the ligand-binding pocket and functions as an endogenous cofactor for the binding of α-MSH to MC4R. With an EC_{50} of ~4 μM (table S7), Ca^{2+} is likely to bind when the receptor is exposed to extracellular Ca^{2+} concentrations (~1.2 mM in the extracellular space of the central nervous system) but might not be bound intracellularly (Ca^{2+} concentration: 100 nM), thus suggesting a potential regulatory role for Ca^{2+} in α-MSH–binding dynamics. It is interesting to speculate that signaling along the phospholipase C pathway can significantly raise the intracellular Ca^{2+} concentration, and this may constitute positive feedback from signaling of MC4R or other receptors that result in Ca^{2+} flux. Our discovery highlights the plasticity and multipronged regulation and control of this receptor and will aid in next-generation structure-based drug design of therapeutics for MC4R-related obesity.

REFERENCES AND NOTES

1. W. Fan, B. A. Boston, R. A. Kesterson, V. J. Hruby, R. D. Cone, *Nature* **385**, 165–168 (1997).
2. D. Huszar *et al.*, *Cell* **88**, 131–141 (1997).
3. E. J. Anderson *et al.*, *J. Mol. Endocrinol.* **56**, T157–T174 (2016).
4. M. D. Ericson *et al.*, *Biochim. Biophys. Acta Mol. Basis Dis.* **1863** (10 Pt A), 2414–2435 (2017).
5. K. G. Mountjoy, M. T. Mortrud, M. J. Low, R. B. Simerly, R. D. Cone, *Mol. Endocrinol.* **8**, 1298–1308 (1994).
6. J. A. Ballesteros, H. Weinstein, in *Receptor Molecular Biology*, S. C. Sealfon, Ed. (Academic Press, 1995), vol. 25, pp. 366-428.
7. C. Lubrano-Berthelier *et al.*, *J. Clin. Endocrinol. Metab.* **91**, 1811–1818 (2006).
8. R. Rong *et al.*, *Clin. Endocrinol. (Oxf.)* **65**, 198–205 (2006).
9. L. A. Lotta *et al.*, *Cell* **177**, 597–607.e9 (2019).
10. M. M. Ollmann *et al.*, *Science* **278**, 135–138 (1997).
11. T. R. Büch, D. Heling, E. Damm, T. Gudermann, A. Breit, *J. Biol. Chem.* **284**, 26411–26420 (2009).
12. M. Asai *et al.*, *Science* **341**, 275–278 (2013).
13. M. Ghamari-Langroudi *et al.*, *Nature* **520**, 94–98 (2015).
14. P. Kühnen *et al.*, *N. Engl. J. Med.* **375**, 240–246 (2016).
15. K. Clément *et al.*, *Nat. Med.* **24**, 551–555 (2018).
16. K. Y. Chen *et al.*, *J. Clin. Endocrinol. Metab.* **100**, 1639–1645 (2015).
17. J. R. Greenfield *et al.*, *N. Engl. J. Med.* **360**, 44–52 (2009).
18. R. Krishna *et al.*, *Clin. Pharmacol. Ther.* **86**, 659–666 (2009).
19. B. Zarzycka, S. A. Zaidi, B. L. Roth, V. Katritch, *Pharmacol. Rev.* **71**, 571–595 (2019).
20. A. D. White *et al.*, *Proc. Natl. Acad. Sci. U.S.A.* **116**, 3294–3299 (2019).
21. C. Zhang *et al.*, *Nature* **492**, 387–392 (2012).
22. W. Liu *et al.*, *Science* **337**, 232–236 (2012).
23. B. Holst, C. E. Elling, T. W. Schwartz, *J. Biol. Chem.* **277**, 47662–47670 (2002).
24. L. Birnbaumer, M. Rodbell, *J. Biol. Chem.* **244**, 3477–3482 (1969).
25. Y. Salomon, *Mol. Cell. Endocrinol.* **70**, 139–145 (1990).
26. P. Popov *et al.*, *eLife* **7**, e34729 (2018).
27. B. Stauch *et al.*, *Nature* **569**, 284–288 (2019).
28. Y. K. Yang *et al.*, *Biochemistry* **39**, 14900–14911 (2000).
29. Y. Yang, C. M. Harmon, *Biochim. Biophys. Acta Mol. Basis Dis.* **1863** (10 Pt A), 2436–2447 (2017).
30. Y. X. Tao, *Mol. Cell. Endocrinol.* **239**, 1–14 (2005).
31. Y. Yang *et al.*, *J. Biol. Chem.* **277**, 20328–20335 (2002).
32. A. J. Venkatakrishnan *et al.*, *Nature* **494**, 185–194 (2013).
33. S. Kopanchuk *et al.*, *Eur. J. Pharmacol.* **512**, 85–95 (2005).
34. M. E. Hadley, B. Anderson, C. B. Heward, T. K. Sawyer, V. J. Hruby, *Science* **213**, 1025–1027 (1981).
35. C. Cao *et al.*, *Nat. Struct. Mol. Biol.* **25**, 488–495 (2018).
36. G. Fenalti *et al.*, *Nature* **506**, 191–196 (2014).
37. J. L. Miller-Gallacher *et al.*, *PLOS ONE* **9**, e92727 (2014).

ACKNOWLEDGMENTS

The synchrotron radiation experiments were performed at the BL41XU and BL45XU of SPring-8 with approval of the Japan Synchrotron Radiation Research Institute (JASRI) (proposal numbers 2019A2520, 2019A2522, 2019A2523, 2019A2524). We thank Z.-J. Liu, T. Hua, L. Shen, and all staff from BL41XU and BL45XU for their help with data collection. We thank the Cloning, Cell Expression, Assay, and Protein Purification Core Facilities of the iHuman Institute for their support. We thank A. Walker for assistance with the manuscript, and we also thank J. Smith, J. Stuckey, and T. Claff for critical insights or reading of the manuscript. We thank P. Popov and V. Katritch for designing the thermostabilizing mutations. R.C.S. acknowledges that USC is his primary affiliation. **Funding:** We thank the Shanghai Municipal Government, ShanghaiTech University, and the GPCR Consortium for financial support. This work was supported by the National Institutes of Health [grants R01DK070332 (to R.D.C.) and R01DK110403 (to G.L.M.)]. B.S. was funded by an EMBO long-term postdoctoral fellowship (ALTF 677-2014). **Author contributions:** R.C.S. started the project while at The Scripps Research Institute and managed its efforts at Scripps, USC, and iHuman Institute. J.Y., L.E.G., C.C.H., A.H.W., K.M., S.R.M., K.B., B.S., S.N.S., A.P., S.Y.W., V.C., R.D.C., and R.C.S. conceptualized the research program and conducted experiments. J.Y., L.E.G., C.C.H., R.D.C., and R.C.S. wrote the manuscript. All authors edited and revised the manuscript. **Competing interests:** R.C.S. is the founder of a GPCR structure–based drug discovery company called ShouTi. R.D.C. is a founder of a melanocortin receptor drug discovery company called Courage Therapeutics. **Data and materials availability:** Coordinates and structure factors have been deposited in the Protein Data Bank (PDB) with identification code 6W25. Other data are available in the manuscript or supplementary materials.

SUPPLEMENTARY MATERIALS

science.sciencemag.org/content/368/6489/428/suppl/DC1
Figs. S1 to S4
Tables S1 to S10
References (*38*–*54*)
Data File S1

21 October 2019; accepted 9 March 2020
10.1126/science.aaz8995

HIGH-LEVEL GLOBAL TALENTS RECRUITMENT

2020 Global Online Job Fair (www.edu.cn/cv)

April 24, 2020 Specialty Session (Science & Engineering)

May 08, 2020 North Area of East China Doctoral Talents Recruitment

May 09, 2020 Hong Kong, Macao, Taiwan and the China Great Bay Area Doctoral Talents Recruitment

May 15, 2020 High-level Global Talents Recruitment

Qualification for Applicants

Global scholars, Doctor and Post-doctor

Key Disciplines

Life Sciences, Health Sciences and Physical Sciences

Participating Approach

Please send your CV to consultant@acabridge.edu.cn for 2020 Global Online Job Fair

Scan to check the sessions

EVEN SEPARATED BY MOUNTAINS AND RIVERS, WE HAVE OUR BLOOD TIGHTLY CONNECTED

The Coronavirus pandemic has forced many of us to consider different ways of working and communicating. Chinese universities and colleges are now holding online job fairs to help overseas scholars explore career options in China.

Fight with One Heart to Combat COVID-19

In these challenging times, Chinese universities and colleges have shot videos, sending greetings and wishes to their overseas compatriots. Please scan below QR code to receive messages of love and well wishes from high schools in your motherland.

香港中文大學(深圳)
The Chinese University of Hong Kong, Shenzhen

Faculty Positions in Biomedical Engineering
The Chinese University of Hong Kong, Shenzhen

The Chinese University of Hong Kong, Shenzhen (CUHK-Shenzhen) invites applications for full-time faculty positions in Biomedical Engineering (BME). Interested candidates in biomaterials and regenerative medicine, biomechanics, biomedical imaging, biomolecular engineering and nanomedicine, biosensors and bioelectronics, immunoengineering, medical devices and robotics, neuroengineering, systems and synthetic biology, tissue engineering and regenerative medicine are welcome to apply at academic ranks of professors/associate professors/assistant professors/lecturers. Qualified candidates must have an earned doctoral degree in biomedical sciences, bioengineering and/or related disciplines, postdoctoral training and work experience. Applicants for Professors and Associate Professors should have an established research program with funding history, teaching experiences and an excellent publication record. Lecturer and Senior Lecturer positions are also available for candidates with teaching experience in biomedical engineering.

Established in 2014, CUHK-Shenzhen is a research-intensive university that inherits the fine academic traditions of The Chinese University of Hong Kong. The University adopts a tenure-track system for Assistant Professors and above. English is the main language for classroom teaching, and graduates receive degrees of The Chinese University of Hong Kong. The BME program was jointly established between the School of Life and Health Sciences (LHS) and the School of Science and Engineering (SSE), with LHS hosting the program and taking part in basic medical teaching/research in the School of Medicine. Qualified applicants may receive primary appointment at either LHS or SSE. Please visit **lhs.cuhk.edu.cn** for additional descriptions of the program. Interested applicants should submit their curriculum vitae, teaching statements and research descriptions to: http://academicrecruit.cuhk.edu.cn/lhs. Applications will be reviewed on a rolling basis until the positions are filled.

2020 High-level Talents Online Job Fair

WITH LOVE BEYOND MOUNTAINS AND SEAS, WE MEET ON "CLOUD" RECRUITMENT.

More than 10 online job fairs
Over 3000 scholars in real-time communication with 90 universities

Time:
00:30-14:30 GMT(08:30-22:30 Beijing time) Friday, 15 May 2020

Qualification: Global scholars, Doctor and Postdoc
Disciplines: All disciplines

www.edu.cn/cv

Contact: Zhao Jia
Tel: (+86) 13426240515（Wechat）
E-mail: zhaojia@eol.cn

Register for applying

Overseas *Chinese Scholars'* Visit to Top Chinese Universities

Check the Details from www.edu.cn/zgx

- **10,000+ academic job vacancies in China**
- **Free one-to-one consultation service**

Send your CV to *consultant@acabridge.edu.cn*

海外学者中国行

上海师范大学 中国石油大学 中南民族大学

Science Careers online @sciencecareers.org

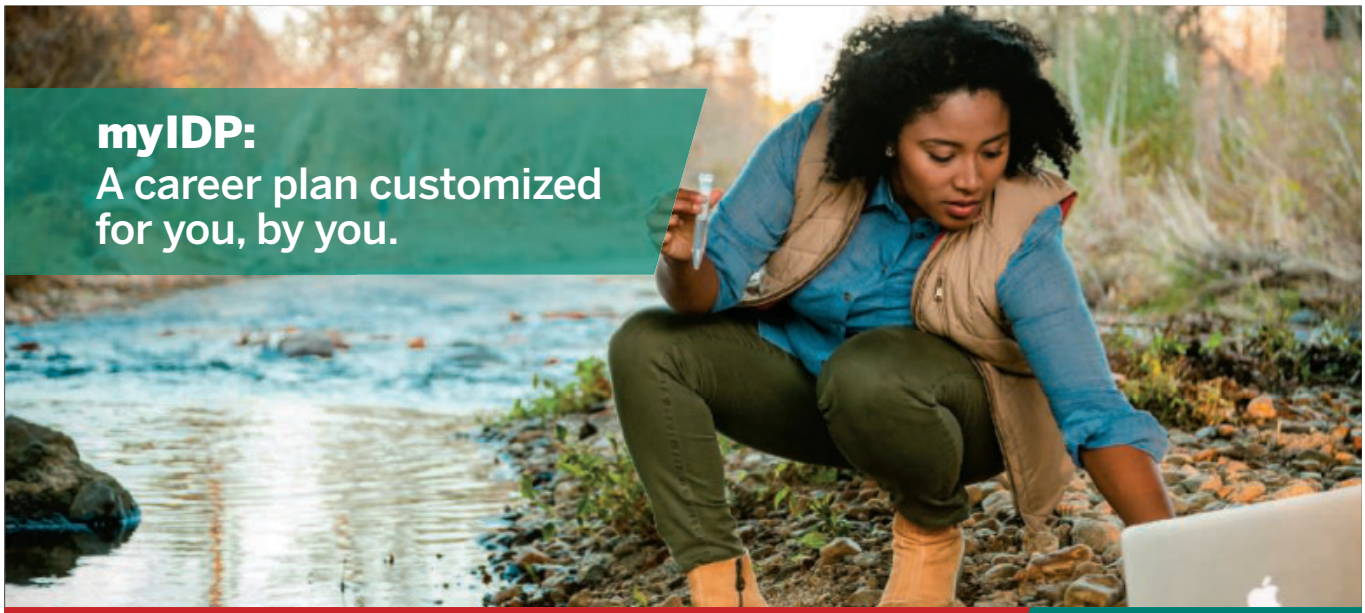

For your career in science, there's only one Science

Features in myIDP include:

- Exercises to help you examine your skills, interests, and values.
- A list of 20 scientific career paths with a prediction of which ones best fit your skills and interests.
- A tool for setting strategic goals for the coming year, with optional reminders to keep you on track.
- Articles and resources to guide you through the process.
- Options to save materials online and print them for further review and discussion.
- Ability to select which portion of your IDP you wish to share with advisors, mentors, or others.
- A certificate of completion for users that finish myIDP.

myIDP

Visit the website and start planning today!
myIDP.sciencecareers.org

Science Careers AAAS In partnership with:

FASEB Federation of American Societies for Experimental Biology
UMASS University of Massachusetts Medical School
UCSF University of California San Francisco
UIC
BURROUGHS WELLCOME FUND

SPECIAL JOB FOCUS:

Biotechnology

Issue date: May 22
Book ads by May 7

Ads accepted until May 15 if space allows

Deliver your message to a global audience of targeted, qualified scientists.

129,566
subscribers in print every week

33,295
yearly unique active job seekers searching for biotechnology jobs

16,250
yearly applications submitted for biotechnology positions

What makes *Science* the best choice for recruiting?

- Read and respected by 400,000 readers around the globe
- Your ad dollars support AAAS and its programs, which strengthens the global scientific community.

Why choose this job focus for your advertisement?

- Relevant ads lead off the career section with a special biotechnology banner.

Expand your exposure by posting your print ad online:

- Additional marketing driving relevant job seekers to the job board.

To book your ad, contact:
advertise@sciencecareers.org

The Americas
202 326 6577
Europe
+44 (0) 1223 326527
Japan
+81 3 6459 4174
China/Korea/Singapore/ Taiwan
+86 131 4114 0012

Science Careers
AAAS
SCIENCECAREERS.ORG

Produced by the *Science*/AAAS Custom Publishing Office.

FOR RECRUITMENT IN SCIENCE, THERE'S ONLY ONE *SCIENCE*.

ScienceCareers online @sciencecareers.org

By **Jennifer Kong** *and* **Steven Chan**

Advice for the worried

Jennifer—a postdoc—had been working from home for 4 weeks. Anxious about the COVID-19 pandemic, she was having trouble focusing on her research. She knew her mental health had deteriorated and that she needed advice to stay motivated. So she reached out to Steven, a friend who also happens to be a practicing psychiatrist. He didn't solve all of Jennifer's problems. But he did provide a new lens to view them through—as well as concrete steps she could take to improve her mental health. Our conversation has been edited for clarity and brevity.

JENNIFER: In academia, we are often encouraged to suck it up when problems arise. I am currently writing two papers. I know others who are writing grants. Should we expect to use this "time away from the lab" to be superproductive?

STEVEN: Working in a COVID-19 world is not normal. You shouldn't dwell on guilt if you're not functioning at maximum productivity levels. You need time to process the grief that comes with the loss of your former work life and social life.

"When dealing with anxiety, it's important to ... practice activities that are restorative."

J: I occasionally find myself spiraling down a hole of despair, spending hours reading about all the terrible things happening in the world. The news makes me feel sad and helpless, which in turn zaps all the motivation out of my day. What should I do?

S: In these spirals, it is important to recognize that there's a lot happening right now that you can't control. Even though it is incredibly hard, shift your attention to things you can control. For example, you cannot control the number of people who are dying from COVID-19. But you can do your part to maintain social distancing.

J: I am worried about members of my family getting sick. I'm also worried about my future in academia because many universities are instituting hiring freezes. How can I get rid of all this worry?

S: Try compartmentalizing the worry into a time block. Spend 20 minutes each day writing down and acknowledging your feelings. Then, think about reasonable solutions. For example, you could brainstorm how you could secure funding to extend your postdoc, which would give you more time to publish papers and apply for academic jobs next year. You could also learn about jobs that might interest you in other sectors, such as industry.

J: Sometimes I wake up in the middle of the night and can't go back to sleep. I'm physically tired, but my brain is restless. I end up just lying there, thinking and worrying about everything that's going on. Is this anxiety?

S: It could be. Anxiety is a persistent feeling of worry. Sometimes it is constant, while other times it rushes over you all at once. When dealing with anxiety, it's important to assess your emotions and talk about what you're going through with trusted friends and family. You should also practice activities that are restorative and relaxing, especially before bedtime. Listen to music, take a hot shower, read a book, or do something else that you enjoy.

J: These past few weeks have been difficult for so many people, and I fear it'll get worse. However, I have also been inspired by good things that people are doing. For example, students, postdocs, and faculty members at our university have donated thousands of dollars to support our furloughed food service workers. It fills me with some confidence that we will overcome this.

S: That's great. These are trying times, but they'll be easier if we do what we can to support one another. A key strategy for combating sadness, stress, and anxiety is to express gratitude for what you do have. Keep that up.

Jennifer Kong is a postdoc and Steven Chan is a clinical assistant professor; both of them are at Stanford University. Steven is also a medical director for the U.S. Department of Veterans Affairs in Palo Alto, California.

ILLUSTRATION: ROBERT NEUBECKER

ScienceRobotics.org

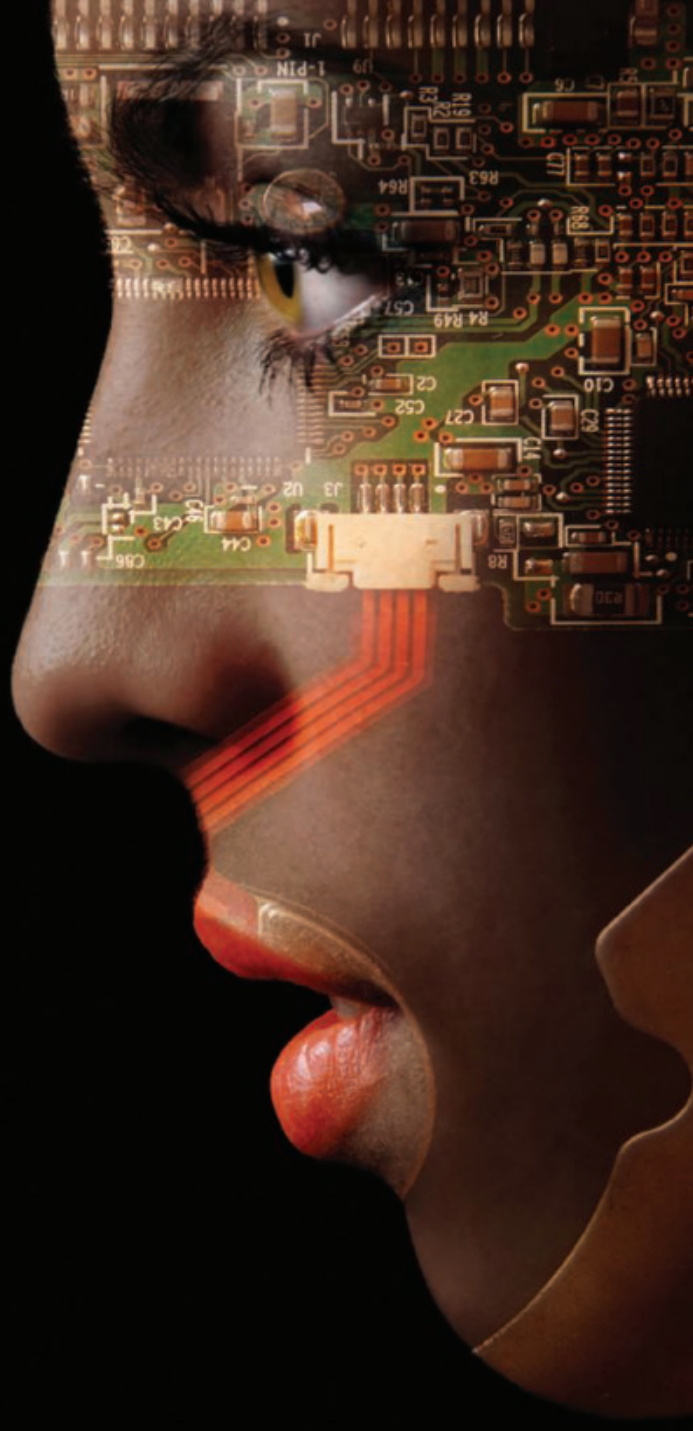

DOESN'T YOUR RESEARCH DESERVE THE BEST READERS?

Submit your research: **cts.ScienceMag.org**

Science Robotics
AAAS

Twitter: @SciRobotics
Facebook: @ScienceRobotics

PINS

RESTORING HOPE

Beijing PINS Medical Equipment Co. Ltd. was established in 2008.

As an innovative high-tech enterprise with focus on neuromodulation, PINS Medical has developed a variety of clinical products, which include stimulators for deep brain, vagus nerve, spinal cord, and sacral nerve stimulation therapies. PINS Medical devotes itself to providing cutting-edge treatments for patients who suffer from neurological disorders, such as Parkinson's disease, epilepsy, chronic pain, and uroclepsia.

The name of PINS is derived from a Chinese word with the original meaning of "Magic Pin," the ability to cure disease. PINS is also an abbreviation of "**P**atient **I**s **N**o. 1 alway**S**." This message clearly represents the goal of PINS Medical for "restoring hope," not simply as an innovation company but also across society to citizens.

www.pinsmedical.com/html/en/ info@pinsmedical.com